STUDIES OF INTERACTION OF DYE MOLECULES WITH TiO₂ BROOKITE CLUSTERS FOR APPLICATION IN DYE SENSITIZED SOLAR CELLS

University of Venda

By

Elegbeleye Ife Fortunate

16023582

Research Thesis for the

Doctor of Philosophy Degree in the Department of Physics

In the

School of Mathematical and Natural Sciences

University of Venda

Thohoyandou, Limpopo

South Africa

Student: Elegbeleye Ife Fortunate (University of Venda)

Promoter 1: Dr. EN Maluta (University of Venda)

Promoter 2: Prof. RR Maphanga (CSIR/UL)

Declaration

I, Ife Elegbeleye declare that this research thesis titled "Studies of interaction of dye molecules with TiO_2 brookite clusters for application in dye sensitized solar cells" is my original work and has not been submitted for any degree at any other university or institution. The research does not contain other persons' writing unless specifically acknowledged and referenced accordingly.

Signed (Student)………………………………….Date…..……………………………..

Elegbeleye Ife Fortunate

Dedication

I dedicate this research to the Almighty God for making it possible for me to complete this degree. To My lovely husband, Femi Elegbeleye, wonderful Children, Ore-Ofe Charis Elegbeleye, Jesulona Emmanuel Elegbeleye and to my supervisors Dr NE Maluta and Prof RR Maphanga without whom this work would not have been completed in record time.

Acknowledgement

My sincere thanks go to almighty God for his unending love and grace towards me.

I am indebted to my supervisor, Dr NE Maluta for his contributions and understanding. He sacrificed so much time to guide me through this research work, reading and guiding me through every stage of my proposal, methodology, results, analysis and write up to make necessary corrections and always encouraging to do better and give my best to my endeavours. May God reward you in multiple folds with more successful years to come sir.

I am very grateful to my Co- supervisor, Prof RR Maphanga for being both a mentor and supervisor to me, I'm grateful to her for her guidance through the rudiments of my research and for her tremendous contributions to the research and for the success of this work as a whole. God bless you Prof.

I am forever grateful to my parents, Mr. and Mrs. Aseweje for their immeasurable love and contributions spiritually, morally and financially towards my success in life and academics. May God satisfy you with long life to enjoy the fruits of your labour.

The incessant love, understanding and care showed to me by Mr. Femi Elegbeleye has further proved your worth, you are a blessing from God and a pillar of strength. I love you. To My wonderful daughter, Ore-ofe Charis Elegbeleye and my Son Elegbeleye Jesulona, Emmanuel. Thanks for your sacrifice and co-operation towards the success of this work. God bless keep and preserve you.

I commend the significant contribution of my siblings: Mr. and Mrs. Omotoso, Ireti, Tolu and Faith, towards my success in life. God made you beautiful fences around my life, you are indeed wonderful. Thanks for the unconditional love and encouragement toward my success in life.

To all the lecturers in the Department of Physics, University of Venda who contributed to this work and to my success, thanks for the love I received in the department, the knowledge imparted and support towards the success of the work.

I would like to acknowledge the financial support from DAAD. I also thank the University of Venda for the support to carry out this research and Centre for High Performance Computing (CHPC) for using their computing resources of CSIR, Capetown, South Africa. Special thanks to the University of Limpopo Materials Modelling Centre for their support towards our

University of Venda

University of Venda

Abstract

Dye sensitized solar cells (DSSCs) have attracted rapid interest over the recent years with prospect of emerging as a viable alternative to conventional silicon based solar cells. The photoanode of DSSCs comprises of dye molecules anchored to the surface of semiconductors such as TiO_2. However, the major drawback of Titanium dioxide (TiO_2) is its wide band gap (3.0 eV to 3.2 eV) which limits its photocatalytic activities to the ultraviolet region of the electromagnetic spectrum. Understanding the interaction of dye molecules with the surfaces of TiO_2 is crucial for optimizing light-harvesting, photoconversion function and photocurrent densities in DSSCs. The three polymorphs of TiO_2 are anatase, brookite and rutile. The optical properties of brookite semiconductor have not been much studied although brookite has been reported to have good photocatalytic properties.

In this work, Density functional theory (DFT) computational approach was used through various computational softwares which are CASTEP, GAUSSIAN, GAUSSUM, GPAW, ASE, and AVOGADRO with B3LYP, LANL2DZ, PBE, and GGA functional to explore the photocatalytic properties of the typical ruthenium N3 complex, polyenediphenyl-aniline dye moiety, croconate dye molecules and three modelled surfaces of brookite which are $(TiO_2)_5$, $(TiO_2)_8$ and $(TiO_2)_{68}$ for application in DSSCs. We also studied the absorption of the corresponding dye molecules on the three surfaces of brookite TiO_2.

Our findings showed strong binding ability, good electronic coupling, efficient charge separation, spontaneous electron injection and good spectral properties upon adsorption of the dye molecules to brookite TiO_2 semiconductor clusters. Our findings on the optical absorption spectra of ruthenium N3 dye, croconate dye and polyenediphenyl-aniline dye molecule absorbed on $(TiO_2)_5$ and $(TiO_2)_8$ brookite cluster shows bathocromatic shift of the absorption maxima to higher wavelength and improve optical response of TiO_2 brookite cluster. A red spectra shift and absorption over a wide range of the solar spectrum in the visible and near infra-red region of the solar spectrum was achieved upon absorption of the ruthenium N3 complex and polyenediphenyl-aniline dye molecules on $(TiO_2)_5$ and $(TiO_2)_8$ brookite cluster.

The results generally suggest that the absorption of dye molecules on TiO_2 brookite cluster improves its spectra responsivity in the UV region and makes it possible to absorb over the whole spectrum range, that is, the UV, visible and near infra – red region of the solar spectrum. Our findings also showed good electron injection kinetics from the dye to TiO_2 brookite clusters, which suggests higher photocurrents density and open circuit voltage in DSSCs.

Table of contents

List of Figures

© University of Venda

List of Tables

University of Venda

List of Abbreviation

Dye sensitized solar cells	DSSCs
Density functional theory	DFT
Time dependent density functional theory	TD-DFT
The intergovernmental panel on climate change	IPCC
Photovoltaic cells	PV
Incident photon conversion efficiency	IPCE
Fill factor	FF
Short circuit current density)	I_{SC}
Open circuit voltage	V_{OC}
Lowest occupied molecular orbital	LUMO
Highest occupied molecular orbital	HOMO
Incident optical power	P_{in}
Cadmium telluride	CdTe
Copper-indium-selenide	CIS
Copper-indium-gallium-diselenide	CIGS
Organic solar cells	OSCs
Titanium dioxide	TiO_2
International energy agency	IEA

Publications/Conferences Presentations

1. Ife Fortunate Elegbeleye, Nnditshedzeni Eric Maluta and Rapela Regina Maphanga (2018) Density functional theory study of promising polyene-diphenylaniline organic chromophores for dye-sensitized solar cell applications. . *Cogent Engineering,* 5, 1532778.2. (Attached)

2. Ife Fortunate Elegbeleye, Nnditshedzeni Eric Maluta and Rapela Regina Maphanga Density Functional Theory Studies of the adsorption of ruthenium (N3) dye on TiO_2 brookite cluster for application in dye sensitized solar cells (Accepted for book publication).

3.Ranwaha Tshifhiwa Steven, Ife Fortunate Elegbeleye, Nnditshedzeni Eric Maluta and Rapela Regina Maphanga Computational study of electronic and optical properties of the croconate dye molecules adsorbed on TiO_2 brookite cluster for dye sensitized solar cell application (In preparation) Presented as poster at South African Institute of Physics conference 2017.

4. Ife Fortunate Elegbeleye, Nnditshedzeni Eric Maluta, Rapela Regina Maphanga, Michael Walter, Oliver Brugner. Adsorption of polyene-diphenylaniline dye on TiO_2 brookite cluster: A density functional theory approach to understand the photocatalytic properties of TiO_2 brookite (In preparation). Presented as poster at South African Institute of Physics conference 2018.

5. Ife Fortunate Elegbeleye, Nnditshedzeni Eric Maluta and Rapela Regina Maphanga. Density Functional theory study of optical and electronic properties of $(TiO_2)_{n=5, 8, 68}$ clusters for application in organic and hybrid organic-inorganic solar cells (In preparation)

Research institutions attended

1. Centre for Scientific and Industrial Research (CSIR), Pretoria, South Africa (June-August 2018).

2. Functional Nanosystem, Freiburg Centre for Interactive Materials and Bioinspired Technologies (FIT), Albert Ludwig's University, Freiburg, Germany. (September 2018-February 2019)

CHAPTER ONE

1.0 GENERAL INTRODUCTION

The escalating world's population is posing unending increase in demand and consumption of energy. According to BP (British petroleum) Statistical Review of World Energy 2015 of (see Figure 1) [1], fossil fuels (coal, oil and natural gas) constitutes larger percentage of energy being produced and utilized in meeting these demands around the world. The continuous combustion of fossil fuel has resulted in emissions of CO_2 and other greenhouses gases into the biomass. High CO_2 levels have raised environmental concerns such as global warming, acidic rain, unhealthy eco systems and deforestation etc. [2]. The Intergovernmental Panel on Climate Change (IPCC), projected that, "the global average surface temperature might rise from 1.8 °C to 4.0 °C this century, and up to 6.4 °C in the worst-case scenario," if no active measure is taken to reduce greenhouse gas emissions [3]. Climate change is undoubtedly one of the major man-made threats globally encountered, as is the case presently. Increase in CO_2 content and other greenhouse gas emissions has already induced high temperatures, extreme floods, droughts, intensified tornadoes and tropical storms. If the alarming combustion of fossil fuel is not checked, it will take humanity to a crossing point of not only floods, droughts and heavier storms occurring but variations in ocean flow, sea rise, melting of glaciers and arctic ice, which will be highly disastrous to mankind [4].

Apart from the climatic trauma of continuous combustion of fossil fuel, the unprecedented flunctuation of fossil fuel prices poses serious threats to the economy and political stability of oil producing nations [5] as economic activities largely require energy demand to boom. The current policies of International Energy Agency (IEA) have projected 45 % increase in the global energy demand by 2040 [6]. Since non-renewables constitute larger percentage presently utilized in meeting energy demands globally, eventually there might be shortage of resources in the future or the environment may become inhabitable to mankind. Hence, the quest of clean, sustainable, environmentally friendly and affordable energy resources is of extreme importance.
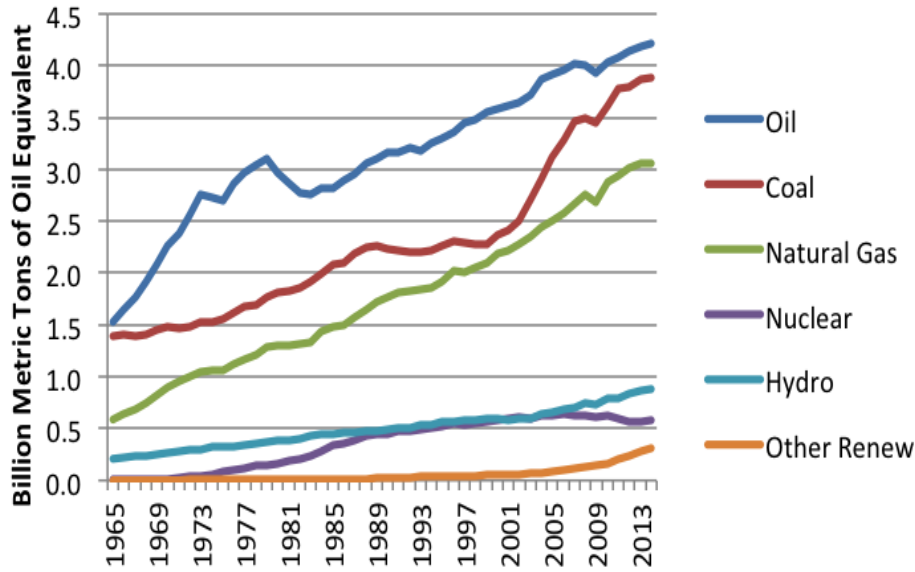
Figure 1: World energy consumption by fuel, showing each fuel separately, according to British petroleum (BP) Statistical Review of World Energy 2015 [1].

According to IEA 2009, the practical global potential of other renewable energy sources such as wind, hydroelectric, bio-mass, and geothermal is estimated to be approximately 13 %, with hydroelectricity constituting a larger percentage. Sunlight provides by far the largest of all carbon-neutral energy sources. More energy from sunlight strikes the Earth in one hour (4.3×10^{20} J) than all the energy consumed on the planet in a year (4.1×10^{20} J) [7], hence, solar energy remains the most abundant clean and energy resource for mankind [8]. Photovoltaic (PV) devices are utilized for harnessing solar energy.

The incident solar radiation that reaches the earth's upper atmosphere is 174 petawatts (PW). About 30 % is reflected to space, the rest is dissipated into clouds, oceans, and land masses. The total solar energy absorbed by earth's atmosphere, oceans and land masses is approximately 3,850 zettajoules (ZJ) per year [8]. According to physicist Steven Chu, US Energy Secretary 2013 and former Director of Lawrence Berkeley National Laboratory "the energy utilized by mankind on earth is approximately 500 exajoules per year which is around 0.01 % of the total yearly incoming solar radiation. All the energy utilized in a year on the earth's surface can be generated from solar radiation reaching the earth in one hour [9, 10]. If

2

well harnessed and maximized, solar energy is a viable and sustainable energy source to mankind [11].

1.1 Solar spectrum

Solar energy is the energy striking the earth from the sun, primarily as visible light, and in other forms as electromagnetic radiation. The sun radiates colossal amount of energy in a year than has been utilized on the earth's surface in mileage [12]. This energy is accountable for virtually all other forms of energy available on the earth's surface. Moontides, radioactive material and partly geothermal energy are the only exceptions. All other forms of energy are either directly or indirectly a residual form of the solar energy. Hydroelectricity is a result of various water cycling processes of transpiration, evaporation, denitrification, condensation and precipitation owing to the sun's radiant heat. The unequal distribution of sun's heat between the equator and the pole of the earth's atmosphere results in wind waves. Fossil fuels and biomass are remains of organic debris fostered by the sun's energy. Photovoltaic electricity is generated directly from sunlight by utilizing light energy from the sun to separate charges within the photovoltaic cell. Basically, most of the energy resources available in the earth are from the sun rays striking the earth's surface [12].

Solar radiation is emitted at the upper atmosphere at temperature of about 5800 K giving a spectral distribution approximately to a black body temperature as shown in Figure 2. Solar radiation spectrum can be characterized by two major quantities which are spectral irradiance (F) and photon flux $\phi_{ph}(\lambda)$ [13]. Spectral irradiance accounts for the electromagnetic radiation incident on a surface at a wavelength per unit area while the photon flux gives information about the numbers of the electrons generated for the flow of current in a solar cell.

From the basics of quantum theory, photon exhibit wave-particle duality and its energy can be characterised by:

$$E = hf. \tag{1}$$

Light travels in vacuum at a speed c with wavelength λ and frequency f given by:

$$c = hf. \tag{2}$$

Combining equations 1 and 2, the energy of a photon can be expressed as:

3

$$E = \frac{hc}{\lambda}, \qquad (3)$$

where h is the Planck's constant and c is the speed of light. The energy of the photon in electrons volts (eV) is thus:

$$E(ev) = \frac{1.24}{\lambda(\mu m)} \qquad (4)$$

The percentage of ultraviolet, visible and near infra-red solar radiation striking the earth's surface is shown in Figure 2.
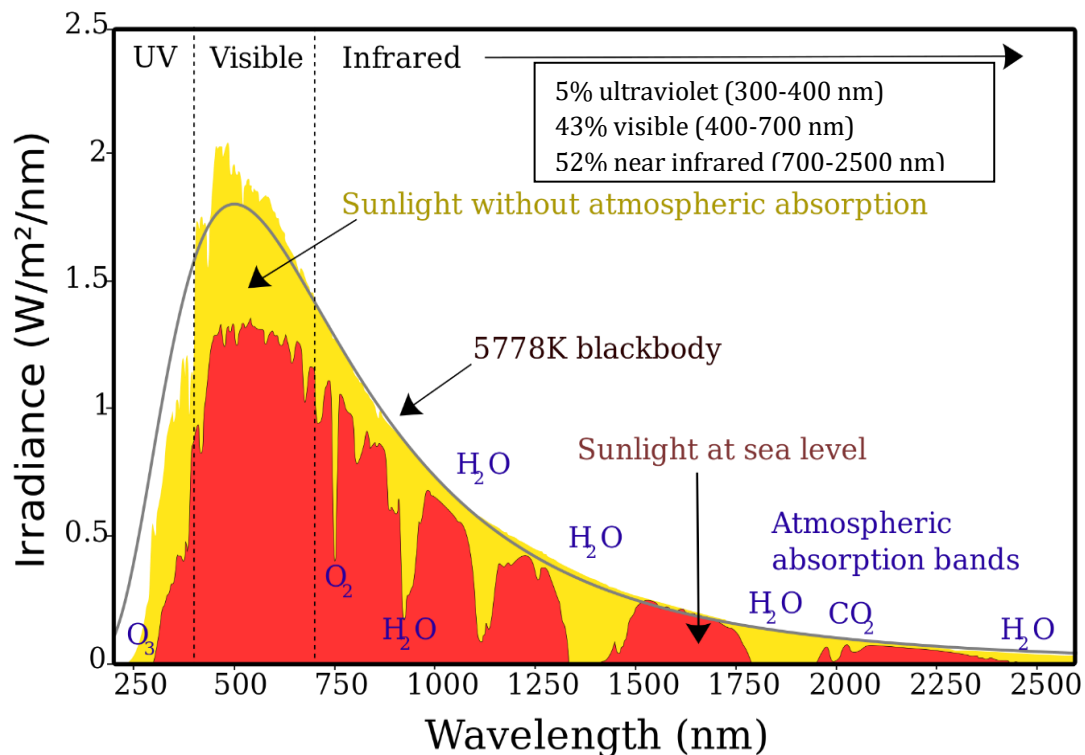
Figure 2: Solar radiation spectrum (illustrating solar radiation at the top of atmosphere, at sea level and black body spectrum) [13].

TiO_2 as a semiconductor is only sensitive to UV radiation, which is relatively small compared to visible and infrared radiation that constitutes 95% of the solar spectrum. The major challenges of researchers is to find a way to effectively harness larger percentage of the solar spectrum to achieve higher photon current density in dye-sensitized solar cells (*DSSCs*).

4

1.1.1. Solar air mass

Solar radiation striking the earth's surface is affected severely by various atmospheric effects such as aerosols, dusts and clouds. Gases such as water vapour (H_2O), ozone (O_3), carbon dioxide (CO_2) and methane (CH_4) absorb incident photons with energies close to atmospheric gases bond energies (see Figure 2). This results in diffuse or indirect constituent of solar radiation and the variation of the incident power and spectral content of terrestrial solar radiation. The magnitude to which these atmospheric effects affect sunlight available at the earth's surface is defined by the "air mass". The air mass is the path length which light takes through the atmosphere normalized to the shortest possible path length (see Figure 3). The air mass estimates the reduction in the power of light passing through the atmosphere due to scattering, absorption by air, dust and reflection in the atmosphere. The air mass is given by:

$$AM = \frac{1}{cos\theta} \tag{5}$$

where θ is the angle from the zenith referred to as the zenith angle.
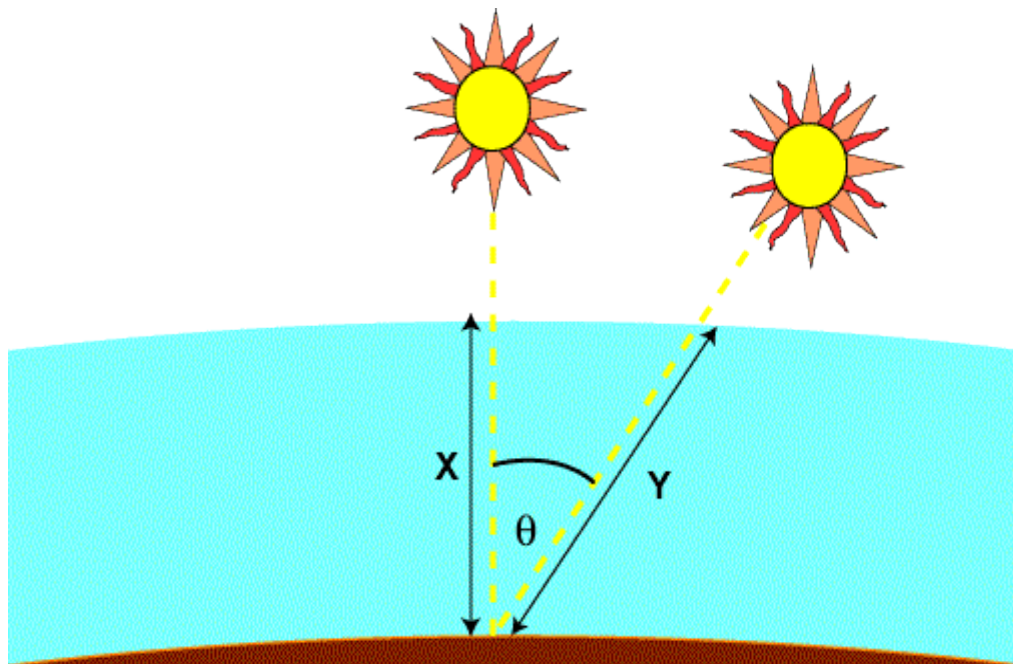
Figure 3: Zenith angle [14]

The solar spectrum striking the earth's surface is called AM1.5G, where G stands for global radiation. Both direct and diffuse radiation are components of global radiation. The AM1.5D

designates the direct radiation, AM0 is the solar spectrum at the top of the atmosphere when the sun is directly overhead the earth's surface as shown in Figure 4, the Air Mass is 1. The AM 1.5G with power density of about 1000 W/m^2 is the standard solar spectrum used for computing the efficiency of a solar/photovoltaic cell on the earth's surface [15].
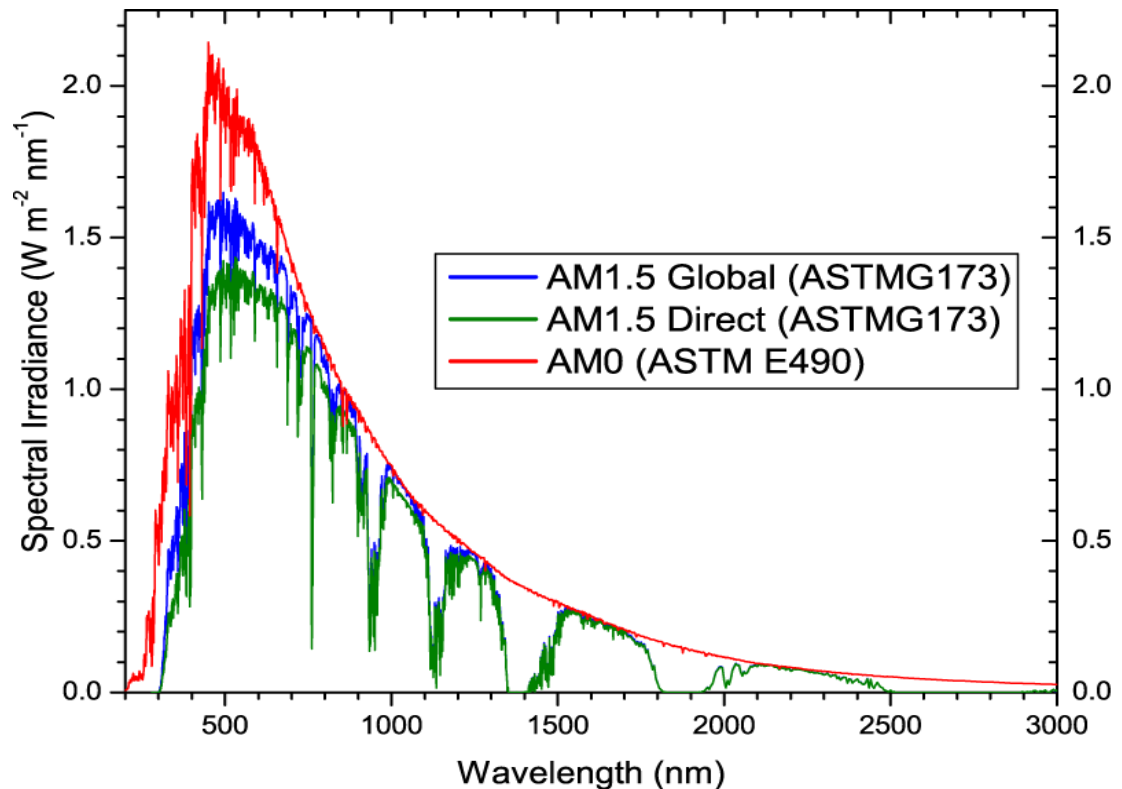
Figure 4: Air mass for solar spectrum: the extra-terrestrial solar radiation (AM0) and the standard terrestrial solar radiation (AM1.5) [13].

1.2 Photovoltaics technologies

The major objective of universal photovoltaic (PV) technologies solar cell research is technological improvement to reduce the cost of PV cells and modules to a level that will be viable and economical than conventional ways of generating power. Increasing the power conversion efficiency of PV materials and devices is instrumental to achieving this goal. Major developments in enhancing the efficiency of most of the leading PV materials and devices have been made in recent years with various extensive technological approaches which include: choosing semiconductor materials with appropriate energy gaps to match the solar spectrum and improving their structural, electrical, optical properties and inventive device engineering for more effective charge collection and better utilization of the solar spectrum through single

and multi-junction approaches [16]. PV cell technologies are classified into three generations based on material engineering, power conversion efficiencies and commercialisations. Some are already on the commercial scale while some are in the production stage, while others are on the research phase [17, 18].

1.2.1. Performance of a photovoltaic cell

The performance and efficiency of a solar photovoltaic cell is described by its current-voltage (IV) characteristics such as short circuit current density (I_{SC}), open circuit voltage (V_{OC}) obtained under standard illumination conditions (AM 1.5) and fill factor (FF) [19]. The fill factor is defined as:

$$FF = \frac{V_{MMP}I_{MMP}}{V_{OC}I_{sc}} \ ,$$
(6)

where I_{MPP} and V_{MPP} are the current density at maximum power point and voltage at the maximum power point respectively.

The incident photon conversion efficiency (IPCE) is a measure of the useful range of the .
and is given by:

$$IPCE = \frac{\frac{P_{in}}{I_{SC}}*e\lambda}{hc}$$
(7)

where λ is wavelength, Pin incident optical power, e is the fundamental electron charge, h Planck's constant and c is the speed of light in vacuum.

The maximum power per unit area delivered by the solar cell is given by:

$$P_{MAX} = FF \times V_{OC} \times I_{SC} \ ,$$
(8)

The light-to-electricity energy conversion efficiency of the solar cell under standard illumination condition is defined as the ratio of the maximum power produced by the cell (W/m^2) to the incident light intensity (W/m^2)

$$\eta = \frac{P_{MAX}}{P_{in}}$$
(9)

The classification, conversion efficiencies and limitations of PV technologies are presented in Table 1.

© University of Venda

Table 1: Classification of photovoltaic technology [20]

	Type		Photo	Features	Module's conversion efficiency
Silicon	Crystal	Monocrystal		Monocrystal about 200 micros thick is used as substrate. The conversion efficiency and reliability are high, but the price is high as well	Up to 22%
		Polycrystal		Polycrystal consisting of relatively small crystals is used as the substrate compare with the monocrystal type this is easy to manufacture and inexpensive, but the efficiency is low	Up to 19%
	Thin Film			This type is made by forming an amorphous or crystalline silicon film (about 1 microns thick) on a glass substrate, but the efficiency is lower than that of crystalline silicon type	Up to 9%
Compound	CIS			This is a thin film PV cell made from copper, indium and selenium. The CIS type features resources saving and mass production and is expected to have high performance.	Up to 16%
	CdTe			This is a thin film PV cell made from cadmium and tellurium. The CdTe features resources saving and mass production and low price	Up to 16%
	Condenser			This type is made by applying multiple junctions and condensing technologies to a compound consisting of group III and group V elements. The performance is high, but the price is high	Up to 42%
Organic	Dye sensitizer			Dye adhering to titanium oxide absorbs light and generates power. The dye sensitizer solar cell type is in the production and commercialization stage	Up to 13%
	Organic thin film			This type is made by coating a film using an organic semiconductor. The organic thin film is in the production and commercialization stage	Up to 8%

8

1.3 Generations of PV cell

1.3.1. First generation of PV cell

The first generation of PV employs the wafer-based crystalline silicon. Crystalline silicon cells are made from thin slices (wafers) cut from a single crystal or a block of silicon [21]. Silicon is a semiconductor and one of the most abundant element on the earth's crust with energy band gap of 1.1 eV, which makes it very suitable for PV applications. Crystalline silicon is classified as single- crystalline silicon (c-Si), poly or multi-crystalline silicon (m-Si) depending on the manufacturing process of the silicon wafer. Crystalline silicon PV cells have been widely commercialized and account for 87% of PV modules available in the market today [17, 22, 23]. The efficiency of commercially manufactured Si-based PV modules ranges between 14% to 22%. However the major drawback of these cells is their high cost at around US$4 /Watt, which is around 4 times too expensive for truly competitive commercial production [24]. c-Si are produced by Czochralski method, which is energy intensive and relatively expensive due to the high cost of purifying, crystallizing and sawing c-Si [25]. Thick Si wafers are required to efficiently absorb sunlight in the m-Si PV cells, hence sophisticated processing and more raw materials are wasted during sawing process. The innovative approach to overcome the drawbacks of Si based PV cells open doors for thin film technologies.

1.3.2 Second generation of PV cell (thin film solar cells)

Optical confinement technique is utilized in the thin film technology to lessen the amount of silicon material in the cell. In this solar cell, continuous thin layers of materials about 1 to 4 µm thick are deposited on a large substrate, thereby minimizing the semiconductor materials needed to absorb sunlight. The advantage of the thin film is; a wide class of multi-junction materials can be fabricated and several deposition techniques can be used to grow materials on substrates. The thin film technology gives room for production of cheaper, light and flexible PV modules that could easily be incorporated into buildings structures. The main thin films solar cells that have been commercialized are amorphous silicon (a-Si) solar cells, cadmium telluride (CdTe), copper-indium-selenide (CIS), copper-indium-gallium-diselenide (CIGS) and are briefly discussed in the next subsections.

.

University of Venda

1.3.2.1 Amorphous silicon cells

Amorphous silicon solar cells are fabricated from thin layers of hydrogenated amorphous silicon (a-Si: -H) deposited on a substrate. Amorphous silicon can be deposited on cheap and very large substrates (up to 5.7 m² of glass) [17, 21], which makes their fabrication much easier and economical than the crystalline silicon solar cells (c-Si). Currently, amorphous silicon PV module efficiencies range from 4% to 8%. Very small cells at laboratory level may reach efficiencies of 12.2 % [26]. However, the major drawback of a-Si PVs is their susceptibility to light-induced degradation [2].

1.3.2.2. Cadmium telluride

Cadmium telluride (CdTe) has optimal bandgap of 1.44 eV and high absorption coefficient, which makes it an appropriate material for PV application [16]. Cadmium and telluride are the two major raw materials for the production of CdTe PV cells. It is one of the most economical PV cell owing to its low-cost manufacturing technique, such as screen printing, closed-space sublimation, spray deposition and electrodeposition. Efficiencies of over 16% have been achieved with these cells in the laboratory [27]. Most recently, 16% efficiency has been reported in a CdTe (3.5-µm) thin-film solar cell in which CdTe films are deposited by closed-space sublimation (CSS) techniques [28]. However, the toxicity of the Cd content of the cell raises true concern for its large-scale production and commercialization.

1.3.2.3. Copper-indium-gallium-di selenide (CIGS)

Copper indium diselenide (CIS) and copper indium gallium diselenide (CIGS) when gallium is added offer the most promising efficiency of all the thin film technologies with characteristics of excellent stability. Present module efficiencies ranges from 7% to 16% [29]. Power conversion efficiency of 12% has been achieved with these materials under laboratory conditions [30]. CIGS is an improved version of the CIS PV technology with gallium added to increase the energy absorption of the cells [18]. CIGSs are produced under high vacuum evaporation conditions. The manufacturing process is quite complicated which increases manufacturing cost. Toxic materials such as Se, Te and Cd in the cell limit their widespread application. The thin film technology successfully reduces the actual material cost of the PV cell, ultimately, the low-cost substrate will lessen the overall cost of the cell, but higher efficiency is a key factor to maintaining the $/W cost reduction trend [24].

1.3.3 Third generation of Photovoltaic cell/Emerging technologies

The possibility of novel potential materials and PV devices which outstrip the limits of single junction devices with ultra-high efficiency and low $/W production costs drives the innovation of third generation of photovoltaic technologies [31]. Third generation PV technologies vary in materials and operational principle. The basic third-generation PV technologies are: concentrating PV (CPV), organic solar cells (OSCs) and dye-sensitized solar cells (DSSCs) and the perovskite solar cell. Third generation technologies that are at the pre-commercial stage are regarded as the "emerging" technology and are briefly discussed in the next subsections.

1.3.3.1 Concentrating PV

Concentrated photovoltaic (CPV) technology utilizes optical devices such as lenses/mirrors to concentrate direct solar radiation onto a multi-junction semiconducting material to generate electricity as shown in Figure 5 [32]. CPV systems are characterized according to the amount of solar concentration measured in suns. The solar concentration factor ranges from 2 to 100 suns (low to medium concentration) up to 1 000 suns (high concentration) as presented in Table 2. The lenses/mirrors must be permanently oriented towards the sun, using single or dual-axis tracking system for it to be efficient. Low to medium concentration systems are associated with silicon solar cells, although their efficiency is reduced at higher temperatures, while high concentration systems (beyond 500 suns) are usually hinged with multi-junction solar cells made from group III and V semiconductors including Ge (0.67 eV). In GaAs (1.4 eV) and GaAs and In Gap (1.85 eV) [33]. Theoretical efficiency of 59% can be achieved with multi-junction cell with band gaps of 0.74, 1.2 and 1.8 eV [33]. Laboratory efficiency of more than 40 % has been achieved with CPV based on multi-junction solar cells [34] while silicon-based commercial CPV modules gives efficiency in the range of 20% to 25%. The multi-junction CPV cells are utilized for space applications or small area solar cells with high sunlight concentration owing to their complexity and high cost [35].

Table 2: Description of concentrating photovoltaic cell classes [36].

Class of CPV	Typical Concentration Ratio	Tracking Systems	Type of Converter
High concentration PV (HCPV)	300-1000	Two-axes	III-V multi-junction solar cells
Low concentration PV (LCPV)	< 100	One or two-axis	c-Si or other cells

The limitations of the CPV cell are the high costs of focusing, tracking, and multi-junction solar cells. CPV modules rely on direct sunlight, they require clear skies and high direct solar irradiation for optimal performance and can only be used in certain regions.

Figure 5: Concentrated PV systems [37].

1.3.3.2 Organic solar cells

Organic solar cells that include both fully organic and hybrid dye sensitized solar cells are composed of organic polymers or small organic molecules [21]. Flexibility of these PVs and ability to work under low light conditions is a significant competitive advantage in consumer applications. Although organic PV modules have less efficiency than commercial solar cells, their cost or per watt production is trice or fourth times lower than the silicon wafer based solar

cells, which makes them better alternatives to the silicon based solar cells and are expected to be widely utilized PV modules in the coming 20 years.

Organic PV module efficiencies are now in the range 4% to 5% for commercial systems and 6% to 8% in the laboratory [38]. Various innovative concepts that include multiple excitonic concepts, band gap engineering, introduction of quantum dots and nanotechnology particles having higher efficiencies are growing in scientific research and on laboratory scale production to improve the absorption level and maximize the efficiency of these solar cells. The major challenge limiting the widespread utilization of solar energy is cost and efficiency of PV cells. Most PVs currently being manufactured and used worldwide are made of solar grade silicon (Si) and widespread use of silicon-based PV technology is limited by the high cost $30/kg of silicon [39]. DSSCs on the other hand offers a low cost and promising high efficiency alternative to the silicon-based PV. The improvement of these DSSCs component/materials to achieve minimum production cost and higher efficiency becomes expedient.

1.4 Dye sensitized solar cells

Dye sensitized solar cells (DSSCs) have attracted rapid interest in the recent years with prospect of emerging as a viable alternative to conventional silicon based solar cells, owing to their low production cost, simplicity in fabrication techniques, unelaborate manufacturing equipment, low CO_2 emission, ability to function under low light conditions and their suitability for indoor applications [40, 41]. The typical DSSC employs a photoanode, which comprises organic dye that is chemically anchored onto a nanostructured TiO_2 semiconductor oxide, a catalyst coated transparent conducting oxide and a redox couple triiodide electrolyte (I^-/I_3^-) to generate electricity from sunlight [42]. The dye plays a vital role in generation of electric current because the basic function of light absorption, charge injection and regeneration of electrons of the oxidized electrolyte is performed by the dye molecules [40, 43]. The dye absorbs photons of solar radiation and transfers photo generated electrons into the band gap of the semiconductor.

1.4.1. Basic configuration of dye sensitized solar cells

The main components of a typical DSSC is illustrated schematically in Figure 6. The DSSC comprises of a transparent conducting glass electrode, nanocrystalline TiO_2 particles, dye molecules (sensitizer) chelated unto the surface of the TiO_2 nanoparticle, electrolyte containing

reduction-oxidation couple, and a catalyst coated counter electrode which enhances the regeneration of the oxidized dye [19, 44]. The transparent conducting electrode and counter-electrode are coated with a thin conductive and transparent film such as fluorine doped tin dioxide (SnO_2) [45, 46]. Nanocrystalline TiO_2 is deposited on the conducting electrode (photoelectrode) to provide the necessary large surface area to adsorb sensitizers (dye molecules) [47].
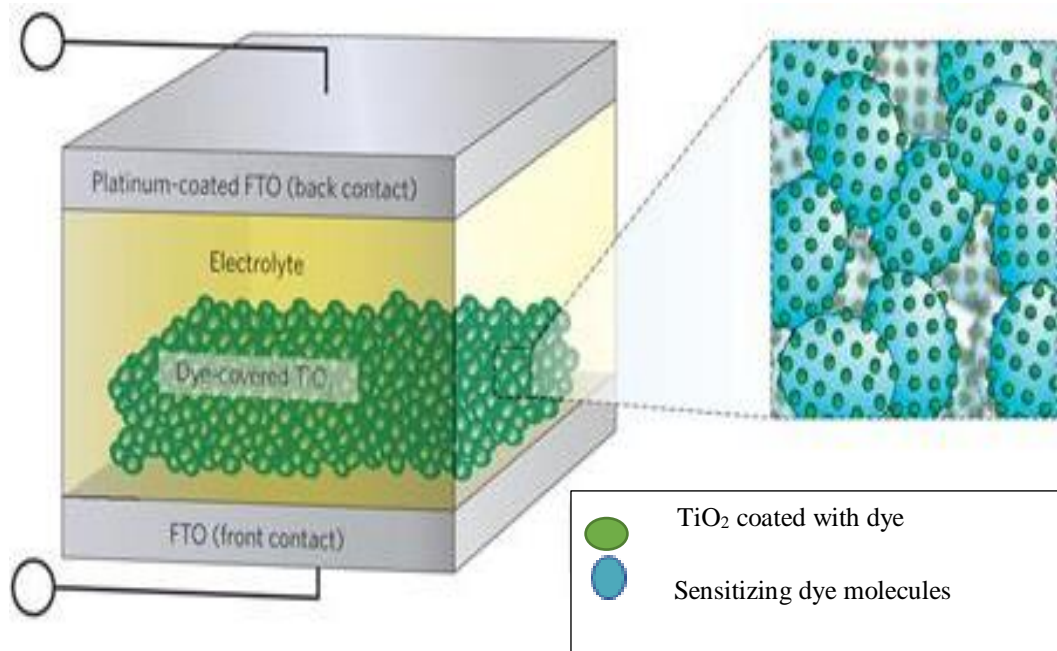
Figure 6: Schematic components of DSSC [48].

1.4.2. Operating principle of DSSCs

The detailed operation of DSSC is illustrated in Figure 7, the operating principle of DSSCs is based on light absorption by a dye anchored to the surface of TiO_2 semiconductor. The photoelectron is transferred from the dye to the wide bandgap semiconductor, the electron moves by diffusion through the semiconductor to the transparent conducting oxide where the photoelectrons are transferred to the external load; at the counter electrode, the holes are transferred to redox electrolyte which also facilitates the regeneration of the sensitizer [40, 49]. The efficiency of the photovoltaic device depends strongly upon the dye and electrolyte used [50, 51]. The conversion efficiency (ŋ) of DSSC is expressed as:

$$\eta = I_{ph} \times V_{oc} \times FF/I_S \, , \qquad (10)$$

where i_{Ph} is the short circuit photon current density, V_{OC} is the open circuit voltage, ff is the fill factor and I_s is the incident light intensity. The terms i_{Ph} and V_{OC} are vital in optimizing the efficiency of DSSC. The photoanode is a major component of the DSSC that determines i_{Ph} and V_{OC}, hence the performance of the cell [52]. The semiconductor oxide and the dye also play an important role and can be tuned to improve the performance.
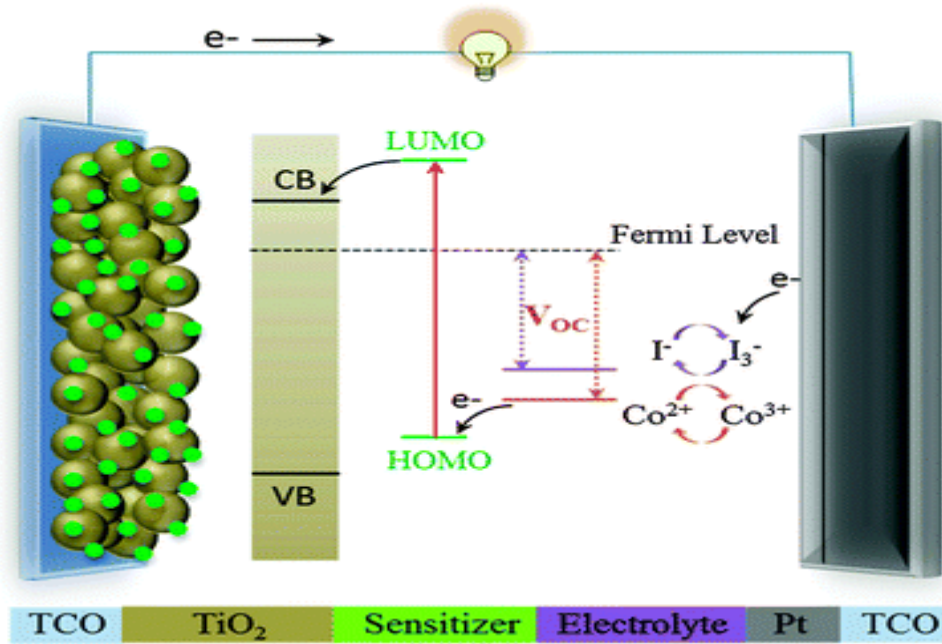
Figure 7: Operation principle of DSSC [53].

The detailed operation of DSSC is illustrated in Figure 7 and can be summarized into six steps as defined by the operational chemical equations outlined below:

(a) Photoexcitation

$$D + hv \rightarrow D^* \tag{11}$$

(b) Electron injection

$$D^* \rightarrow D^+ + e^- (TiO_2 \ CB) \tag{12}$$

(c) Electron Transport and energy generation

$$e^-_{(TiO2)} + C. E \rightarrow TiO_2 + e^- + Electricity \tag{13}$$

(d) Triiodide reduction

$$\frac{1}{2}I_3^- + e^- \rightarrow \frac{3}{2}I^- \tag{14}$$
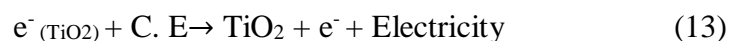
(e) Dye regeneration

$$D^+ + \frac{3}{2}I^- \rightarrow D + \frac{1}{2}I_3^- \qquad (15)$$

(f) Iodide ion oxidation

$$\frac{1}{2}I_3^- + e^-(C.E) = 3I^- \qquad (16)$$

The incoming photon is absorbed by the dye molecule adsorbed on the surface on the nanocrystalline TiO_2 particle and an electron from a molecular ground state D0 (HOMO) is excited to a higher lying excited state D*(LUMO) in Equation (11). The excited electron is injected to the conduction band of the TiO_2 particle leaving the dye molecule to an oxidized state D+ in Equation (12). The injected electron percolates through the porous nanocrystalline structure to the transparent conducting oxide layer of the glass substrate (negative electrode, anode) and through an external load to the counter-electrode (positive electrode, cathode) as defined in Equation (13). At the counter-electrode the electron is transferred to triiodide in the electrolyte to yield iodine in Equation (14). The oxidized dye is regenerated by the reduction of the iodine in the electrolyte in Equation (15). The cycle is completed by the oxidation of the iodide ion by the electron percolating through the external load in Equation (16) [19].

1.4.3. Kinetics of charge injection, transport and recombination in DSSCs

The photo conversion efficiency of DSSC depends on the energy levels of the semiconductor, dye and the electron transfer kinetics processes at the sensitized semiconductor/electrolyte interface and is given by:

$$\eta = FF \frac{V_{oc}J_{sc}}{P_{inc}}, \qquad (17)$$

where V_{OC} is the open circuit voltage, J_{SC} is the short circuit current density, FF is the fill factor and P_{inc} is the incident solar power

$$J_{SC} = \int LHE(\lambda)\phi_{inject}\, n_{collect}\, d\lambda \qquad (18)$$

LHE is the light harvesting efficiency, $n_{collect}$ is the charge collection efficiency and ϕ_{inject} is the electron injection efficiency from the excited state of the dye molecules to the semiconductor substrate [54].

The maximum photovoltage, at open circuit potential (V_{oc}) produced by the cell is determined by the energy separation between the electrolyte chemical potential (E_{redox}) and the Fermi level

(EF) of the TiO$_2$ layer. Small energy separation between the HOMO and LUMO ensures absorption of low energy photons in the solar spectrum. Therefore, the photocurrent level is dependent on the HOMO-LUMO levels separation. Electron injection into the conduction band of TiO$_2$ is energetically favourable with increased energy separation of LUMO and the bottom of the TiO$_2$ conduction band. Furthermore, for the HOMO level to effectively accept the donated electrons from the redox mediator, the energy difference between the HOMO and redox chemical potential must be more positive [55]. Electron injection rate must be faster than the decay of the excited state, also the kinetics of the reaction occurring at the counter electrode must ensure fast regeneration of the sensitizer dye molecules for optimum performance of the cell [52].

Organic dye molecules particularly have received increased interest as sensitizers and light harvesting materials [56, 57], owing to their significant higher molar extinction coefficients (50,000–200,000 M^{-1}cm^{-1}) than the ruthenium-based dye complexes. The organic sensitizers widely compete with the traditional inorganic dye in the solid-state dye sensitized solar cell structure. This is because of the benefit of high extinction coefficients of the dye for light harvesting that is advantageous to charge transport limitations in solid-state devices [58]. The organic dye are relatively cheap and easy to synthesize and are promising alternative to the semiconductor sensitizers based on ruthenium complexes [59].

Although different monocrystalline mesoporous metal oxides such as ZnO, SnO$_2$, Fe$_2$O$_3$, WO$_3$, Nb$_2$O$_5$, Ta$_2$O$_5$, and TiO$_2$ have been employed as semiconductors in DSSCs fabrication [57], titanium dioxide exhibits superior performance as semiconductor for dye-sensitized nanostructured electrodes and is most intensively employed due to its outstanding electrochemical and photocatalytic properties. It has high resistance to heat, impervious to chemicals, non-toxic and possesses high refractive index (n = 2.7) [60-63]. However, the major drawback of naturally occurring TiO$_2$ oxide semiconductor is that it exhibits photocatalytic properties only in the ultraviolet region of the electromagnetic spectrum, which accounts for only 5% of the solar spectrum, [64] owing to its wide band gap (3.0 eV to 3.2 eV) [65, 66]. This wide band gap limits its photocatalytic activity and electron/hole recombination under visible and infra-red radiation [40, 67]. However, it can be energized by adding foreign elements to absorb in the visible and near infra-red region.

Crystalline TiO$_2$ occurs in three different phases under standard conditions with diverse structures, crystal system, and photocatalytic properties. The three phases are anatase, rutile

and brookite. Anatase and rutile crystallizes into tetragonal structure with space group (4/*mmm*), *I4₁amd*$-$D$_{4h}^{19}$ and *P4₂/mnm*$-$D$_{4h}^{14}$ respectively, while brookite crystallizes into orthorhombic system with space group (*mmm*), *Pbca*$-$D$_{2h}^{15}$} [68]. Rutile is the most stable polymorph while anatase and brookite are metastable; and are converted to rutile phase when subjected to heat. Anatase is mainly synthesized from TiO_2 powder by sol-gel method while rutile can be obtained as a by-product of precipitation at low temperature in an acidic medium. Several studies have been done to study the surface interactions of dye with TiO_2, most of which are centered on the anatase and rutile polymorphs of TiO_2 [69, 70]. It is however difficult to synthesize pure brookite without the presence of rutile or anatase phases. Hence, less experimental studies have been done on brookite, such that until recently, there is limited information on its photocatalytic and surface properties. In recent years, the interest in brookite increased as pure brookite emerged to be a fascinating entrant in photocatalytic applications [71, 72].

This current study uses computer simulation methods to investigate the surface properties and interaction between the dye molecules and brookite TiO_2 clusters. In particular, an investigation of reaction mechanism studies between inorganic and organic dye molecules and brookite clusters was explored using density functional theory methods. The various dye molecules were adsorbed on different brookite clusters, from which the formation energies, ultraviolet-visible UV-Vis absorption, the energies of the HOMO, LUMO and HOMO- LUMO energy gap, light harvesting efficiencies (LHE), energy level alignment and free energy of electron injection of the dye/ brookite TiO_2 complex were calculated. The main aim was to understand the possible mechanism for optimization for light harvesting efficiency of TiO_2 in the visible and near infra-red region of the solar spectrum to achieve optimum quantum yield in DSSCs.

1.5 Aim and objectives

This research is geared at the optimization of the adsorption of dye molecules on brookite TiO_2 cluster in order to improve the light harvesting efficiency. Specifically, investigate possible ways of reducing the band gap of TiO_2 such that it can absorb in the visible region and engineer the dye molecules such that they can absorb towards the near infra- red region. Thus, improve the quantum yield of DSSCs. The specific objectives will be to:

- carry out Density Functional Theory (DFT) of UV-Vis absorption of inorganic and organic based dye for determination of their optical absorption spectra, maximum absorption wavelength, excitation energies, oscillator strengths via Gaussian computational software.

- determine the HOMO-LUMO energy levels and gap and light harvesting efficiency of the inorganic and organic based dye complexes using DFT method.

- carry out adsorption studies of dye molecules on TiO_2 brookite clusters via bidentate adsorption mode, which is energetically favourable for adsorption of dye molecules using DFT .

- study the adsorption geometries of the dye molecules adsorbed on TiO_2 brookite clusters using DFT to exploit information about the formation and binding energies.

- determine the HOMO-LUMO energy levels and gap, UV-Vis absorption of the dye adsorbed on TiO_2 brookite cluster, computation of density of states and projected density of states and isodensity surfaces of the key molecular orbitals involved in excitation using DFT.

- carry out DFT calculation of the energy level alignment of the dye with brookite cluster.

- examine the possibility of charge injection and regeneration of the dye molecules.

1.6 Significance of study

Understanding the interaction of dye molecules with the surfaces of TiO_2 is crucial because light harvesting and electron collection determines the efficiency of DSSCs. Light harvesting capability of DSSCs basically depends on the molecular properties and band gaps of the interfacial components between the photoanode materials; which are TiO_2 semiconductor and dye molecules. Therefore, information about the interfaces is of great importance in understanding and optimizing light harvesting, photo conversion function and photocurrent densities in DSSCs.

1.7 Problem statement

TiO_2 metal oxide is typically employed as semiconductor in DSSCs owing to its less susceptibility to corrosion under illumination and non-toxicity. However, the main limitation of TiO_2 is its wide band gap ($E_g = 3.23$ eV), which makes it to absorb only UV portion of the solar spectrum. The dye molecules chemically adsorbed to the surface of TiO_2 are used for the absorption of photons from the sun. The dye molecules become excited and inject electron into

19

the wide band gap of TiO_2. The photo-excited electron moves by diffusion through the semiconductor to the transparent conducting oxide where they are transferred to the external load. This work seeks to investigate the interaction of dye molecules with brookite TiO_2 clusters to overcome the restricted spectral sensitivity of the wide band gap semiconductor and to optimize light harvesting in the visible and near infra-red region of the solar spectrum to achieve optimum quantum yield in DSSCs.

1.8 Research motivation

To improve light harvesting in DSSCs, efforts have been made towards the morphological control of the band gap of TiO_2 polymorphs (rutile, anatase, brookite), as a way of improving the photocurrent yield [41, 50]. Amongst the studies are energy band modulation by elemental doping, monodoping, codoping with non-metals and transition metals and adsorption of dye molecules on TiO_2 surfaces. The results showed improved spectral response and higher photocatalytic performances of TiO_2 [64, 73]. Surfaces of rutile and anatase polymorphs have been greatly exploited and have been a prototypical model for basic studies on TiO_2 [74, 75]. Despite the fact that large synthetic crystals of anatase and rutile have long been available, this is not the case for brookite; relatively little is known about brookite form of TiO_2 [76]. It is only recently that researchers have started focusing on in-depth study of brookite TiO_2.

Recent studies have suggested that brookite is a good photocatalyst and may exhibit higher photocatalytic activity than both rutile and anatase [76]. A previous study was done on the optical absorption edge of brookite TiO_2 at room temperature using natural crystals. The measurement extends up to 3.54 eV in photon energy and 2000 cm^{-1} in absorption coefficient. It was observed that the absorption edge of brookite is broad and extends to the visible region of the solar spectrum, which is quite different from the steep edges in the visible region observed for rutile and anatase polymorphs of TiO_2 [75]. Since brookite surfaces have not been studied much and the fact that it is reported to have better photocatalytic properties, it is of keen interest to study the interactions of dye molecules with brookite TiO_2. Brookite clusters will be investigated, particularly its photocatalytic properties and possible ways to improve the light harvesting efficiency in DSSCs.

1.9 Hypotheses

The introduction of doping material (dye molecules or atoms) in TiO_2 semiconductor could narrow the wide band gap of TiO_2, which restricts its spectral characteristics to the UV region of the solar spectrum. Surface modification of TiO_2 with visible light absorbing dye molecules can lower the band gap and improve its light harvesting efficiency. Optimization of the adsorption of dye molecules on surfaces of TiO_2 brookite semiconductor can narrow the band gap of TiO_2 and improve light harvesting efficiency to absorb in the visible region. Engineering of the dye molecules/TiO_2 complex may also result in absorption towards the near infra-red region and hence improve the optimum quantum yield of DSSCs.

1.10 Structural models

The structural models for the most commonly known polymorphs of TiO_2 are shown in Figure 8. The TiO_2 brookite semiconductor material employed in this study is presented in Figure 8(c) and was used to model TiO_2 clusters. The structures of the three TiO_2 polymorphs were exported from Material Studio Accerlrys Inc 2016 from Dassault Systèmes BIOVIA [77]. Shown in Figure 8 are the structures of anatase, rutile and brookite polymorphs, wherein the building blocks consist of a titanium atom surrounded by six oxygen atoms in a distorted octahedral configuration while brookite has an orthorhombic crystalline structure with eight formula units in the orthorhombic cell.
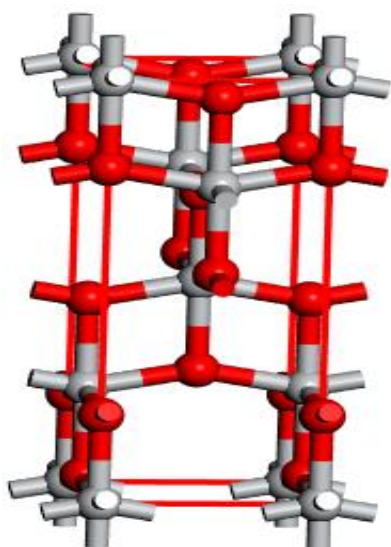
(a) Anatase
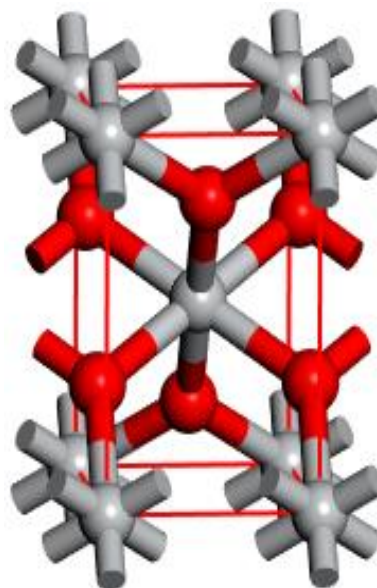
(b) Rutile
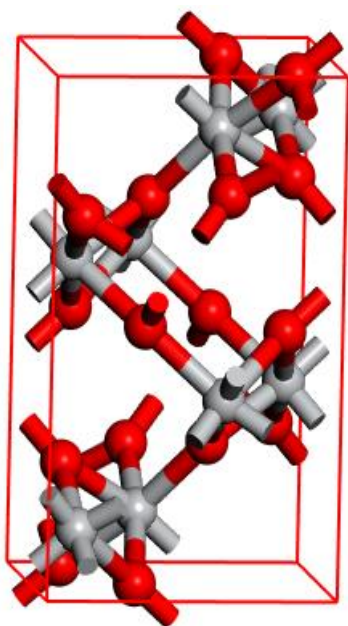
(c) Brookite

Figure 8: Crystallographic forms of TiO_2 (a) anatase (b) rutile (c) brookite. Throughout the report the atoms are represented according to these colour scheme, whereby grey balls are titanium atoms and red balls are oxygen atoms.

Figure 9 is a representation of the first Ruthenium N719 complex reported by Grätzel in 1991. The structure comprises of Di-tetrabutylammonium cis-bis (isothiocyanato) bis (2, 2'-

© University of Venda

bipyridyl 4, 4'dicarboxylato) ruthenium (II). The structure contains three ruthenium complex at the centre. It was the first ruthenium dye to be reported in literature.
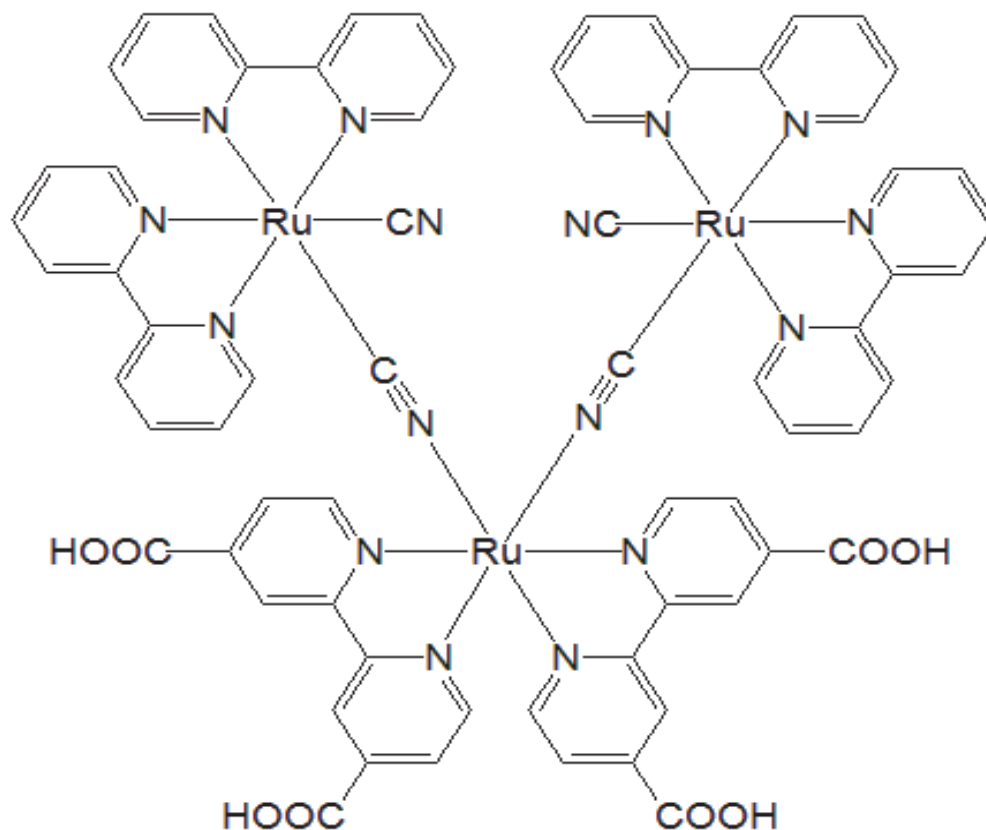
Figure 9: A ruthenium dye molecule structure as first reported by O'Regan and Grätzel in 1991 [48].

Figure 10 is an illustration of the ruthenium N3 complex, which was later reported by Nazeeruzzin *et al*. The structure contains one ruthenium complex at the centre. The structure comprises of *Cis-di* (thiocyanate) bis (2, 2-bipyridine-4, carboxylate) ruthenium (II), and is coded (N3) [51]. In the context of the study, the structure was built using Gaussian 03 quantum chemical package within the framework of Gaussview as presented in figure 10(b) [78]. The ruthenium metal was selected from the periodic table within the Gaussian window, this was followed by the attachment of the two bipyridine moiety and the carboxylic moiety and the two thiocyanate ligands. The metal and the thiocyanate ligands form the donor unit, bipyridine and the carboxylate moiety were the acceptor and anchor units respectively.
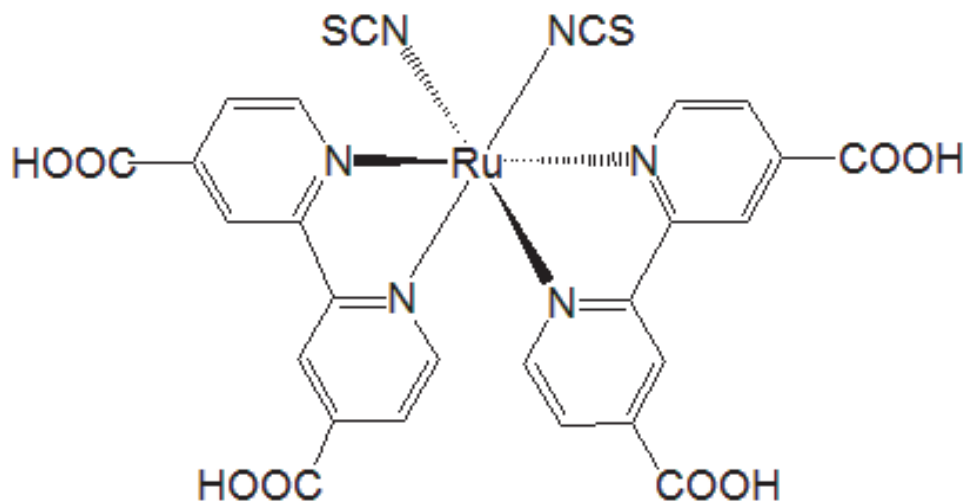
(a)
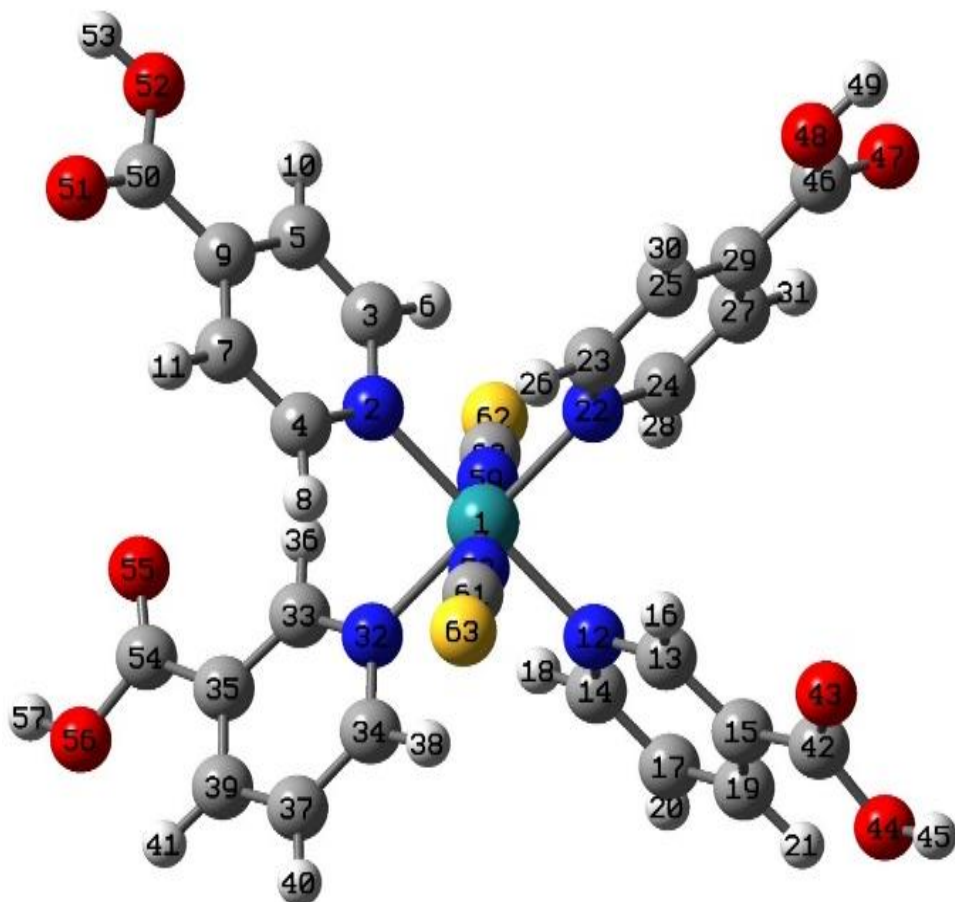
(b)

Figure 10: (a) Cis-di (thiocyanate) bis (2, 2-bipyridine-4, carboxylate) ruthenium (N3) [51].
(b) Cis-di (thiocyanate) bis (2, 2-bipyridine-4, carboxylate) ruthenium (N3) built with Gaussian
03

Figure 11 is an illustration of croconate dye molecule coded CR1 reported by Chitumela *et al.* [79]. CR1 structure contains electron donating methyl group (CH_3), which is an alkyl derived from methane; containing one carbon atom bonded to three hydrogen atoms. The structure was built using Gaussian 03 quantum chemical package within the frame work of Gaussview as shown in Figure 11(b), the oxyallyl moiety was selected from the molecule group within the Gaussian window and placed on the builder interface, this was followed by the two oxygen of the diketo group, the methyl moiety was attached to the oxyallyl moiety and the oxygen.

(a)   (b)
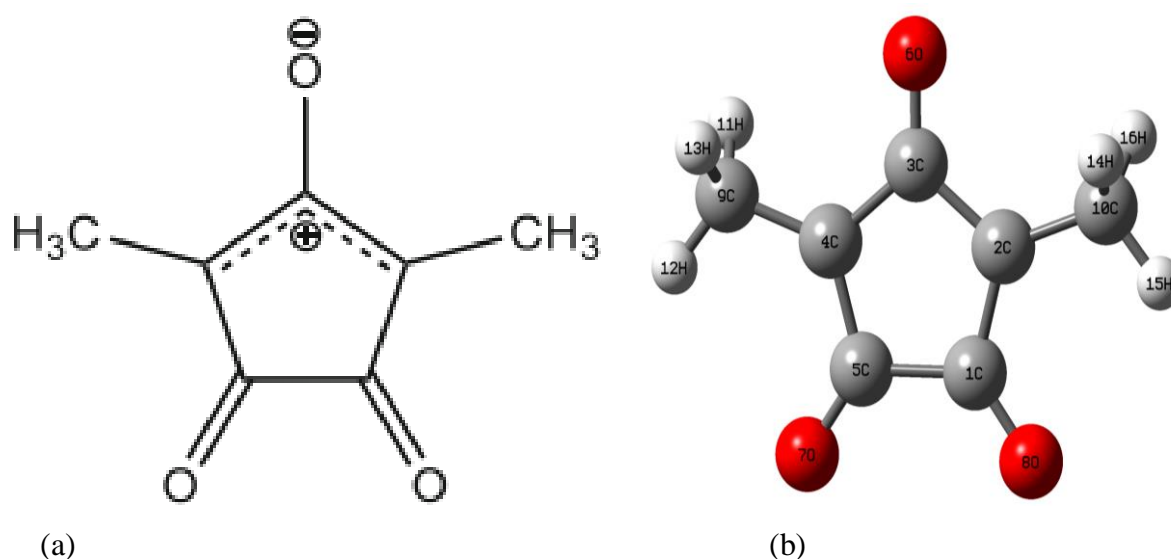
Figure 11: (a) Croconate dye CR1 [79] (b) Croconate dye CR1 built with Gaussian 03

Figure 12 is an illustration of croconate dye molecule coded CR2 also reported by Chitumela *et al.* [79]. The CR2 structure contains electron withdrawing carboxyl group (-COOH), which is an organic compound containing carboxylic acid with one carbon atom bonded to two oxygen atoms and one hydrogen atom [79]. The structure was built using Gaussian 03 quantum chemical package within the framework of Gaussview as shown in Figure 12(b), the oxyallyl moiety was selected from the molecule group within the Gaussian window and placed on the builder interface. That was followed by placing the two oxygen of the diketo group and finally carboxyl moiety was attached to the oxyallyl moiety and the oxygen.

(a)   (b)
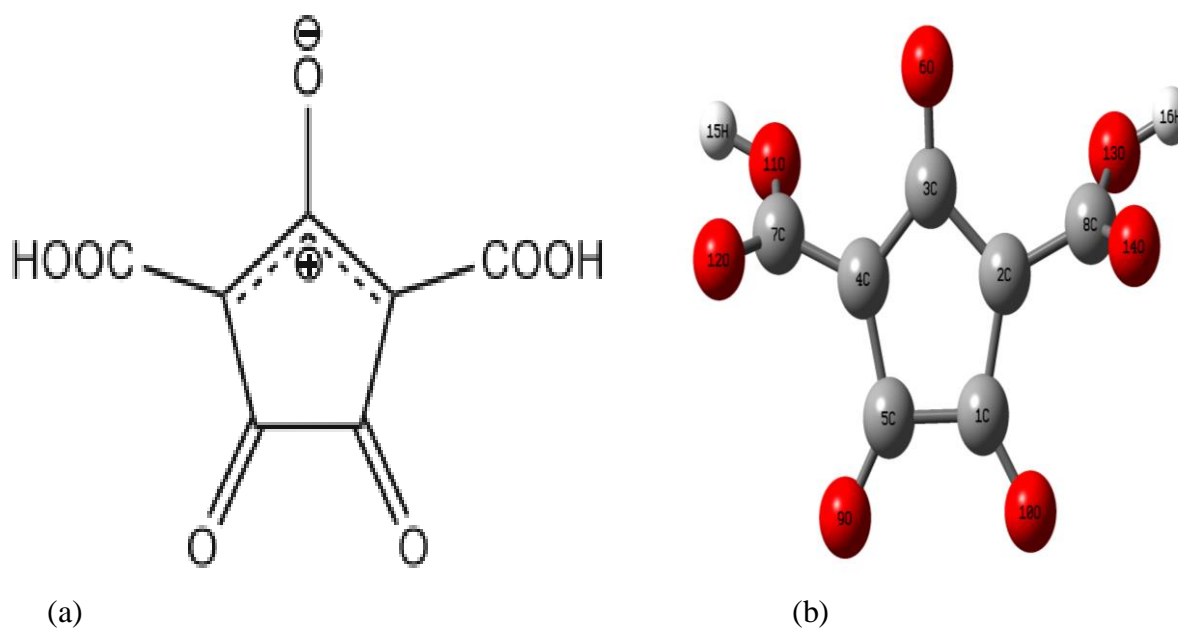
Figure 12: (a) Croconate dye CR2 [79, 80] (b) Croconate dye CR2 built with Gaussian 03

Figure 13 is an illustration of polyene-diphenylaniline dye molecule coded D5 reported by Kuang *et al.* The D5 structure contains 3-(5-(4-(diphenylamine) styrl) thiophen-2-yl)-2-cyanoacrylic acid. Similarly, the model was built using Gaussian 03 quantum chemical package within the frame work of Gaussview as shown in Figure 13(b). The diphenylamine moiety was selected from the molecule group within the Gaussian window and placed on the builder interface. Thereafter, polyene and thiophene group were attached to system; and lastly the cyanoacrylic acid was attached. The diphenylaniline was the donor unit, polyene and thiophene were the π-conjugation to link or bridge the donor acceptor moiety while -COOH and -CN were the acceptor and anchor units respectively.
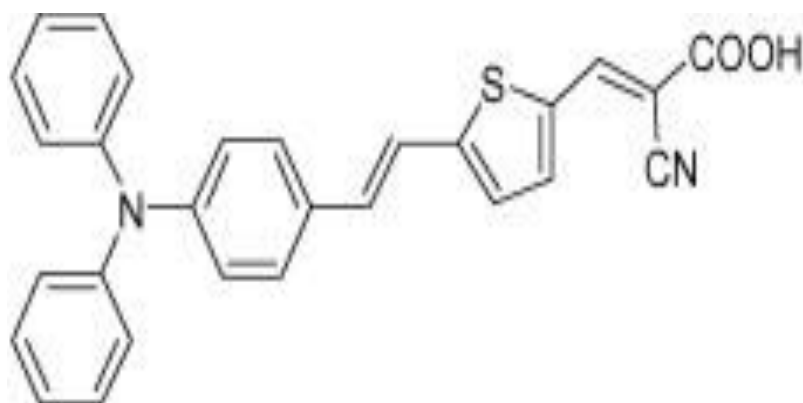
(a)
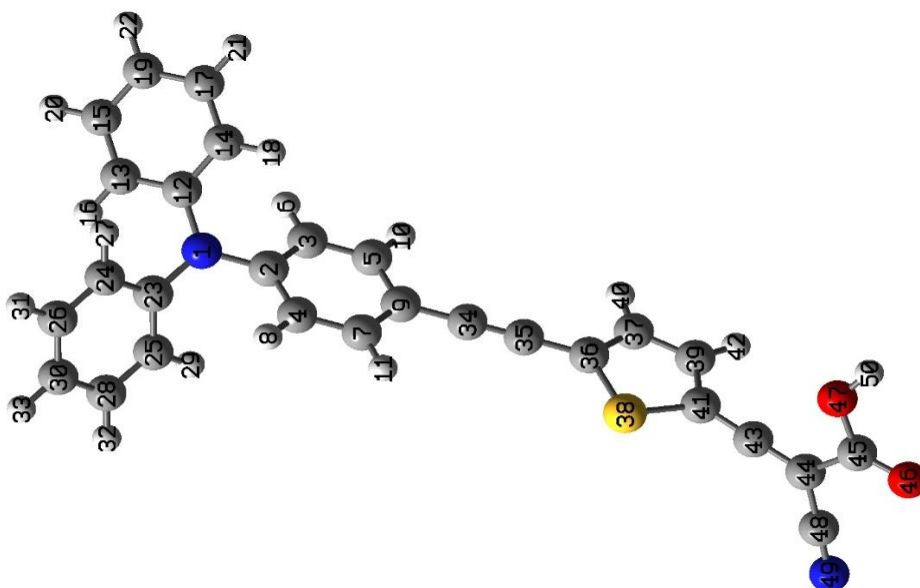
(b)

Figure 13: (a) Polyenediphenyl-aniline dye D5 [81, 82] (b) Polyenediphenyl-aniline dye D5 built with Gaussian 03.

Figure 14 is an illustration of polyene-diphenylaniline molecule coded D7 also reported by Kuang *et al*. The D7 structure contains 3-(5-bis (4-(diphenylamine) styrl) thiophen-2-yl)-2-cyanoacrylic acid. The structure was built using Gaussian 03 quantum chemical package within the frame work of Gaussview as shown in Figure 14(b), the two-diphenylamine moiety was selected from the molecule group within the Gaussian window and placed on the builder interface. Then that was followed by the attachment of the polyene and thiophene group, and lastly the cyanoacrylic acid. The diphenylaniline was the donor unit, polyene and thiophene

were the π-conjugation to link or bridge the donor acceptor moiety while -COOH and -CN were the acceptor and anchor units respectively. The donor unit for D7 and D11 was extended by the addition of diphenylaniline. The diphenylanilines of D9 and D11 were then modified by the addition of methoxy groups.
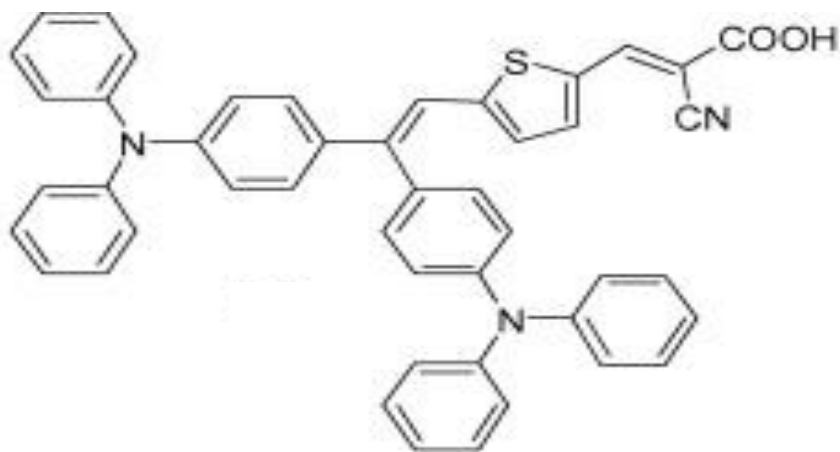
(a)
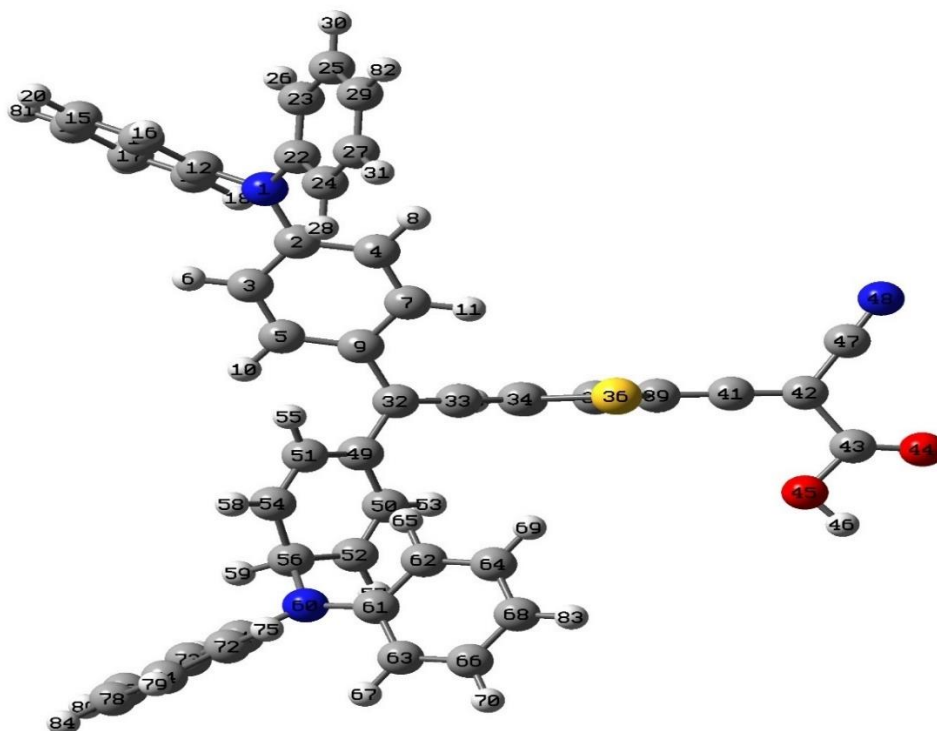
(b)

Figure 14: (a) Polyenediphenyl-aniline dye D7 [82] (b) Polyenediphenyl-aniline dye D7 built with Gaussian 03.

Figure 15 is a representation of polyene-diphenylaniline dye molecule coded D9 reported by Kuang *et al* [82]. The D9 structure contains 5-(4-(bis (4-methoxyphenylamino) styrl) thiophen-2-yl)-2-cyanoacrylic acid. Similarly the structure was built using Gaussian 03 quantum chemical package [78] within the frame work of Gaussview as shown in Figure 15(b). The diphenylamine moiety was selected from the molecule group within the Gaussian window and placed on the builder interface. The diphenylanilines of D9 were then modified by the addition of methoxy groups, this was followed by the attachment of the polyene and thiophene group, and the cyanoacrylic acid. The diphenylaniline was the donor unit, polyene and thiophene were the π-conjugation to link or bridge the donor acceptor moiety while -COOH and -CN were the acceptor and anchor units respectively.
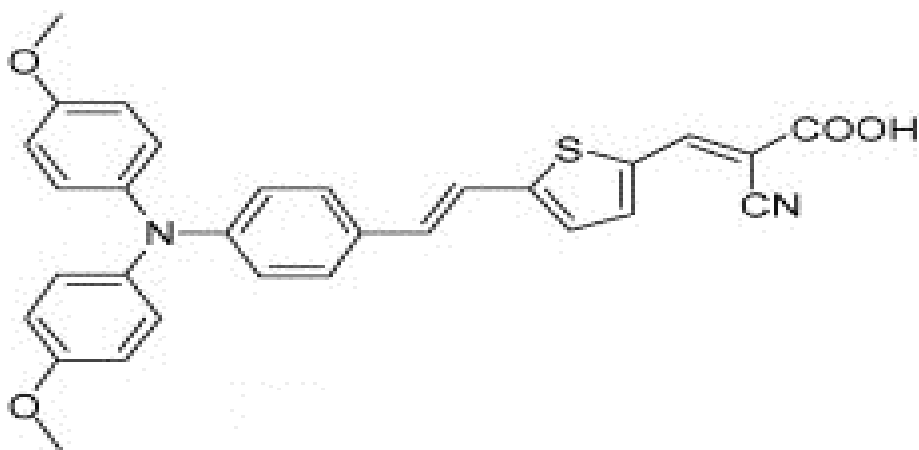
(a)
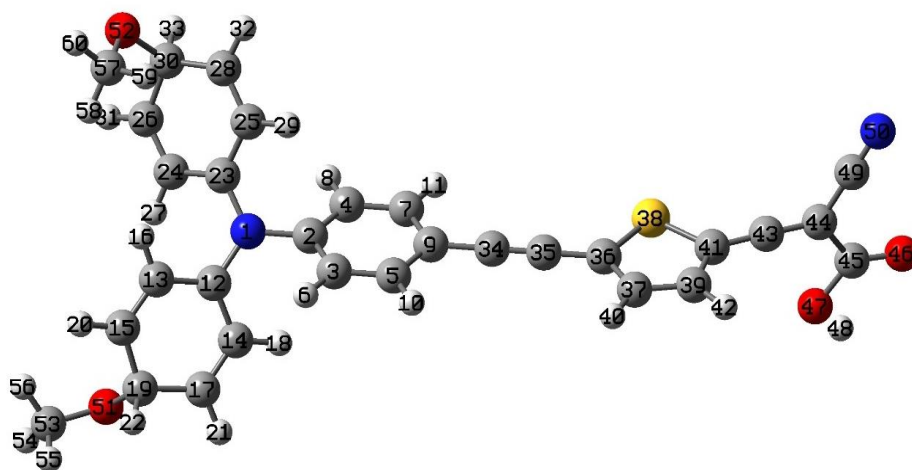
(b)

Figure 15: (a) Polyenediphenyl-aniline dye D9 [82] (b) Polyenediphenyl-aniline dye D9 built with Gaussian 03 [78].

Figure 16 is an illustration of polyene-diphenylaniline dye molecule coded D11 reported by Kuang *et al* [82]. The D11 structure contains 3-(5-bis (4, 4'-dimethoxyphenylamino) styrl) thiophen-2-yl)-2-cyanoacrylic acid. The structure was built using Gaussian 03 quantum chemical package within the frame work of Gaussview as shown in Figure 16(b) where the two-diphenylamine moiety was selected from the molecule group within the Gaussian window and placed on the builder interface. The diphenylamines of D11 were then modified by the addition of methoxy groups, followed by the attachment of the polyene and thiophene group, and the cyanoacrylic acid. The diphenylamines is the donor unit, polyene and thiophene were the π-conjugation to link or bridge the donor acceptor moiety while -COOH and -CN were the acceptor and anchor units respectively.
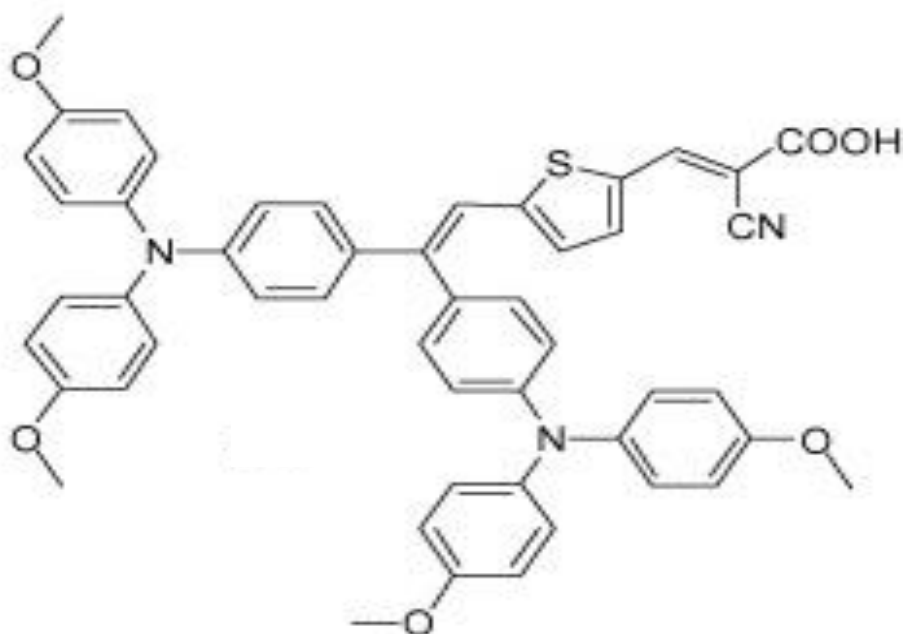
(a)
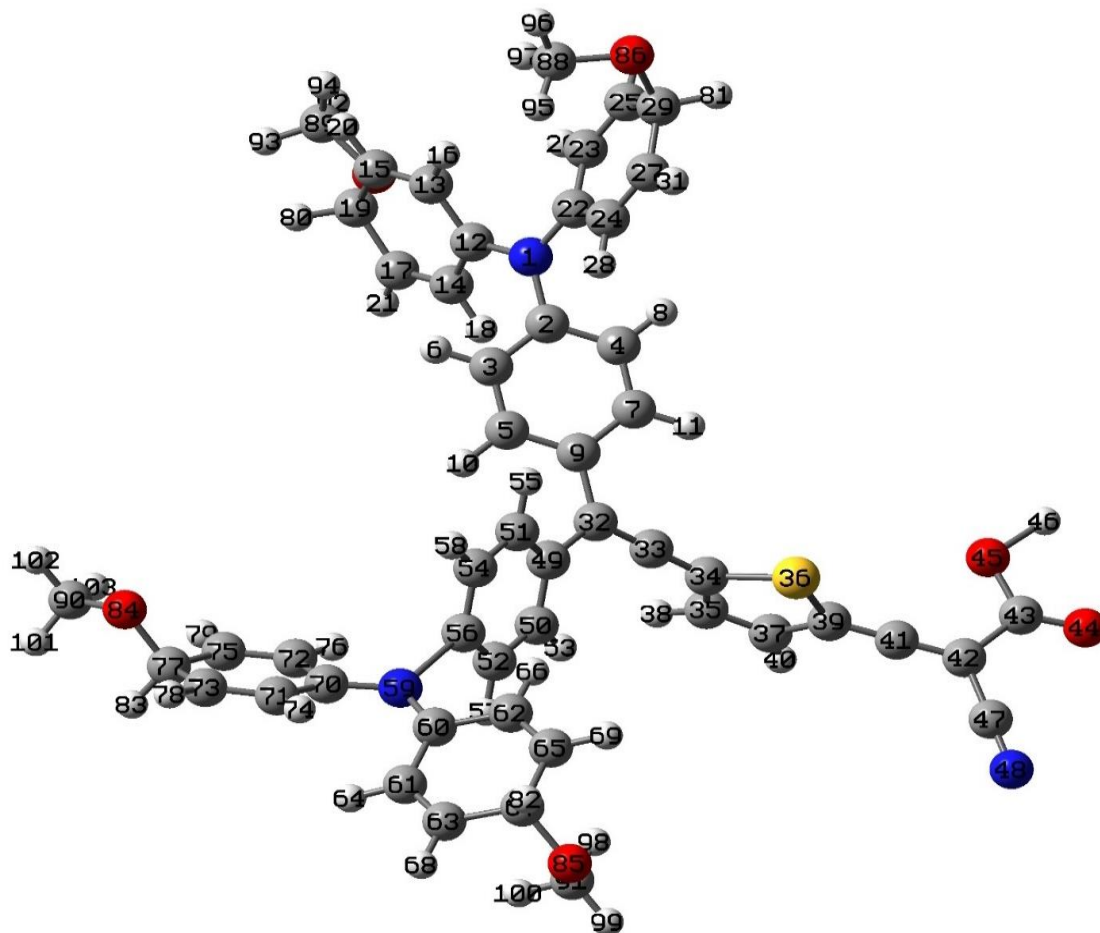
(b)

Figure 16: (a) Polyenediphenyl-aniline dye D11 [82] (b) Polyenediphenyl-aniline dye D11 built with Gaussian 03.

1.11 Outline of the study

The thesis is arranged into seven Chapters and summarised below:

Chapter 1 gives an introduction to the thesis by describing the general background to solar energy and the solar spectrum, the generations and status of photovoltaic technology, the possibilities for cost reductions of the solar cells. A general overview of dye sensitized solar cells was also discussed, the aims, significance, statement of problem, purpose of the study, research motivation, hypotheses as well as the outline of the thesis are presented in this chapter.

Chapter 2 gives a review on some components of dye-sensitized which include the dye sensitizer, nanostructured TiO_2 and the adsorption of dye unto TiO_2. Review of relevant literature on these aforementioned components of DSSCs was presented. The components of the cell are treated individually at each time making a cut-through to the literature by examining

the used materials and their key properties. The application of titanium dioxide, its three polymorphs, its properties and the reviews on semiconductors were highlighted.

Chapter 3 describes the theoretical and computational methods used to carry out the study. Thus, the chapter gives the background information on density functional theory, local density approximation, generalized gradient approximation, pseudopotentials, basis set, k-point sampling. The step by step computational procedures and the software employed in this study were also described in this chapter.

Chapter 4 discusses the results obtained from density functional theory (DFT) and time dependent DFT (TD-DFT) studies of the dye sensitizer molecules. The structural properties obtained by geometrical optimization, UV-VIS, light harvesting efficiencies, HOMO, LUMO, HOMO-LUMO energy gap and isodensity surfaces of the ruthenium N3 complex and metal-free organic dye including polyenediphenyl-aniline dye and the croconate dye are presented and discussed.

Chapter 5 is centred on the results of the computational studies of TiO_2 brookite clusters. The ground state structural properties obtained by structural optimization were presented. The UV-VIS, the density of states and projected density of states of $(TiO_2)n$ brookite cluster where n =5, 8 and 68 were presented .

Chapter 6 presents the results of the dye molecules absorbed on TiO_2 brookite cluster. The UV-VIS absorption spectra, formation energies, HOMO, LUMO, HOMO-LUMO energy gap, isodensity surfaces, free energy of electron injection of both organic and inorganic dye molecules adsorbed on TiO_2 clusters, density of states, the projected density of states and the isodensity surfaces of the key molecular orbital involved in excitations are presented and discussed.

Chapter 7 gives summary and conclusions obtained from the results of this study. Also, recommendations for future studies are also presented.

CHAPTER TWO

2.0 LITERATURE REVIEW

2.1 Sensitizers

Sensitizing dye molecules are used in DSSCs to sensitize the wide bandgap nanostructured photoelectrode/semiconductor. The sensitizing dye is usually chelated to the semiconductor metal oxide surface in DSSC architecture [47]. The dye molecules absorb energy from sunlight usually photons, the dye molecules upon absorption of photon; the dye molecule gets oxidized and the excited electron is injected into the nanostructured TiO_2 [48]. An efficient dye sensitizer for solar cell should bind strongly to the surface of the semiconductor oxide via the anchoring groups, exhibit strong absorption in the UV, visible and near infra-red part of the spectrum, and possess appropriate energy level for alignment of the dye excited state and the conduction band edge of the semiconductor [19]. Three classes of dye sensitizers are used in DSSCs: metal complex sensitizers, metal-free organic sensitizers and natural sensitizers [46]. The ruthenium metal complex sensitizers and the metal free organic sensitizers are the main focus in this study.

2.1.1 Ruthenium sensitizers

Among the first kind of promising sensitizers were the N719 ruthenium complexes shown in Figure 9, which was first reported in 1991 by O'Regan and Grätzel. Conversion efficiency of 7.1 % was achieved with the N719 ruthenium dye [83]. However, this ruthenium dye contained three ruthenium metal at the centres and the structures were complex. In 1993, a new ruthenium dye sensitizer (N3, [*cis*-di (thiocyanate) bis(2,2-bipyridine-4,4-dicarboxylate) ruthenium]) shown in Figure 10 was published by Nazeeruzzin *et al.* with 10.3 % DSSC conversion efficiency [84]. The N3 dye has one ruthenium at its center and the structure was much simpler than the ruthenium N719 dye reported in 1991.

The ruthenium complexes have been investigated extensively. Many researchers have focused on molecular engineering of ruthenium compounds. Nazeeruddin *et al.* reported on the "black dye" as promising charge transfer sensitizer in DSSCs [84]. Kelly *et.al* studied other ruthenium complexes Ru(dcb)(bpy)2 [85] while Farzad *et al.* explored the Ru(dcbH2) (bpy)2(PF6)2 and Os(dcbH2)(bpy)2-(PF6)2 [86]. Other authors investigated various dye molecules and they include, Qu *et al.* who studied *cis*-Ru(bpy)2 (ina)2(PF6)2 [87] , Shoute *et al.* who investigated the *cis*-Ru(dcbH2)2(NCS) [88], and Kleverlaan *et al.* who investigated OsIII-bpa-Ru [89]. So far, the best performances in excess of 12 % power conversion efficiency reported in literature

have been obtained with cells composed of a titania nanoparticle thin film sensitized by a ruthenium (N3) polypyridine complex dye [47, 90-92].

2.1.2 Organic sensitizers

Organic dye are consequently attracting a lot of attention as alternative sensitizers to the ruthenium complexes for DSSCs application [48]. The advantages of the organic dye include higher extinction coefficient, low cost, environmentally friendly and electrochemical properties [93, 94, 82]. The organic dye with basic configuration donor-π-acceptor are relatively cheap, easy to synthesize and possess chemical structure that can easily be altered to optimize photocatalytic properties of the semiconductor [95].

Several organic dye such as coumarins [53], indolines [96], anthocyanidin [54] porphyrins, perylenes, cyanines, mecrocyannines, quinolones, croconate [80], phenothiazine [59], triphenylamine [97] polyene-diphenyl aniline [82], have been reported as sensitizers for DSSCs. These metal-free organic dye have high molar absorption coefficient, various structures, low cost and relatively simple synthesis procedure.

Boschloo *et. al.* [81] carried out investigations on series of synthesized dye and tested them in DSSCs. It was discovered that polyene-diphenyl aniline dye (D5) was easy to synthesize. The study established that D5 demonstrated 5% efficiency with iodide/triiodide based redox electrolyte. The study compared the organic sensitizer (D5) with the standard ruthenium complex sensitizer Ru(dcbpy)2(NCS)2 (N719) using a thin layer of TiO_2 semiconductor to fabricate the DSSCs. It was observed that D5 outperformed the N719 because of its high extinction coefficient and it displayed a better performance for sensitization of mesoporous ZnO with iodide/triiodide electrolyte and amorphous hole conductor (spiro-OMeTAD). The report concluded that the hole conductivity observed in monolayers of D5 absorbed at TiO_2 may possibly lead to improved performance [81].

Diabin *et. al.* [82] experimentally investigated a series of polyene-diphenyl aniline organic based dye coded as D5, D7, D9, and D11 for application in ionic liquid electrolyte-based dye sensitized solar cells. A conversion efficiency of 6.5% under standard 1.5 sunlight at 100

mW/m^2 was obtained with the D11 dye in combination with a binary ionic liquid electrolyte [82].

Chitumella *et al.* studied two croconate dye, CR1 with electron-donating substituent and the other dye CR2 with electron withdrawing substituent using density functional theory. The study calculated electronic and optical properties of these two dye to determine the effect of electron donating/withdrawing substituent on the properties of the dye. The study reported that a bathochromic shift was observed on the dye with the electron withdrawing substituent [79].

Kensuke *et al.* investigated some croconate dye with donor-acceptor-donor structure. The croconate dye were deposited on a thin film on optically transparent electrode film, forming the croconate dye-TiO$_2$ complex. It was found that H- aggregates with a blue shifted absorption maximum around 660 nm. The excitons formed upon excitation of the dye aggregates undergo charge separation at the surface of TiO$_2$. The H-aggregates in the film are photoactive and produce anodic current (IPCE = 1.2 % at 650 nm) when employed in photoelectrochemical cell [98].

Emildo explored the absorption spectra, excited states and electronic properties of anthocynin pigments for application in dye sensitized solar cells using DFT method. The study reported that the distribution of the HOMO and LUMO for the dye molecules spread over the entire molecules, which lead to an efficient electronic delocalization while the methoxy group in the peodin molecule leads to largest oscillator strength and the calculated light harvesting efficiencies are near unity [54].

Jiwon *et al.* performed density functional theory and time dependent density functional theory calculations to elucidate the electronic and optical properties of naphthoxaphospholes (R-NOPs) dye. The results suggested that the poor π overlap between the $3p_z$ orbital and the $2p_z$ orbitals of the other atoms and increasing polarity of P atom results in a reduced energy gap between the highest occupied molecular orbital and the lowest unoccupied molecular orbital. The study elucidated the role of P atom in the control of the electronic and optical properties of R-NOPs [99].

Reda *et al.* investigated the electronic absorption spectra, ground state geometries and electronic structures of symmetric and assymetric squararine dye (SQD1-SQD4) using density functional theory and time-dependent density functional theory at B3LYP/6-311++G** level. The calculated ground state geometries revealed pronounced conjugation in the dye. Long-range-corrected time-dependent density functionals Perdew, Burke and Ernzerhof (PBE, PBE1PBE1 (PBE0)) and the exchange functionals of Tao, Perdew, Staroverov and Scuseria (TPSSH) with 6-311++G** basis set were employed to examine the optical absorption properties of dye molecules. Extensive comparison between the optical data and DFT benchmark calculations indicated that B3LYP functional with 6-311++G** basis set was found to be most appropriate in describing the electronic absorption spectra of the symmetric and assymetric squararine dye. Also, the aromaticity computation of the dye are in good agreement with data obtained optically and geometrically with SQD4 as the highest aromatic structure [100].

Malki *et al.* studied twelve series of novel acceptor-donor organic materials containing thiadiazolothienopyrazine linked to cyanoacrylic acid via dithiophene based alternating donors. The geometries, electronic absorption and emission spectra of the dye were investigated using DFT and TD-DFT calculations. The study reported that the calculated geometries indicated that the molecules are all co-planar. The study also revealed that the electronic excitations to the lowest singlet excited state of the studied models are dominated by HOMO to LUMO+1 electronic transition [101].

Cai-Rong *et al.* studied the geometry, electronic, polarizabilities and hyperpolarizabilities of organic dye sensitizer TA-St-CA containing a π-conjugated oligo-phenylenevinylene unit with an electron donor-acceptor moiety using density functional theory. The electronic absorption spectrum of the dye was investigated using time dependent (TD-DFT) with several hybrid functionals. The calculated geometry indicated strong conjugated effects in the dye molecule. The absorption bands in the visible and near UV regions were attributed to the photoinduced electron transfer process and the diphenylaniline group was the major chromophore that contributed to the sensitization [91].

Zhang *et al.* studied the geometry, electronic, polarizabilities and hyperpolarizabilities of D5, DST and DSS organic dye sensitizer using density functional theory. The calculated geometry indicated that strong conjugated effects were formed in the dye. The polarizabilities were found to depend on the length of the conjugated bridge, also the UV-Vis features were assigned to the π-π^* transitions according to qualitative agreement between the experiment and the TD-DFT calculations. The absorption spectra in the visible region were attributed to the photoinduced electron transfer process and the diphenylaniline group in D5 and aniline group in DST and DSS was the major chromophore that contributed to the sensitization [102].

2.2 Titanium dioxide

Titanium dioxide (TiO_2) belongs to the family of transition metal oxides [103], also known as titania. TiO_2 has been a subject of increasing interest due to its application in pigments, proven ability to function as a photocatalyst and facilitation of important environmentally beneficial reactions, such as water splitting to generate hydrogen and treatment of polluted air, water and semiconductor material in dye sensitized solar cells [64, 104-106]. Also it has been widely used in the medical field, and environmental protection and renewable energy [107].

2.3 Applications of titanium dioxide

2.3.1 Environmental improvement applications

The non-toxicity of TiO_2 makes it an environmental benign. Also, TiO_2 is an effective photocatalyst that when exposed to sunlight results in excitation of supra-band gap photons, which enhance the removal and breaking down of environmental pollutant substances such as NO_2 emitted by exhaust gas into the air and hazardous inorganic matter like SO_2 in the atmosphere, which is washed away by rainfall [108].

2.3.2 Deodorization applications

The good photocatalytic properties of TiO_2 make it applicable in antiseptic and antibacterial compositions. It causes degradation of organic contaminants and germs. It actually attacks the root of the smell by causing the breakdown of the origin of the odour resulting from ammonia and aldehyde gas (smoke). When light strikes titanium dioxide, a chemical reaction is initiated in its immediate region and causes the breakdown of organic toxins, odors, etc. [108].

2.3.4 Water purification applications

TiO_2 causes the removal of organic matter such as organic chlorine compounds, tetrachlorethylene, trihalomethane, and trichloroethylene and methyl-tert-butyl ether from water, and inhibits toxins produced by bluegreen algae and other harmful substances in water to be broken down [109]. For example, chloroform breaks down according to the process shown below:

$$H_2O + CHCl_3 + (1/2) O2 \rightarrow CO_2 + 3HCl \qquad (19)$$
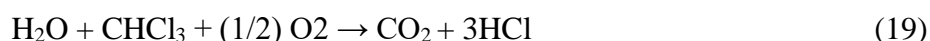
2.3.5 Pharmaceutical applications

TiO_2 photocatalyst can destroy the membrane of cells, solidify the proteins of viruses and restrain virus activation. It has widely been used in the pharmaceutical industries for sterilization of equipment and restraining of virus. A study reported that TiO_2 can kill up to 99.97% bacteria [110]. TiO_2 can kill coliform, green suppuration bacillus, golden grape coccus, mildew, suppuration fungus. The ability of sterilization has been tested through coliform and golden grape coccus. According to John *et al*. [110] at the beginning of the experiment, there were 3.3×10^5 coliforms and 3.2×10^5 golden grape coccus and after 24 hours of the reaction with TiO_2, only ten were left [110].

2.3.6 Photocatalytic application

Photocatalysis refers to the chemical reaction that occurs when light strikes a chemical compound that is light sensitive and photons are emitted from the surface of the compound. Under illumination the TiO_2 photocatalyst absorbs photons with energy equal or higher than its band gap energy ($\lambda < 385$ nm). This will delocalize a valence electron and excite it to the conduction band of the semiconductor. The photo excited charge carriers can initiate the degradation of the adsorbed chemical species by one or more forms of electron transfer reactions. However, they can recombine radiatively or non-radiatively and dissipate the input energy as heat [109]. To improve the efficiency of TiO_2 under light illumination, additives can be added to TiO_2 so that it can be active in the visible region as the band gap energy reduces [108].

TiO_2 thin films are extensively studied owing to their fascinating chemical, electrical and optical properties. The interest in TiO_2 as semiconductor for dye sensitized solar cell is motivated by its non-toxicity and good stability upon illumination [53, 64, 76, 104]. Despite

38

the existence of various semiconductor metal oxide with wide band-gap such as SnO_2 and ZnO, TiO_2 thin films are the most investigated material as photo-electrode for DSSCs application owing to their less susceptibility to photo degradation under illumination to sunlight. Also, the efficiency of DSSCs constructed with TiO_2 electrodes yields the highest values of I_{sc}, V_{oc}, ŋ and the incident photon conversion efficiency (IPCE) [111].

2.4 Physical properties of TiO₂

Titanium oxide is quite abundant in nature with combination of other elements such as iron. It occurs in small amounts in igneous, sedimentary and metarmorphic rocks. Titanium dioxide nanoparticles appear in the form of black hexagonal crystals. The chemical composition of titanium dioxide is 40.55% oxygen and 59.45% titanium atoms and its chemical formula is TiO_2 [112]. Electronic configuration for Ti is [Ar] $3d^24s^2$ and O_2 is [He] $2s^22p^4$.

With molar mass of 79.938 g/mol, density of 4.23 g/cm^3, melting point of 1.843 ^{0}C and boiling point of 2.972 ^{0}C.

2.5 Crystal structural properties of TiO₂

Titanium dioxide exists in three commonly known crystalline structures, namely; rutile, anatase, and brookite and were shown previously in Figure 8. Rutile is the most stable while anatase and brookite are metastable. These polymorphs exhibit different properties as listed in Table 3 and consequently different photocatalytic performances [103].

Table 3: Properties of rutile, brookite and anatase polymorphs of TiO_2 [63, 105].

	Lattice Parameter (Å)	Space Group	System Type	Energy Band Gap (eV)
Rutile	a = 4.594 c = 2.958	$P4_2/mnm-D_{4h}^{14}$	Tetragonal	3.0
Anatase	a = 3.784 c = 9:515	$I4_1amd-D_{4h}^{19}$	Tetragonal	3.4
Brookite	a = 9.166 b = 5.436 c = 5.135	$Pbca-D_{2h}^{15}$	Orthorhombic	3.3

Figure 8 shows the structures of anatase, rutile and brookite polymorphs of TiO_2. In the structures of anatase and rutile, the building blocks consists of a titanium atom surrounded by six oxygen atoms in a distorted octahedral configuration. In each structure, the two bonds between the titanium and the oxygen atoms of the octahedron are slightly longer, the octahedral in the rutile phase forms chains that share edges along the c-direction and shares vertices in the ab-plane, while in anatase structure the octahedral forms zigzag chains along the a- and b-directions with each octahedron sharing four edges [63, 103, 104].

Brookite has an orthorhombic crystalline structure with eight formula units in the orthorhombic cell, its unit cell is described by the space group *Pbca* [63, 65, 71]. Brookite formation may be envisioned as the joining of TiO_6 distorted octahedral sharing three edges, each with a titanium atom at its center and oxygen atoms at its corners as shown in Figure 8. The octahedral share edges and corners with each other to such an extent as to give the crystal the correct chemical composition. The octahedral are distorted and present the oxygen atoms in two different positions [65]. The bond lengths between the titanium and oxygen atoms are all different [71]. Rutile and anatase polymorphs have been widely employed in DSSCs architecture [76, 113]. However brookite has been least employed and explored owing to its difficult synthetic route.

2.6 Semiconductor properties of TiO₂

Electrons in an isolated atom have certain discrete energy levels, when large groups of atoms combine to form molecules or solid mass, atomic interaction causes varying energy level due to the mass amounts of different molecular orbital which may be close or even completely degenerate. These energy levels are said to form continuous bands of energy. The band of energy in the highest energy molecular orbital (HOMO), where all the valence electrons reside is the valence band (VB) and it may be completely or partially filled. The band energy where positive or negative mobile charge carriers exist is the conduction band (CB). The maximum attainable valence-band energy is denoted E_V and the minimum attainable conduction-band energy is denoted E_C. The energy difference between the edges of these two bands is called the band gap energy or band gap (E_G) and the description is illustrated in Figure 17. Thus

$$E_G = E_C - E_V \qquad\qquad (20)$$

At low temperatures, the valance band is full while the conduction band is empty. Positive mobile charge carriers are holes while negative mobile charge carriers are simply electrons. When the electrons acquire enough energy, they escape the valence band leaving holes behind and jump to the conduction band where they are able to move freely throughout the crystal lattice and are directly responsible for conduction in semiconductor materials [114,115].
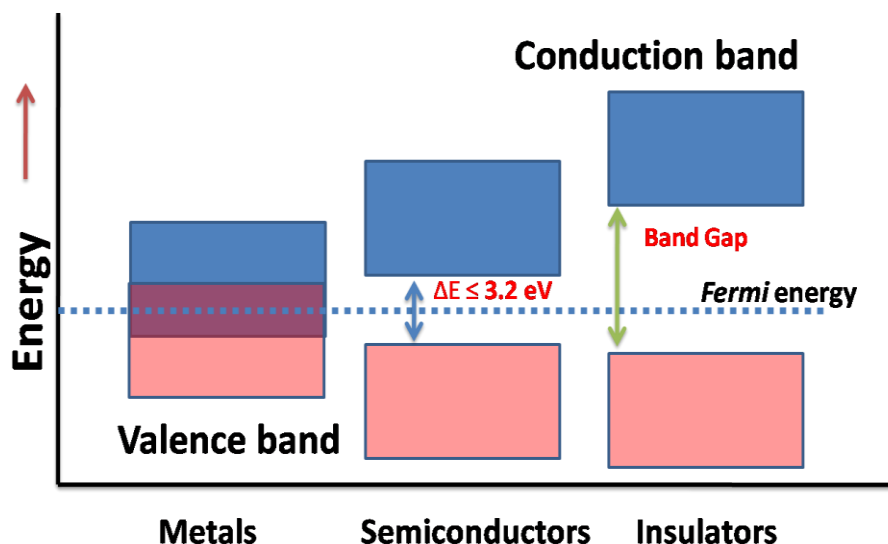
Figure 17: Conduction bands (blue), valence bands (peach), Fermi energy levels and band gaps for insulators, semiconductors and conductors.

In metals, the conduction band lies directly above the valence band as shown in Figure 17, and the highest occupied energy level sits at the boundary between these two bands, electrons at the top of the valence band needs only infinitesimal amount of energy to jump into the conduction band [114]. In insulators, the energy gap that separates the valence band and the conduction band is very large. The forbidden gap is of the order of a few electron volts and is so large that it is not usually practicable to obtain sufficient energy to move electrons across from the valence band to the conduction band. Thermal excitations and conventional electric circuit voltages within a material provide energies that are smaller than 1 eV on an atomic scale. This energy is not enough to overcome the energy gap between the valence and the conduction band in insulators [115]. In order to increase the conductivity of semiconductors, small amounts of doping material can be used. This results in significant increase in conductivity as a result of the narrowing of the band gap between the conduction and valence bands. Semiconductors are basically characterized by charge carriers, which are holes and electrons. The charge carriers exhibit conductivity intermediate in magnitude between conductors and insulators. Their resistivity ranges between 10^9 and 10^{-2} Ωcm. [114]. The concentration of free electrons and holes increases with increasing temperature. Semiconductors that conduct in chemically pure states are called intrinsic semiconductor, examples include silicon and germanium.

Semiconductors have similar band structure as insulators but with a much smaller band gap. Some electrons can jump to the empty conduction band by thermal or optical excitation. The working principle of the photovoltaic cells is based on the optical excitations and photovoltaic effect [116]. The photovoltaic effect was innovated by a French experimental physicist 'Edmund Becquerel' in 1839 while conducting experiment with an electrolytic cell consisting of two metal electrodes, where discovered that two brass plates immersed in a liquid produced current when exposed to light [117].

The photovoltaic effect describes the phenomenon in which electromagnetic radiation incident on a material creates charge carriers (hole-electron pair) within the materials that are separated and recombined through an external circuit to generate electricity. The photovoltaic cell (PV) captures photons from sunlight, proficiently separates charges, and creates a potential difference/voltage and a corresponding electric current when illuminated. The separation of the

photo-generated charges typically occurs in semiconductor materials. The operation of the photovoltaic cell is hinged on semiconductor materials [118].

When photons are absorbed by a photovoltaic cell that contains semiconducting materials sandwiched together, a p-n junction that is formed by the intimate contact of p-type and n-type semiconductors exist within the PV cell. The p-n junction creates an internal electric field within the cell and the energy from the photon is transferred to an electron in an atom of the PV cell as shown in Figure 18. The energized electron is excited to a higher energy level thereby leaving a hole behind. The holes move in the opposite direction from electrons, thereby producing electric current with a given load resistance.
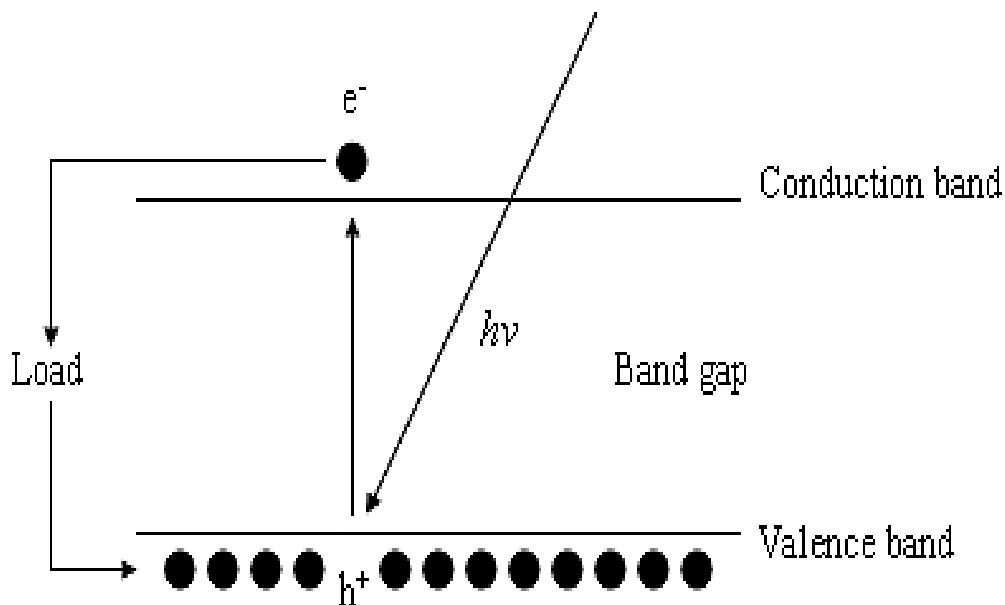
Figure 18: How Photovoltaic cell generates electricity [14].

2.6.1 Direct and indirect band gaps

The energy-momentum *(E-k)* relationship for carriers in a lattice and the interactions of photons and phonons where energy and momentum must be conserved (electrons and holes) leads to the concept of energy gap. The band structure of a crystalline solid, that is, the energy-momentum *(E-k)* relationship, is usually obtained by solving the Schrödinger equation of an approximate one-electron problem [119].

$$\left(\frac{-h^2}{2m}\nabla^2 + V(R)\right)\varphi(r,k) = E(k)\varphi(r,k) \tag{21}$$

© University of Venda

The energy E of a particle is always associated with a wave vector k (or momentum), hence for any transition between bands, both energy and momentum must be conserved. When an electron acquires enough energy to exceed the energy gap E_G, the electron can jump from the valence band into the conduction band. The source of the energy could be photons, phonons, or electric field. [120].

The band gap in semiconductor material is essential for its application in electronic devices, thermoelectric devices, solar cells and lasers. The two types of band gaps in semiconductors are *direct* and *indirect band gap*. In direct-band gap semiconductors, the minimum of the conduction band and maximum of the valance band lie at the same momentum (k) values as shown in Figure 19. When an electron sitting at the bottom of the CB recombines with a hole sitting at the top of the VB, there will be no change in momentum values. Energy is conserved by means of emitting a photon and such transitions are called a radiative transition. In indirect band gap material, the minimum of the CB and maximum of the VB lie at different k-values as shown in Figure 19. When an electron and hole recombine in an indirect-band gap semiconductor material, phonons must be involved to conserve momentum [121].
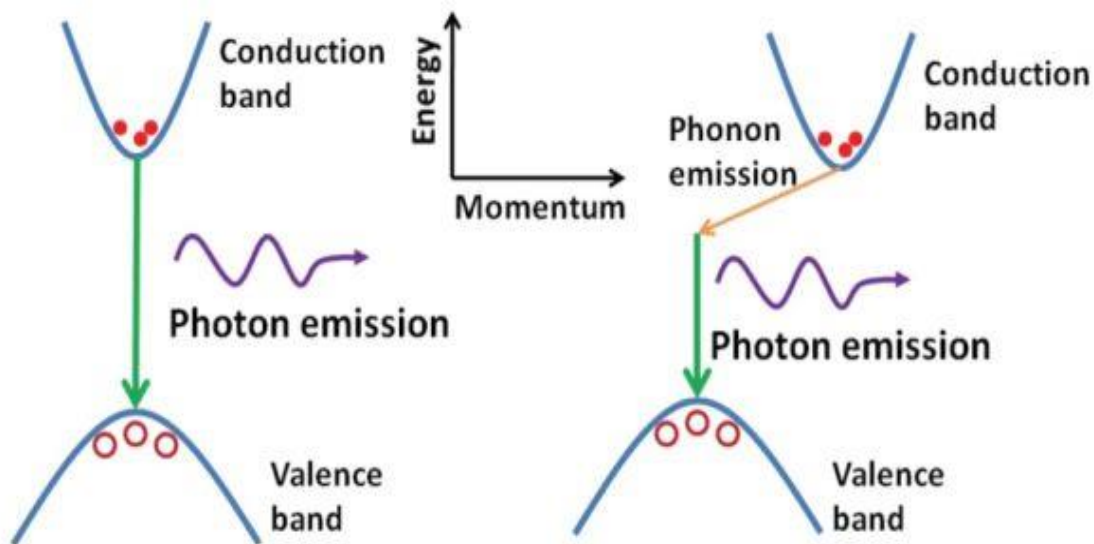
Figure 19: photon emission in direct and indirect band gap semiconductors [55].

2.6.2 Fermi levels in semiconductors

The conduction band in a semiconductor material consists of many allowed empty energy levels. The probability function called the Fermi-Dirac distribution function f (E) is the probability that a level with energy E will be filled by an electron at thermal equilibrium. Fermi-Dirac distribution function f (E) is given by the expression:

$$f(E) = \frac{1}{1 + exp\left(\frac{E - E_F}{k_B T}\right)},$$ (22)

where k_B is Boltzmann's constant, T is the temperature in Kelvins and E_F is the Fermi energy or Fermi level. The Fermi energy is the electrochemical potential of the electrons in a semiconductor material. It represents the average energy of electrons in the material. $f(E)$ is the probability that the energy level E will be filled by an electron while $\left(1 - f(E)\right)$ is the probability that the energy level E will be empty or the probability that the energy level E in the valence band will have a hole equivalently [114, 122].

2.6.3 Density of states and carrier concentration

Energy band can be described as a collection of discrete energy states. In quantum mechanics, each state represents a unique spin (up and down) and unique solution to the Schrödinger's wave equation for the periodic electric potential function of the semiconductor [120]. For an intrinsic semiconductor, the number of electrons (occupied conduction-band levels) is given by the total number of states N(E) multiplied by the occupancy F (E), integrated over the conduction band as presented in Equation (23),

$$n = \int_{E_c}^{\infty} N(E) F(E) dE \,;$$ (23)

Each state can hold either one electron or none. The number of states in a small range of energy ΔE in the energy bands is the *density of states* [18] given by:

$$D(E) = \frac{number\,of\,states\,\Delta E}{\Delta E \times Volume}.$$ (24)

The density of states of conduction-band CB and valence-band VB, denoted by Dc and Dv respectively is a function of E where ΔE is located.

$$D_c(E) = \frac{8\pi m_n \sqrt{2m_n(E-E_c)}}{h^3} E \geq E_C \tag{25}$$

$$D_v(E) = \frac{8\pi m_p \sqrt{2m_p(E_v-E)}}{h^3} E \leq E_v \tag{26}$$

where m_n and m_p are the effective masses of electrons and holes respectively, averaged over different directions to take anisotropy into account. $Dc(E)$ and $Dv(E)$ have the dimensions of number per cubic centimeter per electron Volt. The product $Dc(E)\ dE$ and $Dv(E)\ dE$ are the numbers of energy states located in the energy range between E and $E + dE$ per cubic centimeter of the semiconductor volume. The photovoltaic effect and separation of charge carries in semiconductors is the operating principle applied in photovoltaic technologies to generate electricity.

Significant studies established that TiO₂ is much more effective as a photocatalyst in the form of nanoparticle than in bulk structure. It was reported that the reduction in the diameter of a crystalline semiconductor particle below a critical radius of 10 nm makes the charge carrier appear to behave quantum mechanically as a simple particle in a box [123]. Mill and Le Hunte [124] reported that because the absorption edge blue shifts with decreasing particle size, the redox potential of photogenerated holes and electrons increases in a quantized semiconductor particle; implying that quantized particles show higher photoactivity than microcrystalline semiconductor particles.

Tong *et al.* [103] used DFT-GGA+D+U calculations to study the enthalpies of nine TiO₂ polymorphs under hydrostatic pressure from 0 to 70 GPa. An enthalpy order agreeing with the experimental order of rutile < brookite < anatase was obtained. Amongst all the polymorphs studied brookite and tridymite structured TiO₂ polymorphs were reported to have a direct band gap [105].

Recent studies have suggested that brookite is a good photocatalyst and may exhibit higher photocatalytic activity than both rutile and anatase [61]. Density functional theory studies

performed on brookite (210) and anatase (101) surfaces demonstrated that brookite (210) surface has similar building blocks as anatase (101) surface. Brookite (210) surface is one of the most stable and relaxed surface of brookite polymorphs [61].

Beltran *et. al.* [104] used density functional theory to investigate the structural and electronic properties of the low index surfaces of brookite form of titania. The surface energies, band energy values and hydrostatic pressure response of the bulk structure were investigated. The study reported that the orthorhombic structure and fractional coordinates of brookite vary isotopically with the rise in pressure. The calculated band gap for bulk brookite was found to be 3.78eV while the surface stability follows the sequence (010) < (110) < (100). The minimum gap energy was observed for brookite (110) surface [104].

Zallen *et. al.* [75] measured the optical absorption edge of brookite TiO_2 at room temperature using natural crystals. The measurement extended up to 3.54 eV in photon energy and 2000 cm^{-1} in absorption coefficient. The study reported that the absorption edge of brookite was broad and extends to the visible region of the solar spectrum which is quite different from the steep edges in the visible region observed for rutile and anatase polymorphs of TiO_2 [75].

Again recent study on TiO_2 brookite suggested that it is a good photocatalyst and may exhibit higher photocatalytic activity [76]. The absorption edge of brookite observed in a prior study was also reported to be broad and extends to the visible region of the solar spectrum in contrast to steep edges in the visible region observed for rutile and anatase polymorphs of TiO_2 [75]. Since brookite surfaces have not been studied much and the fact that it is reported to have better photocatalytic properties, it is of keen interest to study the interactions of dye molecules with brookite TiO_2 for optimization of photon current density in dye sensitized solar cell.

2.7 Adsorption of dye to TiO_2 surfaces and anchor group

Dye molecules are absorbed to the surface of nanocrystalline semiconductors through one or more anchoring groups. The binding modes of dye to the surface of TiO_2 and the electronic coupling between the dye-excited states and the unoccupied states of the semiconductor affects the performance of DSSCs. There are various binding modes of an adsorbate to a metal oxide surface through adsorbate oxygen atoms and surface metal atoms. The coordination can either

be mono (1M), bi (2M) or tridentate (3M), depending on how many oxygen atoms the molecule use to coordinate to the surface metal atom. When there are several metal-oxygen bonds, the adsorption modes can also be distinguished by the number of metal atoms involved (1M, 2M) in the adsorption process. The carboxylic acid group together with the phosphonic acid is the most frequently used anchor group for attachment of sensitizers to semiconductor surfaces [50, 125, 126]. Figure 20 schematically shows some of the possible structures for various adsorption modes for carboxylic acid.

| (a) | (b) | (c) |
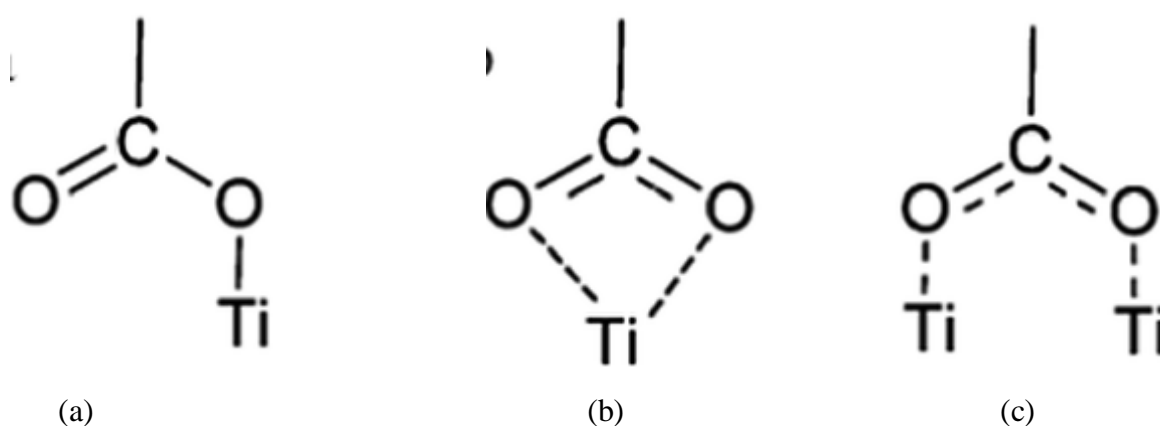
Figure 20 (a) monodentate (b) bidentate chelating (c) bidentate bridging. [127, 128].

Recent studies on the adsorption of dye bearing carboxylic acid on TiO_2 surfaces reported that the preferred adsorption mode is bidentate bridging (BB) depicted in Figure 20c with one proton transferred to a nearby surface oxygen. [50, 125, 129, 130, 131].

A systematic density functional theory on adsorption geometry of Ru and YE05 sensitizer on TiO_2 substrate for DSSCs application was reported by Fillipo *et. al.* [50]. The results showed that the dye bearing two bipyridine ligands functionalized with four carboxylic groups adsorb onto TiO_2 surface by exploiting the carboxylic groups [50].

Prajongtat *et al.* studied the structural and electronic properties of eight isolated azo dye (Ar-N=N-Ar, where Ar and Ar' denote the aryl group containing benzene and naphthalene skeletons) and its absorption unto anatase TiO_2 using density functional theory. The calculated adsorption energies indicate that the adsorbed dye preferentially take configuration of the bidentate bridging rather than chelating or monodentate geometries. Furthermore, the azo compounds having two carboxyl groups are coordinated to the TiO_2 surface more preferentially

through the carboxyl group connecting to the benzene skeleton than the naphthalene skeleton [132].

Babara *et al.* used vacuum tight attenuated total reflection infrared (ATIR-IR) and vacuum spectrometer to monitor infiltration of dye molecules unto porous TiO_2 film at high sensitivity and the influence of anchor and backbone of perylene dye molecules. Their findings showed that the dye with acidic anchor group adsorb better to the thin films than those with anhydride group. The simulation results generally suggest that anchoring group has a strong effect on the adsorption rate [41].

Chiara *et al.* used FTIR measurements and computer simulations to study the energetically favourable TiO_2 adsorption mode of acetic acid as a meaningful model for realistic organic dye. The findings showed that a bridged bidentate adsorption mode was found to closely match the FT-IR frequency pattern and was found to be the most stable binding for realistic organic dye bearing cyanoacrylic anchoring groups. For rhodamine-3-acetic acid anchoring group, undissociated monodentate adsorption mode was found to be of comparable stability, although a stronger coupling and faster electron injection were obtained for the bridged bidentate mode. The assessment generally showed that the structural differences induced by the different anchoring groups were related to the different electron injection/recombination with oxidized dye properties [133].

A significant number of studies has been done on surface modification of TiO_2 crystals with atoms/sensitizing dye molecules to subsequently reduce the band gap and further enhance its activities in the visible and near infra-red region of the solar spectrum. Anatase and rutile polymorphs of TiO_2 have been commonly used models for such studies to improve photocurrent yield and light harvesting in DSSCs [41, 53]. Energy band modulation by elemental doping, monodoping, codoping with nonmetals and transition metals and adsorption of dye molecules on TiO_2 surfaces have been attested. The results showed improved spectral response and enhanced photocatalytic performances of TiO_2 [73, 134]. Surfaces of rutile and anatase polymorphs have been greatly exploited and have been a prototypical model for basic

studies on TiO_2 oxide [74, 75]. Thus, relatively limited work has been done on brookite form of TiO_2 in contrast to rutile and anatase polymorphs that have been greatly exploited [76].

Hou *et al*. studied the electronic band structures of TiO_2 3d transition doped metal ions (V, Cr and Fe) using ab initio band calculations based on a self-consistent full potential linearized augmented plane-wave method within the first principle formalism. The experimental and calculated results show that the optical band gap of TiO_2 films is narrowed by ion implantation. The study established that the 3d state of V, Cr and Fe ions plays a significant role in the red shifting of UV-Vis absorbance spectrum [134].

Jun *et al*. studied alkaline earth metal Ca and N co-doped anatase TiO_2 sheets with exposed (001) facets obtained though hydrothermal methods. The X-ray diffractometer and X-ray photoelectron spectroscopy results confirm that Ca and N co-doped TiO_2 have higher crystallinity than N monodoped TiO_2. The study reported that the hydroxyl radicals (OH) producing the photocatalytic experiment reveals that Ca and N co-doped can effectively decrease the generation of recombination centres and enhance the separation efficiency of photo-induced electrons and holes as well as photocatalytic activity of TiO_2 [135].

Yaqin *et al*. studied the electronic structures, formation energies and band edge positions of anatase TiO_2 doped with transition metal using ab *initio* band calculations based on density functional theory with planewave ultrasoft pseudopotential method. The model structures of transition metal doped TiO_2 were doped by replacing one Ti atom with a transition metal atom. The results indicated that transition metal doping can narrow the band gap of TiO_2, thus improve the photo-reactivity of TiO_2 and simultaneously maintain strong redox potential [64].

Xu *et al*. studied transition metals (V or C) and non-metals (N or C) co-doped anatase TiO_2 to modify the photoelectrochemical properties of anatase TiO_2. The dopant formation energies and electronic structures were performed to investigate the stability and visible light photoactivity by first principles plane wave ultrasoft pseudopotential calculations. The study showed that co-doping with transition metals facilitates the enhancement of the concentration

of p-type dopants. Compensated co-doping reduced the energy gap, enhanced the optical absorption, improved the carrier mobility and conversion efficiency and also kept the oxidation-reduction potential of the conduction band edge [136].

Puyad *et al.* studied two model croconate dye labelled CR1 and CR2, one with an electron-donating substituent (CR1) and the other with an electron-withdrawing group (CR2) and its adsorption on the stoichiometric TiO_2 anatase (101) surface using the periodic density functional theory to understand the adsorption of the diketo (-COCO-) groups. The findings showed that the acidic group (-COOH) possesses a strong binding ability to the TiO_2 surface. Other theoretical studies also predicted the binding strength of the diketo group to be significant and comparable with that of the -COOH group. This causes a competitive binding between the diketo groups and the acid groups on the TiO_2 surface in the case of croconate dye [78].

Chitumalla *et al.* later reported on the two croconate dye, CR1 and CR2 using density functional theory. The study was based on calculations of the electronic and optical properties of these dye. The work investigated the adsorption behaviour of the two dye on a TiO_2 (101) anatase surface by employing periodic DFT simulations. The periodic and electronic-structure calculations revealed that the diketo group of CR1 bind more strongly to the TiO_2 surface than that of CR2, with a binding strength comparable to that of a typical organic d–π–a dye. The study suggested that the nature of the substituent plays a vital role on the electronic, optical and adsorption properties of the croconate dye [77].

Leonardo *et. al.* [137] reported a periodic density study of adsorption of a tertiary trimethylamine on the three most exposed surfaces of stoichiometric anatase TiO_2 nanorods. The energetic, structural and electronic properties were studied and characterized and trimethylamine was found to introduce new molecular states at the edge of the valence band of TiO_2 [137].

Hao Yang *et. al.* [53] investigated the adsorption behaviour of ruthenium (N3) sensitizer on anatase TiO_2 (001) surface employing density functional theory. The study concluded that the interplay of N3 with the (001) surface is considerably stronger than N3 interacting with (101) surface resulting in a larger dye coverage on (001) surface. The energy gap of the N3 sensitizer decreased upon adsorption, suggesting larger range for the absorption spectrum than the

isolated N3 sensitizer. Moreover, the TiO_2 (001) surface was found to have higher conduction band minimum compared with the TiO_2 (101) surface, which indicated higher open circuit voltage. The results gave useful clues and insight in understanding the high solar to electricity conversion efficiency of DSSCs with nanocrystals of TiO_2 (101) exposed surfaces [53].

Corneliu *et. al.* 2013 [66] reported DFT studies of several coumarin based dye: C343, NKX-2398, NKX-2311, NKX-2766 and NKX2700 adsorbed on TiO_2 nanoclusters. The findings showed that NKX-2398 and NKX-2311 have good energy level alignment and electron transfer properties and these dye systems are expected to perform better as DSSCs sensitizers [66].

Monique *et al.* studied the interactions of CO_2 with (210) surface of brookite TiO_2 using first principle calculations on cluster and periodic slab systems. The charge spin density analyses were implemented to determine the charge transfer to CO_2 molecule and compared to the charge transfer to anatase TiO_2 (101) surface. The study reported that brookite (210) surface provide energetically similar CO_2 interactions as compared to the anatase (101) surface. The findings suggested that the modification of brookite surface through the creation of oxygen vacancies may enhance the reduction of CO_2. The laboratory data generated using diffuse reflectance Fourier Transform Infra-Red spectroscopy confirms the presence of CO_2^- at significant levels of the oxygen deficient brookite [61].

Veronica *et al.* studied the interaction of TiO_2 surface reactivity with H_2O, CH_3OH, H_2O_2 and HCO_2H with anatase (101) and rutile (101) surfaces in aqueous solution employing a continuum model in a DFT framework with periodic boundary conditions. Their findings showed that molecular adsorption was found to be most stable for water and methanol, positive adsorption energy obtained suggests that CH_3OH and H_2O_2 will poorly absorb from aqueous solution at titania surface. Formic acid was found to exhibit higher affinity for the surface of TiO_2 [138].

Density functional theory and time-dependent density functional calculations of the geometries, electronic structures and absorption spectra of phenothiazine-based dye were

reported by Asif *et. al.* [59]. Phenothiazine dye with electron deficient thiadiazole derivatives as π spacer and the binding of the dye to TiO_2 were investigated. Enhanced spectral responses in the red spectral region of the solar spectrum were observed with the phenothiazine dye with electron deficient thiadiazole derivatives when adsorbed on TiO_2. The dye also demonstrated desirable energetic and spectroscopic parameters and are regarded as efficient organic dye for DSSCs [59].

To the best of our knowledge, no work has been done on the adsorption and studies of the interaction of dye molecules on brookite TiO_2. Hence this research work is tailored towards the investigation of interaction and the study of the adsorption of ruthenium dye and some organic dye molecules on brookite clusters using computer simulation based on Gaussian 03 quantum chemical package and other computational softwares implemented in first principle density functional theory calculations. The UV-Vis absorption, electronic excitations energies and light harvesting efficiencies of the dye molecules were investigated. The dye were then adsorbed on various brookite $(TiO_2)_n$ cluster with n=5, 8 and 68. Their formation energies, UV-Vis absorption, HOMO- LUMO energy levels and energy gap, energy level alignment and free energy of electron injection, density of states and projected density of states of the dye/brookite TiO_2 complex were studied. The aim is to optimize the optical properties of dye/ brookite TiO_2 interface to further understand the absorption mechanisms and subsequently improve the photon to current conversion efficiency in DSSCs.

CHAPTER THREE

3.0 THEORETICAL METHODS

3.1. Schrödinger Equation

The Schrödinger equation is the fundamental equation of physics for describing quantum mechanical behaviour of a system. It is a partial differential equation that describes how the wave function of a physical system evolves over time. The time-dependent one-dimensional Schrödinger equation is given by:

$$i\hbar \frac{\partial \varphi(r,t)}{\partial t} = \left(\frac{-\hbar^2}{2m} \nabla^2 + V \right) \varphi(r,t), \tag{27}$$

where φ is a wavefunction, r is the position, t is the time, ∇^2 is the Laplace operator, V is the potential energy, $\hbar$ is Planck's constant divided by 2π and m is the mass of the electron. The term $\left(\frac{-\hbar^2}{2m} \nabla^2 + V \right)$ is the Hamiltonian operator defined as:

$$H = \left(\frac{-\hbar^2}{2m} \nabla^2 + V \right), \tag{28}$$

When the Hamiltonian operates on a wavefunction, it gives the energy of the wavefunction

$$\left(\frac{-\hbar^2}{2m} \nabla^2 + V(R) \right) \varphi(r,k) = E(k)\varphi(r,k), \tag{29}$$

The band structure of a crystalline solid, that is, the energy-momentum (E-k) relationship, is usually obtained by solving the Schrodinger equation of an approximate one-electron problem [68, 69].

3.2. Density Functional Theory

Density functional theory (DFT) is a quantum mechanical theory of correlated many-body systems in which the ground state energy and other electronic properties of atoms, molecules and solids are described from ground state electron density p(r). DFT is a ground-state theory in which the emphasis is on the charge density as the relevant physical quantity [139, 140]. The theory has proved to be highly successful in describing structural and electronic properties of

© University of Venda

a vast class of materials, ranging from atoms and molecules to simple crystals and complex extended systems. Furthermore, DFT is computationally flexible. Hence, DFT is a common tool in first-principles calculations aimed at describing and predicting properties of molecular and condensed matter systems [140].

Thomas and Fermi [141, 142], first reported using electron density as a functional for the ground state energy, based on the uniform electron gas. Thomas and Fermi proposed the following functional for the kinetic energy:

$$T_{TF}[\rho(r)] = \frac{3}{10}(3\pi^2)^{2/3} \int \rho^{5/3}(\vec{r})d\vec{r}. \tag{30}$$

The energy of an atom is finally obtained using the classical expression for the nuclear potential and the electron-electron potential [141, 142]. Hohenberg and Kohn [143] illustrated that the external potential $V_{ext}(\vec{r})$ is a unique functional of $\rho(\vec{r})$; since, in turn $V_{ext}(\vec{r})$ fixes H, the Hamiltonian is a unique functional of the electron density. For many-electron Hamiltonian is given by:

$$H = T + U + V, \tag{31}$$

with ground state wavefunction Ψ. The parameter T is the kinetic energy, U is the electron-electron interaction, V is the external potential. The charge density $\rho(r)$ is defined as:

$$\rho(r) = N \int \varphi. \tag{32}$$

Thus, $\rho(\vec{r})$ determines N and $V_{ext}(\vec{r})$ and hence all the properties of the ground state, for example the kinetic energy T[ρ], the potential energy V [ρ], and the total energy E[ρ]. The total ground state energy is thus given as:

$$E[\rho] = E_{NE}[\rho] + T[\rho] + E_{ee}[\rho] = \int \rho(\vec{r})V_{Ne}(\vec{r})d\vec{r} + F_{HK}[\rho], \tag{33}$$

where $F_{HK}[\rho]$ is a functional of the charge density, $F_{HK}[\rho]$ contains the contributions of the kinetic energy, the electron electron interactions, the classical Coulomb interaction and the non-classical portion given as [143]:

$$F_{HK}[\rho] = T[\rho] + E_{ee}[\rho] + \text{J}[\rho], \tag{34}$$

55

$$E_{ee}[\rho] = E_{ncl}[\rho] + J[\rho]. \tag{35}$$

E_{ncl} is the non-classical contribution to the electron-electron interaction: self-Interaction correction, exchange and Coulomb correlation. Only J[ρ] is known, the exact form of $T[\rho]$ and $E_{ncl}[\rho]$ is not known, if the mathematical form of the universal functional were known, the exact electron density function of the ground state would provide a reference for the utilization of the variational principle [144]. This form is not known and cannot be precisely determined or systematically improved. This leads to the formalism of the DFT which was developed by Kohn and Sham who proposed that the exact density for interacting electrons should also be specified in terms of the spin orbitals, $\{\psi_i(\mathbf{r})\}$ and can be illustrated as [145]:

$$\rho s(\vec{r}) = \sum_i^N \sum_s \psi(r,s)^2 = \rho s(\vec{r}). \tag{36}$$

They further proposed the exact kinetic energy of a non-interacting reference system with the same density as the real, interacting one.

$$T_S = \frac{-1}{2} \sum_i^N \langle \psi_i | \nabla^2 | \psi_i \rangle, \tag{37}$$

where ψ_i denotes the orbital of the non-interacting system. T_S is not the true kinetic energy of the system. Kohn and Sham accounted for that by introducing the following separation of the functional [145].

$$F[\rho] = T_S[\rho] + J[\rho] + E_{XC}[\rho], \tag{38}$$

$$E_{XC}[\rho] = (T[\rho] - T_S[\rho]) + (E_{ee}[\rho] - J[\rho]), \tag{39}$$

where $E_{XC}[\rho]$ is the exchange-correlation energy, considering the corrections with respect to a system of non-interacting electrons. Correction to the kinetic energy $(T[\rho] - T_S[\rho])$ and correction to the electron-electron interaction energy $(E_{ee}[\rho] - J[\rho])$, $E_{XC}[\rho]$ replaces the exact Hatree- Fock (HF) exchange for a single determinant by a more general expression, including terms accounting for both exchange energy and the electron correlation (while the latter is omitted from HF energy). The exchange and correlation energy E_{XC} is the functional that

contains everything that is unknown. This idea paved way in quantum chemistry since a system with complicated N electron wave functions can be described by one scalar function p(r) with three variables.

$E_{XC}[\rho]$ also, has an associated exchange-correlation potential, $V_{XC}(r)$:

$$V_{XC}(r) = \frac{\delta E_{XC}\rho(\vec{r})}{\delta\rho(\vec{r})}. \tag{40}$$

The ensuing eigenvalue equation (Kohn-Sham equations) has the form:

$$\left\{\frac{-1}{2}\nabla^2 + V(r) + \int\frac{\rho(\vec{r})}{(r-\vec{r})}dr + V_{XC}(r)\right\}\psi_i(r) = \varepsilon_i\psi_i(r). \tag{41}$$

3.2.1. Local Density Approximation

Local Density Approximations (LDA) is central to all approximation for the exchange correlation functional. The LDA approximates the exchange correlation energy at each point of the system as the energy of a uniform electron gas emanating from the same density. However, for the study of molecular systems, it underestimates the exchange energy by -10%, thus introducing errors that are larger than the whole correlation energy while the normally much smaller correlation energy is generally overestimated by up to a factor of two.

$$E_{XC}^{LDA} = \int\rho(\vec{r})\,\varepsilon_{XC}\rho(\vec{r})d\vec{r}. \tag{42}$$

The exchange correlation potential is given by:

$$V_{XC}^{LDA} = \frac{\delta E_{XC}^{LDA}}{\delta\rho} = \int\varepsilon_{XC}\rho(\vec{r})\,d\vec{r} + \int\rho(\vec{r})\frac{d\varepsilon_{XC}(\rho(\vec{r}))}{dp}\rho(\vec{r})d\vec{r}. \tag{43}$$

In LDA method, only the electron density (ρ) at a point $\vec{r}$ is considered for the approximation of the exchange correlation energy, the gradient of the charge density ($\nabla\rho$) is not utilized to approximate the exchange correlation energy, this led to the development of generalized gradient approximation (GGA) method.

3.2.2. Generalized Gradient Approximation

The Generalized Gradient Approximation (GGA) method is an improvement of the LDA in which not only the electron density (ρ) at a point $\vec{r}$ is considered, the gradient of the charge

density ($\nabla\rho$) is also utilized to approximate the exchange correlation energy to account for the non-homogeneity of the true electron density given by [146]:

$$E_{XC}^{GGA} = E\left[\rho(\vec{r}), |\nabla\rho(\vec{r})|\right].\qquad(44)$$

The generalized gradient approximation includes only the first derivatives of the density (plus the condition that the Fermi and Coulomb holes integrate to the required values). Although there are various GGAs, one of the most commonly employed one is the GGA by Perdew, Burke, and Ernzerhof (PBE) [147]. GGA-PBE is the default exchange-correlation functional. It is recommended, especially for studies of molecules interacting with metal surfaces, although it is also reliable for bulk calculations. Generalized gradient approximation provides a better overall description of the electronic subsystem than the LDA functionals.

3.2.3. Hybrid Density Functionals

Hybrid density functionals mix a portion of the density functional exchange energy for electron gas (i.e. GGAs or the LDA) with the exchange energy from Hartree-Fock calculation [148]. A popular gradient-corrected exchange functional is the one proposed by Becke in 1988 [149]. A widely-used gradient-corrected correlation functional is the LYP functional of Lee, Yang and Parr [150]. The combination of the two functionals (Becke for the exchange component and LYP for the correlation component) is denoted as B-LYP. The B3LYP is one of the most widely used hybrid functionals from the Becke's three-parameter formulations.

The mathematical form of B3LYP functional contains three semi-empirical parameters, a, b and c, whose values enable one to reproduce the exchange-correlation energy of 31 pre-selected molecular species.

$$E_{XC}^{B3YLP} = (1-a)E_X^{LDA} + aE_X^{HF} + b\Delta E_X^{BECKY} + cE_C^{LYP} + (1-c)a_C E_C^{VWN},\quad(45)$$

E_{XC}^{LDA} is the exchange energy from the local density approximation, E_X^{HF} is the exchange energy from a Hartree-Fock calculation, ΔE_X^{BECKY} is the gradient correction to the LDA exchange by Becke [151], E_C^{LYP} is the gradient corrected correlation energy by Lee, Yang and Parr [150], and E_C^{VWN} is the LDA correlation energy by Vosko, Wilk, and Nusair which are used as basis set in the computational aspect of the work [152]. The mixing parameters take the values a = 0.2, b = 0.72, c = 0.81[153]. All the DFT calculations that are performed in this work utilize

the B3LYP functional. Density functional theory is often the preferred electronic structure method to study moderate to large systems. This preference reflects the efficiency of DFT compared to correlated wave function theories such as coupled cluster theory, even though accuracy and, more importantly, predictability (i.e., systematic convergence to the right answer), are sacrificed [149, 153].

3.3 DFT Plane wave basis set approximation

Basis sets are set of (non-orthogonal) one-particle functions used to build molecular orbitals. [154]. In 1951 Roothaan [155] and Hall [156, 157], proposed the development of the orbitals as a linear combination of a known basis set. The molecular orbitals in a molecule are written as a linear combination of atomic orbitals (LCAO).

3.3.1 Linear combination of atomic orbitals method

The general equation for the expansion of a molecular orbital ψ is

$$\psi_i = \sum_{i=1}^{n} c_i \chi_i(r) \tag{46}$$

The χ_1, χ_2 ... is called the *basis set* and each function χ_1 is called a *basis function*. The c_i are the molecular orbital expansion coefficients which express the contribution of each atomic function to the given molecular orbital and are calculated variationally.

When including this development of the orbitals in the HF equations, a set of algebraic equations is obtained, which is known as Hartree-Fock-Roothaan-Hall equations. The equation can be solved using matrix techniques if the set in which the orbitals are expanded were a complete basis set. The expansion of the wavefunction as a linear combination of basis functions affects the accuracy of the Hartree-Fock-Roothaan-Hall equations. Since the basis set is not complete its choice is a source of error in the ab initio molecular calculations.

3.3.2 Grid based projector augmented wave method (GPAW)

The projected augmented-wave method was developed by Blochl [158]. The projected augmented approach is similar to the pseudo-potential approach. The spheres around the atoms are called augmentation spheres in PAW formalism. In PAW formalism, there is pseudo (PS) wave function $|\psi\rangle$ that is defined everywhere in space as:

$$|\psi\rangle = |\psi\rangle + \sum_a c_a(|\phi^a\rangle - |\check{\phi}^a\rangle) \qquad (47)$$

The real implementation of real space called GPAW was derived by Monrtesen *et al.* [159] GPAW is a DFT code wherein the wave functions and densities are stored in a real space grid. The memory requirement can be cut by the use of different grids.

3.3.3. Gaussian basis functions

Functions that resemble hydrogen atomic orbitals (AOs) are very suitable for expansion of Molecular Orbitals (MOs) because they have the correct shape near the nucleus and far from the nucleus. Gaussian functions are most preferable for quantum mechanical calculation because they are much easier to compute and allow for efficient computation of molecular integrals.

$$g_v r = e^{-\alpha_v r^2} = e^{-\alpha_v(x^2+y^2+z^2)} \qquad (48)$$

where α is the GTO exponent.

A single Gaussian function is called the primitive Gaussian type function (GTOs), there are spherical GTOs and cartesian GTOs. The spherical GTOs were proposed for the first time by Boys [160] and McWeeny [161]. These functions are defined by:

$$g_v r = Y_{l,m}(\theta, \phi) r^l e^{-\alpha_v(x^2+y^2+z^2)} \qquad (49)$$

With α being the GTO exponent, l and m are the azimuthal and magnetic quantum numbers respectively, where $m = -l \dots \dots l$. Cartesian GTOs are used in molecular calculations because the multicenter integrals are easily evaluated due to the Gaussian theorem that allows to express the product of two Gaussian functions centered in two different points of the space as another Gaussian function centered in a third point located on the line that joins the two initial points. These cartesian GTOs are defined by:

$$g_v r = x^k y^m z^n e^{-\alpha_v (x^2 + y^2 + z^2)}, \tag{50}$$

k, m and n are components of angular momentum quantum number l, where $l = k + m + n$.

Spherical and cartesian functions are the same for up to $l = 1$ (p functions) but differ slightly for $l = 2$ or higher. The main advantage of the GTO is the fact that their mathematical form is much more convenient for the calculation of integrals, above all the electron repulsion integrals. Because of their simplicity, the GTOs enable all the integrals required for a molecular calculation to be evaluated analytically, easily and efficiently [162] and they have therefore become the preferred basis functions for molecular calculations.

Fixed linear combinations of primitive Gaussian function are called Contracted Gaussians (CGs). CGs are expressed as:

$$G_\alpha(r) = \sum_{v=1}^{N_\alpha} c_v g_v(r) \tag{51}$$

These basis sets are approximate Slater-type orbitals (STOs) by "n" primitive Gaussians, the simplest kind of CGs are the STO-nG basis set. STO-nG basis sets are not satisfactory because they include only one CG per orbital, these basis sets can be improved by either including:

(i) More than one CG per atomic orbital, examples are: double zeta (DZ), Triple zeta (TZ) and quadruple zeta (QZ)

(ii) One CG per core atomic orbital and more than one for the valence atomic orbitals, examples are 3-21G, 4-31G, 6-31G and 6-311G.

3.4 The composition and size of the basis set

The composition and size of a basis set are more simply and clearly discussed in terms of atomic orbitals as their functions. To this purpose, the atomic orbitals can be classified as follows:

(i) core orbitals, i.e. the orbitals pertaining to shells that are completely occupied;

(ii) valence orbitals, i.e. the orbitals pertaining to the outer most, partially occupied shell;

(iii) virtual orbitals, i.e. the orbitals that are unoccupied in the ground state.

The basis sets differ in size according to the types of constituting orbitals. The most commonly utilised basis sets are described in the next subsections.

3.4.1. Minimal basis sets

The minimal basis set of a given molecule contains only the occupied orbitals of all the atoms constituting that molecule. Minimal basis sets that are widely used are those in which STOs are approximated by means of contracted GTO. These basis functions are denoted with acronyms informing about the number of GTO utilized in the expansion of a single orbital. In general, STO-nG is a minimal basis set in which each orbital is the linear combination of n Gaussian primitives. For example. STO-3G is a minimal basis set in which each orbital is a linear combination of three Gaussian primitives.

3.4.2. Split-valence basis sets

In these basis sets, the core orbitals and the valence orbitals are described differently. The functions describing the valence orbitals are doubled, or tripled, etc., while the functions describing the core orbitals are each represented by only one function. The resulting linear combination expressing the molecular orbital allows the atomic orbitals to adjust independently for a given molecular environment. Split valence basis sets are characterized by the number of functions assigned to valence orbitals and are termed accordingly: *double zeta* basis set, *triple zeta* basis set and so forth.

The general notation N-MPG [149] is used for *double zeta* basis sets, where N is the number of Gaussian functions used in the expansion of each core orbital (Equation 51) and the hyphen stands for the split of the description of orbitals. The numbers M and P are the numbers of Gaussian primitives utilized in the expression of the more contracted basis functions and the more diffuse one, respectively. For example, the split-valence basis set 3-21G is a basis set in which each core orbital is a linear combination of three primitive GTO, while, each valence orbital is represented by a more contracted function expanded as a linear combination of two primitive GTO and a more diffuse function represented by a single primitive GTO. In the split valence basis set 6-31G, there are six GTO for the core orbitals; the inner orbitals are represented by three GTO while the outer orbitals are represented by a single GTO.

3.4.3. Polarization basis sets

These basis sets contain also basis functions with higher angular momentum quantum number than that of any occupied orbital of the atomic ground state. The addition of these functions is done to account for the distortion of the charge distribution (*polarization*) of the atom due to the molecular context [163] and the added orbitals are called *polarization functions*. Adding or mixing a p-type orbital to an s-type orbital can distort the s-type orbital; similarly, adding or mixing a d-type orbital to a p-type orbital can distort the p-type orbital. In this way, orbitals are allowed to change shape depending on the molecular context.

Polarization functions are usually indicated by asterisks (∗) or by indicating the added functions explicitly in parentheses. Thus, one asterisk (e.g., 6-31G*) indicates that polarization functions are added for the heavier atoms but not for the hydrogen and helium atoms; two asterisks (e.g., 6-31G**) indicate that polarization functions are added also for hydrogen and helium atoms. Similarly, 6-31G(d) indicates that d-type polarization functions are added for the 2nd row atoms and 6-31G (d, p) indicates that d-type functions are added for the 2nd row atoms and p-type functions are added for the H (and He, if concerned) atoms. The addition of p-orbitals to hydrogen is particularly important in systems where hydrogen is a bridging atom, i.e., where hydrogen bonds are present [163].

3.4.4. Diffuse basis sets

Diffuse Gaussian functions have much smaller exponents than standard functions and therefore they decay slowly with the distance from the nucleus. The addition of these functions is important for species with significant electron density far away from the nuclear centres, to account for the outermost weakly bound electrons. Such species include anions and excited-state systems. Diffuse basis sets do well for calculation of electron affinities, proton affinities, inversion barriers and bond angles in anions. The addition of diffuse s- and p-type Gaussian functions to non-hydrogen atoms is denoted by a plus sign + before the G (e.g., 6-31+G); the addition of diffuse functions also for the hydrogen atoms (as well as for the heavier atoms) is denoted by ++ (e.g., 6-31++G). Diffuse functions on hydrogen atoms seldom make a significant difference in accuracy [149]

University of Venda

3.5. Pseudopotentials

The concept of a pseudopotential is related to replacing the effects of the core electrons with an effective potential. The pseudopotential generation procedure starts with the solution of the atomic problem using the Kohn-Sham (KS) approach [145]. Once the KS orbitals are obtained, an arbitrary distinction between valence and core states is made. The core states are assumed to change very little due to changes in the environment, so their effect is replaced by a model potential derived in the atomic configuration and it is assumed to be transferable. The valence states are seen to oscillate rapidly close to the core regions. With the introduction of the new potential, the valence states are made smoother.

For a Hamiltonian $\hat{H}$ with core states $\varphi\rangle$ and core eigenvalues $E_n\rangle$ and for a single valence state $\varphi\rangle$ the valence states can be replaced with $\phi\rangle$ and expand in terms of the core states as follows:

$$\varphi\rangle = \phi\rangle + \sum_n^{Core} a_n \vee \chi_n\rangle \tag{52}$$

For orthogonality of the valence states:

$$\langle X_n|\varphi\rangle = \langle \chi_n|\phi_n\rangle + \sum_n^{Core} a_n \langle X_n|X_n\rangle = 0 \tag{53}$$

In terms of the pseudopotential

$$\varphi\rangle = \phi\rangle - \sum_n \langle X_m \vee \phi \vee X_n\rangle \tag{54}$$

Applying the Hamiltonians:

$$\hat{H}\varphi\rangle + \sum_n^{Core}(E - E_n) \vee X_n\rangle\langle X_n \vee \phi\rangle = E\phi\rangle \sum_n \langle X_m \vee \phi \vee X_n\rangle \tag{55}$$

The pseudo wavefunction satisfies an effective equation with the same eigen energy of the real valence wave function. In the case of isolated atoms, the indices n correspond to the combined index *nlml* including the principal quantum number n, the angular momentum quantum number l and the magnetic quantum number *ml*.

$$\left(\hat{H} + V_{nl}\right)\phi\rangle = E\varphi\rangle \tag{56}$$

where V_{nl} is the extra potential and E is the repulsive potential.

3.5.1 Norm-conserving pseudopotentials

Electron-ionic core interactions are typically represented by a nonlocal Norm-conserving pseudopotential (NCPP): a soft potential for valence electrons only having pseudo-wavefunctions (see equation 57) containing no orthonormality wiggles [164].

In many systems, NCPP's allow accurate calculations with moderate-size plane-wave basis sets. From an all-electron self-consistent DFT calculation in an atom with a given reference configuration.

$$-\frac{\hbar^2}{2m}\frac{d^2\phi)_l(r)}{dr^2} + \left(\frac{\hbar^2}{2m}\frac{l(l+1)}{r^2} + V(r) - E_l\right)\phi_l(r) = 0 \tag{57}$$

To generate pseudopotential V_{nl} for valence state in such a way that ϕ_l and E_l obey the norm conserving conditions, the Kohn Sham equations is inverted as:

$$V_{nl,total}r = E_l - \left[\frac{l(l+1)}{2r^2} - \frac{\frac{d^2}{dr^2}\phi_{nl}^{ps}(r)}{\phi_{nl}^{ps}(r)}\right] \tag{58}$$

The potential $V_{nltotal}(\text{r})$ obtained by inversion of the Schrödinger equation is not only the ionic potential that is required but includes also contributions from the Hartree and exchange-correlation terms. Therefore subtract the contributions from the Hartree and exchange-correlation terms are subtracted as:

$$V_{nl}(r) = V_{l,total}(\text{r}) - V_{Hxc}^{PS}(\text{r}) \tag{59}$$

This operation is called unscreening.

3.5.1.1 Features of Norm-conserving pseudopotentials

Transferability: transferability can be estimated from atomic calculations on different configurations. In many cases simple unscreening produces an unacceptable loss of transferability. May require the nonlinear core correction

$$V_{nl}(r) = V_l(r) - V_{Hxc}^{PS}(\text{r}) + n^{ps}(r) \tag{60}$$

Softness: atoms with strongly oscillating pseudo-wave functions (first-row elements, elements with 3d and 4f valence electrons) will produce hard pseudopotentials requiring many plane waves in calculations. Larger core radius means better softness but worse transferability. This is a recipe to get optimal smoothness without compromising transferability [164].

3.5.2 Ultrasoft pseudopotentials

In 1990, Vanderbilt [165] proposed a new and radical method for generating pseudopotentials by relaxing the norm-conservation constraint. Pseudopotentials generated in this way due to their softness require a much smaller planewave cutoff and thus a much smaller number of planewaves. For this reason, they are usually called ultrasoft pseudopotentials. When the ultrasoft pseudopotential is integrated into the Kohn-Sham equations, the total energy in the presence of ultrasoft pseudopotentials is written as:

$$E_e = \sum_i \sum_i \langle \phi_i \vee - \frac{1}{2}\nabla^2 + V_{NL}\phi_i \rangle + \frac{1}{2}\int \int d\vec{r}d\vec{r}\frac{n(\vec{r})n\vec{r}'}{\vec{r}-\vec{r}'} + E_{XC}\lfloor n \rfloor + \int d\vec{r}V_{LOC}(\vec{r})n(\vec{r}) \tag{61}$$

where the Hartree, exchange-correlation, local and kinetic terms have the usual form. The nonlocal part of the pseudopotential instead is given in terms of a new set of projection operators as:

$$V_{NL} = D_{nm} \vee B_n^I \rangle \langle B_m^I \vee, \tag{62}$$

where the superscript I indicates that the projector is centred on atom I. The norm-conserving condition is relaxed by introducing a generalized orthonormality condition through the overlap matrix

$$\text{S}=\delta_{ij} = 1 + \sum_{nm,l} q_{nm} \vee B_n^I \rangle \langle B_m^I \vee, \tag{63}$$

University of Venda

where $q_{nm} = \int d\vec{r} Q_{nm}(\vec{r})$.

Because the norm-conserving condition is now relaxed, the electronic density needs to be augmented in order to preserve the correct number of electrons. The new density is then:

$$n(r) = \sum_i |\phi_i(r)|^2 + \sum_i \sum_{jk} \langle\phi_i|B_j\rangle Q_{ij}(r)\langle B_k|\psi_i\rangle \tag{64}$$

where Q_{ij} are the augmentation charges.

$$Q_{ij}(r) = \phi_i^*(r)\phi_j(r) - \tilde{\phi}_i^*(r)\tilde{\phi}_j^*(r) \tag{65}$$

$|B_i\rangle$ are projectors where $|B_i\rangle = \sum_j (\beta^{-1})ij \vee \chi_j\rangle$, $\beta_{ij} = \langle\phi_i|\chi_j\rangle$ and $|B_i\rangle$ satisfy $\langle\beta_i|\phi_j\rangle$
$|\phi_i\rangle$ are atomic states
$|\phi_l\rangle$ are pseudowaves such that $\phi_l(r) = \phi_l(r)$ for r>$r_{c,l}$
$|\chi_i\rangle$ are set of functions vanishing for r>$r_{c,l}$
$|\chi_i\rangle = (E_i\text{-T-}V_{loc})|\phi_i\rangle$

In practical ultrasoft pseudopotential, the Q_{jk} are pseudized. The matching radii r_c may be set to large values than norm-conserving pseudopotential without transferability. For a local pseudopotential $V_{loc}(r)$, $V_{loc}(r) = V(r)$ for r>r_l

$$D_{ij} = \beta_{ij} + E_j Q_{ij} , \tag{66}$$

where $Q_{ij} = \int_{r>r_{c,i}}^0 \left(\phi_i^*(r)\phi_j(r) - \tilde{\phi}_i^*(r)\tilde{\phi}_j^*(r)\right)dr$.

Unscreening D_{ij} and V_{loc}:

$$D_{ij}^0 = D_{ij} - \int Q_{jk}(r) V_{loc}(r)dr, \tag{67}$$

where $V_{loc}^{10n} = V_{loc}(r)\text{-}\int dr' \frac{n(r)'}{r-r'} - V_{xc}(r)$

The ultrasoft pseudopotential is finally given as:

$$V_{US} = V_{loc}^{10n} \sum_{ij} D_{ij}^0 |B_i\rangle. \tag{68}$$

The ultrasoft pseudopotential was adopted for this study because it is good for computational accuracy, saves lot of CPU on calculations and all electron potentials are possible.

3.6 Cutoff energy

Each of the Fourier basis functions $e^{iG.r}$ represents a plane-wave travelling in space, perpendicular to the vector G. There are an infinite number of allowed G, but the coefficients C_{Gk} become smaller and smaller as G^2 becomes larger and larger. A cut-off energy is defined in equation (69) and only includes plane waves with energies less than the cut-off.

$$E^{Cut} = \frac{\hbar^2}{2m} |G|^2. \tag{69}$$

The cut-off energy must always be high enough to give accurate results. This can be achieved by repeating the calculations with higher and higher cut-off energies until the properties have converged.

3.7 K-points sampling

Bloch's theorem eigenstates in a system under a periodic potential *U(r)* can be written as:

$$\psi_i(\vec{r}; \vec{k}) = e^{i\vec{k}.\vec{r}} U_i(\vec{r}.\vec{k}) \tag{70}$$

Operators such as the Hamiltonian are block-diagonal by *k*-point:

$$\begin{matrix} h_{ki} & 0 & 0 \\ 0 & h_{k2} & 0 \\ 0 & 0 & h_{k3} \end{matrix} \tag{71}$$

It is important to describe waves and correlation lengths longer than unit cell in solids (especially conductors / semiconductors), when only the Γ point is sampled (*k* = 0).

Ⓒ **University of Venda**

$$\psi_k(r) = e^{i(k.r)} U_k(r) \tag{72}$$

where $U_k(\text{r+L}) = U_k(r)$ and $e^{i(k.r)}$ are arbitrary phase factor

$$\psi_k(r + L) = e^{ik(r+L)} U_k(r + L) \tag{73}$$

$$e^{ik.L} \psi_k(\text{r}) \tag{74}$$

In principle, we need to integrate over all possible k when constructing the density. Fortunately, the wave functions changes slowly ask is varied, such that the integral is approximated with a summation.

$$\text{P(r)} = \int |\psi_k(r)|^2 d^3 k \tag{75}$$

$$\text{P(r)} \quad \sum_k |\psi_k(r)|^2. \tag{76}$$

To get accurate results, enough k-points must be used.

3.8 Finding the ground state

Planewave basis is used to express the wave functions when finding the ground state in calculations, and these are sampled at a discrete number of k-points. The ground state is found by iteratively improving an initial guess until the change in energy differences is small to make sure the structure converges as shown in Figure 21.

The concept of a pseudopotentials is related to replacing the effects of the core electrons with an effective potential, the use of pseudopotentials reduces the number of states needed from Schrödinger equation.

$$\psi_{m,k}(r) = \sum_k C_{Gmk} e^{-i(G+K)r} . \tag{77}$$

The Hamiltonian $\hat{H}_k[P]\psi_{m,k} = E_{m,k}\psi_{m,k}$ must be solved to get the lowest energy states for each k, but the Hamiltonian depends on the electron density p(r), which depends on the wave functions as:

$$\text{p(r)} = \sum_{m=1}^{N_e} \sum_{k=1}^{N_k} |\psi_{m,k}(r)|^2. \tag{78}$$
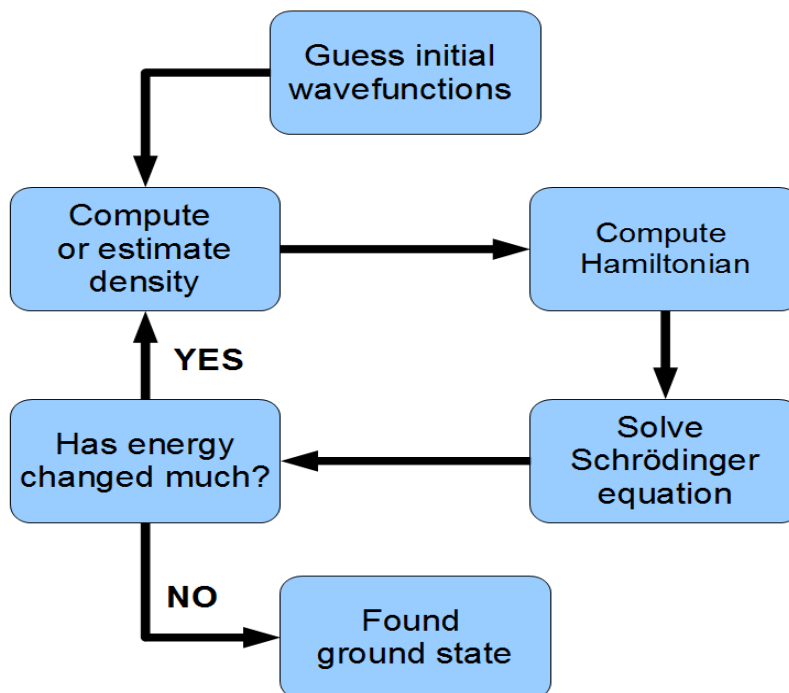
Figure 21: Algorithm for finding the ground state

In order to test for the acceptable energy change, an energy convergence tolerance is set accordingly. The smaller this tolerance, the closer it is to get to the ground state. The forces can also be computed, and a convergence tolerance can be set on the forces as well as the energies. For many spectral properties, the force is an accurate measure of how far the calculation is from the true ground state. There are two different methods used in finding the ground state, that is;

(i)   Density Mixing (DM)

The advantages of the density mixing methods is that it estimates density, it is fast and the energy converges quickly. However, the disadvantage of DM method is that the forces converge slowly, and it can be unstable.

(ii)   Ensemble Density Functional Theory (EDFT)

Similarly to DM, The advantage of the ensemble density functional theory method is that it computes density, it is stable and the energy and forces converge quickly although it can be sometimes slow.

The EDFT method is adopted in this study because the energy and forces converge quickly and are stable.

70

University of Venda

3.9 SOFTWARE

3.9.1 Gaussian Quantum Chemical Package

Gaussian quantum chemical package is an electronic structure package capable of predicting many properties of atoms, molecules and reactive systems. Properties of systems are studied/predicted utilizing ab initio, density functional theory, semi-empirical, molecular mechanics, and hybrid methods [78]. Gaussian is an electronic structure-based program used by chemists, chemical engineers, biochemists, physicists and other scientists worldwide. Starting from the fundamental laws of quantum mechanics, Gaussian package can model reactions of very large systems, carry out geometrical optimizations, study excited states in the gas phase and in solution, predict the energies, molecular structures, vibrational frequencies and molecular properties of molecules and reactions in a wide variety of chemical environments. With Gaussian package, larger systems and more complex problems can be solved. Gaussian models can be applied to both stable species and compounds which are difficult or impossible to observe experimentally (e.g., short-lived intermediates and transition structures). Gaussian offers new features and performance enhancements which will enable users to model molecular systems of large/increasing size, with more accuracy, and/or under a broader range of real world conditions. In this work Gaussian package was used to build the ruthenium and the organic dye molecules used for this study. The geometrical optimization of the dye molecules, TD-DFT simulation of their absorption spectra, HOMO-LUMO energy levels, HOMO-LUMO energy gap and the isodensity surfaces of the key molecular orbitals were computed using Gaussian 03 quantum chemical package.

3.9.2 CASTEP

CASTEP is a commercial software package which uses density functional theory with a plane wave basis set to calculate the electronic properties of crystalline solids, surfaces, molecules, liquids and amorphous materials from first principles [166]. The abbreviation stands for Cambridge Serial Total Energy Package. CASTEP permits geometry optimization and finite temperature molecular dynamics with implicit symmetry and geometry constraints, as well as calculation of a wide variety of derived properties of the electronic configuration. Using density functional theory, it can simulate a wide range of properties of materials proprieties including energetics, structure at the atomic level, vibrational properties, electronic response properties etc. It has a wide range of spectroscopic features that link directly to experiment, such as infra-red and Raman spectroscopies, NMR, and core level spectra. In this study CASTEP was used

for first principle calculations based on density functional theory with GGA combined with the PBE functional/approximation for geometrical optimization and investigation of the convergence parameters (cutoff energy and k-points) of TiO_2 brookite bulk structure, the brookite $(TiO_2)_n$ with n =5, 8, 68 cluster was modelled from the optimized bulk structure.

3.9.3 Gaussum Software

Gaussum software is an application that helps to analyse, extract and monitor the progress of SCF cycles, geometrical optimizations, plot density of state spectrum, crystal overlap population spectrum, UV-Vis spectrum, molecular orbital and molecular orbital contributions, circular spectrum, IR and Raman spectra [167]. It is especially designed for parsing output files of ADF, GAMESS, GAMESS UK, Gaussian, Jaguar and PC GAMESS calculations to extract and display useful data. Files are imported into the working environment using built in browse button, OUT, LOG and ADFOUT file format and can also handle compressed log files such as ZIP, GZ and BZ2. In this work, Gaussum software was used in this study to compute the total density of states plot of $(TiO_2)_5$ from the LOG output file.

3.9.4 Avogadro software

Avogadro software is an advanced molecule editor and visualizer designed for cross-platform use in computational chemistry, molecular modelling, bioinformatics, materials science, and related areas. It offers flexible high quality rendering and a powerful plugin architecture [168]. In this study, Avogadro software was used to import and visualize the dye molecules and the $(TiO_2)_n$, brookite cluster with n=5, 8 and 68 for computational analysis.

3.10 COMPUTATIONAL PROCEDURES

The Gaussian03 program chemical package [78] within the frame work of the Gauss View 4.1 software of Gaussian Inc. was used for first principle calculation based on density functional theory to study the electronic structures and UV-Vis simulated spectra of the dye molecules and dye complex adsorbed on the TiO_2 brookite systems. The dye molecules that were studied in the thesis are the ruthenium N3 complex, polyene diphenyl-based dye and the croconate dye.

3.10.1. Building of dye molecules

The dye model structures were built using the Gauss View molecular builder interface within the Gaussian package [78]. The ruthenium N3 dye molecule was built as illustrated in Figure

22. Firstly, a ruthenium metal was selected from the periodic table within the Gaussian window and was placed in the built window. This was followed by the attachment of the two bipyridine moiety, the carboxylic moiety and the two thiocyanate ligands. The structures were cleaned for reorientation of the atoms in their lattice positions. Same procedure was followed for the dye molecules that were investigated in this study, the detailed description of building the dye was presented in section 1.10 of Chapter 1. The structural properties of the modelled dye molecules' such as the number of atoms, empirical formula of the dye were obtained from the Gauss view and compared with the theoretically reported values to validate the accuracy of the built dye model structures.
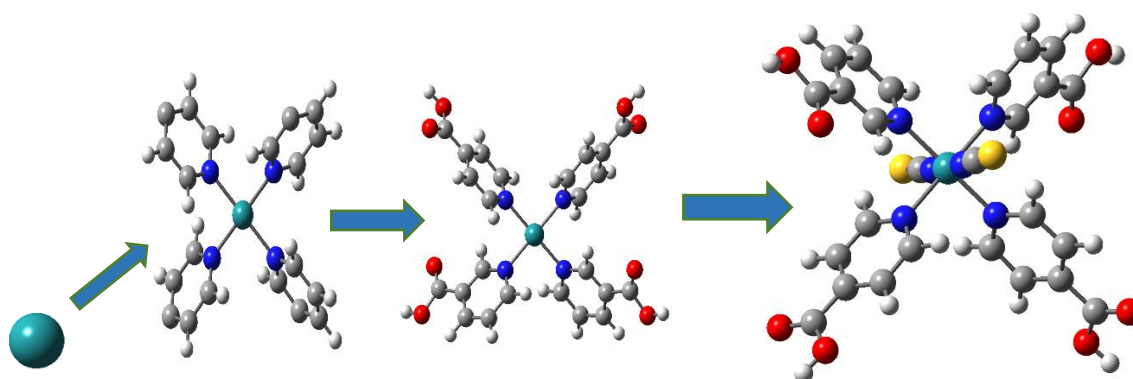
Figure 22: Detailed description for building of ruthenium N3 complex (Ru metal→Ru+bipyridine→Ru+bipyridine+carboxylate→Ru+bipyridine+carboxylate+ thiocyanate)

3.10.2. Structural optimization

Structure optimization of the ground state geometries of the dye molecules in vacuum was performed by DFT using the hybrid B3LYP (equation 45) exchange correlation functional and Pople's slit valence basis set with polarization and diffuse functions 6-311 + G*(d, p) basis set for metal free organic dye while LANL2DZ basis set was used for the metal based complexes to account for the formation charge of the metal based complexes. The optimized structure of the ruthenium metal is illustrated in Figure 23. The minimum geometry of the dye structures obtained was used for further studies. The optimization energy, maximum internal forces and stress acting on the atoms of the molecules were computed from the geometrical optimization calculations.
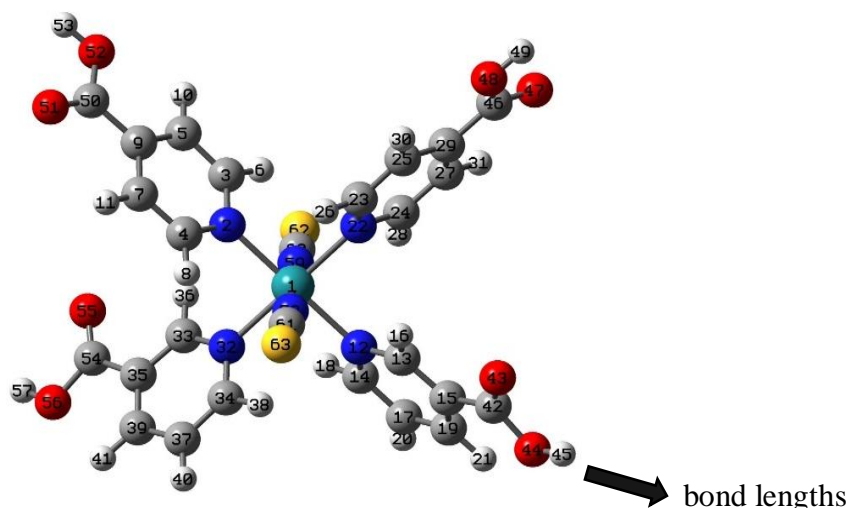
Figure 23: Optimized structure of ruthenium N3 complex

3.10.3. Computing the absorption spectrum of the dye structures

The UV-Vis simulated absorption spectrum of the dye molecules was calculated by TD-DFT in gas phase. The Pople's slit valence basis set with polarization and diffuse functions 6-311 + G*(d, p) was used for metal free organic dye while LANL2DZ basis set, the same functionals and basis set was used for the ruthenium N3 complex. 30-100 singlet to singlet electronic transitions for the excitations depending on the size of the dye molecules [125]. The UV-Vis simulated absorption spectra for ruthenium N3 complex is illustrated in Figure 24.

The UV-Vis spectra, maximum excitation wavelength, excitation energies, oscillator strength and light harvesting efficiency (LHE) of the dye were computed from the calculations. Their matching with the solar spectrum will also be discussed later and are related by the relation:

$$LHE = 1 - 10^{-f}. \tag{79}$$

where f is the absorption also called the oscillator strength of the dye associated with the maximum absorption of the dye [59, 79, 95].
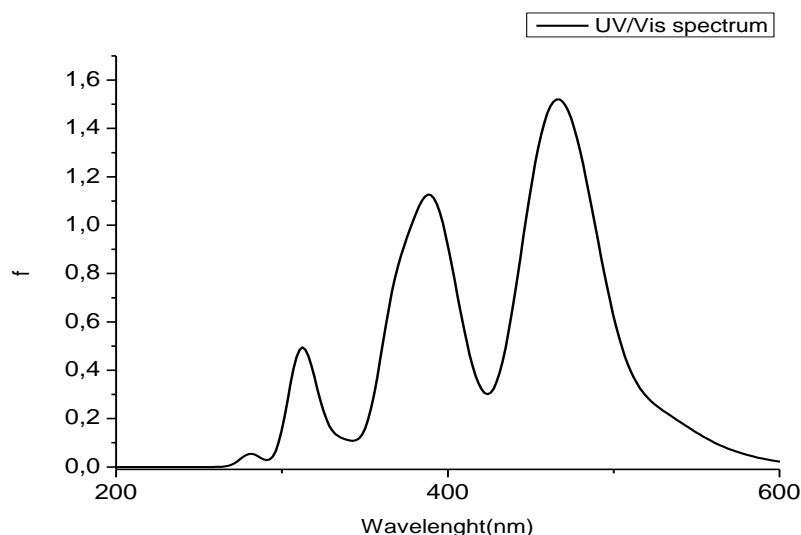
Figure 24: The UV-Vis simulated absorption spectra for the ruthenium N3 complex

3.10.4. Determination of electron transfer properties of the dye complex

To investigate the charge injection possibility unto the semiconductor, the HOMO-LUMO energy gap of the dye molecules was computed. The HOMO-LUMO isodensity surfaces of the dye molecules were computed as illustrated in Figure 25. The electron density of molecular orbitals, DFT calculation of the energy levels alignment of the dye excited state and the conduction band edge of the semiconductor were investigated using TD-DFT (B3LYP/LANL2-DZVP). Electron injection into the conduction band of TiO_2 is energetically favourable with increased energy separation of LUMO and the bottom of the TiO_2 conduction band. Furthermore, for the HOMO level to effectively accept the donated electrons from the redox mediator, the energy difference between the HOMO and redox chemical potential must be more positive [59, 125].
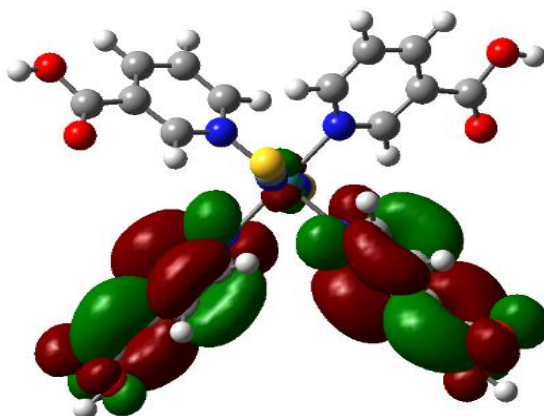
Figure 25: Isodensity surfaces of ruthenium N3 dye molecule.

75

3.11. Structural optimization of TiO₂ brookite crystal

The Cambridge Serial Total Energy (CASTEP) program package [166] within the frame work of the Materials Studio software of BIOVIA [77] was used for first principle calculations based on density functional theory with GGA-PBE functional/approximation for geometrical optimization and investigation of the convergence parameters (cutoff energy and k-points) of TiO_2 brookite structures. Structural optimization was performed to obtain the ground state properties of the brookite nanocluster. The EDFT and Ultrasoft pseudopotential were used throughout the DFT calculations. Shown in Figure 26 is the bulk TiO_2 brookite structure used for this study.
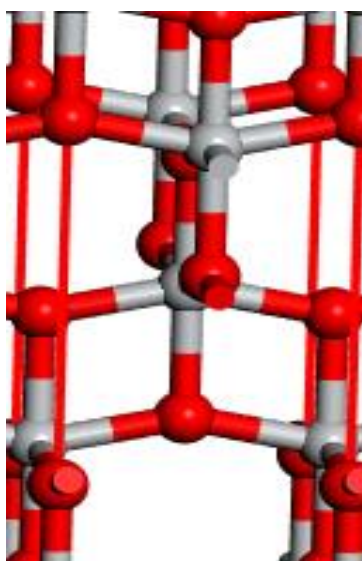
Figure 26: Bulk TiO_2 brookite structure.

3.11.1. Determination of convergence parameter (cutoff energy and K- points) for the bulk structure of TiO₂ Brookite

Several values of plane wave basis set cut-off energy were selected for geometrical optimizations to investigate the convergence of bulk TiO_2 structure. The cut off energies were plotted against the total energy to obtain the convergence energy of the bulk structure and dye molecules. The k-point will be set to Monkhorst Pack grid [169]. The grid parameters were varied to obtain close spacing of the bond length followed by geometrical optimization. Then the number of iterations obtained for the grid parameters was plotted against the energy values obtained from the optimization to determine the k-points at which the system converges.

3.11.2. Cleaving of TiO₂ brookite nanocluster

The ground state bulk structure obtained through geometrical optimization was optimized with the convergence parameters to obtain the minimum structure. The minimum structure was then imported into a new 3D atomic window. Then TiO₂ brookite cluster was cleaved from the optimized ground state bulk structure using a Build module of Materials Studio. The TiO₂ brookite nanocluster was built using a simple box shape with dimension 5 Å in x, y, z directions with stoichiometry $(TiO_2)_n$ where n = 5 for Ti atoms and n = 10 for O_2 atoms as shown in Figure 27. The brookite nanocluster was imported to Gauss view within the framework of Gaussian 03 quantum chemical package software. The imported structure of the TiO₂ brookite nanocluster was cleaned in the Gaussview interface of Gaussian 03 for reorientation of the atoms. The electronic properties, density of states and optical properties were calculated for the brookite TiO₂ nanoclusters.
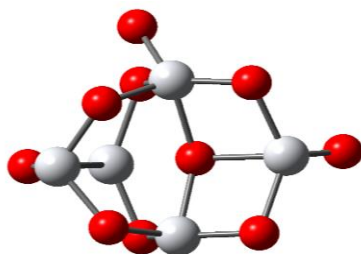
Figure 27: Brookite $(TiO_2)_5$ cluster

3.12 Adsorption of dye molecules on TiO₂ complex

The dye molecules were absorbed unto the TiO₂ cluster via the carboxylic group. The bidentate bridging (BB) adsorption mode in which each of the oxygen of the carboxylic moiety binds to a four-fold coordinate titanium atom was used because it was previously reported to be more energetically favorable, the picture of ruthenium N3 complex adsorbed on $(TiO_2)_5$ brookite cluster is depicted in Figure 28 [59, 125].
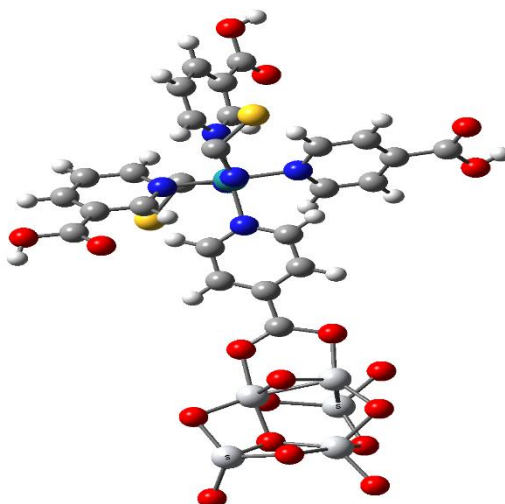
Figure 28: Ruthenium N3 complex adsorbed on (TiO$_2$)$_5$ brookite cluster

3.12.1 The excitation spectra (UV/VIS)

The absorption spectra of the semiconductor/dye complex excited states were calculated using TD-DFT simulation of the UV-Vis spectra of the TiO$_2$/dye complex via TD-DFT B3LYP calculations of 30-100 singlet to singlet transitions.

3.13. Calculation of properties

3.13.1 Adsorption energy of the dye molecules @ TiO2 brookite semiconductor

The dye molecules were adsorbed on the brookite nanocluster structure by bidentate bridging mode because it is energetically favourable [59, 125, 129, 130]. The formation/adsorption energies of the dye/TiO$_2$ complex were calculated using equation 80 below:

$$E_{ads} = E_{slab + molecule} - (E_{slab} + E_{molecule}), \tag{80}$$

where E_{slab} is the energy of the slab surface complex (surfaces in the slab), $E_{molecule}$ is the energy of the adsorbate, and $E_{slab + molecule}$ is the total energy of the slab with the molecule placed in the centre of the vacuum gap, where the interaction with the surface is very small. This approach allows an effective cancellation of errors from the two terms in the right-hand side of equation (80) and cancels out the small contributions from lateral interactions between the molecule. A positive value of $E_{ads} > 0$ indicates stable adsorption [53, 125].

3.13.2 Free energy of electron injection (ΔG^{inject})

Calculation of (ΔG^{inject}) is crucial for investigation of electron injection efficiency into the semiconductor and is given by equation 81:

$$(\Delta G^{inject}) = Eox^{dye*} - E_{CB}, \tag{81}$$

where Eox^{dye*} is the oxidation potential energy of the excited state of the dye, E_{cB} is the reduction potential energy of TiO$_2$ conduction band. The more positive is (ΔG^{inject}), the higher the electron injection efficiency (ϕ_{inject}) because (ΔG^{inject}) is proportional to (ϕ_{inject}) [95].

$$Eox^{dye*=Eox^{dye}-\Delta E}, \tag{82}$$

Eox^{dye} is the ground state oxidation potential (negative E$_{HOMO}$) [54, 59, 127] and ΔE is the lowest absorption energy associated with maximum wavelength [54, 59, 95].

3.13.3. Convolution of density of states and projected density of states spectrum

The density of states (DOS) was simulated using the keywords "pop=full" and the output log file obtained from the simulation imported Gausssum software to view the spectrum for the total density of states (TDOS) for the occupied and the unoccupied orbitals. The total density of states spectrum for (TiO$_2$)$_5$ brookite cluster was convoluted using full weight at half maximum value of 0.3 and energy scale of -20 eV to 20 eV as shown in Figure 29.
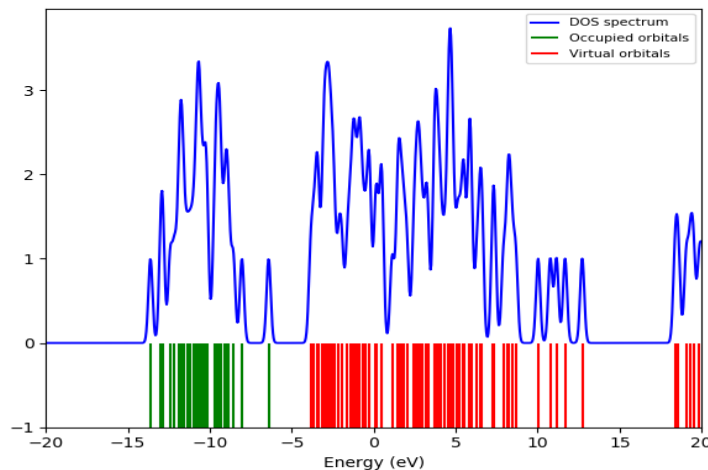
Figure 29: Total density of states spectrum for (TiO$_2$)$_5$ brookite cluster.

CHAPTER FOUR

4.0 RESULTS AND DISCUSSIONS
4.1 Studies of ruthenium II and organic dye molecules

In this chapter, employed first principles density functional theory (DFT) and time-dependent DFT (TD-DFT) were employed to study the molecular structures, geometrical optimization parameters, UV/VIS, light harvesting efficiencies, HOMO, LUMO, HOMO-LUMO energy gap and isodensity surfaces of ruthenium N3 complex owing to its excellent performance for application in DSSCs. Also, using the same methods, some promising metal free organic dye which are polyene diphenyl-aniline dye and the croconate dye are investigated.

4.2 Ruthenium (N3) Complex
4.2.1 Introduction

The so-called N3 dye developed by Grätzel and co-workers [83] is one of the most successful, widely investigated and applied dye in DSSCs. Some of the salient features of the ruthenium N3 complex are good chemical strength under illumination, proficient metal-to-ligand charge transfer (MLCT), long life-time excited state and suitable energy levels for electron injection with the use of TiO_2 nanostructures as photoanode. The acidic ligands (carboxylic) in the dye are attracted to the surface OH of TiO_2 semiconductor [53]. Efficiencies of 12.3% have been achieved with the use of ruthenium dye as TiO_2 semiconductors sensitizer. The ruthenium N3 has been reported as one of the most efficient sensitizer for DSSCs [56-59].

4.2.2. Computational Procedures

Gaussian 03 quantum chemical package [78] software was used to carry out first principle calculations based on density functional theory. The structure of ruthenium N3 complex was built as discussed in section 1.10 as shown in Figure 10 using the Gaussview molecular builder interface within the Gaussian package. The structure was cleaned for reorientation of the atoms in their lattice positions. Geometrical optimization of the ruthenium N3 structure was performed to obtain the ground state geometries of the dye molecule in vacuum. The geometrical optimization of the ruthenium N3 was performed using DFT with hybrid B3LYP exchange correlation functional [150, 151] and LanL2DZ basis set to account for the charge formation of the ruthenium N3 complex. The minimum geometry of the dye structure was obtained and further used for subsequent calculations.

The UV-Vis simulated absorption spectrum of the ruthenium dye molecule was calculated using TD-DFT in vacuum. The LanL2DZ basis set was used to compute the optical excitation spectrum while considering 80 singlets to singlet electronic transitions for the excitation. The UV-Vis spectra, maximum excitation wavelength, excitation energies, oscillator strength and light harvesting efficiency of the dye were computed from the calculation. Their matching with the solar spectrum was discussed.

The light harvesting efficiency at λ_{max} was computed for the ruthenium N3 complex using Equation 79. The HOMO, LUMO, HOMO-LUMO energy gap and isodensity surfaces of the molecular orbital involved in excitation of the ruthenium N3 complex were computed from the FCHK file obtained from the simulations and will be discussed in detail.

4.2.3 Structural properties of ruthenium N3 complex

Structural optimization of the ground state geometries of the dye molecules in vacuum were performed by DFT using the hybrid B3LYP exchange correlation functional and LanL2DZ basis set to account for the charge formation on the ruthenium metal. The optimized structure is presented in Figure 30. The dipole moments obtained after optimization was 2.863 Debye. The geometrical optimizations converged when the internal forces acting on all the atoms were less than 4.9 x 10^{-5} eV and a threshold value of 4.5×10^{-4} eV/A. The optimized structure of ruthenium complex in Figure 30 shows that ruthenium metal is octahedrally coordinated to six nitrogen atoms provided by the two thiocyanate ligands and the four carboxylic acids of the two bipyridyl ligands. Selected bond lengths (Å) and bond angles (degrees) of the ruthenium N3 after optimization are presented in Table 4. The angle between the ruthenium metal and the nitrogen atom of the thiocyanate ligands is <NRuN =180º while the angle between the ruthenium metal and the nitrogen atom of the carboxylic acid is <NRuN= 90º.

Table 4: Selected bond lengths (Å) and bond angles (º) for ruthenium N3 complex

Bond Length (Å)		Bond Angles (°)	
Ru-N2	2.096	N2-Ru-N12	89.800
Ru-N12	2.109	N2-Ru-N12	89.800
Ru-N22	2.096	N32-Ru-N59	89.800
Ru-N32	2.109	N12-Ru-N59	89.210
Ru-N58	2.065	N32-Ru-N12	90.300
Ru-N59	2.065	N58-Ru-12	89.800
		N22-Ru-N59	90.560
		N58-Ru-N59	178.600
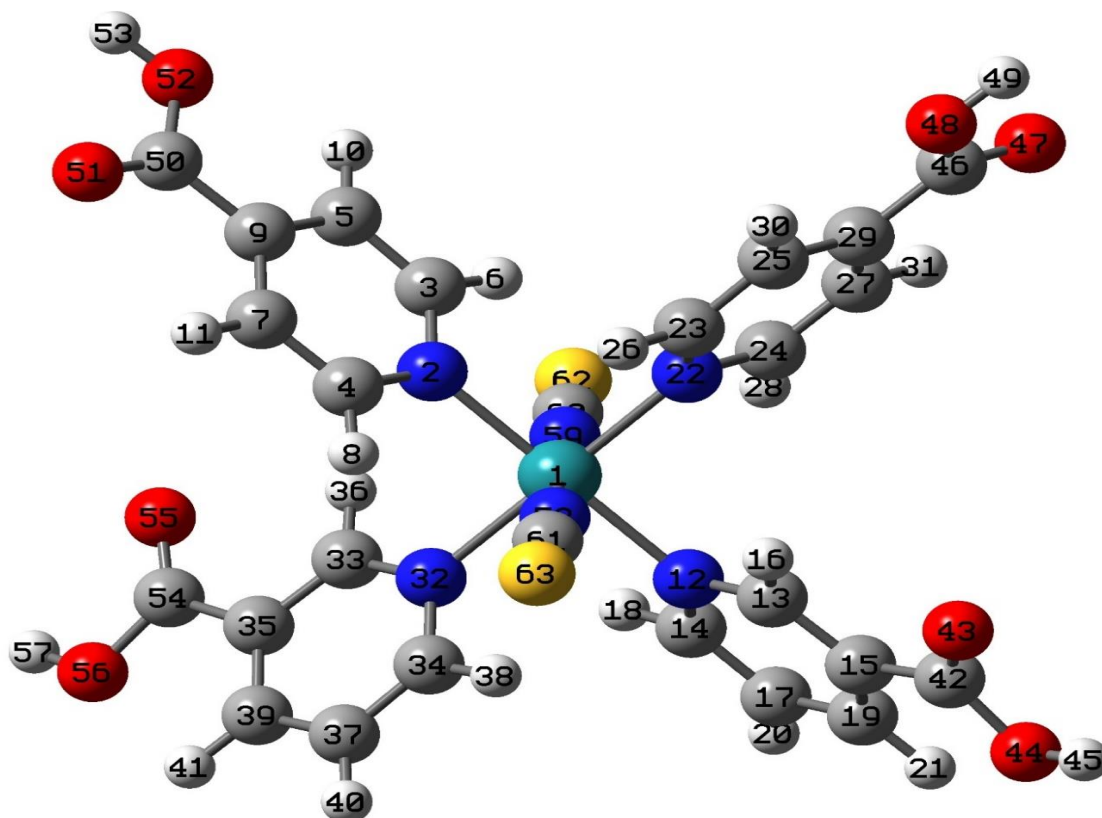
Figure 30: Optimized structure of ruthenium N3 complex [cis-di (thiocyanate) bis(2,2-bipyridine-4,4-dicarboxylate) ruthenium]]) Ru(dcbpy)(NCS)2 (Colour- Olive green represents ruthenium atoms, blue represents nitrogen atoms, yellow represents sulphur atoms, grey represents carbon atoms and red represents oxygen atoms).

4.2.4. UV/VIS absorption spectrum of ruthenium N3 complex

An efficient photosensitizer must have good excited state properties and intense absorption in the visible and near infra-red region of the solar spectrum. To understand the excited state properties and the absorption spectra of the ruthenium N3 complex, TD-DFT calculations in gas phase were performed using B3LYP and LanL2DZ functional. The 80 singlets to singlet transitions were considered in order to account for the whole spectrum.

The absorption spectrum of ruthenium N3 sensitizer in gas phase is presented in Figure 31. The ruthenium sensitizer shows a good absorption in the UV and visible region of the solar spectrum with intense absorption around 311 nm, 388 nm and 480nm. However, the peak/λ_{max}

is more notable at 480 nm. The simulated absorption peak of the ruthenium N3 sensitizer is in close agreement with experimental and theoretical reported literature values [95, 170]. Hence B3LYP/LANZ2DZ level of theory is suggested to be appropriate for simulation of absorption spectra of ruthenium N3 complex dye molecule.
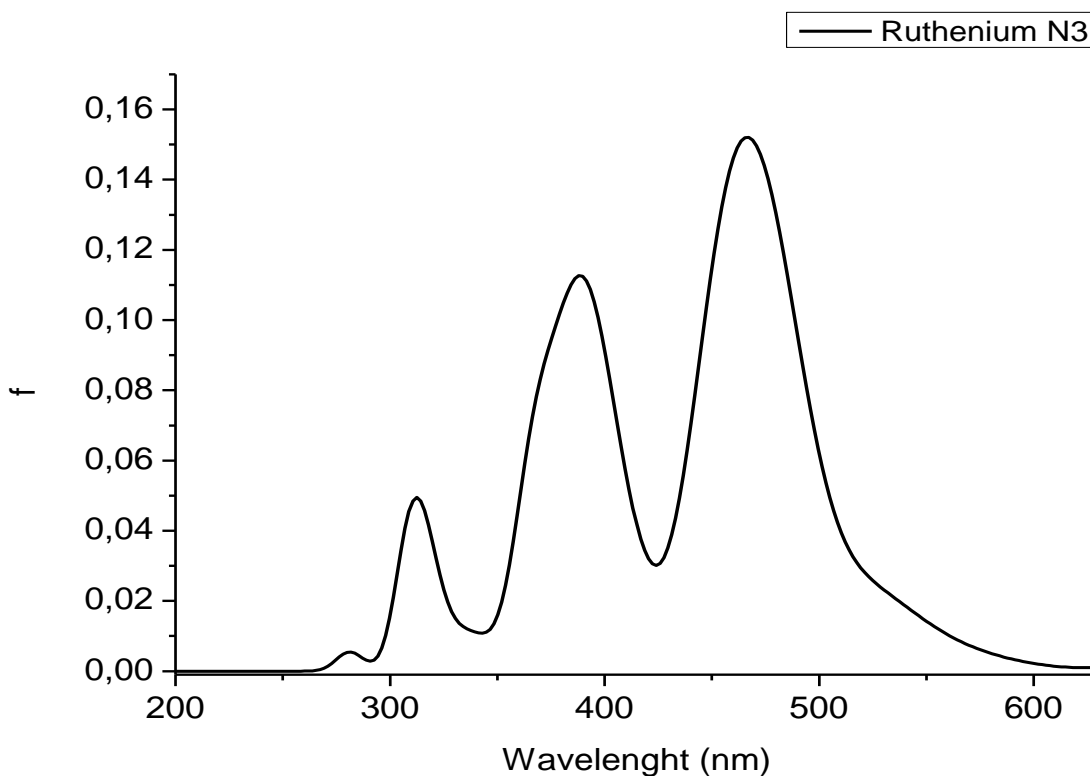
Figure 31: Simulated absorption spectra of ruthenium N3 complex

4.2.5. Light harvesting efficiency of ruthenium N3 complex

High LHE designates a good photocatalytic/light harvesting property. The light harvesting efficiencies of the dye molecules were calculated theoretically using Equation (79). The highest oscillator strength of the ruthenium N3 complex is 0.15, yielding a corresponding calculated light harvesting efficiency value of 0.292, as shown in Table 5. The ruthenium complex has an average LHE value of 0.23.

Table 5: Computed light harvesting efficiencies of ruthenium N3 complex at λ_{max}

Wavelength (nm)	Absorption	LHE	LHE (%)
312	0.050	0.108	10
388	0.110	0.224	22
467	0.150	0.292	29

4.2.6 Electronic properties of ruthenium N3 complex

The simulated HOMO, LUMO, HOMO-LUMO energy gaps of the ruthenium N3 complex are presented in Table 6. The HOMO of N3 lies at -5.03 eV while the LUMO lies at -3.01 eV, therefore the HOMO-LUMO energy gap is 2.02 eV compared to other findings whereby -5.67 eV, -3.63 eV, 1.96 for the HOMO, LUMO and HOMO-LUMO energy gap respectively were obtained using the same level of theory. The experimentally reported values for the HOMO, LUMO and HOMO-LUMO energy gap of the ruthenium N3 complex are -5.36 eV, -3.47 eV and 1.89. Our results compare favourably well with the simulated and experimental result [95, 170].

Table 6: HOMO, LUMO, HOMO-LUMO energy gap of the ruthenium N3 complex

Dye (N3)	HOMO (eV)	LUMO (eV)	H-L gap (eV)
Experimental work [170]	-5.360	-3.470	1.890
Simulated [95]	-5.670	-3.630	1.960
This work	-5.030	-3.010	2.020

The isodensity surfaces of HOMO and LUMO of ruthenium N3 complex are presented in Figure 32. The HOMO of the ruthenium N3 sensitizer is localized on the centre of the thiocyanate ligands while the LUMO is delocalized over the two dcbpy 4, 4_-dicarboxy-2, 2_-bipyridine ligands. The different position/localization of the HOMO- LUMO indicates good

electron injection properties of the ruthenium N3 complex. Our findings on the ruthenium N3 complex generally corroborated with findings from other authors reported in literature [95, 170].
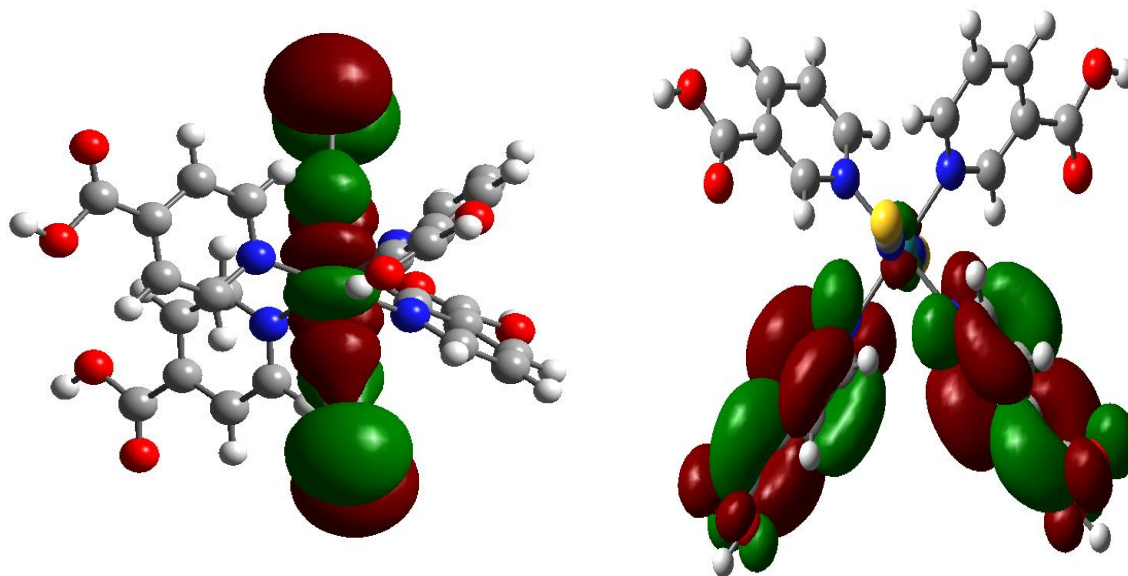
 (a) Ruthenium N3 HOMO   (b) Ruthenium N3 LUMO

Figure 32: Isodensity surfaces of ruthenium N3 complex (a) highest occupied molecular orbital and (b) lowest unoccupied molecular orbital

4.3 Metal free organic sensitizers

The ruthenium (II) polypyridyl complexes (N3) have demonstrated good chemical stability and excellent performance as sensitizer for DSSCs. Conversion efficiencies of more than 12 % have been achieved with the use of ruthenium N3 as dye sensitizer for TiO_2 semiconductor in DSSCs architecture [47, 53, 80, 90, 125]. However, ruthenium dye are relatively scarce and expensive, while their toxicity has raised environmental concern, thus limiting their application as a sensitizers for DSSCs [49]. Consequently, organic dye have now attracted a lot of attention as alternative sensitizers for DSSCs applications [48]. The advantages of the organic dye include higher extinction coefficient, low cost, good environmental compatibility and electrochemical properties [82, 93, 105]. The organic dye with basic configuration donor-π-acceptor are relatively cheap, easy to synthesize and possess chemical structures that can easily be altered to optimize photocatalytic properties of the semiconductor [56].

Several organic dye such as coumarins [125], indolines [96], porphyrins, perylenes, cyanines, mecrocyannines, quinolones, croconate [79, 80], phenothiazine [59], triphenylamine [97] and polyene-diphenylaniline [63, 64] have been reported as sensitizers for DSSCs. These metal-free organic dye have high molar absorption coefficients, various structures, low costs and relatively simple synthesis procedures. Efficiency of about 5- 9 % has been achieved with organic sensitizers [93, 97, 125, 171]. On the other hand, DSSCs based on natural sensitizers have efficiency of about 3.04 % [172]. Organic sensitizers steered up lots of interest from research community owing to their better efficiencies than the natural sensitizers.

4.4 Polyenediphenyl-aniline dye

4.4.1 Introduction

In this section, we employed density functional theory to study the geometrical, electronic and optical properties of D5, D7, D9 and D11 to gain more insight into the spectral characteristics that influence their light harvesting properties and a key factor to achieving higher incident photon to power conversion efficiency [125, 133]. Time-dependent density functional theory (TD-DFT) was employed to compute the ground state, excited state, absorption spectra and light harvesting efficiency of the series polyenediphenyl-aniline dye.

The polyenediphenyl-aniline dye shown in Figures 13-16 belong to the group of organic sensitizers which have demonstrated promising performance as DSSCs sensitizers. They have a short synthesis route and are readily adsorbed on TiO_2 under a variety of dye-bath conditions. The overall solar-to-energy conversion efficiency of the polyenediphenyl-aniline was reported to be over 5% in the preliminary tests. Boschloo and co-workers successfully synthesized polyene-diphenylaniline (D5) dye and compared the results with the performance of the standard N719 when tested on DSSCs [41]. The D5 outperformed the standard ruthenium N719 for sensitization of mesoporous TiO_2 with iodide/triiodide electrolyte and amorphous hole conductor (spiro-OMeTAD) (D5) when absorbed on TiO_2. A series of polyene based organic dye coded (D5, D7, D9, D11) was later reported by Kuang and co-workers. These dye demonstrated excellent stability under standard 1.5 air mass (AM) illumination while used with ionic liquid electrolyte with power conversion efficiency of 6.5 %.

4.4.2 Computational Procedures

In this study, the structures of four dye molecules were built using Gaussview molecular builder interface. All DFT/TD-DFT calculations were executed by Gaussian 03 quantum chemical package [78]. The structural optimization of the ground state of the polyenediphenyl-aniline dye in gas phase was performed using the hybrid density functional B3LYP and 6-31G* basis sets [149, 150]. The same basis sets were used to simulate the UV-Vis spectra of the dye in gas phase. About 70-100 singlet-singlet transitions were considered in order to account for the excitation energy in the whole of the absorption spectrum.

4.4.3 Structural Properties

Four organic dye were considered in this study and are listed below:

1. (D5): 3-(5-(4-(diphenylamine) styrl) thiophen-2-yl)-2-cyanoacrylic acid
2. (D7): 3-(5-bis(4-(diphenylamino) styrl)thiophen-2-yl)-2-cyanoacrylic acid
3. (D9): 5-(4-(bis(4-methoxyphenylamino) styrl) thiophen-2-yl)-2-cyanoacrylic acid
4. (D11): 3-(5-bis (4, 4'-dimethoxyphenylamino) styrl) thiophen-2-yl)-2-cyanoacrylic acid.

The structures of the four dye listed above were built in Gauss View as reported by Kuang and co-workers [82]. The optimized structures of D5, D7, D9 and D11 are shown in Figures 33, 34, 35 and 36 respectively. In these structures, the diphenylaniline was the donor unit, polyene and thiophene were the π-conjugation to link or bridge the donor acceptor moiety while -COOH and -CN were the acceptor and anchor units respectively. The donor unit for D7 and D11 was extended by the addition of diphenylaniline. The diphenylaniline of D9 and D11 were then modified by the addition of methoxy group as shown in Figures 35 and 36.
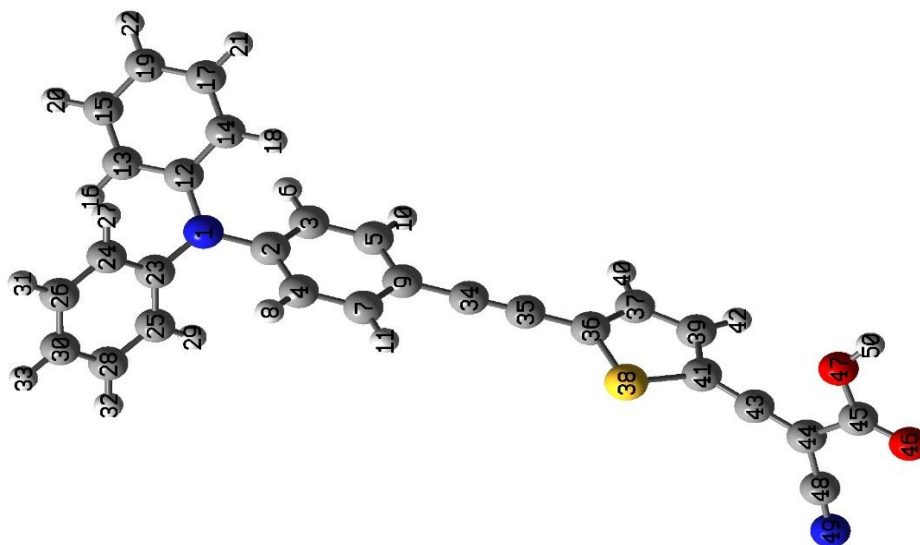
Figure 33: Optimized structure of D5: 3-(5-(4-(diphenylamine) styrl) thiophen-2-cyanoacrylic acid. Atoms are represented according to colour with carbon in grey, nitrogen in blue, sulphur in yellow, oxygen in red and hydrogen in white.
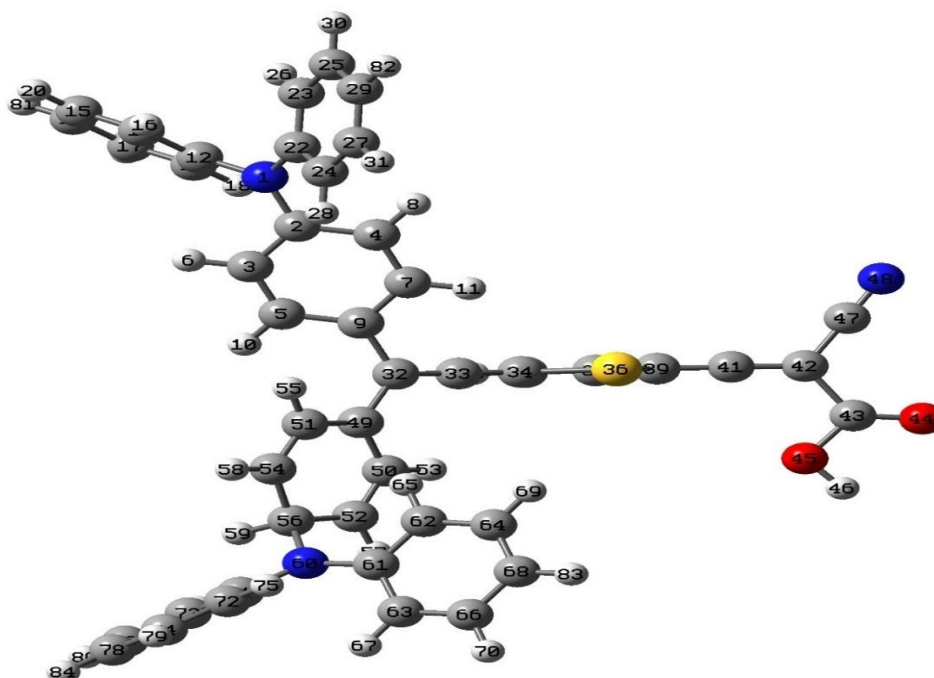
Figure 34. Optimized structure of D7: 3-(5-bis (4-(diphenylamino) styrl) thiophen-2-yl)-2-cyanoacrylic acid. Atoms are represented according to colour with carbon in grey, nitrogen in blue, sulphur in yellow, oxygen in red and hydrogen in white.
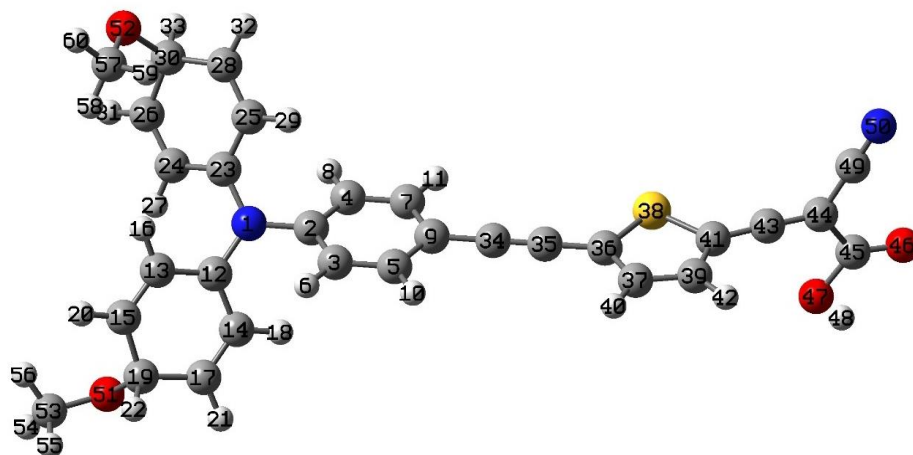
Figure 35: Optimized structure of D9: 5-(4-(bis (4-methoxyphenylamino) styrl) thiophen2yl)-2-cyanoacrylic acid. Atoms are represented according to colour with carbon in grey, nitrogen in blue, sulphur in yellow, oxygen in red and hydrogen in white.
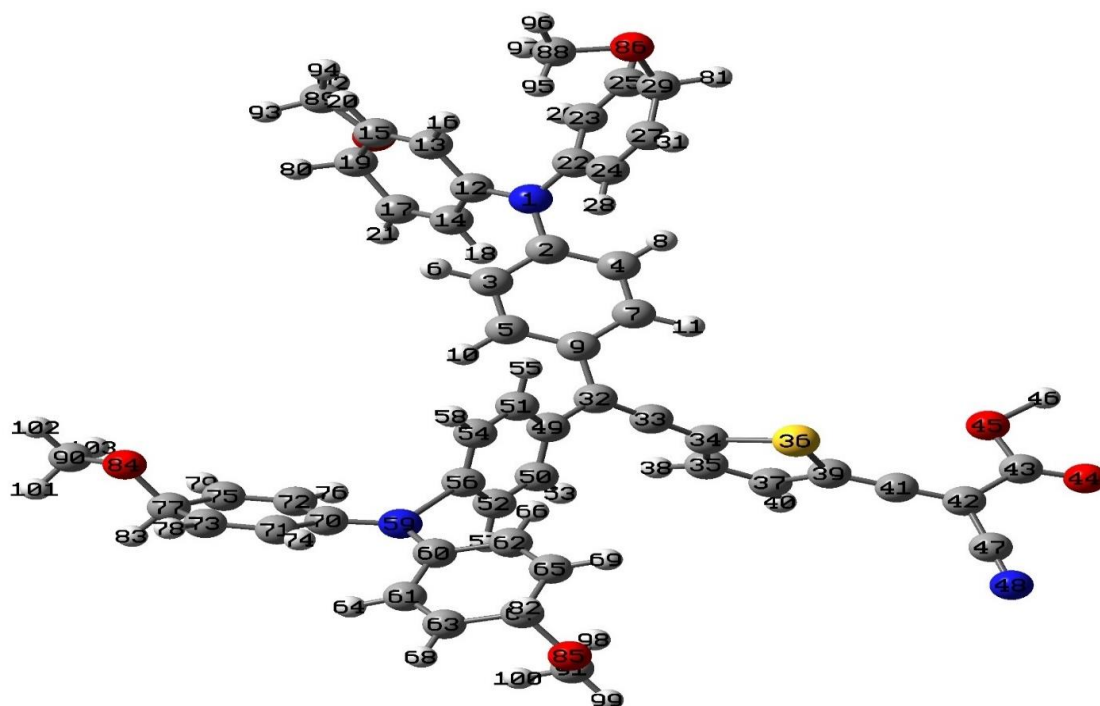
Figure 36: Optimized structure of D11: 3-(5-bis (4.4-dimethoxyphenylamiono) styrl) thiophen-2-yl) -2-cyanoacrylic acid Atoms are represented according to colour with: carbon in grey, nitrogen in blue, sulphur in yellow, oxygen in red and hydrogen in white.

4.4.3.1 Structural parameters

In this study, the molecular structures of the four dye were fully optimized in their ground state without symmetry constraints using hybrid density functional theory B3LYP and the 6-31G* basis set. The dipole moments and the internal forces obtained for the dye structures after optimization are summarized in Table 7.

Table 7. Internal forces (eV) and dipole moments (Debye) of optimized dye.

Sensitizer	Internal forces threshold value (eV/atom)	Dipole moment (Debye)
D5	4.5×10^{-4}	6.784
D7	4.5×10^{-4}	5.930
D9	4.5×10^{-4}	4.852
D11	4.5×10^{-4}	7.550

The geometrical optimizations converged when the internal forces acting on all the atoms were less than a threshold value of 4.5×10^{-4} eV/Å. D5 and D11 show the highest dipole moments, which explains the polarity between the molecules. For further analysis on structural properties, selected bond lengths, bond angles and dihedrals of D5, D7, D9 and D11 are listed in Tables 8, 9, 10 and 11 respectively. The numbers represents the number of atoms on the molecules, The bond lengths is the distance between the two atoms in the molecules, the bond angle is the angle between the three atoms in the molecule while the dihedrals is the dihedral angle between four atoms in the molecule.

Table 8. Selected bond lengths (Å), bond angles (°) and dihedral (°) of D5 dye.

D5	Bond length
1-2	1.413
1-12	1.435
1-23	1.435
41-43	1.328
9-35	1.412
35-36	1.379
	Bond Angles
2-1-23	120.600
2-1-12	120.600
9-34-35	178.800
41-43-44	177.800
	Dihedral
4-2-1-23	31.500
2-1-12-14	46.700
43-44-45-47	0.100

Table 9. Selected bond lengths (Å), bond angles (°) and dihedral (°) D7 dye.

D7	Bond length
1-2 / 59-56	1.419
1-12 /59-60	1.435
1-23/59-70	1.419
39-41	1.312
9-32 /49-32	1.491
33-34	1.311
	Angles
2-1-22 / 56-59-60	120.380
22-1-12 / 60-59-70	120.0
9-32-33 / 49-32-33	120.130
39-41-42	179.600
	Dihedral
3-2-1-12 /52-56-59-60	35.400
2-1-22-24 / 56-59-70-72	44.500
41-42-43-44	0.500

Table 10. Selected bond lengths (Å), bond angles (°) and dihedral (°) of D9 dye.

D9	Bond length
1-2	1.413
1-12	1.421
1-23	1.421
41-43	1.323
9-35	1.403
35-36	1.372
	Angles
2-1-23	120.2
2-1-12	120.3
9-34-35	179.25
41-43-44	177.2
	Dihedral
4-2-1-23	37.2
2-1-12-14	40.0
43-44-45-47	1.224

Table 11. Selected bond lengths (Å), bond angles (°) and dihedral (°) of D11 dye.

D11	Bond length
1-2 / 59-56	1.448
1-12 /59-60	1.389
1-23/59-70	1.389
39-41	1.312
9-32 /49-32	1.495
33-34	1.311
	Angles
2-1-22 / 56-59-60	118.72
22-1-12 / 60-59-70	122.5
9-32-33 / 49-32-33	120.13
39-41-42	179.6
	Dihedral
3-2-1-12 /52-56-59-60	51.08
2-1-22-24 / 56-59-70-72	32.0
41-42-43-44	0.1

The calculated geometrical properties of D5 dye are in close agreement with those reported in the literature [102]. Similar geometrical characteristics resulting from similar geometry of the dye structures were observed for D5, D7, D9 and D11. The distances between the C atom in carboxyl and N atom in aniline were 1.435 Å, 1.435 Å, 1.421Å and 1.389 Å for D5, D7, D9 and D11, respectively. These values account for the lengths of the conjugation bridges. These conjugation lengths aid electron transfer in the conjugation chain [173].

4.4.3.3. UV-Vis absorption spectra of the dye

The UV-Vis spectra of the dye were calculated using TD-DFT/B3LYP in gas phase for all the dye. The absorption spectra graph is shown in Figure 37.
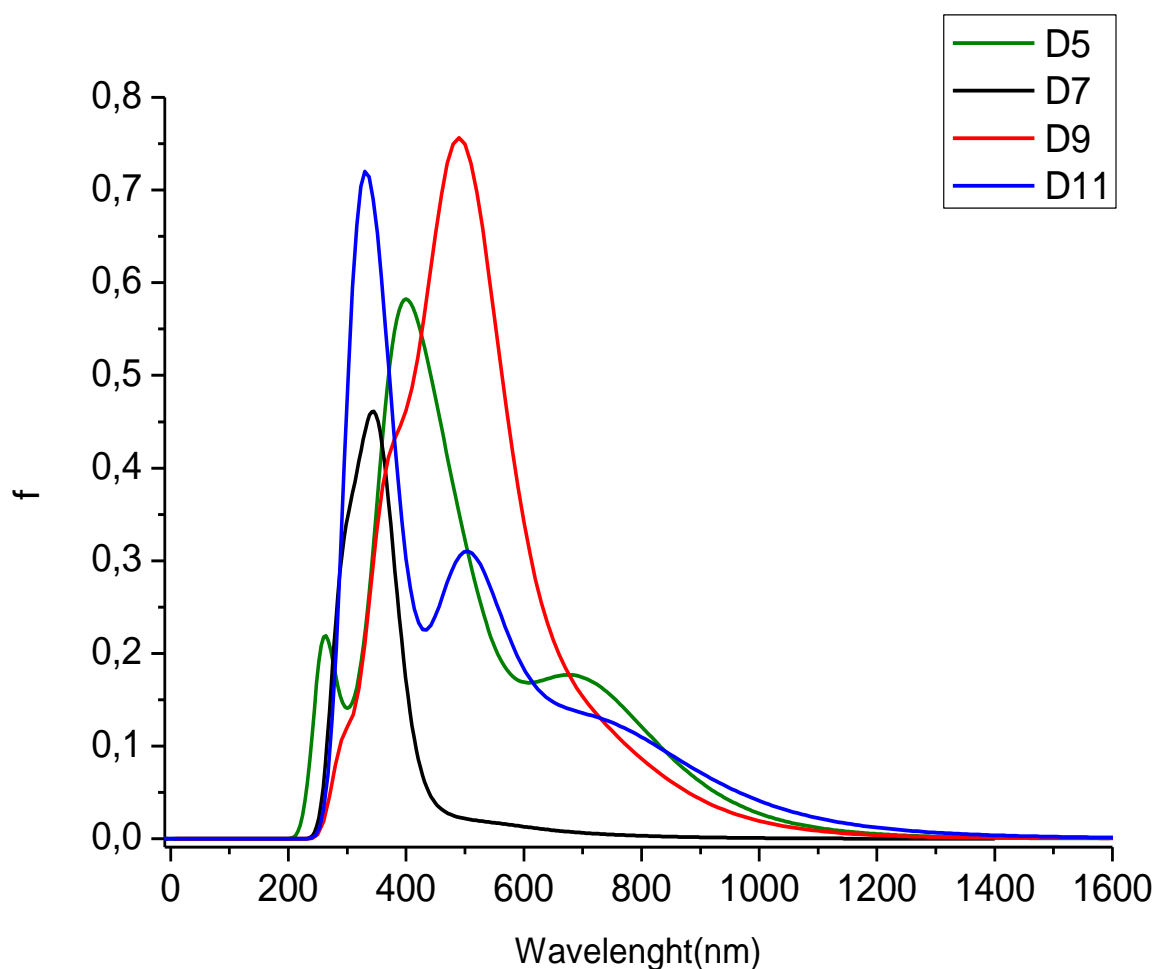
Figure 37: Simulated absorption spectra of D5, D7, D9 and D11 dye.

The absorption peak for D5 dye is located at 400 nm while that of D7 dye is located at 380 nm. D9 shows an absorption peak at 490 nm while D11 shows an absorption double peaks at 330 nm and 504 nm. The highest absorption wavelength was notable for both D9 and D11. The molar absorption reported by Kuang's electrochemical experiment are 33,000 M^{-1} cm^{-1} (441 nm) 31,000 M^{-1} cm^{-1} (441 nm) 33,000 M^{-1} cm^{-1} (464 nm) 38, 000 M^{-1} cm^{-1} (458 nm) for D5, D7, D9 and D11 respectively. The study reported that D9 and D11 show spectral red shifts and better current-voltage characteristics than the corresponding D5 and D7 [82]. This explains the red shifted spectral peak observed for D9 and near infra-red absorption observed for D11. The calculated results agree fairly well with Kuang's findings.

Interestingly, the HOMO-LUMO energy gaps obtained for D9 and D11 were found to be relatively low as compared to D5 and D7. This suggests the bathochromic shift observed in their absorption spectra. The light harvesting efficiencies of the dye were calculated using equation (79) and are   presented in Table 12.

Table 12. Computed maximum absorption(λ_{max}/nm), excitation energy (eV), oscillator strength (f) and light harvesting efficiency (LHE) of the dye.

Dye	$\lambda_{max}(nm)$	E (eV)	F	LHE
D5	400	3.09	0.58	0.74
D7	380	3.26	0.46	0.65
D9	490	2.53	0.75	0.82
D11	504	2.46	0.72	0.81

From the calculation results in Table 12, D9 and D11 show the highest light harvesting efficiencies. This is in agreement with simulated absorption spectra as presented in Figure 37 whereby D11 showed more spectral red shift absorption than D5, D7 and D9. This explains the highest current-voltage characteristics observed for D11 as reported by Kuang's electrochemical experiment [82]. The results obtained from this study agree very well with Kuang's report. The calculated LHE values range from 0.653 to 0.822 and are relatively high, suggesting that the dye molecules will demonstrate good performance when used as photosensitizers for DSSCs.

4.4.3.4. Energy levels of the dye

The energy levels (HOMO, LUMO, energy gap) provide the driving force for electron charge transfer of the dye sensitizer [80, 82, 173]. Low band gap energy between the HOMO and LUMO of the photosensitizers enhances absorption of photons in the red spectral region of the solar spectrum [52, 96]. The HOMO and LUMO isodensity plots of the photosensitizers were calculated and are presented in Figure 38.

The HOMOs in D5 is more delocalized over the entire molecular region whereas the HOMOs in D7, D9 and D11 are mainly distributed in the electron donor moiety but extend to linker groups in D7. The LUMOs in D5, D7, D9 and D11 are localized over the cyanoacrylic acid anchor and the linker groups although they extend to some of the polyenediphenyl in D11 dye. Different electronic density distribution between HOMO and LUMO results in intermolecular charge separation between the donor and the acceptor group of the sensitizer when excited [91]. Computed HOMO levels of D5, D7, D9 and D11 lie at -4.90 eV, -5.13 eV, -4.46 eV and -4.44 eV respectively. The HOMOs are in the order D7<D5<D9<D11. The LUMO levels are located at -2.62 eV for D5, -2.41 eV for D7, -2.94 for D9 and -2.90 eV for D11. Thus, the LUMOs are in the order D9<D11<D5<D7. However, the HOMO- LUMO gaps are 2.27 eV, 2.72 eV, 1.51 eV and 1.53 eV for D5, D7, D9 and D11 respectively. Smaller HOMO- LUMO gaps observed in D9 and D11 suggest that the addition of methoxy groups to the donor moiety of the photosensitizers influences their energy levels.   The computed values of -4.90 eV, -2.62 eV, 2.27 eV for HOMO, LUMO, HOMO- LUMO energy gap of D5 are in good agreement with literature results -4.96 eV, -2.68 eV, 2.28 eV [91] and -5.14 eV, -2.66 eV and 2.48 eV [102] that were obtained using the same level of theory. Hence the hybrid B3LYP/6-31G* basis sets are effective for computing molecular energy levels and isodensity plots for dye molecules.

University of Venda
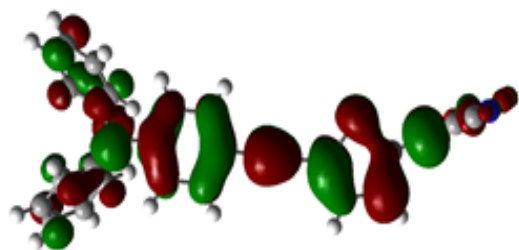
D5 HOMO
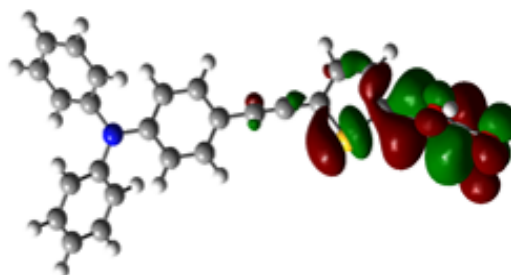
D5 LUMO
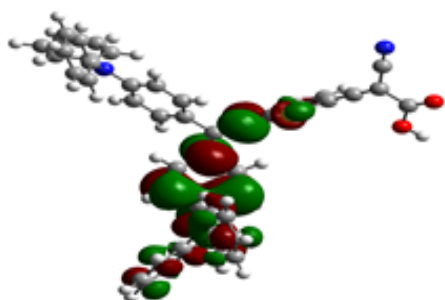
D7 HOMO
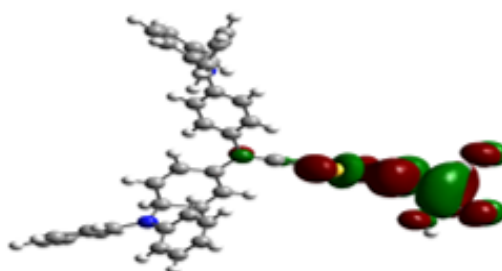
D7 LUMO
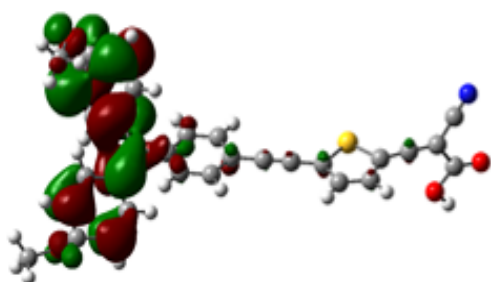
D9 HOMO
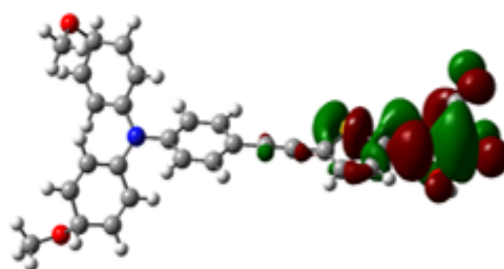
D9 LUMO
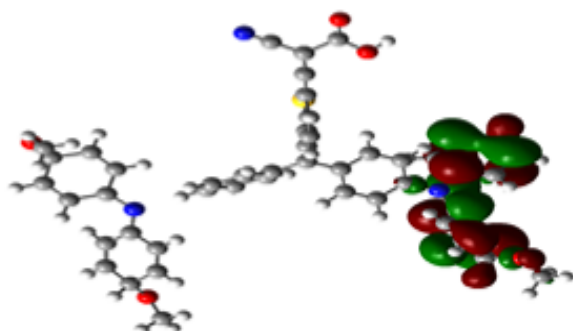
D11 HOMO
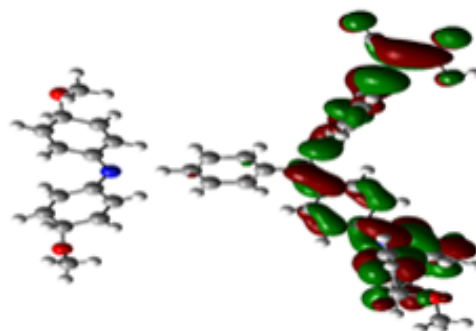
D11 LUMO

Figure 38: Frontier molecular orbitals calculated using B3LYP/6-31G* theory and isodensity surfaces of HOMO and LUMO of D5, D7, D9 and D11 dye.

4.5 Croconate dye

4.5.1 Introduction

In this work, DFT and TD-DFT methods were used to study the optical and absorption properties of two croconate dye. The two croconate dye are CR1 and CR2 as described in section 1.10 of chapter 1 and were presented in Figures 11 and 12 respectively. The major difference between the two dye is that CR1 contains electron donating methyl while CR2 contains electron withdrawing carboxylic acid moiety. In this section conjugate length, absorption bands, light harvesting efficiency and HOMO-LUMO energy levels for electron injection of the dye and are discusses and compared with other findings reported in literature. Croconate dye are important class of organic dye with short backbone and oxyallyl subgroup. Some of their salient features are easy synthesis route, good interaction with light, narrow bands and intense absorption in the near infrared region and their ability to absorb light even at wavelengths greater than 1100 nm. Their characteristic strong interaction with light has been attributed to their biradical character. The short oxyallyl subgroup in the backbones of these dye makes it easily synthesizable, thereby producing DSSCs that are flexible with strong light interaction.

Puyad *et al.* studied two model croconate dye labelled CR1 and CR2, one with an electron-donating substituent (CR1) and the other with an electron-withdrawing group (CR2) and their adsorption on the stoichiometric TiO_2 anatase (101). The findings showed that the acidic group (-COOH) possesses a strong binding ability to the TiO_2 surface [80]. Chitumalla *et al*. later reported on the two croconate dye, CR1 and CR2 using density functional theory. The periodic and electronic-structure calculations revealed that the diketo group of CR1 bind more strongly to the TiO_2 surface than that of CR2, with a binding strength comparable to that of a typical organic d–π–a dye. The study suggested that the nature of the substituent plays a vital role on the electronic, optical and adsorption properties of the croconate dye [79].

4.5.2 Computational procedure

The structures of the dye molecules were built in Gaussian 03 quantum chemical package [78]. Geometrical optimization calculations of the dye molecules in vacuum were performed using the first principles calculations based on density functional theory while employing the hybrid density functional-B3LYP and Pople's split valence basis set with polarization and diffuse functions [6-31G*] using the default integration grid as implemented in Gaussian 03. The UV/Vis simulations of the absorption spectrum were performed on the ground state structure

obtained after optimization using the same basis sets while considering 50 singlet to singlet transitions. This was followed by the calculation of the light harvesting efficiencies at λ_{max} and the excited properties of the dye molecules.

4.5.3 Results and discussions

4.5.3.1 Structural optimization

Hybrid density functional B3LYP exchange correlation functional and 6-31G* basis set level were used to optimize the ground state geometries of the croconate dye molecules in vacuum via Gaussian 03. The optimized molecular geometries are shown in Figure 39. CR1 contains electron donating methyl group (CH_3) which is an alkyl derived from methane, containing one carbon atom bonded to three hydrogen atoms while CR2 contains electron withdrawing carboxyl group (-COOH), which is an organic compound contained in carboxylic acid, one carbon atom bonded to two oxygen atoms and one hydrogen atom. The geometrical optimizations converged when the internal forces acting on all the atoms were less than 4.5x10^{-4} eV/A. The optimized geometry parameters, i.e., bond lengths and bond angles are presented in Table 13. The O6-C3 bond length of the oxyallyl moiety in CR1 is 1.236 Å. This is longer than the bond length of C5-O7/ C1-C8 which is 1.220 Å. This was also the case for the bond length of O6-C3 (1.243 Å) and C5-O9/C1-O10 (1.238 Å) in CR2. This suggests a more single bond character of the oxyallyl compared to C5-O7/ C1-C8 and C5-O9/C1-O10. Other findings obtained values of 1.299 Å O6-C3 bond length for the oxyallyl moiety and 1.213 Å for C5-O7/ C1-C8 in CR1, and O6-C3 (1.216 Å) and C5-O9/C1-O10 (1.208 Å) in CR2 [77]. Our findings compare favourably well with other findings [79, 80].

CR1   CR2
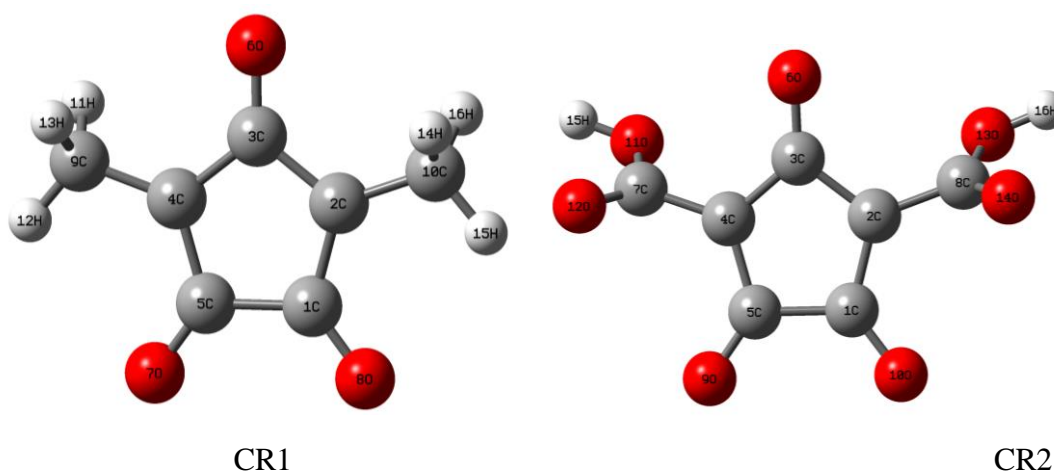
Figure 39: Optimized structures of CR1 and CR2, red ball represents oxygen, grey balls represent carbon and white balls represent hydrogen.

Table 13: Optimized structural parameters of two model croconate dye, CR1 and CR2. Bond distance in units of Å and degrees (º) respectively.

Dye	O6 -C3(Å)	C3 – C4/ C3 –C2 (Å)	C4 – R/ C2 – R (Å)	C5 – O7/ C1-O8. C5-O9/C1 – O10 (Å)	O6C3C4/ O6C3C2 (º)	C4C3C2(º)
CR1	1.236	1.459	1.464	1.220	127.3	105.1
CR2	1.243	1.468	1.469	1.238	128.6	102.3

4.5.3.2 Excitation and absorption spectrum of the dye

Figure 40 illustrates UV-Vis spectra of the two dye molecules. The absorption maxima of CR2 is situated at 225 nm and 550 nm while the absorption peaks of CR2 are notably at 160 nm, 220 nm, 440 nm and 680 nm. CR2 demonstrates more red shifted absorption than CR1. This may be as a result of the electron withdrawing carboxylic group in the structure of CR2. This suggests that the structure of CR1 and CR2 can be fine-tuned with the addition or substitution of chemical constituents to absorb more photons in the near infrared region. Other findings obtained absorption maxima of 535 nm and 635 nm for CR1 and CR2 respectively, which are in agreement with this study [79].
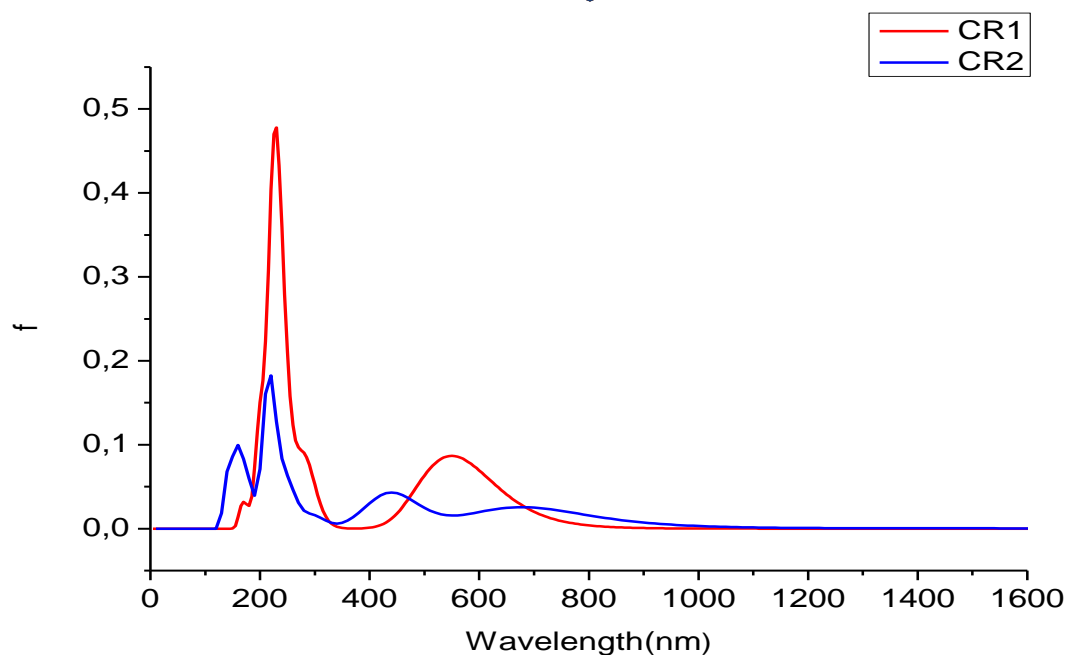
Figure 40: Simulated UV-Vis spectrum for CR1 and CR2 dye molecules.

4. 5.3.3 Light harvesting efficiency of the CR1 and CR2 dye

Light harvesting efficiency of CR1 and CR2 at the absorption peaks was calculated using Equation (79). The computed light harvesting efficiencies of CR1 and CR2 are presented in Table 14 and Table 15 respectively.

Table 14: LHE of CR1 at a particular wavelength

Wavelength (nm)	Absorption	LHE	LHE (%)
225	0.470	0.661	66
550	0.086	0.176	17

Table 15: LHE of CR2 at a particular wavelength

Wavelength (nm)	Absorption	LHE	LHE (%)
160	0.090	0.187	18.7
220	0.180	0.339	33.9
440	0.040	0.087	8.7
680	0.030	0.067	6.7

© University of Venda

An increase in the LHE raises the photocurrent response and therefore the corresponding device efficiency. The calculated percentage of LHE and λ_{max} is found to be 66.0 % with $\lambda_{max} = 550$ nm for CR1 and 33.9% with $\lambda_{max} = 680$ nm for CR2. The LHE depends on the absorption (oscillator strength) at a known wavelength. The higher percentage of light harvesting efficiency of 66.0% was demonstrated by CR1 owing to its high oscillator strength at 225 nm, although CR2 has the highest λ_{max} of 680 nm.

4.5.3.4 Energy levels and isodensity surfaces of the CR1 and CR2 dye

Isodensity surfaces of the dye depicting the HOMO, LUMO and HOMO-LUMO of the dye molecules are presented in Figure 41. The energy gap is generally the lowest energy electronic excitation that is possible in a molecule. The HOMO, LUMO and HOMO-LUMO energy gap of CR1 and CR2 dye molecules are represented in Table 16.

Table 16: The HOMO, LUMO, HOMO-LUMO energy gap of CR1 and CR2 dye molecules.

DYE MOLECULE	HOMO (eV)	LUMO (eV)	HOMO-LUMO GAP (eV)
CR1	-7.490	-5.080	2.320
CR2	-8.080	-6.040	2.040

(a)   (b)

(c)   (d)
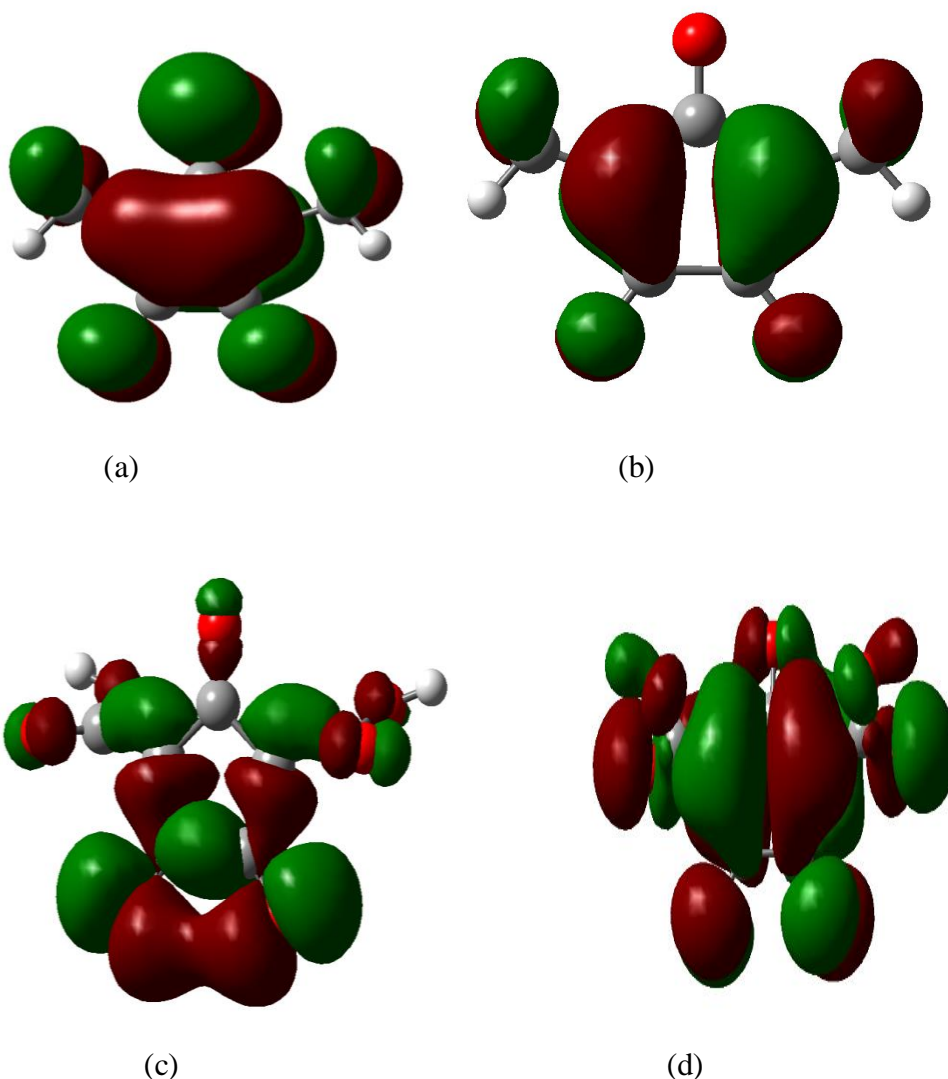
Figure 41: Isodensity surfaces of the molecular orbitals of (a) highest occupied molecular orbital of CR1 (b) lowest unoccupied molecular orbital of CR1 (c) highest occupied molecular orbital of CR1 (d) lowest unoccupied molecular orbital of CR2.

The HOMO energies of CR1 and CR2 are −7.49 eV and −8.08 eV respectively, the LUMO energies of CR1 and CR2 are found to be 5.08 eV and −6.04 eV respectively. The HOMO–LUMO energy gap (HLG) values of CR1 and CR2 are 2.32 eV and 2.04 eV respectively. The lower the HOMO-LUMO energy gap of the sensitizer enhance absorption at higher wavelength and the photocurrent response of DSSCs. Low energy gap between the HOMO and LUMO of sensitizer enhances the absorption of photons in higher spectral regions of the solar spectrum. The two dye relatively have low HOMO-LUMO energy gap, but with CR2 giving the least HOMO-LUMO energy gap. The lower HOMO-LUMO energy gap of CR2 suggests the red shifted absorption observed for CR2 in Figure 41. The findings compare favourably well with

values of -7.43 eV, -5.07 eV and 2.36 eV for HOMO, LUMO and HLG of CR1 respectively, -8.08 eV, -6.06 eV and 2.02 eV for HOMO, LUMO and HLG of CR2 respectively obtained in literature previously [79, 80].

The HOMO of CR1 is delocalized on the oxyallyl group, and partly localized on the diketo group and electron donating methyl while the LUMO is delocalized on the carbon atoms of the cyclopentane and the methyl group and the electron donating methyl. The HOMO of CR2 is delocalized on the diketo moiety while the LUMO is delocalized on the carbon atoms of the cyclopentane. The different concentration of the electron densities of HOMO and LUMO for CR1 and CR2 dye molecules suggest good electron transfer properties of the croconate dye, implying that both CR1 and CR2 can efficiently inject electron into the large band gap of TiO_2 semiconductor and hence improve the overall performance of DSSCs.

CHAPTER FIVE

5.0 TiO$_2$)$_n$ BROOKITE NANOCLUSTERS

5.1 Introduction

The photoanode of DSSC comprises of dye molecules anchored to the surface of semiconductors. Nanostructured TiO$_2$ are typically employed in most DSSCs [175, 176]. In this chapter, DFT/TD-DFT studies on the geometrical, electronic (TDOS) and optical properties (UV/Vis) of TiO$_2$ brookite clusters are carried out in order to understand the photocatalytic properties of brookite nanocluster. The brookite polymorph of TiO$_2$ has not been studied extensively and it has been reported to have good photocatalytic properties. It is therefore of keen interest to understand the electronic and optical properties of this polymorph for its application as a semiconductor material in DSSCs architecture. Recent studies have suggested that brookite is a good photocatalyst and exhibit higher photocatalytic activity than both rutile and anatase. Density functional theory studies performed on brookite (210) and anatase (101) surfaces demonstrated that brookite (210) surface has similar building blocks as anatase (101) surface. The study also reported that brookite (210) surface is one of the most stable and relaxed surface of brookite polymorphs [75, 76].

5.2 Computational procedure

Geometrical optimization of brookite bulk structure was performed using first principles calculations based on density functional theory using a plane-wave pseudopotential method. Generalized gradient approximation in the scheme of Perdew-Bruke-Ernzerhof (PBE) [147] was used to describe the exchange-correlation functional using the fine quality and all band/EDFT as electronic minimizer. The calculations were carried out using CASTEP code [166], which is a package within the framework of the Materials Studio software to obtain the ground state structure of brookite TiO$_2$ bulk system.

Several values of plane wave basis set cut-off energy ranging from 100 eV to 800 eV were evaluated for geometrical optimizations to determine convergence energy cut-off of the bulk structure of TiO$_2$ brookite. The suitable convergence energy cut-off was found to be 650 eV. Then the Monkhorst-Pack [169] grid parameters were varied to obtain a close spacing of the bond length followed by geometrical optimization of the structure. The number of k-points obtained for the grid parameters was plotted against the energy values obtained from the geometrical optimization and the convergence k-point grid with value of 30 was found to be suitable to converge the nanocluster systems. The corresponding k-mesh parameters are 4x7x7.

The minimum structure was then imported into a new 3D atomic window and three TiO_2 brookite clusters namely $(TiO_2)_n$ where n = 5, 8 and 68 were cleaved from the optimized ground state bulk structure. The TiO_2 brookite nanoclusters were composed from a simple box shape with dimension 5 Å in x, y and z directions with stoichiometry $(TiO_2)_n$ where n = 5, 8 and 68. The brookite nanoclusters were imported to Gaussview within the framework of Gaussian 03 quantum chemical package software. The imported structures of the TiO_2 brookite nanoclusters were then cleaned via Gaussview build interface of Gaussian 03 for reorientation of the atoms. This was followed by the structural optimization of the nanoclusters whereby the hybrid density functional B3LYP and LanL2DZ basis set were used to account for the charge formation on the Ti atoms. The UV/VIS simulations of the absorption spectrum in vacuum were performed using the same basis set with 40 singlets to singlet transitions. The density of states were simulated using the keywords "pop=full" and the output log file obtained from the simulation results was opened with Gausssum software to view the spectrum for the total density of states for the occupied and the unoccupied orbitals. The total density of states spectrum was convoluted using Full Weight at Half Maximum (FWHM) value of 0.3 and energy scale of -20 eV to 20 eV.

5.3 Results and Discussions

5.3.1 Structural Properties of $(TiO_2)_5$

The structures of the nanocluster modelled from the optimized minimum bulk structure obtained from BIOVIA material studio CASTEP [77, 165] was exported to Gaussview in Gaussian 03 quantum chemical package software. Structural optimization of the nanocluster was done while using the hybrid density functional B3LYP and LanL2DZ basis sets. The optimized structure is shown in Figure 42. The optimized parameters that includes the bond length and bond angles are presented in Table 17. The calculated bond lengths between Ti and O atoms of brookite nanocluster range from 1.83 Å to 2.02 Å while the bond angles between O- Ti-O range from 78 ^{0} to 113 ^{0}. The calculated parameters agree with the bond length value range of 1.87 Å to 2.04 Å and fairly agree with the bond angles values ranging from 77.00 to 105 ^{0} for brookite nanocluster structure as reported in literature [103]. The average bond length is 1.89 Å

Table 17: Selected bond lengths (Å) and bond angles (º).

Bond length (Å)		Bond Angles (º)	
Ti1-O3	1.830	O3-Ti1-O8	114.000
Ti1-O8	1.830	O8-Ti1-O9	106.000
Ti1-O5	1.850	O4-Ti5-O12	113.000
Ti5-O4	1.950	O4-Ti5-O14	78.000
Ti5-O6	1.940	O12-Ti5-O14	113.000
Ti5-O14	2.010	O3-Ti10-O14	93.700
Ti10-O2	1.900	O3-Ti10-O11	104.000
Ti10-O14	2.000	O2-Ti10-O3	105.000
Ti10-O3	1.830	O4-Ti13-O14	83.000
Ti13-O4	1.780	O7-Ti13-O4	81.000
Ti13-O9	1.810	O7-Ti13-O9	104.000
Ti13-O7	1.850	O9-Ti13-O14	101.000
Ti13-O14	1.94	O7-Ti15-O8	106
Ti15-O7	1.84	08-Ti15-O7	106
Ti15-O8	1.83	O8-Ti15-O11	107
Ti15-O11	2.02		
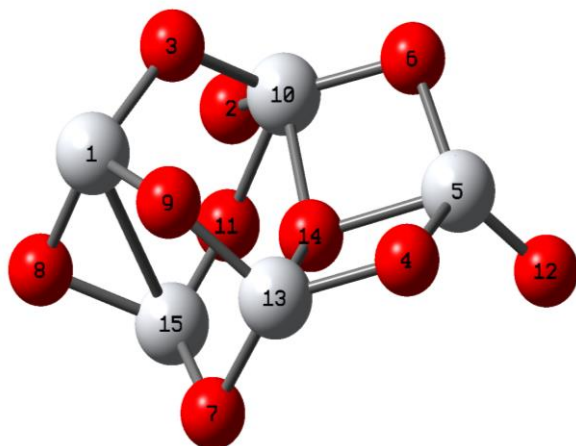
Figure 42: Optimized structure of TiO$_2$ brookite nanocluster

5.3.2 Optical Properties of (TiO$_2$)$_5$

The absorption spectrum of TiO$_2$ brookite excited states was simulated using TD-DFT method, the hybrid density functional theory B3LYP approximation with the LanL2DZ basis set was used considering 40 singlets to singlet transitions. The absorption plot of brookite TiO$_2$ is presented in Figure 43. The absorption maximum was located at 410 nm, showing that the maximum absorption is mainly situated at the UV region of the solar spectrum. This agrees with findings from literature that TiO$_2$ is majorly sensitive in the UV region of the solar spectrum owing to its wide band gap (3.0-3.2 eV) [65, 66]. It was also observed that the absorption maximum extends slightly to the visible region by a value of 10 nm. This agrees closely with findings of Zallen *et al.* [75], wherein measurement of the optical absorption edge of brookite TiO$_2$ at room temperature showed that the absorption edge of brookite was broad and extends to the visible region of the solar spectrum. This correlates with the slight extension of 10 nm of the absorption maximum observed in the absorption spectrum of brookite nanocluster.
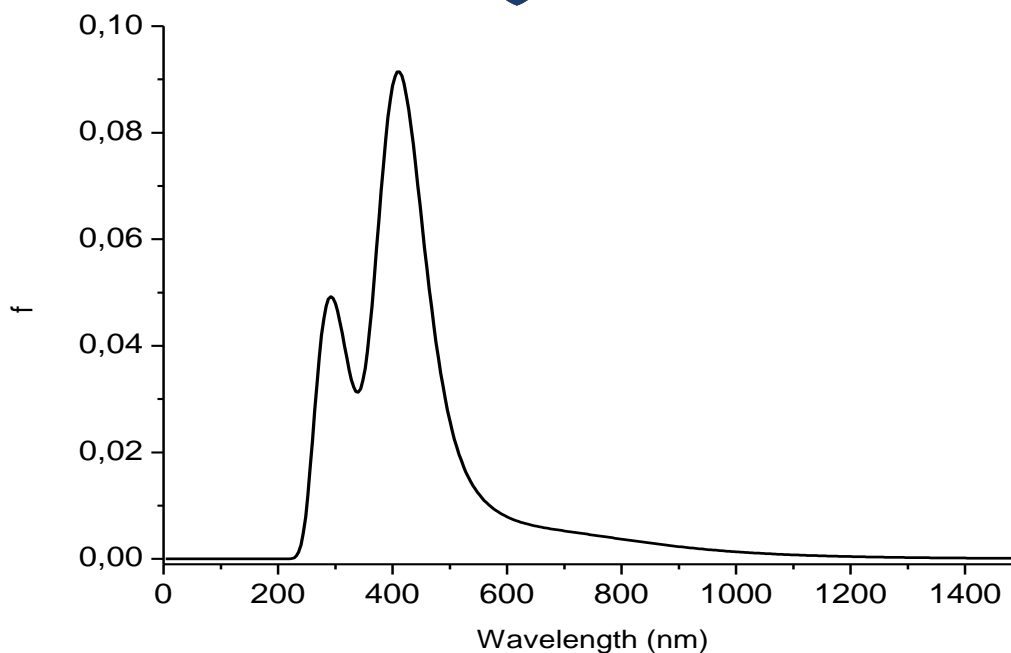
Figure 43: Simulated UV-Vis spectrum of $(TiO_2)_5$ brookite nanocluster.

5.3.3 Electronic Properties of $(TiO_2)_5$

The total density of states (TDOS) for the TiO_2 cluster shown in Figure 44 for the TiO_2 cluster was computed to understand the electronic coupling between the occupied and unoccupied molecular orbitals. The TDOS of the TiO_2 nanocluster showed broad space between the occupied and unoccupied state separated by a gap of 2.9 eV. There is a slight deviation of 0. 3 eV from the experimentally reported values of 3.2 eV [65 -67] for band gap of brookite bulk structure. The slight deviation may be as a result that a TiO_2 brookite nanostructure is geometrically different relative to the bulk system or could be because the estimated gap is the separation between the occupied and the unoccupied states of the nanocluster itself. However, the band gap agrees fairly with values reported from previous literature [65, 66].
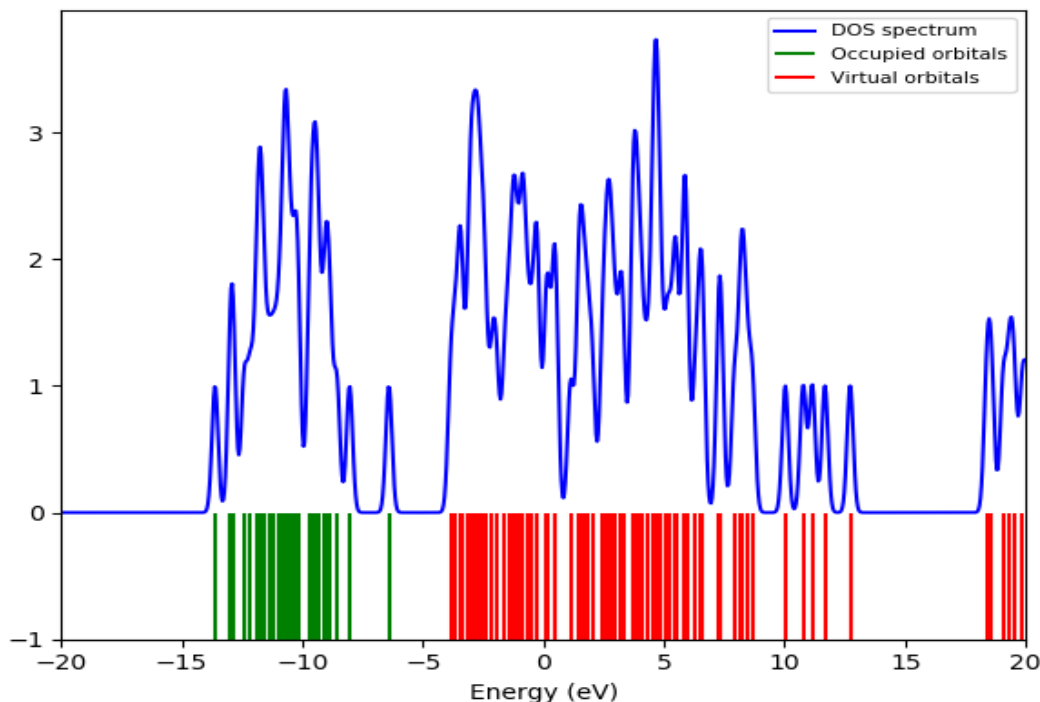
Figure 44: Total density of states (TDOS) spectrum of brookite $(TiO_2)_5$ nanocluster

5.4 Generation of larger $(TiO_2)_n$ brookite nanoclusters

Nanoclusters with large number of atoms were studied using DFT and the three brookite nanoclusters, namely; Ti_5O_{10}, Ti_8O_{16} and $Ti_{68}O_{136}$ are considered in this thesis. The adsorption of polyenediphenyl-aniline, croconate and ruthenium N3 dye molecules on three brookite TiO_2 surfaces, their interactions, adsorption energies, optical properties, electronic properties and electron injection kinetics of dye molecules are investigated.

5.5 Computational procedures

The bulk structure of brookite TiO_2 that was used throughout the study was optimized using CASTEP module in Materials studio BIOVIA [165] to obtain the ground state structure of the TiO_2 brookite semiconductor. The convergence energy cut-off and k-points were 650 eV and 4x7x7 respectively. The three brookite nanoclusters were cleaved from the optimized ground state bulk structure. The selected modelled clusters are (i) TiO_2 brookite nanocluster with dimension 5 Å in x, y and z directions, the stoichiometry of TiO_2 brookite nanocluster is

(TiO$_2$)$_n$ where n = 5, (ii) cluster with stoichiometry of (TiO$_2$)$_n$ where n = 8, was modelled and (iii) cluster with stoichiometry of (TiO$_2$)$_n$ where n = 68, which were created from a periodic repetition of the unit cell 2 x 2 x 2 Å supercell in x, y and z directions, cleaved from optimized TiO$_2$ brookite bulk structure. The clusters were then exported to GPAW software via crystallographic information format (cif) and were visualized using Avogadro software for further analysis and calculations.

All DFT calculations were performed within an atomic simulation environment (ASE) with GPAW software [159]. The structures were visualized with Avogadro. GPAW is a Python based program-package formulated with density-functional theory (DFT) combined with the grid space projector-augmented wave (GPAW). The three TiO$_2$ brookite clusters that were generated are presented in Figures 45-47.

All the structures were relaxed in vacuum using GPAW with the PBE exchange correlation functional. The structures were considered to have converged when the maximum forces that were acting on all the atoms were about 0.05 eV. The periodic boundary conditions were implemented on the supercell during the relaxation and were set to none for the non-periodic brookite (TiO$_2$)$_5$ and (TiO$_2$)$_8$ cluster models. The atoms of the cluster were reoriented during the relaxation until the ground state structure was reached where they become stable and the forces converge to a maximum value of 0.05 N.

The UV/Vis, total density of states and partial density of states of the nanocluster structures were computed using the trajectory files obtained from the relaxed structures. The UV-Vis was calculated in vacuum, the TDOS and PDOS were computed from the GPW files computed using the PBE functional.
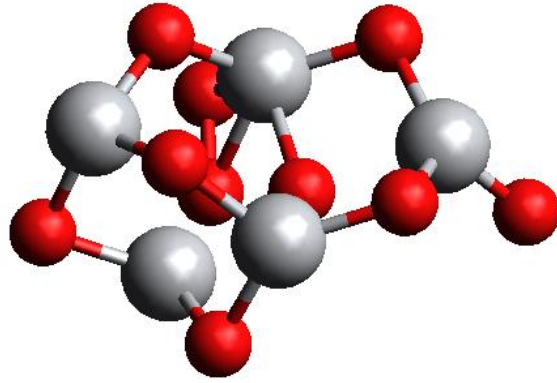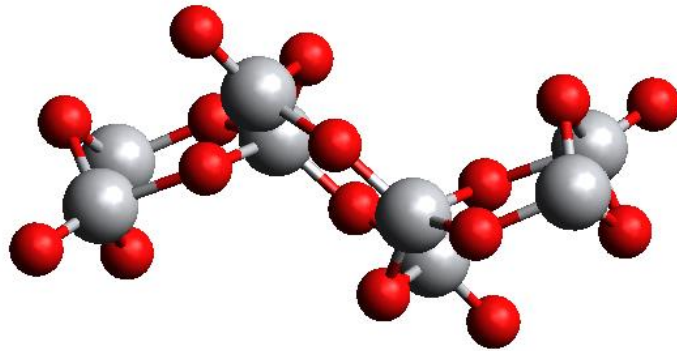
Figure 45: $(TiO_2)_5$ brookite nanocluster

Figure 46: $(TiO_2)_8$ brookite cluster

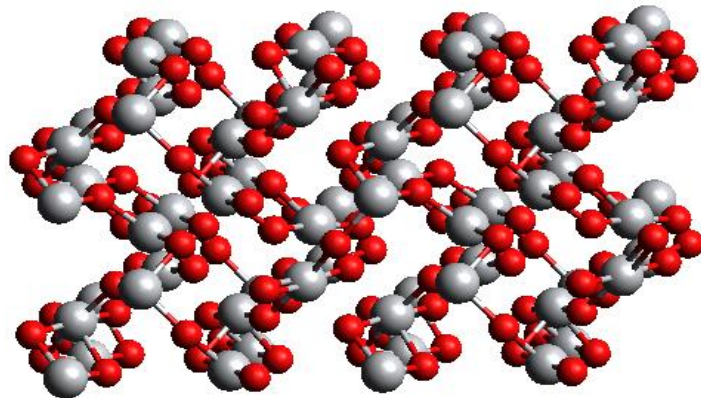Figure 47: $(TiO_2)_{68}$ brookite supercell

5.6 Results and Discussions

5.6.1 Optical Properties of $(TiO_2)_5$ and $(TiO_2)_8$ brookite clusters

The absorption spectra of $(TiO_2)_5$ and $(TiO_2)_8$ brookite clusters were simulated in vacuum using TD-DFT method with the PBE exchange correlation functional. Absorption spectra of $(TiO_2)_{68}$ was not computed owing to its periodicity. The UV-Vis absorption spectra for $(TiO_2)_5$ brookite nanoclusters and $(TiO_2)_8$ brookite clusters are presented in Figures 48 and 49 respectively. The absorption spectra of $(TiO_2)_5$ presented in Figure 43 was computed using hybrid density functional theory B3LYP approximation with the LanL2DZ basis set while the absorption spectra of the complex presented in Figure 48 is computed using GPAW with the PBE exchange correlation functional.

The results agree fairly well as they both show absorption in the UV region. Although Figure 48 shows higher peaks, this may be due to the different functional used in the simulation of the absorption spectra. The $(TiO_2)_5$ and $(TiO_2)_8$ brookite clusters presented in Figures 48 and 49 both show absorption in the UV region of the solar spectrum, with the absorption peaks predominantly situated around 200 nm. The $(TiO_2)_5$ also shows a slight absorption peak at around 400 nm, suggesting the absorption peak at higher wavelength than $(TiO_2)_8$. Higher peak height indicates that the higher absorbance is notable in $(TiO_2)_8$ brookite absorption spectra presented than in the $(TiO_2)_5$ absorption spectra. The results of the absorption spectra of $(TiO_2)_5$ and $(TiO_2)_8$ generally agree with findings from literature in the sense that TiO_2 is majorly sensitive in the UV region of the solar spectrum owing to its wide band gap (3.0-3.2 eV) [65, 66]. This is in agreement with the results obtained using a different method in the previous section.
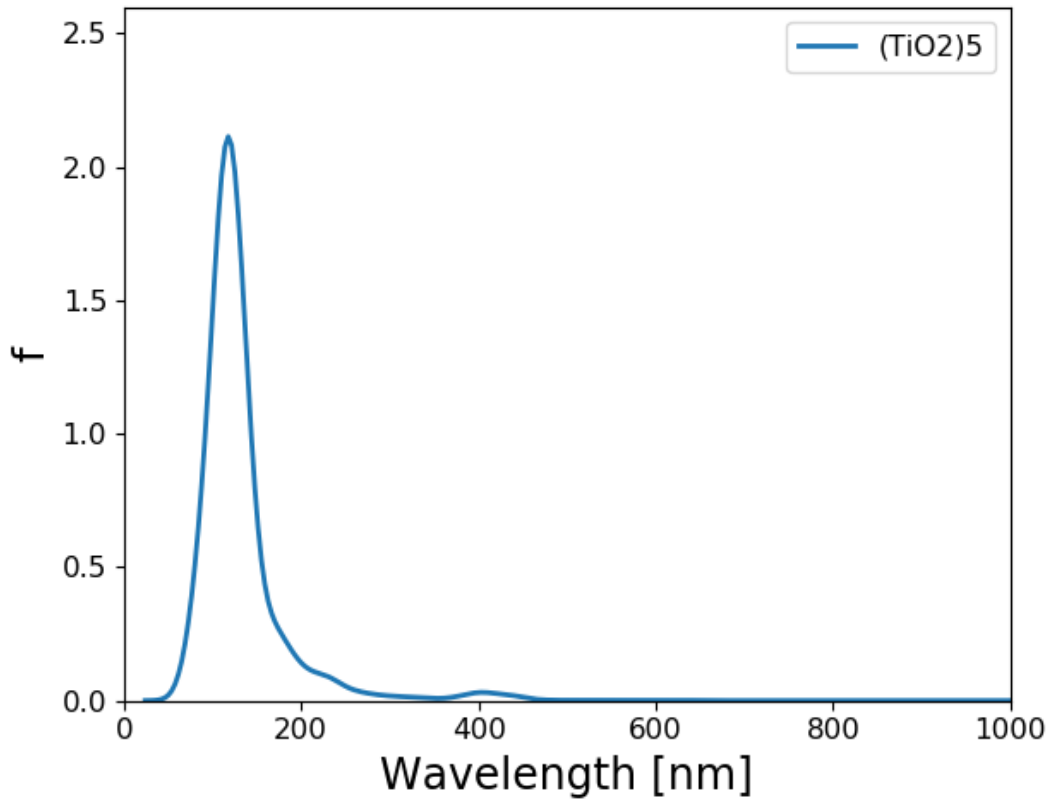
Figure 48: UV/Vis absorption spectrum for $(TiO_2)_5$ brookite cluster
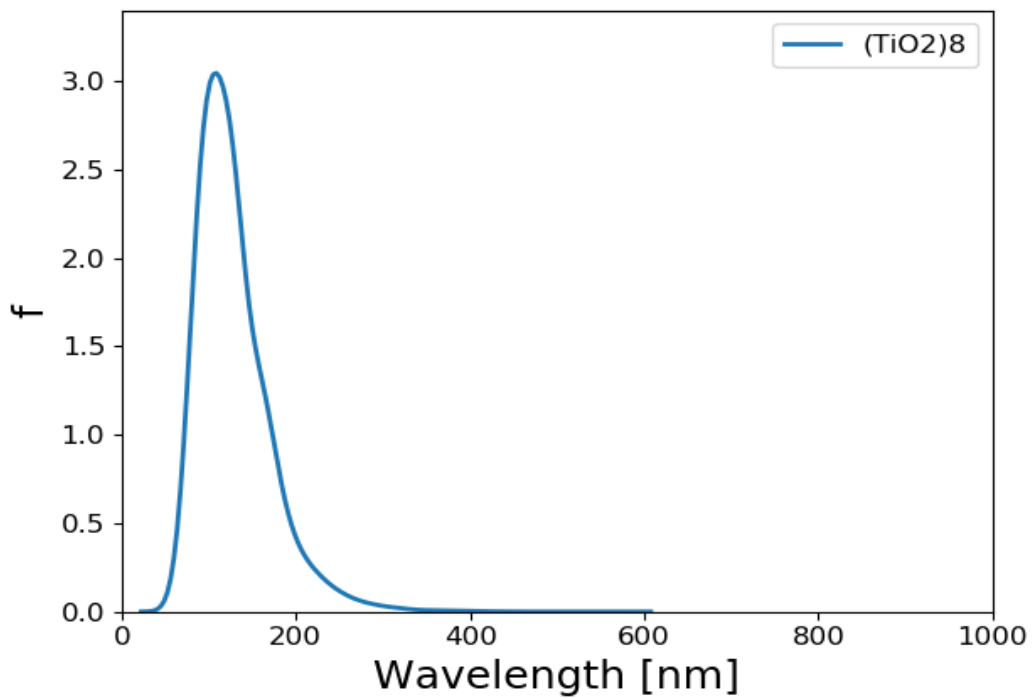
Figure 49: UV/Vis absorption spectrum for $(TiO_2)_8$ brookite cluster

5.6.2 Electronic Properties of (TiO₂) ₙ n= 5, 8, 68 brookite clusters

The density of states and the projected density of states of $(TiO_2)_5$, $(TiO_2)_8$ and $(TiO_2)_{68}$ nanoclusters was computed using GPAW and PBE exchange correction functional in order to further understand their electronic structure. The TDOS and PDOS of $(TiO_2)_5$, $(TiO_2)_8$ and $(TiO_2)_{68}$ are presented in Figures 50 -52 respectively. The DOS is composed of the surface valence and conduction bands separated by a wide band gap. The PDOS results for the clusters show that both the oxygen and titanium atomic orbitals contribute to the valence states, with the oxygen 2*p* atomic orbitals contributing mostly to the highest occupied valence band (VB) state, whereas the lowest unoccupied state of the conduction band is mainly dominated by the contributions of titanium 3*d* atomic orbitals as illustrated. The valence band is dominated by the *p* atomic orbitals of oxygen with a little contribution from the *p* atomic orbitals of titanium. The key contribution in the conduction band comes from the titanium orbitals, especially the *d* and *p* ones, whereas the contributions of oxygen atoms are minimal.

Figure 50: TDOS (top) and the projected DOS (bottom) for $(TiO_2)_5$ nanocluster with the red line representing titanium atom contributions and blue line representing oxygen contributions for PDOS.

Figure 51: TDOS (top) and the projected DOS (bottom) for $(TiO_2)_8$ nanocluster with the red line representing titanium atom contributions and while blue line representing oxygen contributions for PDOS.
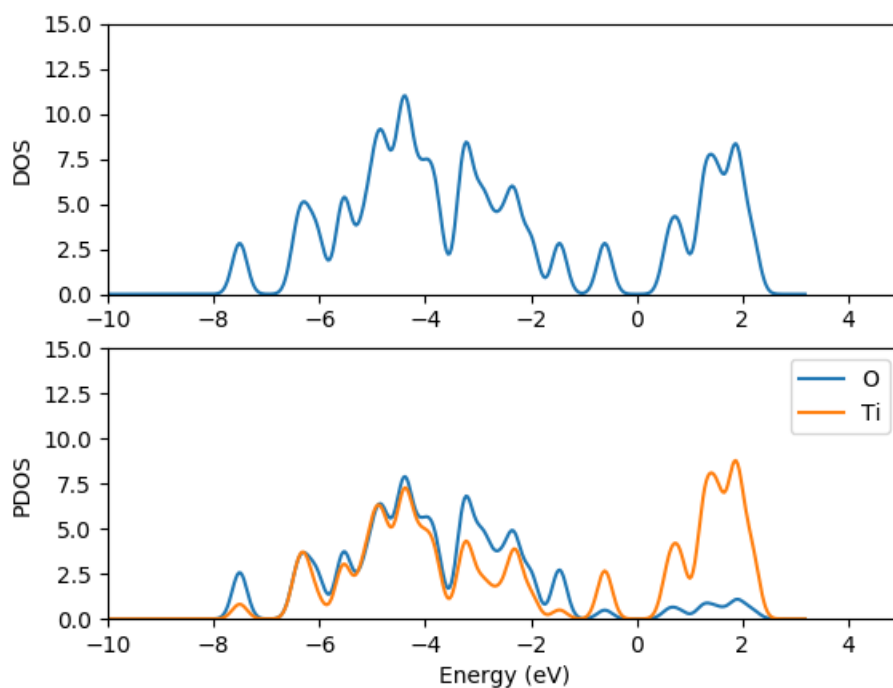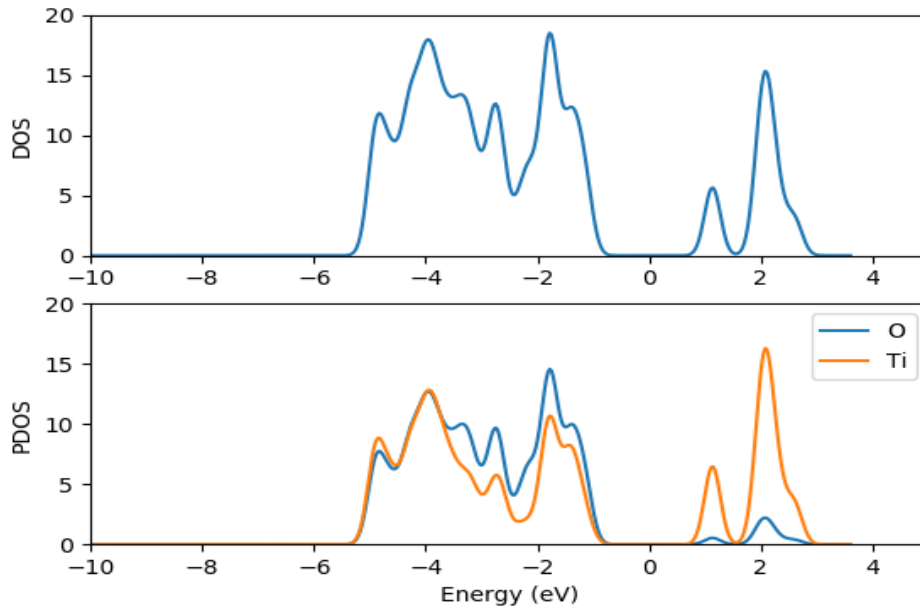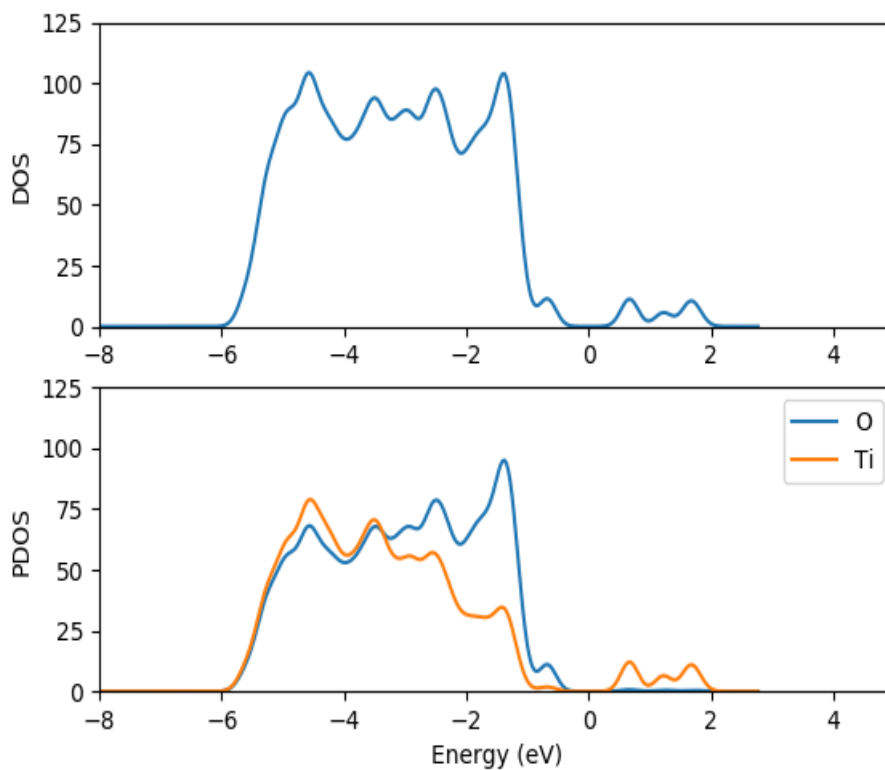
Figure 52: TDOS (top) and the projected DOS (bottom) for $(TiO_2)_{68}$ nanocluster with the red line representing titanium atom contributions and while blue line representing oxygen contributions for PDOS.

CHAPTER SIX

6.0 ADSORPTION OF DYE MOLECULES ON $(TiO_2)_n$, n= 5, 8, 68 BROOKITE CLUSTERS

6.1 Introduction

Understanding the interaction of dye molecules with the surfaces of TiO_2 is crucial because light harvesting and electron collection determine the efficiency of DSSC occur at the interface. Light harvesting capability of DSSCs basically depends on the molecular properties and band gaps of the interfacial components between the photoanode materials typically TiO_2 semiconductor and the dye molecules [133]. Therefore, reaction mechanisms at the interface are of great importance in understanding and optimizing light harvesting, photo conversion function and photocurrent densities in DSSCs.

In this chapter, DFT/TD-DFT was used to investigate the adsorption on and interaction of dye molecules with TiO_2 brookite semiconductor clusters in order to understand the interfacial interaction between the photoanode components. Also the photocatalytic properties of brookite TiO_2 are studied to give insights on how absorption in the near infra-red region of the solar spectrum can be improved. Furthermore, the electron injection dynamics which are key in optimizing photon to current densities and optimizing DSSC device efficiency are investigated. Three groups of dye molecules discussed previously in this study (i.e., typical ruthenium N3 complex, promising polyenediphenyl aniline dye and croconate dye) are considered for adsorption on TiO_2 nanoclusters. In this section, results on the binding ability of the dye to TiO_2 clusters, adsorption energies, UV-Vis absorption spectrum, electron injection efficiencies, electron densities of the key molecular orbitals involved in excitation and their isodensity surfaces, density of states and the projected density of states are presented and discussed.

6.2 Computational procedure

The croconate dye molecules were chemisorbed unto TiO_2 nanocluster surfaces by bidentate absorption mode via the diketo group. The bidentate absorption mode was considered for this study because it was reported to be more energetically favorable [59, 124]. The dye@TiO_2 structures were then relaxed, from which the formation energies, optical and electronic properties of the dye@TiO_2 complex were computed upon adsorption.

6.3 Results and Discussions

6.3.1 Adsorption of polyenediphenyl-aniline dye on TiO₂ brookite clusters

Polyenediphenyl aniline dye has been reported to demonstrate promising performance potential for application in ionic liquid based electrolyte and iodide/triiodide based redox electrolyte dye sensitized solar cells, with power conversion efficiency of 6.5% and 5% achieved respectively [81, 82]. Four polyenediphenyl-aniline dye molecules coded D5, D7, D9 and D11 described in the earlier section of this study were separately adsorbed on three TiO_2 clusters with stoichiometry $(TiO_2)_5$, $(TiO_2)_8$ and $(TiO_2)_{68}$. The four dye molecules were adsorbed on $(TiO_2)_5$, $(TiO_2)_8$ and $(TiO_2)_{68}$ clusters by bidentate adsorption mode as presented in Figures 53(a-d), 54(a-d) and 55(a-d) respectively. All dye@TiO_2 complexes were relaxed upon adsorption. The relaxed structures of the dye molecules adsorbed on $(TiO_2)_5$, $(TiO_2)_8$ and $(TiO_2)_{68}$ clusters are presented in Figures 53-55. The relaxation energies of the dye molecules, $(TiO_2)_5$, $(TiO_2)_8$, $(TiO_2)_{68}$ brookite clusters and polyenediphenyl-aniline dye absorbed on the TiO_2 clusters were computed and are presented in Table 18. The relaxation energies of the polyenediphenyl-aniline dye molecules are -358.273 eV, -575.417 eV, -404.610 eV, -667.852 eV for D5, D7, D9 and D11 respectively. The energies of the clusters are -119.98 eV, -198.31 eV, -1635.55 eV for $(TiO_2)_5$, $(TiO_2)_8$ and $(TiO_2)_{68}$ respectively.

(a)   (b)

(c)

(d)
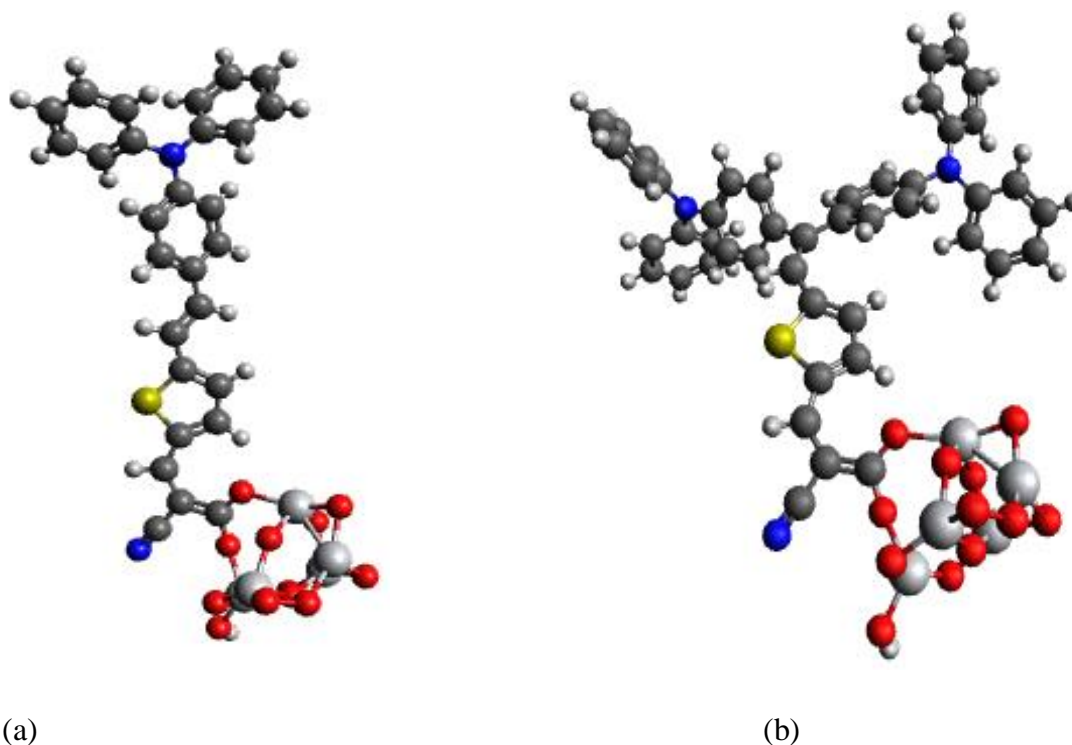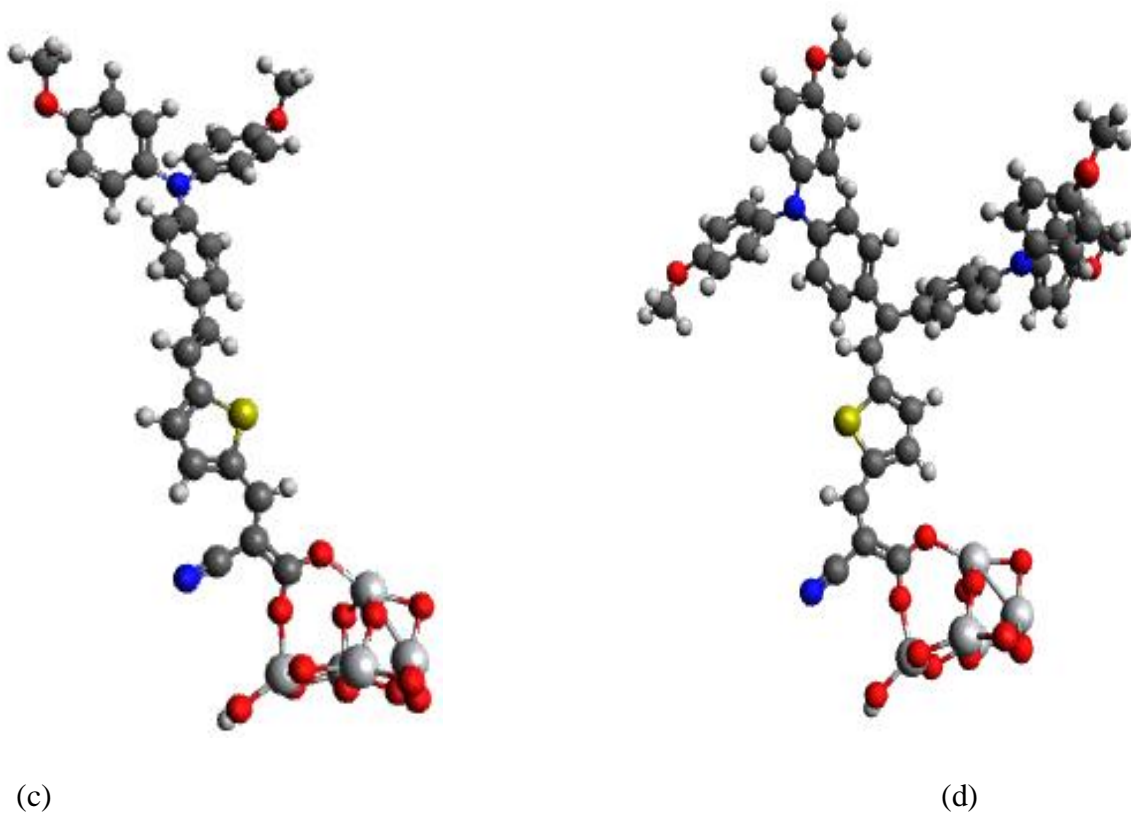
Figure 53: Polyenediphenyl-aniline dye absorbed on $(TiO_2)_5$ (a) D5@ $(TiO_2)_5$ (b) D7@ $(TiO_2)_5$ (c) D9@ $(TiO_2)_5$ (d) D11@ $(TiO_2)_5$

(a)

(b)
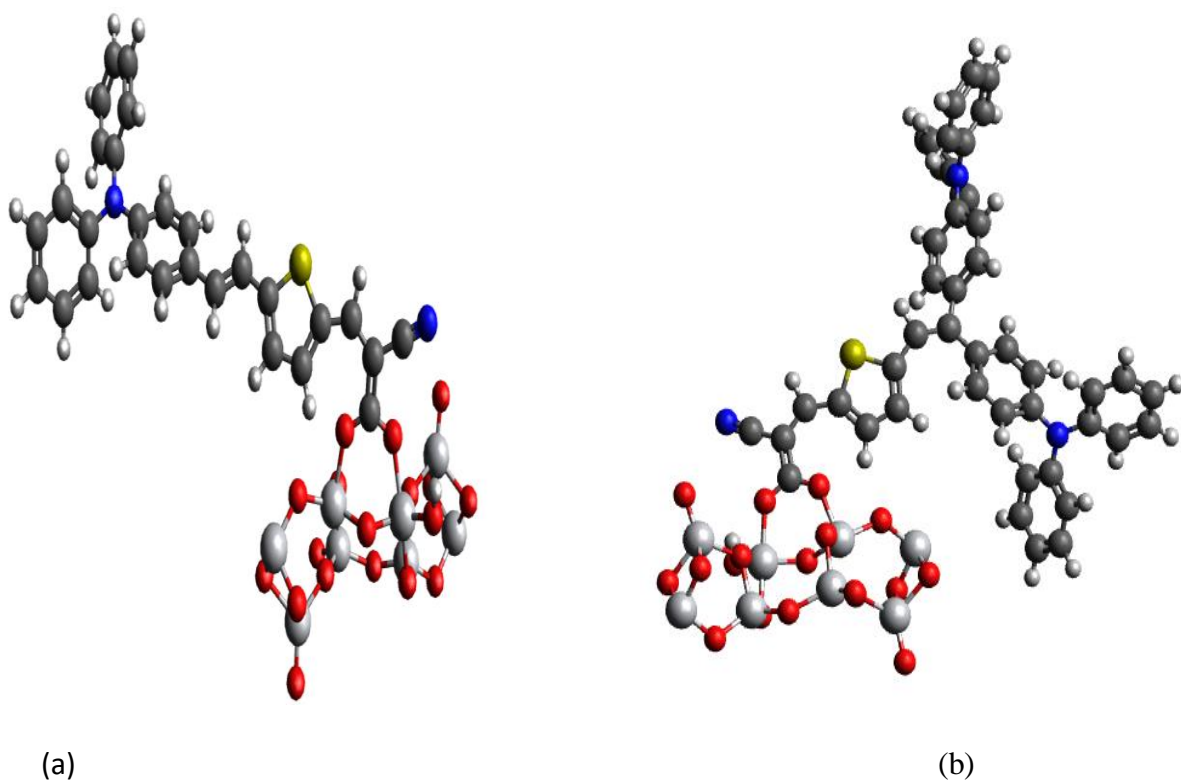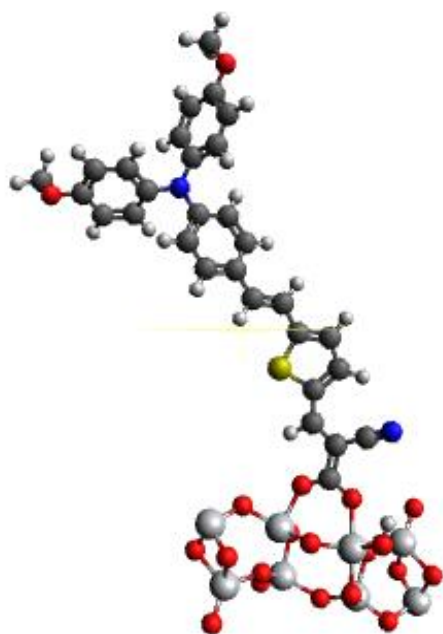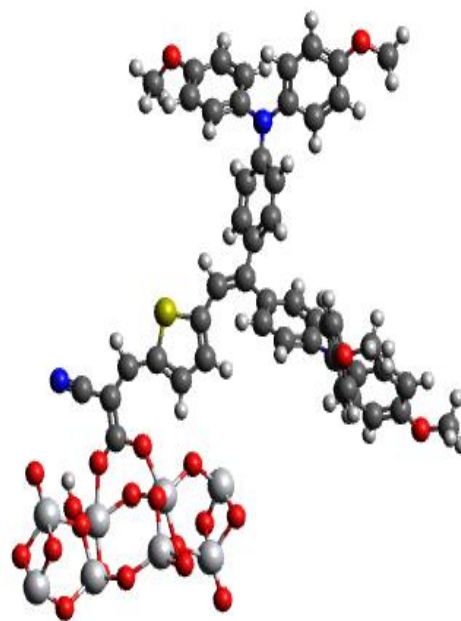
(c)   (d)

Figure 54: Polyenediphenyl-aniline dye absorbed on $(TiO_2)_8$ (a) D5@ $(TiO_2)_8$ (b) D7@ $(TiO_2)_8$
(c) D9@ $(TiO_2)_8$ (d) D11@ $(TiO_2)_8$

(a)   (b)
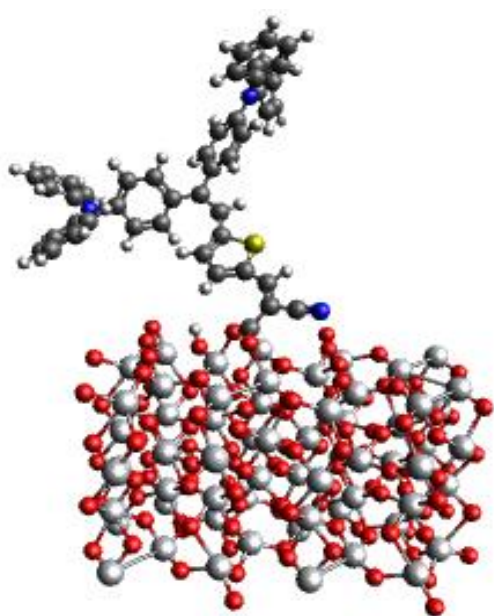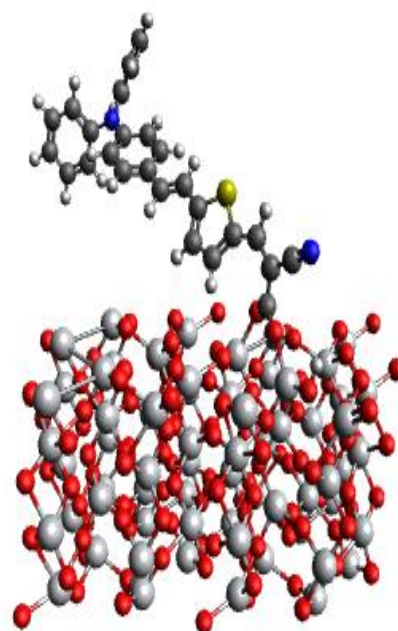
(c)   (b)
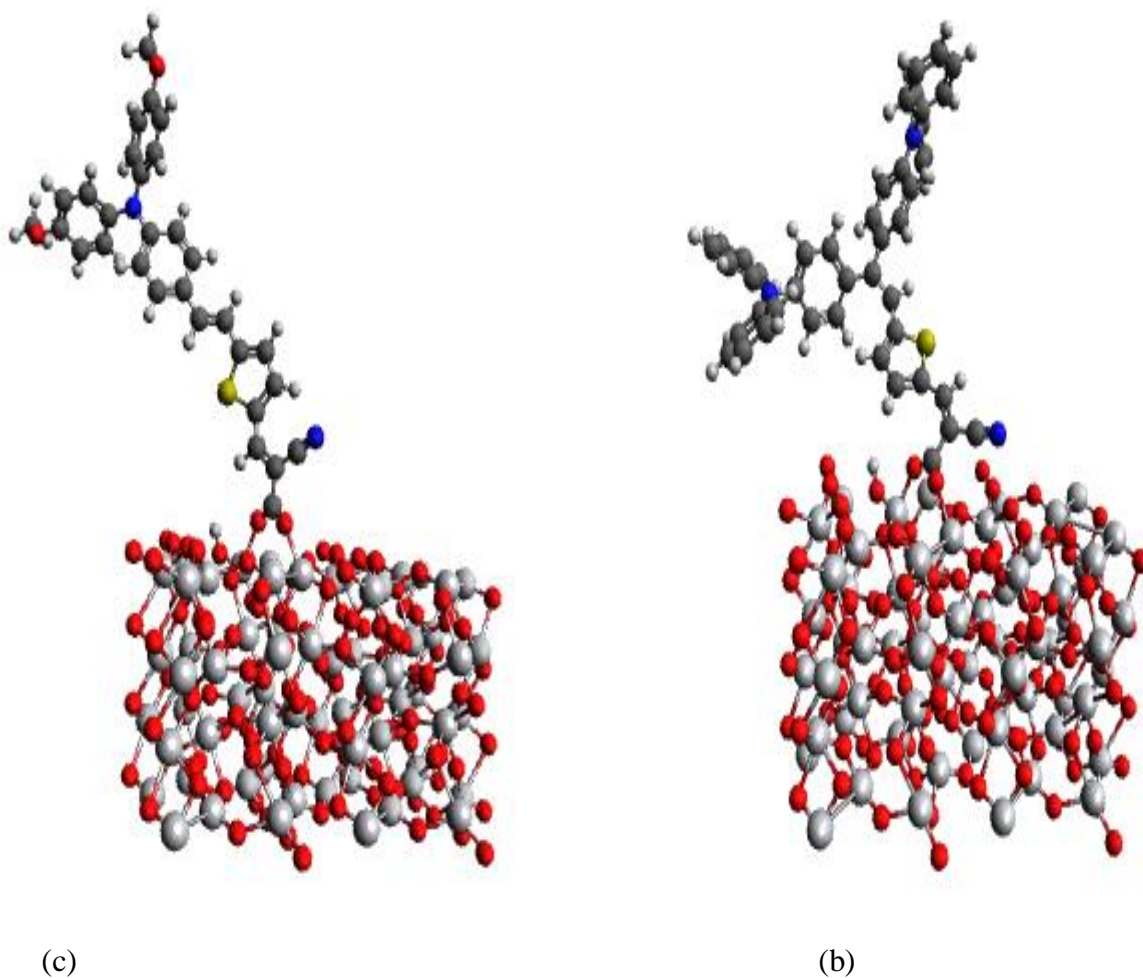
Figure 55: Polyenediphenyl-aniline dye absorbed on $(TiO_2)_{68}$ (a) D5@ $(TiO_2)_{68}$ (b) D7@ $(TiO_2)_{68}$ (c) D9@ $(TiO_2)_{68}$ (d) D11@ $(TiO_2)_{68}$

Table 18: Relaxation energies of the polyenediphenyl-aniline dye molecules, TiO$_2$ clusters and polyenediphenyl-aniline dye absorbed on brookite TiO$_2$ complex.

System	Relaxed Energy (eV)	Energy$_{slab}$ (TiO$_2$)$_n$ cluster (eV)	Energy$_{(slab + molecule)}$ Dye@(TiO$_2$)$_n$ (eV)
D5	-358.273		
D7	-575.417		
D9	-404.610		
D11	-667.852		
(TiO$_2$)$_5$		-119.985	
(TiO$_2$)$_8$		-198.308	
(TiO$_2$)$_{68}$		-1635.558	
D5@(TiO$_2$)$_5$			-480.127
D7@(TiO$_2$)$_5$			-697.313
D9@(TiO$_2$)$_5$			-526.535
D11@(TiO$_2$)$_5$			789.899
D5@(TiO$_2$)$_8$			-558.182
D7@(TiO$_2$)$_8$			-775.340
D9@(TiO$_2$)$_8$			-604.583
D11@(TiO$_2$)$_8$			-867.970
D5@(TiO$_2$)$_{68}$			-1998.665
D7@(TiO$_2$)$_{68}$			-2215.756
D9@(TiO$_2$)$_{68}$			-2044.859
D11@(TiO$_2$)$_{68}$			-2308.388

6.4. Adsorption energies of polyenediphenyl-aniline dye on TiO_2 brookite clusters

The adsorption energies of D5, D7, D9 and D11 dye adsorbed on $(TiO_2)_5$, $(TiO_2)_8$ and $(TiO_2)_{68}$ are computed using Equation (79) and the results are listed in Table 19.

The adsorption energy denotes the binding ability of the dye molecules [80]. All the results show a positive adsorption value, which suggests stable grafting of the dye molecules unto the surface of TiO_2. The adsorption energies of D5@ $(TiO_2)_5$, D7@ $(TiO_2)_5$, D9@ $(TiO_2)_5$, D11@ $(TiO_2)_5$ are 1.87 eV, 1.91 eV, 1.94 eV and 2.06 eV. The adsorption energies are in the order $D5@(TiO_2)_5 < D7@(TiO_2)_5 < D9@(TiO_2)_5 < D11@(TiO_2)_5$. This implies that D11 dye molecule binds more strongly to the $(TiO_2)_5$ brookite surface than the corresponding dye molecules.

Table 19: Adsorption energies of D5, D7, D9 and D11 dye adsorbed on $(TiO_2)_5$, $(TiO_2)_8$ and $(TiO_2)_{68}$ brookite clusters

Adsorption Energy of Dye@$(TiO_2)_{n=5,8,68}$ (eV)		
Dye@$(TiO_2)_5$	D5@$(TiO_2)_5$	1.869
	D7@$(TiO_2)_5$	1.911
	D9@$(TiO_2)_5$	1.940
	D11@$(TiO_2)_5$	2.062
Dye@$(TiO_2)_8$	D5@$(TiO_2)_8$	1.601
	D7@$(TiO_2)_8$	1.615
	D9@$(TiO_2)_8$	1.665
	D11@$(TiO_2)_8$	1.810
Dye@$(TiO_2)_{68}$	D5@$(TiO_2)_{68}$	4.838
	D7@$(TiO_2)_{68}$	4.781
	D9@$(TiO_2)_{68}$	4.661
	D11@$(TiO_2)_{68}$	4.928

The adsorption energies of D5@ $(TiO_2)_8$, D7@ $(TiO_2)_8$, D9@ $(TiO_2)_8$, D11@ $(TiO_2)_8$ are 1.60 eV, 1.62 eV, 1.67 eV and 1.81 eV. The adsorption energies are in the order $D5@(TiO_2)_8 < D7@(TiO_2)_8 < D9@(TiO_2)_8 < D11@(TiO_2)_8$. This implies that D11 dye molecule reacts more

strongly to the $(TiO_2)_8$ brookite cluster than the corresponding dye molecules. The adsorption energies of D5@ $(TiO_2)_{68}$, D7@ $(TiO_2)_{68}$, D9@ $(TiO_2)_{68}$, D11@ $(TiO_2)_{68}$ are 4.84 eV, 4.78 eV, 4.66 eV and 4.92 eV. The adsorption energies are in the order D11@ $(TiO_2)_{68} >$ D5@ $(TiO_2)_{68} >$ D7@ $(TiO_2)_{68} >$ D9@ $(TiO_2)_{68}$. This implies that D11 dye molecule reacts more strongly to the $(TiO_2)_{68}$ brookite surface than the corresponding dye molecules. The discrepancies between the values obtained for the adsorption energies of all the four dye molecules on the various surfaces of brookite suggest that the size of the clusters has an effect on the binding ability of the molecules. The molecules react differently with the different surface of TiO_2 based on the size of the nanocluster. The overall results of the adsorption energies of all the dye molecules and their TiO_2 nanocluster complexes indicate that the polyenediphenyl-aniline dye molecules bind strongly to the surface of TiO_2. The stable grafting of the dye molecules unto TiO_2 semiconductor enhances stability of DSSCs.

6.4.1 Absorption spectra of polyene-diphenylaniline dye molecules adsorbed on TiO_2 brookite clusters

The absorption spectra of the D5, D7, D9 and D11 polyenediphenyl-aniline dye on $(TiO_2)_5$ and $(TiO_2)_8$ are presented in Figures 56 and 57 respectively. The absorption spectra depict the excited state properties of the dye absorbed on TiO_2 clusters. The polyenediphenyl-aniline dye molecules were absorbed on the clusters by carboxylic acid moiety through bidentate bridging adsorption mode where each of the two oxygen atoms bind to a coordinated titanium atom on the surface of the cluster. The hydrogen atom was transferred into a nearby oxygen atom to achieve stability of the system for TD-DFT calculations. The structures were relaxed using GPAW and PBE functional. The relaxed structure was then used for TD-DFT study of the excited state properties of the dye. Both spectra show absorption in the UV, visible and near infra-red region of solar spectrum due to excitation.

The UV/Vis spectra of $(TiO_2)_5$ brookite cluster computed using the same theory GPAW/TD-DFT were presented previously in Figure 48. In that case the spectra only showed absorption peaks in the UV region at 200 nm and 400 nm. Upon absorption of the dye on $(TiO_2)_5$ brookite cluster and the absorption peaks were shifted to higher wavelength upon excitation. In this case the absorption maximum of D5@$(TiO_2)_5$ is located at 800 nm in the near infra-red region, absorption maximum of D7@$(TiO_2)_5$ is situated at 600 nm in the visible region, absorption maximum of D9@$(TiO_2)_5$ situated at 900 nm in the near infra-red region and absorption

University of Venda

maximum of D11@(TiO$_2$)$_5$ occurs at 1050 nm in the visible region. D5@ (TiO$_2$)$_5$ shows the highest absorption peak and the highest absorption maximum situated in the near infra-red region.

The UV/Vis spectra of (TiO$_2$)$_8$ brookite cluster computed using the GPAW/TD-DFT was presented in Figure 49. The spectra only shows absorption in the UV region around 200 nm to 400 nm and the absorption of the dye on (TiO$_2$)$_8$ brookite cluster shifts the absorption peaks to higher wavelength upon excitation. In this case, the absorption maximum of D5@(TiO$_2$)$_8$ is situated at 750 nm in the near infra-red region, absorption maximum of D7@(TiO$_2$)$_8$ at 850 nm in the near infra-red region, absorption maximum of D9@(TiO$_2$)$_8$ at 850 nm in the near infra-red region and absorption maximum of D11@(TiO$_2$)$_8$ at 900 nm in the visible region. D11@ (TiO$_2$)$_8$ shows the highest absorption peak and absorption maximum, which is situated in the near infra-red region. The results generally suggest that the absorption of dye molecules on TiO$_2$ brookite cluster improve its spectra responsivity to the UV region. Thus, the complex can absorb in the whole spectra range, including the UV visible and near infra–red region. The shifting of the absorption maxima to higher wavelength improves absorption and enhances excitation over a wide spectra range of the solar spectrum which suggests higher photocurrents densities in DSSCs
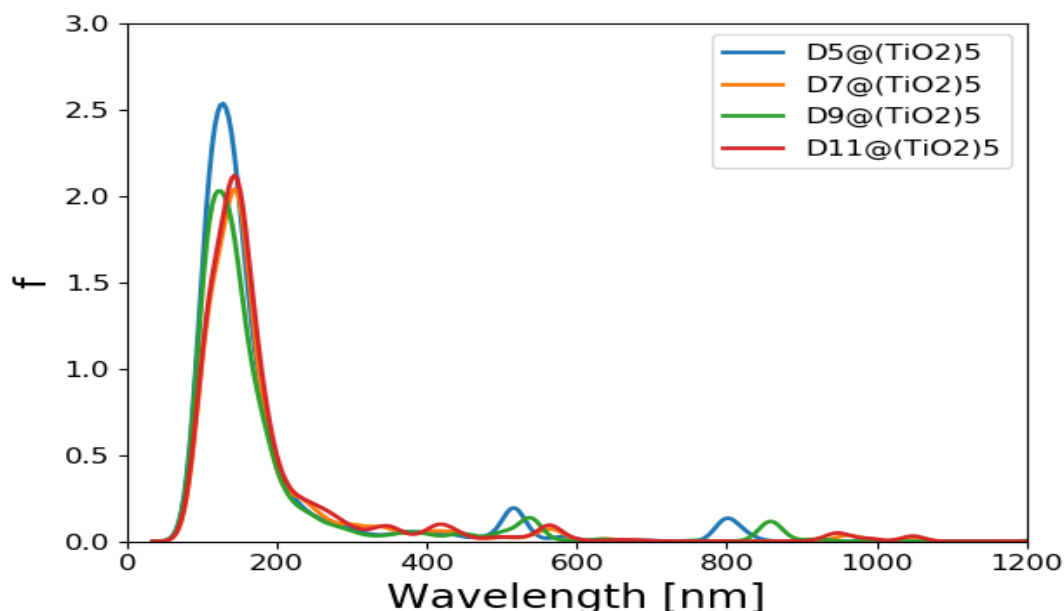

Figure 56: UV/Vis spectra of dye-TiO$_2$ complex
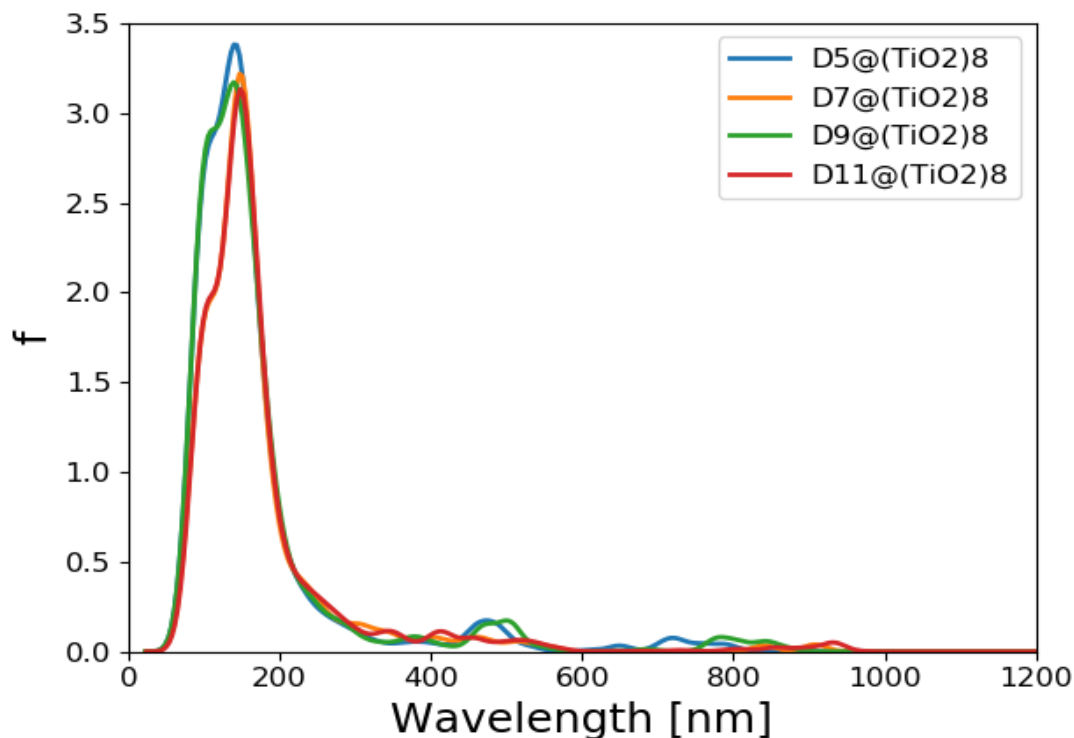
Figure 57: UV/Vis spectra of dye-TiO$_2$ complex

6.4.2 Isodensity surfaces of polyene-diphenylaniline dye molecules adsorbed on TiO$_2$ brookite cluster

The isodensity surfaces of the molecular orbitals involved in excitation were created from cube files created with GPAW and were visualized with Avogadro. The isodensity surfaces of the different molecular orbital involved in photoexcitation of the four polyenediphenyl-aniline dye@ (TiO$_2$)$_5$, (TiO$_2$)$_8$ and (TiO$_2$)$_{68}$ brookite clusters are presented in Figures 58(a-h), 59(a-h) and 60(a-h) respectively. All the results show that the HOMO is delocalized on the dye molecule and it is mainly situated on the donor moiety where the unoccupied electronic states are situated while the LUMO is delocalized entirely over the TiO$_2$ clusters where the unoccupied electronic state are located. The localization of the electron densities of the HOMO on the dye molecules and the electron densities of LUMO on the TiO$_2$ brookite suggest good electronic coupling between the occupied excited state of the dye and the unoccupied acceptor levels of the semiconductor conduction band. The HOMO electronic levels on the dye and the LUMO electronic levels on TiO$_2$ clusters imply efficient separation of charge upon adsorption and electron injection from the dye excited state into the TiO$_2$ semiconductor conduction band.

127
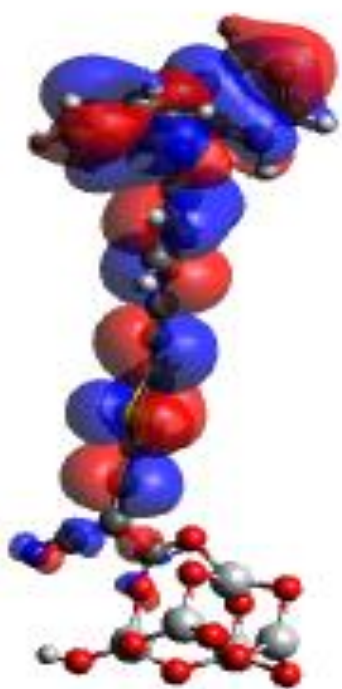
(a)
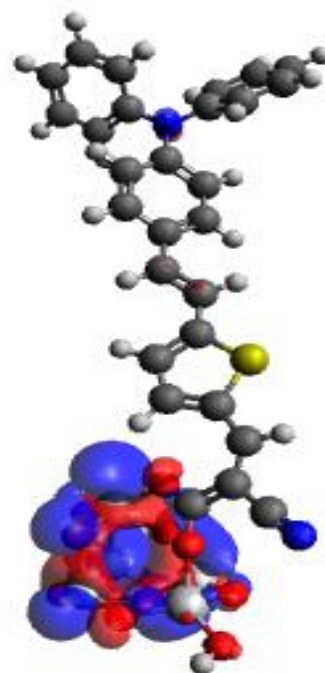
(b)
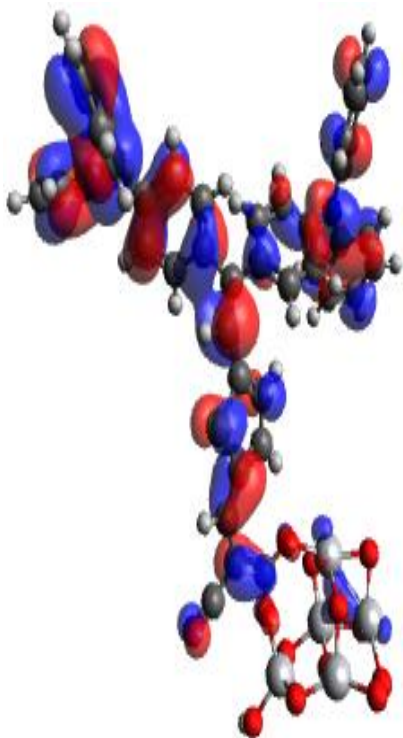
(c)
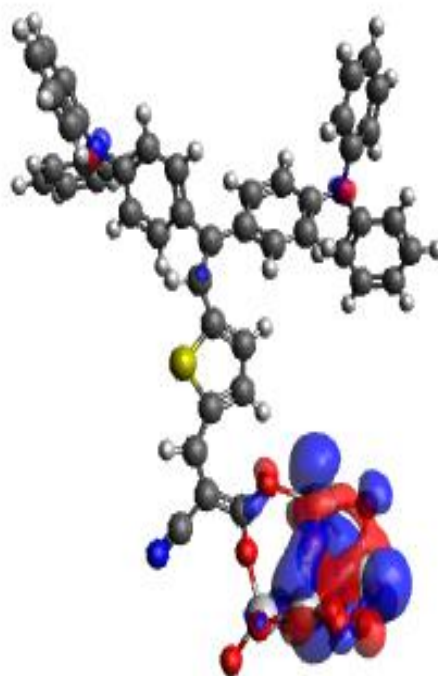
(d)
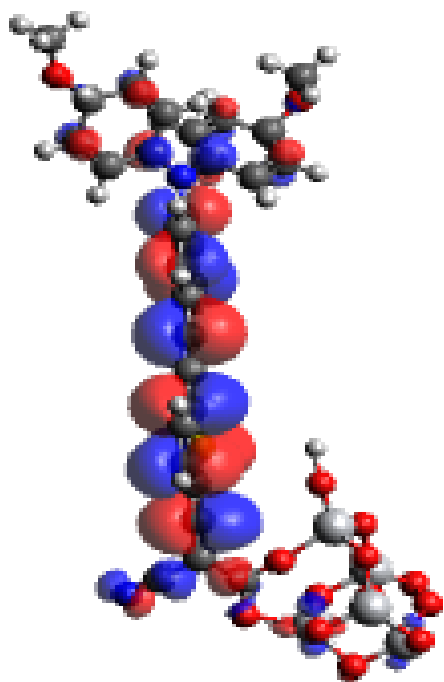
(e)
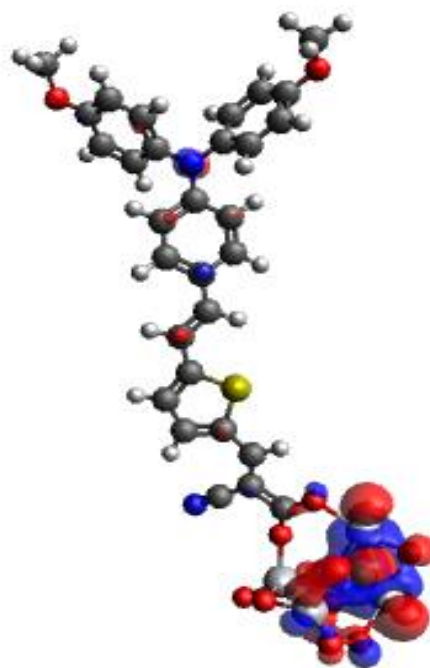
(f)
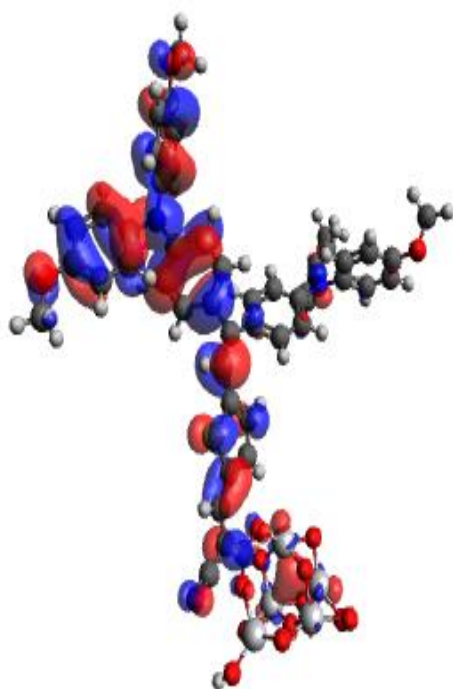
(g)
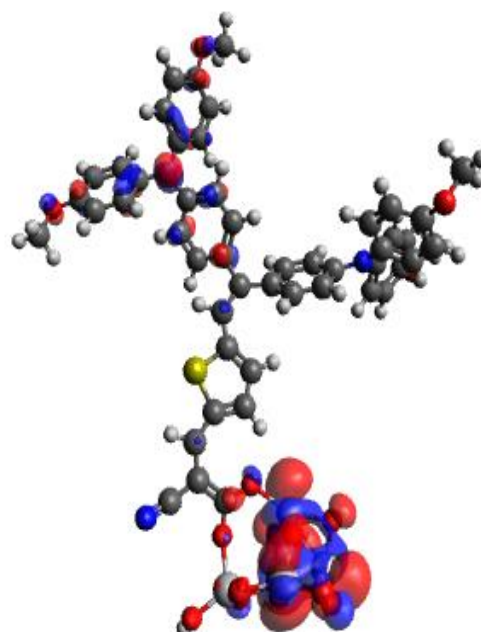
(h)

Figure 58: Isodensity surfaces of molecular orbitals of dye@ $(TiO_2)_5$ complex (a) D5@$(TiO_2)_5$ HOMO (b) D5@$(TiO_2)_5$ LUMO(c) D7@$(TiO_2)_5$ HOMO (d) D7@$(TiO_2)_5$ LUMO (e) D9@$(TiO_2)_5$ HOMO (f) D9@$(TiO_2)_5$ LUMO (g) D11@$(TiO_2)_5$ HOMO (h) D11@$(TiO_2)_5$ LUMO
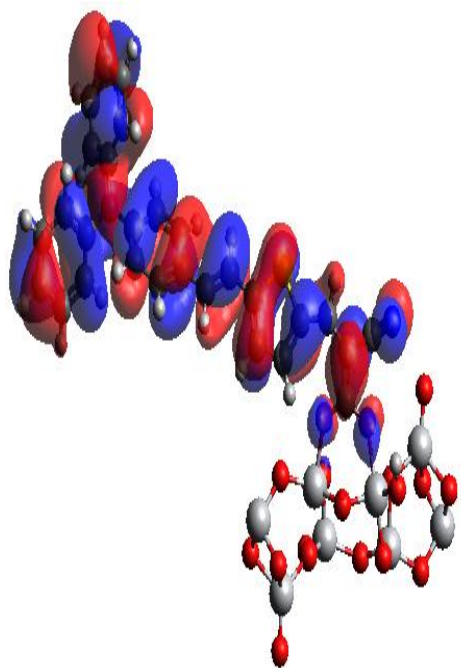
(a)
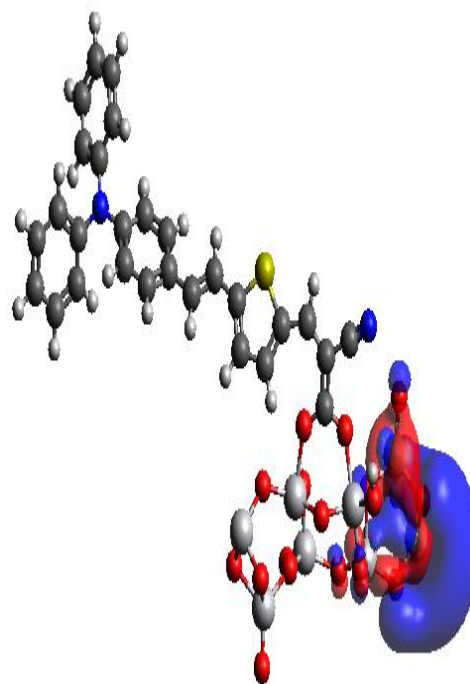
(b)
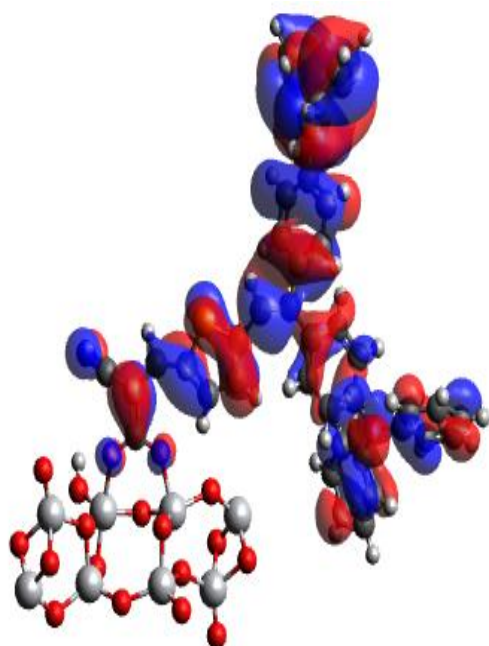
(c)
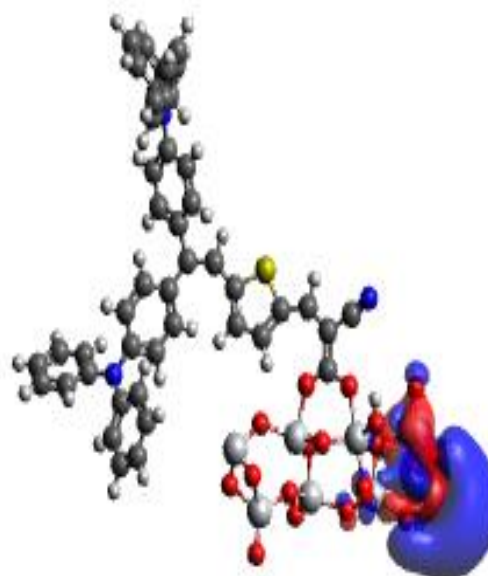
(d)
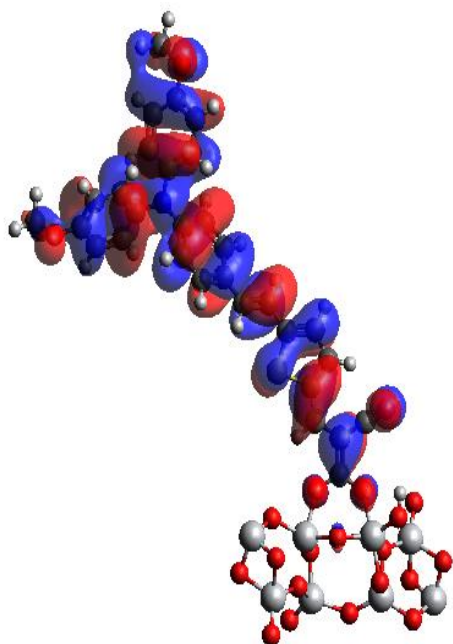
(e)
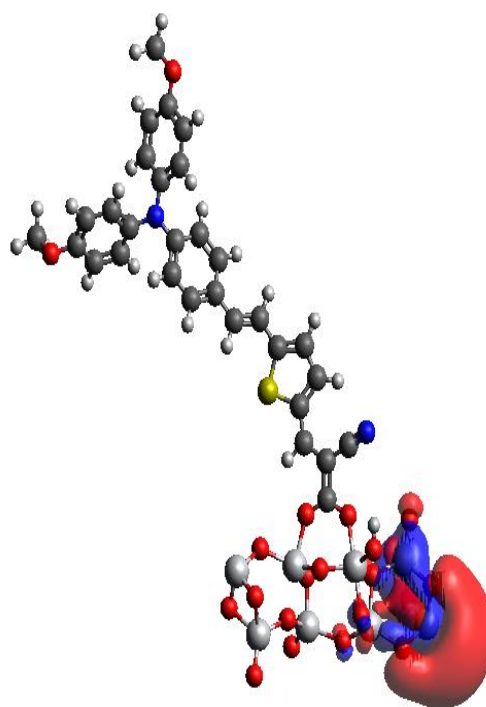
(f)
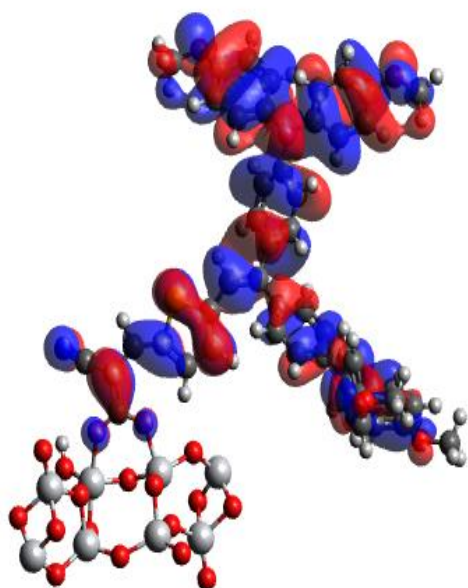
(g)
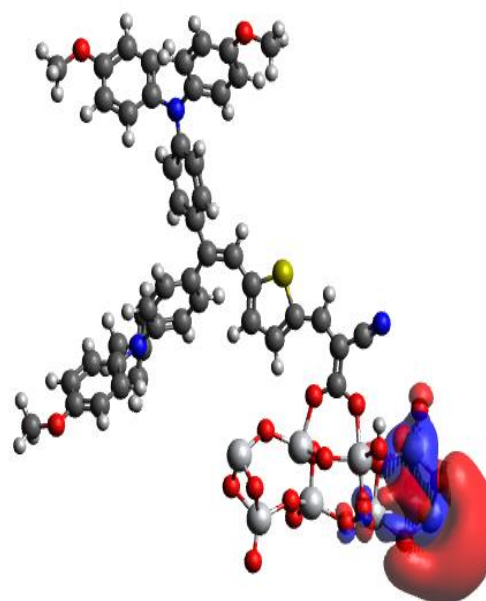
(h)

Figure 59 (): Isodensity surfaces of molecular orbitals of dye@ (TiO$_2$)$_8$ complex (a) D5@ (TiO$_2$)$_8$ HOMO (b) D5@ (TiO$_2$)$_8$ LUMO(c) D7@ (TiO$_2$)$_8$ HOMO (d) D7@ (TiO$_2$)$_8$ LUMO (e) D9@ (TiO$_2$)$_8$ HOMO (f) D9@ (TiO$_2$)$_8$ LUMO (g) D11@ (TiO$_2$)$_8$ HOMO (h) D11@ (TiO$_2$)$_8$ LUMO

(a)

(b)

(c)

(d)

© University of Venda
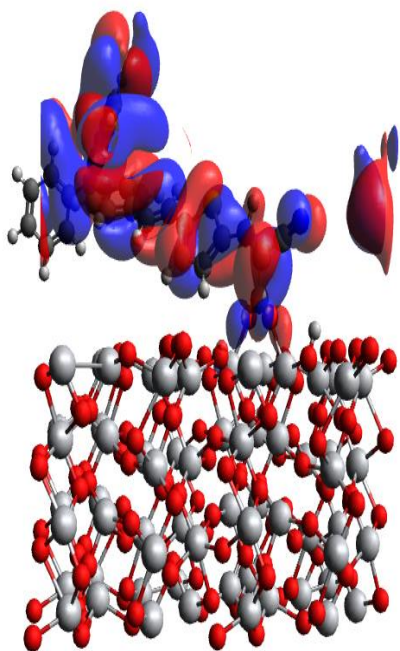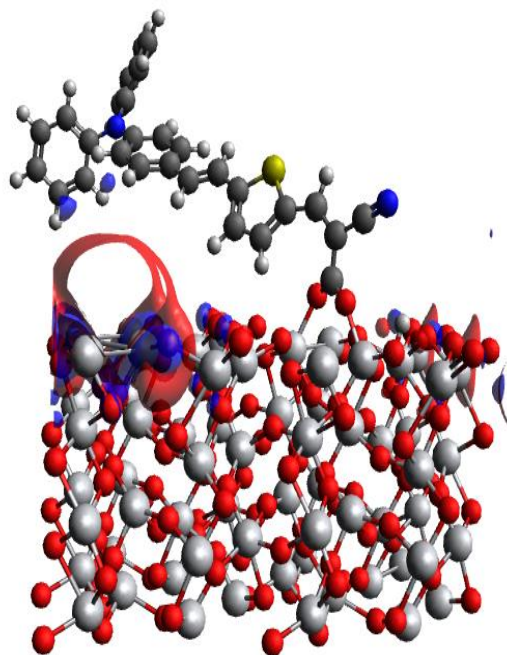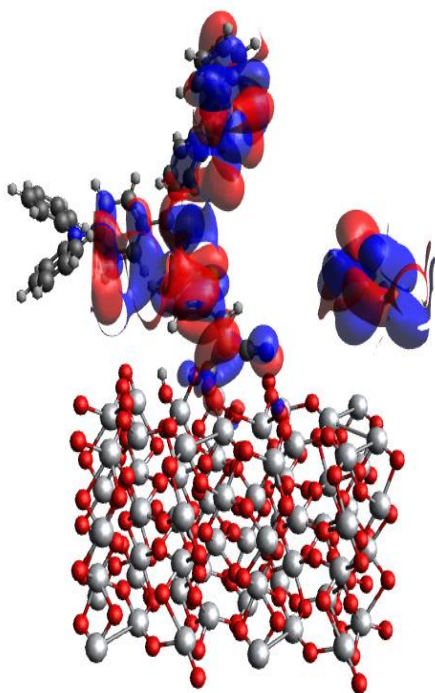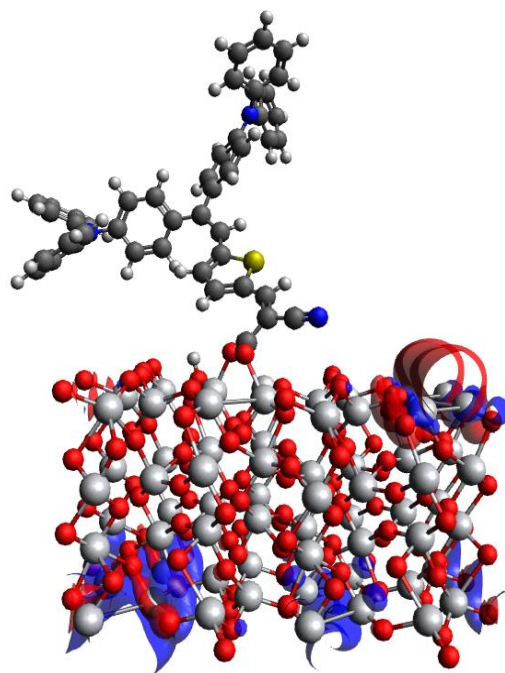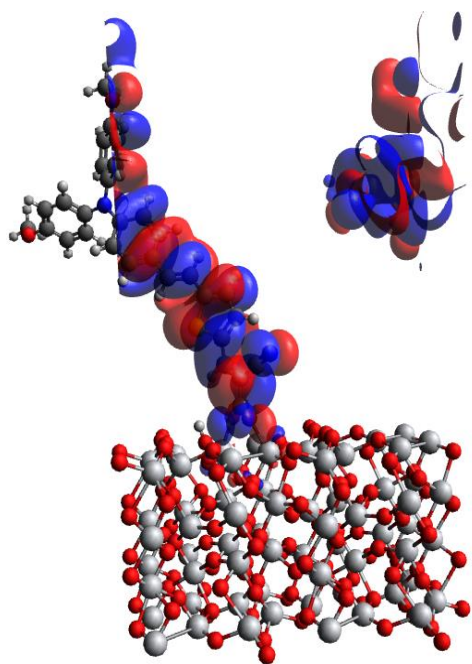
(e)
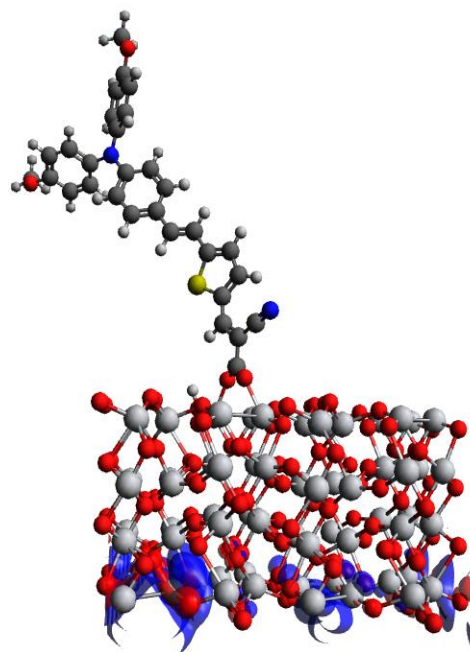
(g)
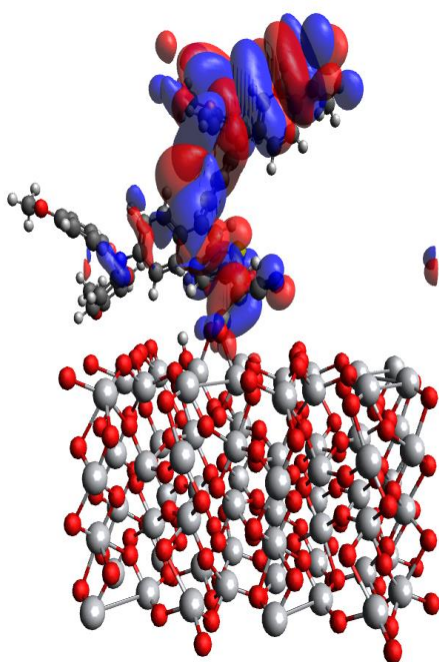
(f)
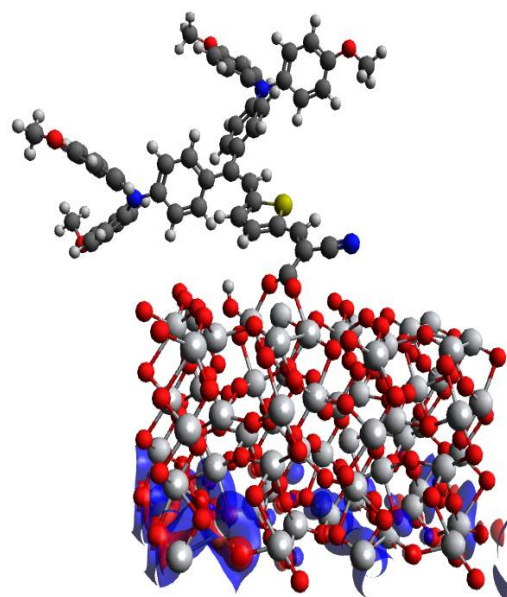
(h)

Figure 60: Isodensity surfaces of molecular orbitals of dye@ $(TiO_2)_{68}$ complex (a) D5@(TiO_2) $_{68}$ HOMO (b) D5@(TiO_2) $_{68}$ LUMO(c) D7@(TiO_2) $_{68}$ HOMO (d) D7@(TiO_2) $_{68}$ LUMO (e) D9@(TiO_2) $_{68}$ HOMO (f) D9@(TiO_2) $_{68}$ LUMO (g) D11@(TiO_2) $_{68}$ HOMO (h) D11@$(TiO_2)_{68}$ LUMO

6.4.3 Free Energy of dye molecules

Free energy of electron injection (ΔG^{inject}) is the driving force of electrons injection from the dye excited state to the semiconductor substrate. It is expressed as the difference between the oxidation potential energy of the dye excited state and the reduction potential energy of TiO$_2$ conduction band [95]. The reduction potential energy of TiO$_2$ conduction band is $E_{cB} = 4.0$ eV [95, 177, 178]. Calculation of (ΔG^{inject}) is crucial for investigation of electron injection efficiency (ϕ_{inject}) of the dye into the semiconductor. (ΔG^{inject}) is proportional to (ϕ_{inject}), the free energy of electron injection (ΔG^{inject}). Negative ΔG^{inject} indicates spontaneous electron injection from the dye molecule to TiO$_2$ cluster [59].

The ΔG^{inject} and Eox^{dye*} for all the D5, D7, D9 and D11 dye were calculated using Equations (81) and (82) and the results are presented in Table 20. The calculated ΔG^{inject} values for D5, D7, D9 and D11 dye molecules imply that the excited state of all the dye lies above the conduction band of TiO$_2$, which favours electron injection into TiO$_2$. The negative values of ΔG^{inject} for D5, D7, D9 and D11 dye indicate spontaneous injection of electron from the dye into the conduction band of TiO$_2$.

Table 20: Free energy of electron injection (ΔG^{inject}) of D5, D7, D9 and D11 dye molecules

Dye	Eox^{dye} (eV)	ΔE (eV)	Eox^{dye*} (eV)	(ΔG^{inject}) (eV)
D5	4.900	3.090	1.810	-2.820
D7	5.130	3.260	1.870	-2.130
D9	4.460	2.530	1.930	-2.070
D11	4.440	2.470	1.970	-2.030

6.4.4 Electronic Properties of dye molecules absorbed on TiO$_2$ clusters

The total density of states and the projected density of states of D5, D7, D9 and D11 dye molecules absorbed on (TiO$_2$)$_5$, (TiO$_2$)$_8$ and (TiO$_2$)$_{68}$ were computed using GPAW and PBE exchange correction functional in order to further understand their electronic structure. The TDOS and PDOS of dye@ (TiO$_2$)$_5$, dye$_@$ (TiO$_2$)$_8$ and dye@ (TiO$_2$)$_{68}$ are presented in Figures

© University of Venda

61 (a-d), 62 (a-d) and 63 (a-d) respectively. The DOS is comprised of the surface valence and conduction bands separated by a wide band gap. The density of states for the clean $(TiO_2)_5$, $(TiO_2)_8$ and $(TiO_2)_{68}$ clusters before the dye were adsorbed were presented previously in Figures 50-52 respectively. The DOS spectrum for the TiO_2 cluster alone and the DOS spectrum of dye@TiO_2 complex are compared in order to further understand the electronic coupling between the occupied and unoccupied molecular orbitals. Upon the adsorption of the dye molecules on TiO_2 clusters, the dye introduce sharp occupied molecular energy levels in the band gap as seen in Figures 61-63. Comparing the TDOS spectrum of the clean $(TiO_2)_5$, $(TiO_2)_8$ and $(TiO_2)_{68}$ clusters in Figures 50-52 and the TDOS spectrum of the dye absorbed on the clusters in Figures 61-63 (a-d), it is evident that the adsorption of the dye on TiO_2 clusters results in a shift of the conduction band edge of TiO_2 to higher energy levels and consequently narrowing the band gap between the occupied valence states and the unoccupied conduction band. Also upon absorption of the dye molecules on the TiO_2 clusters, the TDOS results reveal that the adsorption of the dye introduces new occupied electronic orbitals between the two states where there was a broad band gap initially and in the conduction band of the TiO_2 clusters.

It is observed that the occupied and unoccupied states are broadened and shifted upon absorption due to coupling of the electronic states between the orbitals of the TiO_2 and the adsorbed dye molecules. Also, the edge of the occupied orbital shifted to higher energy level, the effect of the shifting of the two states results in narrowed band gap between the two states. This suggests the red spectral shift observed in the optical absorption spectrum of the dye@TiO_2 presented in Figures 56 and 57 observed upon the absorption of the dye unto the TiO_2 cluster.

The PDOS spectra of the dye@ $(TiO_2)_5$, dye@ $(TiO_2)_8$ and dye@ $(TiO_2)_{68}$ presented in Figures 61 - 63 respectively, clearly show the contribution of the dye atomic orbitals in the occupied states and unoccupied states. The PDOS results for the clusters alone showed that both the oxygen and titanium atomic orbitals contribute to the valence states, the oxygen $2p$ atomic orbitals contribute mostly to the highest occupied valence band (VB) state, whereas the lowest unoccupied state of the conduction band is mainly dominated by the contributions of titanium $3d$ atomic orbitals.

The valence band is dominated by the *p* atomic orbitals of oxygen with a little contribution from the *p* atomic orbitals of titanium. The key contribution in the conduction band comes from the titanium orbitals, especially the *d* and *p* ones. The PDOS spectra of the dye@ $(TiO_2)_5$, dye@ $(TiO_2)_8$ and dye@ $(TiO_2)_{68}$ presented in Figures 61 (a-d), 62 (a-d) 63 (a-d) show major contributions from the $3d$ orbitals of titanium, $2p$ orbitals of carbon, $2p$ orbitals oxygen, $2p$ orbitals of nitrogen and $3p$ orbitals of sulphur to the valence states. Sulphur and oxygen *p* orbitals show minor contribution in the conduction band. The valence band is dominated by the *p* atomic orbitals of sulphur and oxygen with a little contribution from the *p* atomic orbitals of carbon and nitrogen. The key contributions in the valence states come from the sulphur $3p$ orbitals. The main atomic orbital contributing majorly to the valence state belongs to the dye molecules. This explains the concentration of the electron densities of the highest occupied molecular orbital on the dye molecules as seen in the Figures 58-60.

..
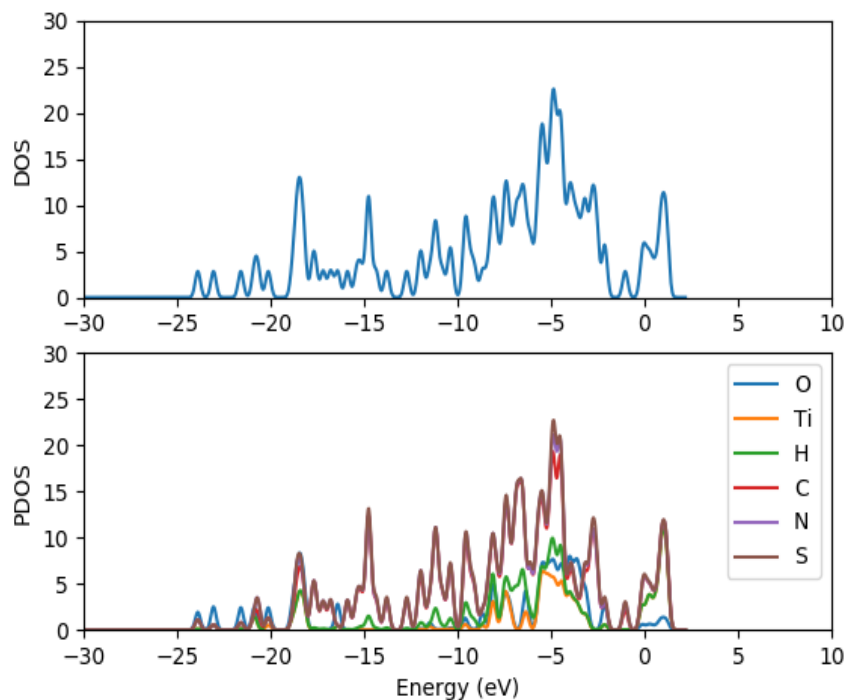
(a) D5@$(TiO_2)_5$ DOS
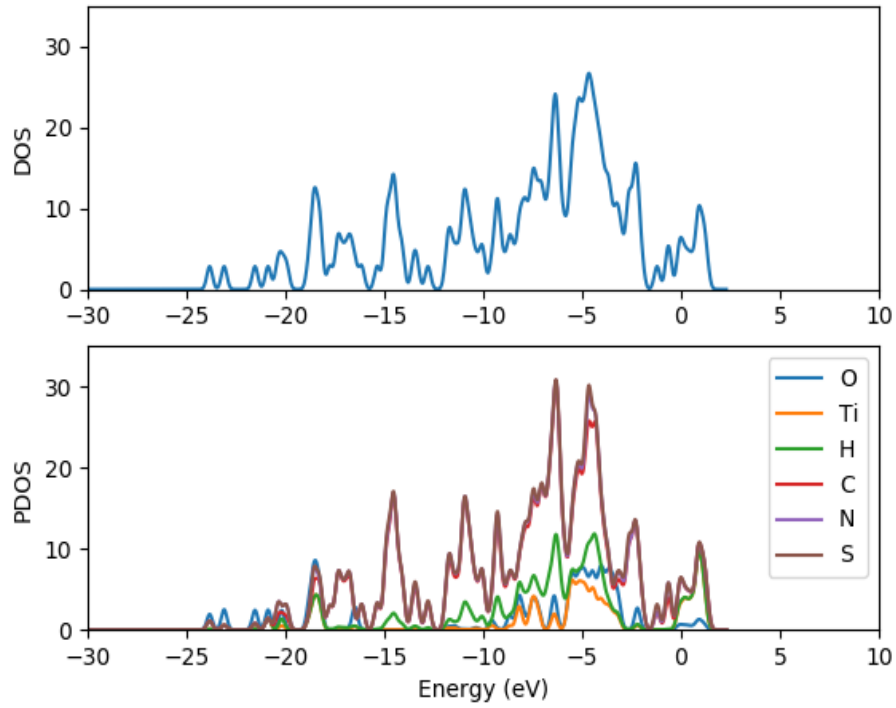
(b) D7@(TiO$_2$)$_5$ DOS

(c) D9@(TiO$_2$)$_5$ DOS

137
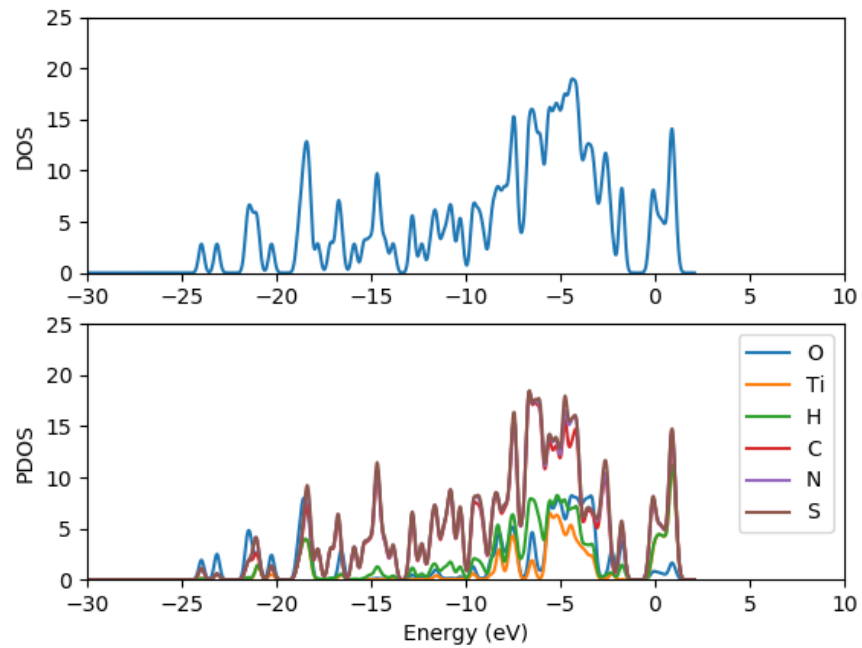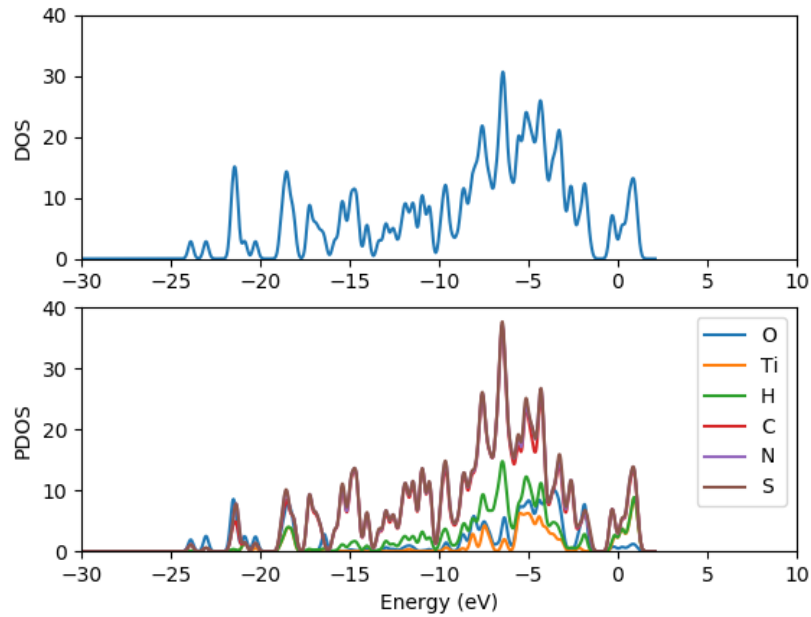
(d) D11@(TiO$_2$)$_5$ DOS

Figure 61 : Density of states and projected density of state spectra of dye absorbed on (TiO$_2$)$_5$ nanocluster (a) D5@(TiO$_2$)$_5$ DOS and PDOS (b) D7@(TiO$_2$)$_5$ DOS and PDOS (c) D9@(TiO$_2$)$_5$ DOS and PDOS (d) D11@(TiO$_2$)$_5$ DOS and PDOS.
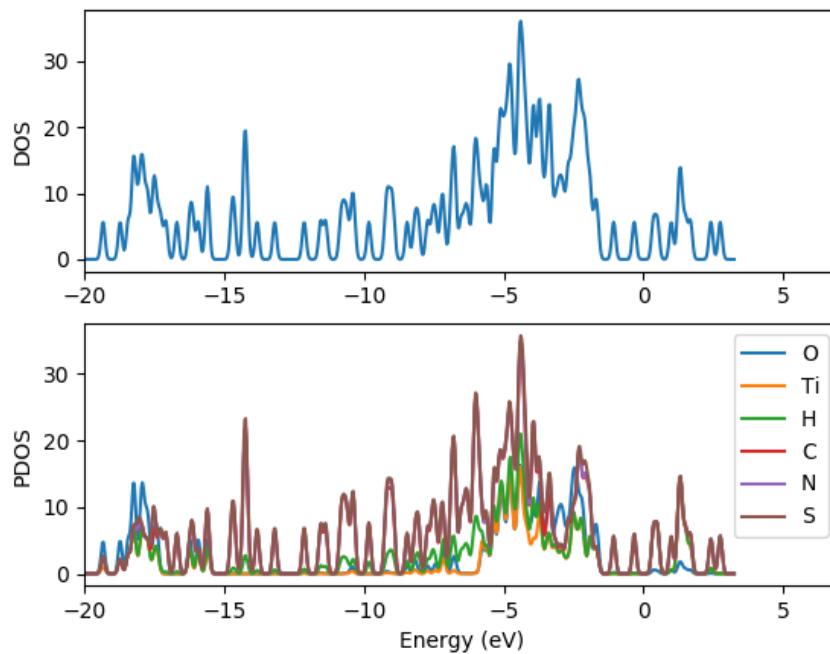
(a) D5@(TiO$_2$)$_8$ DOS
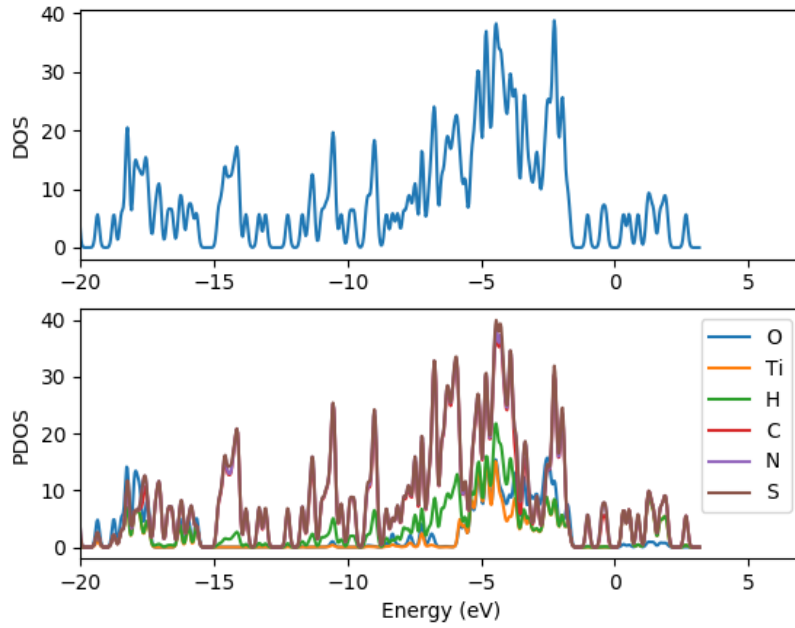
(b) D7@(TiO$_2$)$_8$ DOS

(c) D9@ (TiO$_2$)$_8$ DOS

139
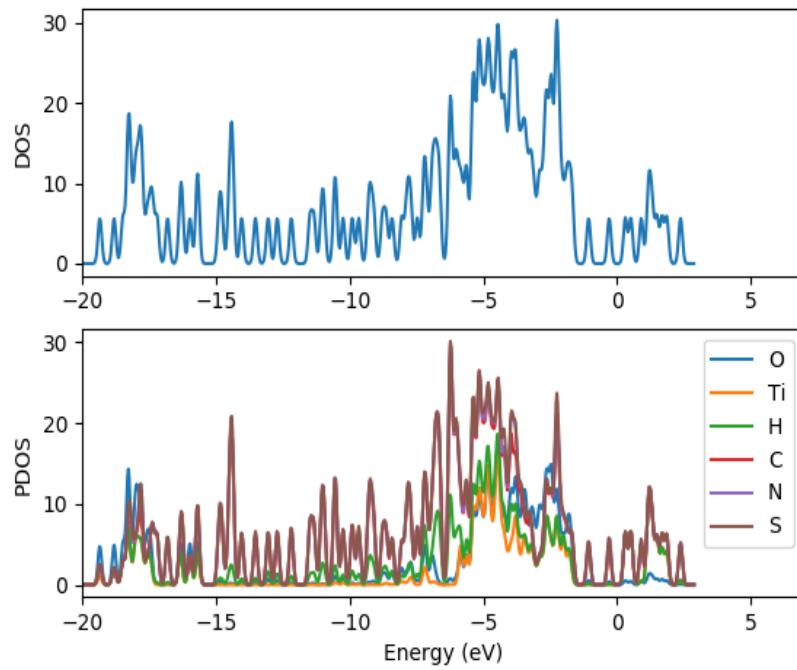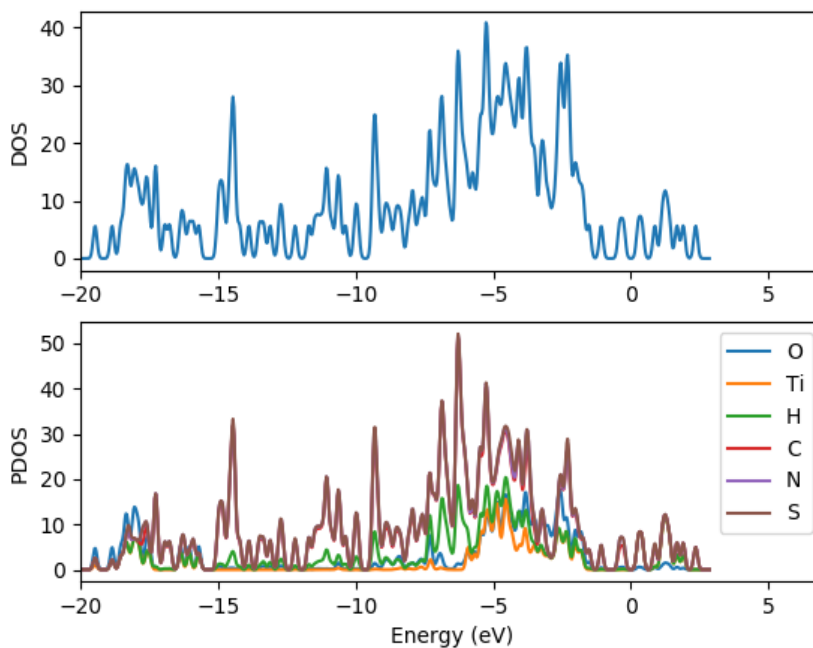
(d)D11@ (TiO₂)₈ DOS

Figure 62: Density of states and projected density of state spectra of dye absorbed on (TiO₂)₈ nanocluster (a) D5@(TiO₂)₈ DOS and PDOS (b) D7@(TiO₂)₈ DOS and PDOS (c) D9@(TiO₂)₈ DOS and PDOS (d) D11@(TiO₂)₈ DOS and PDOS.
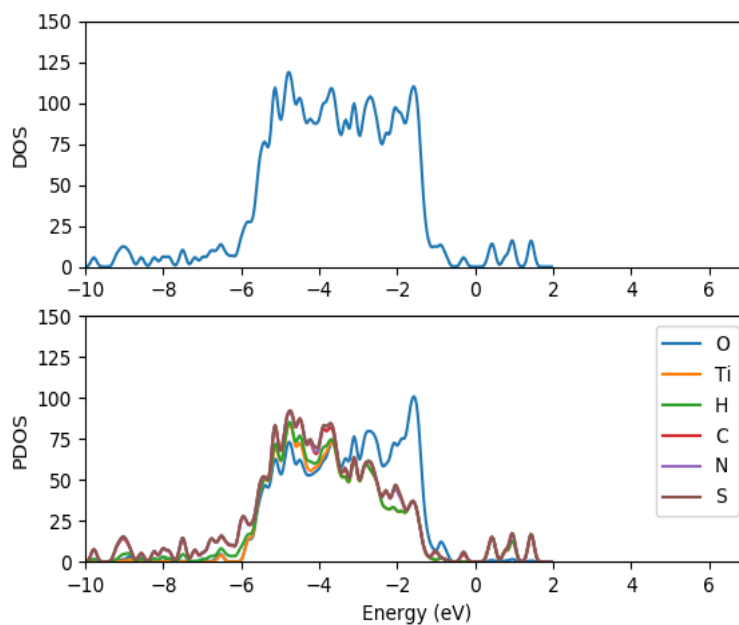
(a) D5@(TiO₂)₆₈ DOS
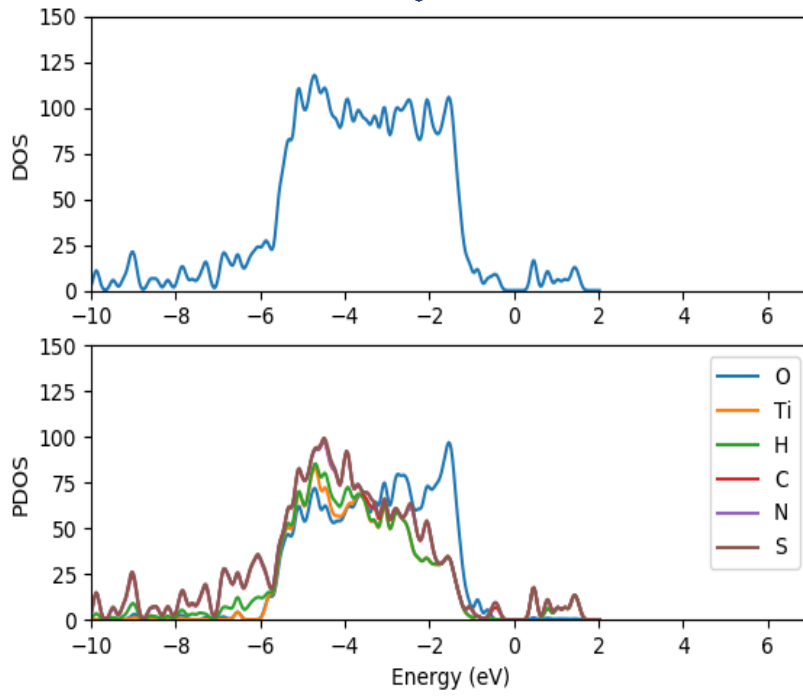
(b) D7@$(TiO_2)_{68}$ DOS
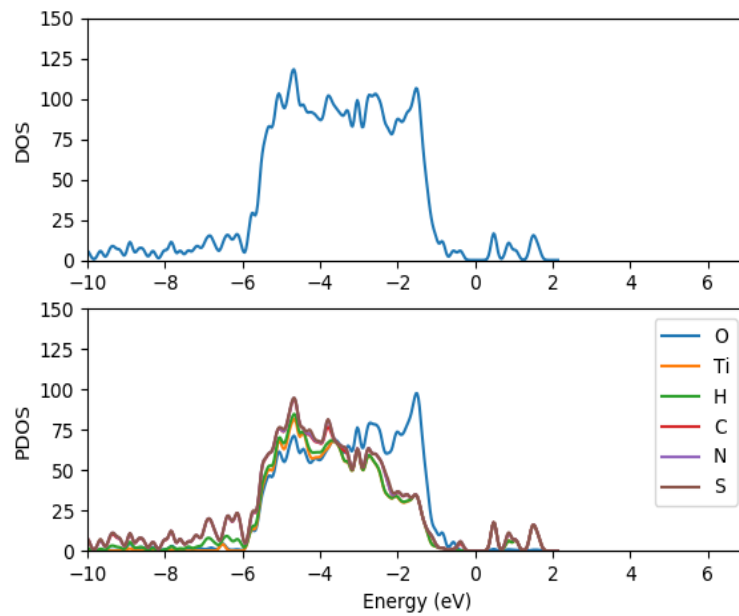
(c) D9@$(TiO_2)_{68}$ DOS
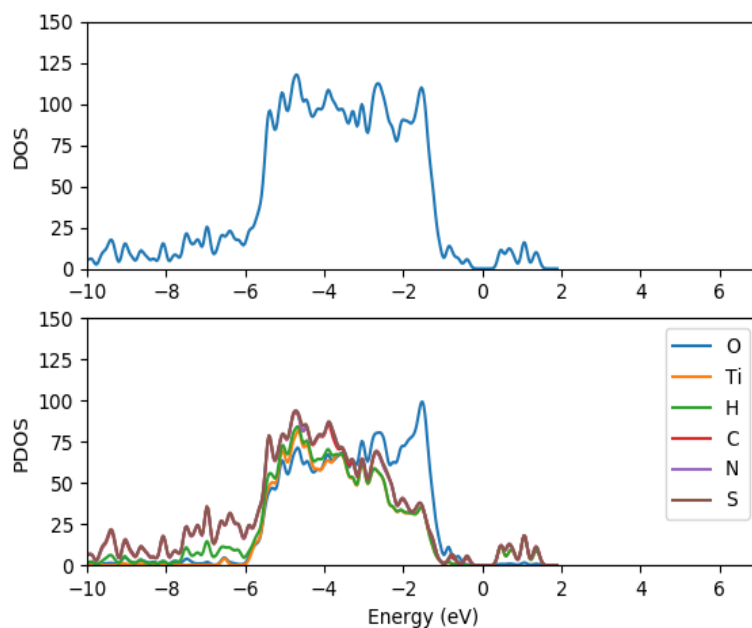
(d) D11@$(TiO_2)_{68}$ DOS

Figure 63: Density of states and projected density of state spectra of dye absorbed on $(TiO_2)_{68}$ nanocluster (a) D5@$(TiO_2)_{68}$ DOS and PDOS (b) D7@$(TiO_2)_{68}$ DOS and PDOS (c) D9@$(TiO_2)_{68}$ DOS and PDOS (d) D11@$(TiO_2)_{68}$ DOS and PDOS.

6.5 Adsorption of croconate dye on $(TiO_2)_n$ n=5, 8, 68 brookite clusters

6.5.1 Introduction

The fascinating features about croconate dye is their good solvatochromic shift, they can absorb photons in the near infrared region [135]. Croconate dye contained short oxyallyl sub group as a backbone, which makes them easily synthesizable thereby producing DSSCs that are flexible and interact strongly with light [79]. Additionally, croconate dye exhibit narrow and intense absorption bands in the near infrared (IR) region of the solar spectrum [79, 80, 10, 179]. The optical properties and electron injection efficiency of two croconate dye coded CR1 and CR2 adsorbed on $(TiO_2)_5$, $(TiO_2)_8$ and $(TiO_2)_{68}$ brookite clusters are investigated in this section. The croconate dye CR1 and CR2 are adsorbed unto the surface of $(TiO_2)_5$, $(TiO_2)_8$ and $(TiO_2)_{68}$ brookite clusters through the diketo group as presented in Figure 64(a-b), Figure 65(a-b) and Figure 66(a-b) respectively. The bidentate bridging (BB) adsorption mode in which each of the oxygen of the keto moiety binds to a three-fold coordinate titanium atom was adopted. All dye@TiO_2 complexes were relaxed upon adsorption. The relaxed structure of the dye molecules adsorbed on $(TiO_2)_5$, $(TiO_2)_8$ and $(TiO_2)_{68}$ clusters are presented in Figures 64-66 respectively. The results on relaxation energies, adsorption energies, excitation spectrum, free

energy of electron injection, TDOS, PDOS and isodensity surfaces of the key molecular orbital involved in excitation are presented and discussed.

<div align="center">(a)   (b)</div>
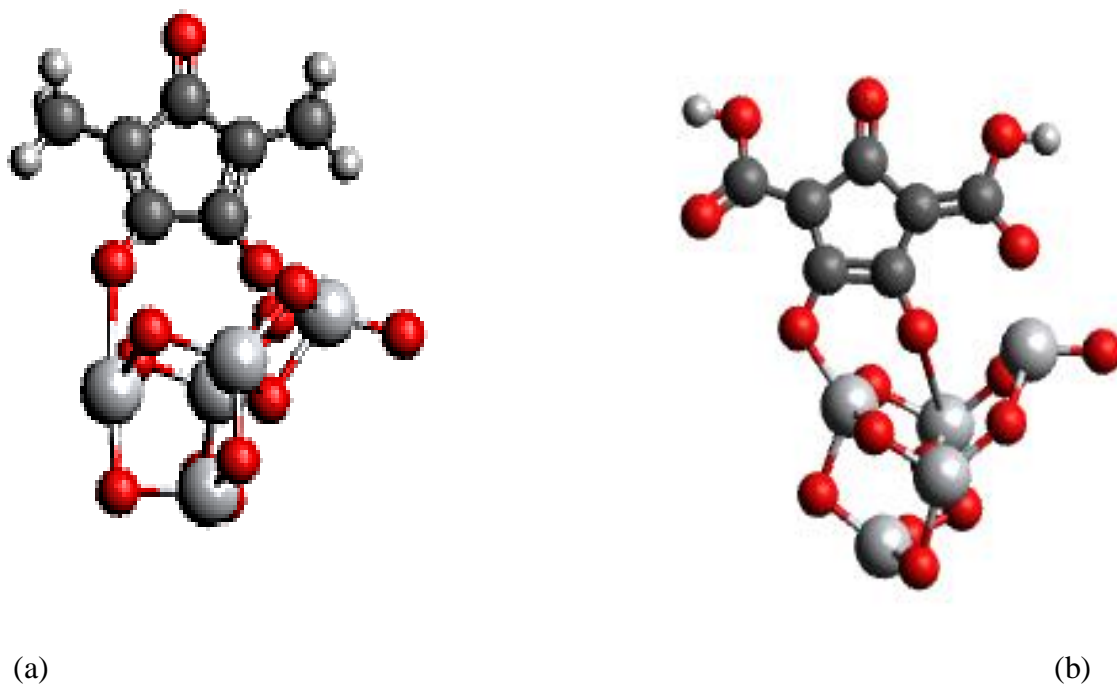
Figure 64: Croconate dye absorbed on $(TiO_2)_5$ nanocluster (a) CR1@ $(TiO_2)_5$ (b) CR2@ $(TiO_2)_5$

<div align="center">(a)   (b)</div>
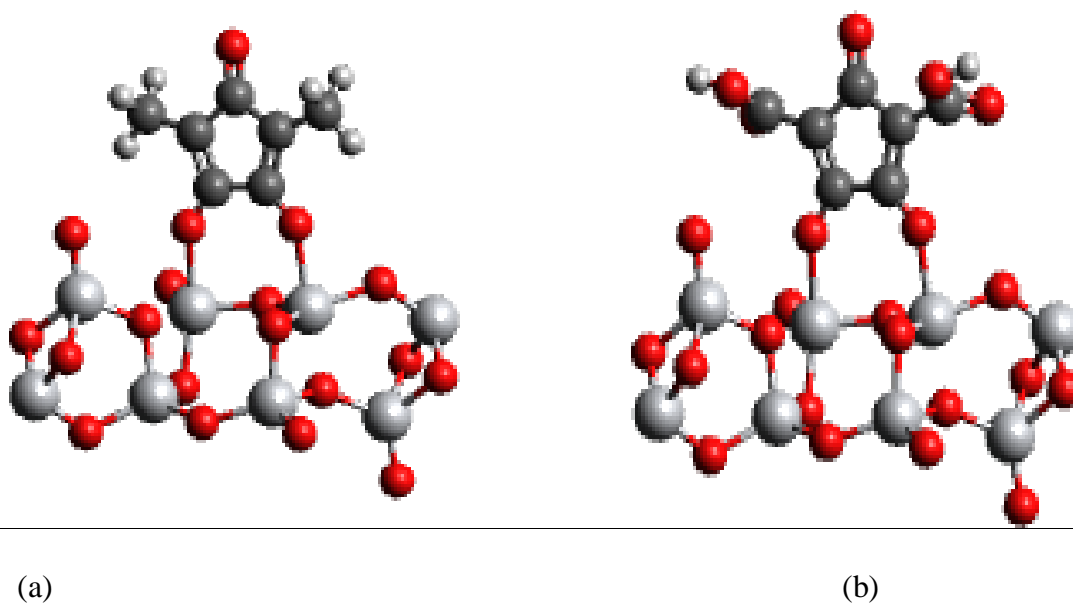
Figure 65: Croconate dye absorbed on $(TiO_2)_8$ nanocluster (a) CR1@ $(TiO_2)_8$ (b) CR2@ $(TiO_2)_8$

(a)   (b)
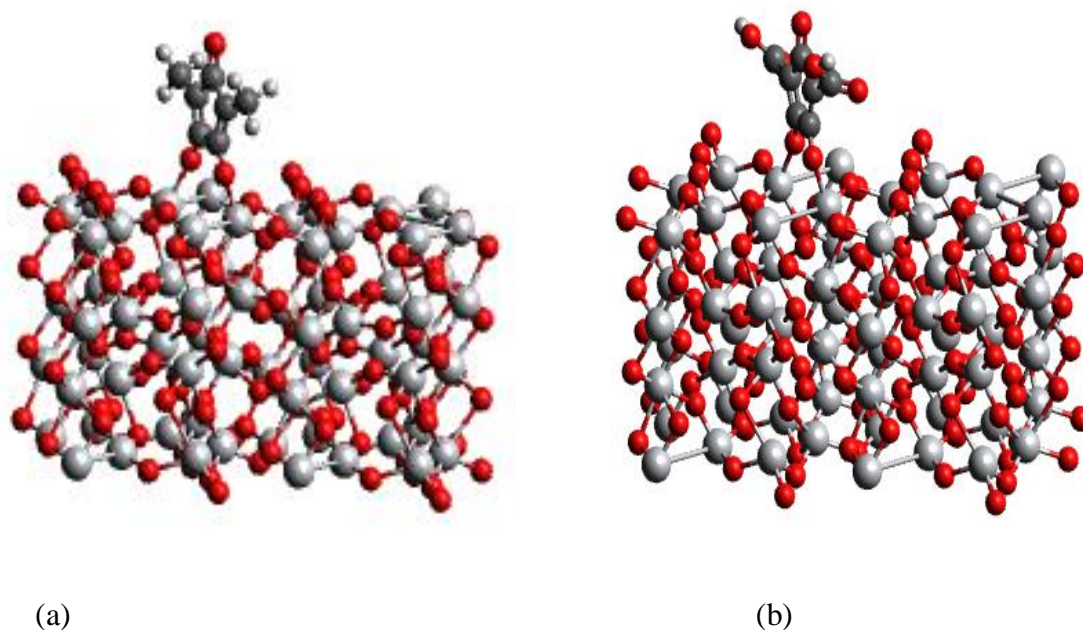
Figure 66: Croconate dye absorbed on $(TiO_2)_{68}$ nanoclusters (a) CR1@ $(TiO_2)_8$ (b) CR2@ $(TiO_2)_{68}$.

6.5.2 Adsorption energy of croconate dye adsorbed on $(TiO_2)_n$ n=5, 8, 68 brookite complex

The relaxation energies of the CR1 and CR2 dye molecules, $(TiO_2)_5$, $(TiO_2)_8$, $(TiO_2)_{68}$ brookite clusters and the croconate dye@TiO_2 complex were computed and are presented in Table 21. The relaxation energies of the CR1 and CR2 dye molecules are -104.31 eV and -117.36 eV respectively. The energy of the clusters are -119.98 eV, -198.31 eV and -1635.55 eV for $(TiO_2)_5$, $(TiO_2)_8$ and $(TiO_2)_{68}$ respectively.

Table 21: Relaxation energies of croconate dye molecules, TiO_2 clusters and dye@TiO_2 complex

System	Relaxed Energy (eV)	Energy$_{slab}$ $(TiO_2)_n$ cluster (eV)	Energy$_{(slab +molecule)}$ Dye@$(TiO_2)_n$ (eV)
CR1	-104.306		
CR2	-117.363		
$(TiO_2)_5$		-119.985	
$(TiO_2)_8$		-198.308	
$(TiO_2)_{68}$		-1635.558	
CR1@$(TiO_2)_5$			-228.223
CR2@$(TiO_2)_5$			-242.879
CR1@$(TiO_2)_8$			-303.365
CR2@$(TiO_2)_8$			-316.353
CR1@$(TiO_2)_{68}$			-1744.607
CR2@$(TiO_2)_{68}$			-1757.868

The computed adsorption energies are presented in Table 22. The adsorption energy of CR1@$(TiO_2)_5$ is 3.93 eV, CR2 @$(TiO_2)_5$ is 5.53 eV, CR1@$(TiO_2)_8$ is 0.75 eV, CR2 @$(TiO_2)_8$ is 0.68 eV, CR1 @$(TiO_2)_{68}$ is 4.74 eV, CR2 @$(TiO_2)_{68}$ is 4.95 eV. The positive adsorption energies denote the binding ability of the dye molecules to the surface of TiO_2 nanocluster [80]. The results show that the dye with the electron donating methyl (CR1) binds more strongly to the surface of $(TiO_2)_8$ brookite cluster than the one with the electron withdrawing moiety (CR2). But the dye with the electron withdrawing moiety (CR2) binds more strongly to $(TiO_2)_5$ and $(TiO_2)_{68}$ brookite cluster than the dye with the electron donating methyl (CR1). The results suggest that the dye molecules react differently with different surfaces and sizes of TiO_2 brookite clusters.

Table 22: Adsorption energies of croconate dye molecules absorbed on TiO_2 complex

Adsorption Energy of Dye@$(TiO_2)_{n=5,8,68}$ (eV)		
Dye@$(TiO_2)_5$	CR1@$(TiO_2)_5$	3.932
	CR2@$(TiO_2)_5$	5.531
Dye@$(TiO_2)_8$	CR1@$(TiO_2)_8$	0.751
	CR2@$(TiO_2)_8$	0.682
Dye@$(TiO_2)_{68}$	D5@$(TiO_2)_{68}$	4.743
	D7@$(TiO_2)_{68}$	4.947

6.5.3 Absorption spectrum of CR1 and CR2 dye absorbed on $(TiO_2)_n$ n=5, 8 brookite cluster

The optical spectra of CR1 and CR2 dye absorbed on the $(TiO_2)_5$ are presented in Figure 67. The spectrum in Figure 67 is compared with the optical spectrum of $(TiO_2)_5$ cluster alone presented in Figure 48. Evidently the absorption maxima of the dye have been shifted to higher wavelength. The absorption maxima of cluster which was located around 200 nm has now been shifted to higher wavelength. The optical spectra of CR1 and CR2 dye absorbed on the $(TiO_2)_8$ are presented in Figure 68. Compared with the spectrum for the optical spectra of $(TiO_2)_8$ cluster alone presented in Figure 49, it is evident that the absorption maxima of the dye have shifted to higher wavelength. The absorption maxima of cluster which was situated around 200 nm have now been shifted to higher wavelength around 600 nm. In both cases the CR1 and CR2 dye show a bathochromic shift upon adsorption of the dye on TiO_2 cluster. The bathochromic shift observed after absorption of CR1 and CR2 dye molecules on TiO_2 brookite cluster suggests good optical properties of the dye molecules and corroborates with reports

University of Venda

from literature that the absorption of dye molecules on TiO$_2$ improves its optical response and helps overcome its limited spectral sensitivity in the UV region, thereby improving its photocatalytic properties and overall DSSCs device efficiencies [71, 180].
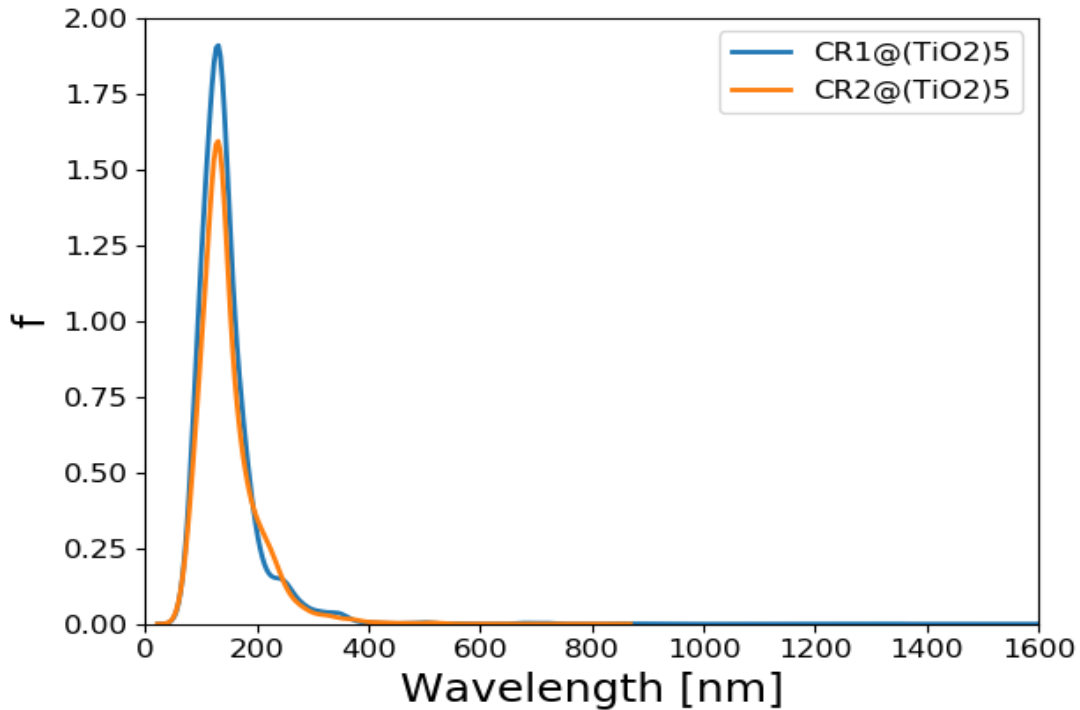
Figure 67: Simulated UV-Vis spectrum of CR1 and CR2 absorbed on (TiO$_2$)$_5$ brookite cluster.
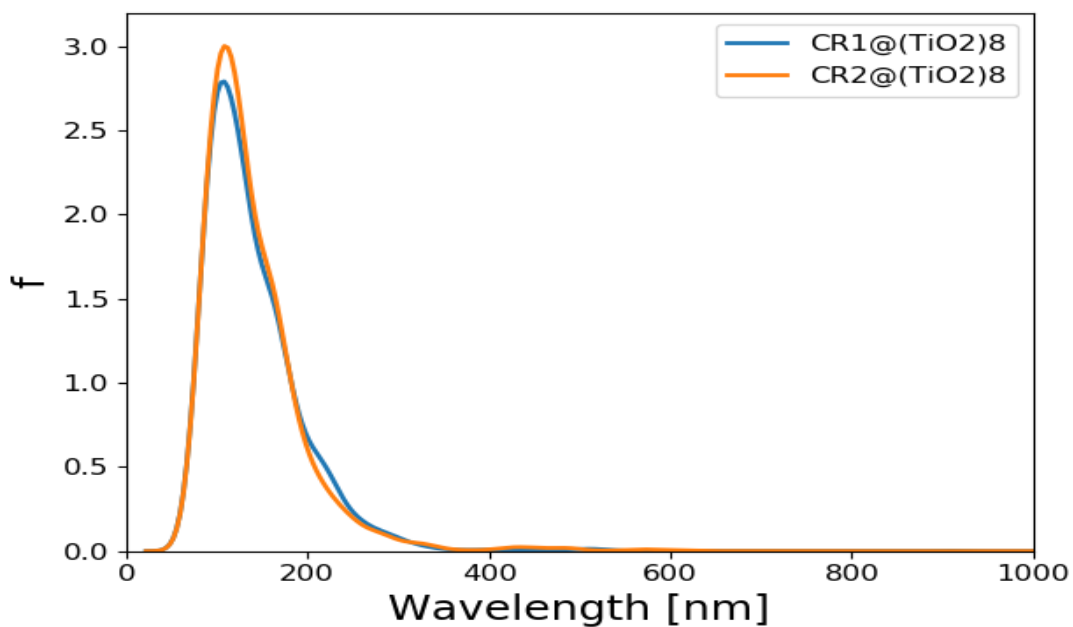
Figure 68: Simulated UV-Vis spectrum of CR1 and CR2 absorbed on (TiO$_2$)$_8$ brookite cluster.

6.5.4 Isodensity surfaces of the croconate dye absorbed on $(TiO_2)_n$ n=5, 8.68 brookite cluster

The isodensity surfaces of the molecular orbital involved in photoexcitation of the CR1 and CR2 dye molecules absorbed on $(TiO_2)_5$, $(TiO_2)_8$ and $(TiO_2)_{68}$ brookite cluster are presented in Figures 69(a-d), 70(a-d) and 71(a-d) respectively. All the results show that the HOMO is localized on the dye molecule and it is mainly concentrated on the donor moiety where the occupied electronic orbital are located while the LUMO is localized over the TiO_2 clusters where the unoccupied electronic state are situated. These suggest good electronic coupling between the occupied excited state of the dye and the unoccupied acceptor levels of the semiconductor conduction band. The localization of the HOMO electronic level on the dye molecules and the LUMO electronic level on the TiO_2 clusters implies efficient separation of charge upon adsorption and electron injection from the dye excited state into the TiO_2 semiconductor conduction band.
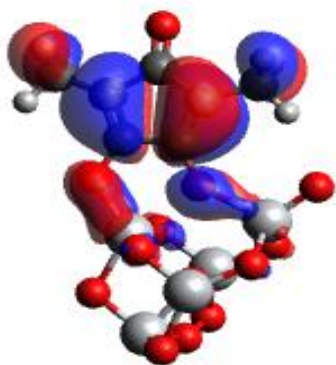
(a)

(b)
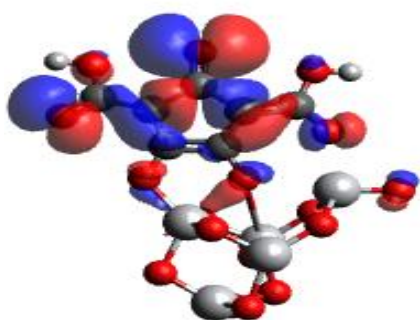
(c)
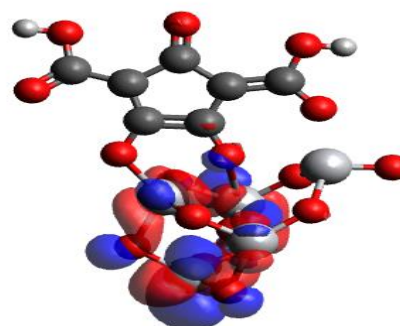
(d)

Figure 69: Isodensity surfaces of the molecular orbitals of (a) HOMO of CR1@ $(TiO_2)_5$ brookite cluster (b) LUMO of CR1@$(TiO_2)_5$ brookite cluster (c) HOMO of CR2@$(TiO_2)_5$ brookite cluster (d) LUMO of CR2@$(TiO_2)_5$ brookite cluster
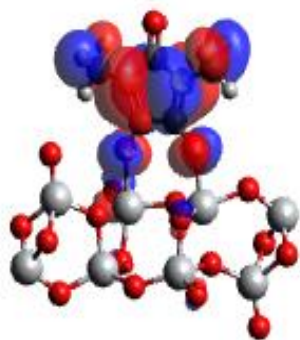
(a)

(b)
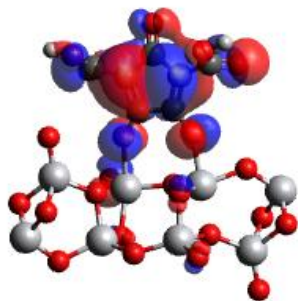
(c)

(d)

Figure 70: Isodensity surfaces of the molecular orbitals of (a) HOMO of CR1@ $(TiO_2)_8$ brookite cluster (b) LUMO of CR1@ $(TiO_2)_8$ brookite cluster (c) HOMO of CR2@ $(TiO_2)_8$ brookite cluster (d) LUMO of CR2@ $(TiO_2)_8$ brookite cluster
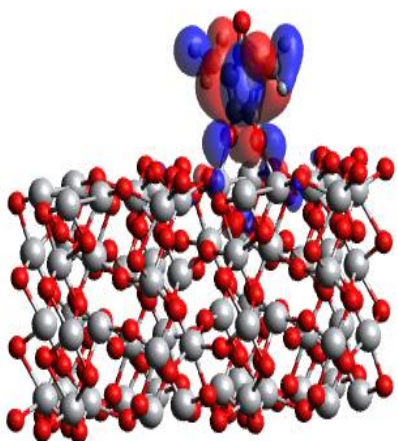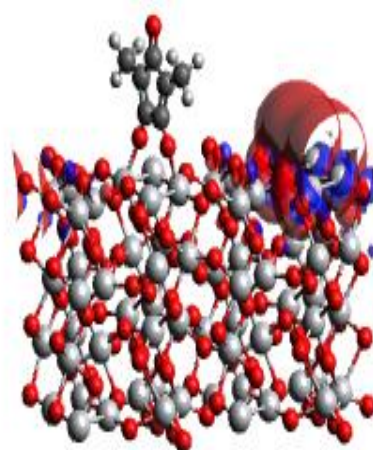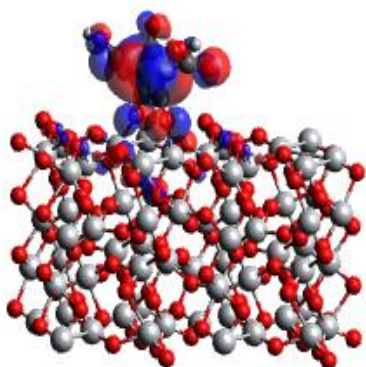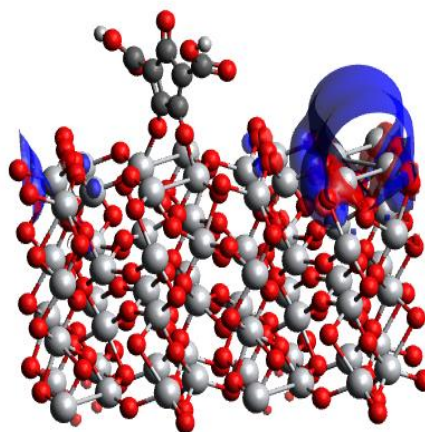
Figure 71: Isodensity surfaces of the molecular orbitals of (a) HOMO of CR1@ (TiO$_2$) $_{68}$ brookite cluster (b) LUMO of CR1@ (TiO$_2$)$_{68}$ brookite cluster (c) HOMO of CR2@ (TiO$_2$) $_{68}$ brookite cluster (b) LUMO of CR2@ (TiO$_2$) $_{68}$ brookite cluster.

6.5.5 Free Energy of Electron Injection (ΔG^{inject}) of CR1 and CR2 dye molecules

We computed the free energy of electron injection (ΔG^{inject}) of CR1 and CR2 dye molecules in order to investigate electron injection kinetics from the dye into the conduction band of TiO_2. The (ΔG^{inject}) was computed using equation (81) and the results are shown in Table 23.

Table 23: Free energy of electron injection (ΔG^{inject}) of CR1 and CR2 dye molecules

Dye	Eox^{dye} (eV)	ΔE (eV)	Eox^{dye*} (eV)	(ΔG^{inject}) (eV)
CR1	7.490	2.250	5.240	1.240
CR2	8.080	1.820	6.250	2.250

The calculated ΔG^{inject} values for CR1 and CR2 dye molecules imply that dye excited state all lies above the conduction band of TiO_2, which favours electron injection into TiO_2. The computed values of ΔG^{inject} for CR1 and CR2 dye are positive, suggesting that the injection of electron from the dye into the conduction band of TiO_2 is not spontaneous.

6.5.6 Electronic properties of CR1 and CR2 dye molecules absorbed on TiO_2 clusters

In order to further understand the electronic structure of CR1 and CR2 dye molecules absorbed on TiO_2 clusters, the density of states and the projected density of states of CR1 and CR2 dye molecules absorbed on $(TiO_2)_5$, $(TiO_2)_8$ and $(TiO_2)_{68}$ were computed using GPAW and PBE exchange correction functional. The DOS and PDOS spectra are presented Figure 72 (a-b), 73 (a-b) and 74 (a-b) for dye@ $(TiO_2)_5$, dye@ $(TiO_2)_8$ and dye@ $(TiO_2)_{68}$ respectively. The DOS is composed of the surface valence and conduction bands separated by a wide band gap. The densities of states for the clean $(TiO_2)_5$, $(TiO_2)_8$ and $(TiO_2)_{68}$ clusters before the dye were adsorbed were presented previously in Figure 51-53 respectively. When comparing the DOS spectrum for the TiO_2 cluster alone and the DOS spectrum of croconate dye absorbed on TiO_2 clusters, it is observed that new occupied molecular orbitals are introduced to the band gap of the TiO_2 clusters upon the absorption of the dye molecules as seen in Figures 72-74. Comparing between the DOS spectra of all the clean $(TiO_2)_5$, $(TiO_2)_8$ and $(TiO_2)_{68}$ clusters and the DOS spectra of the dye absorbed on the clusters, it is clear that the adsorption of the dye on TiO_2 clusters results in a shift of the conduction band edge of TiO_2 to higher energy levels,

and consequently narrowing of the band gap between the occupied valence states and the unoccupied conduction band. Also upon absorption of the dye molecules on the TiO_2 clusters, the DOS results reveal that the adsorption of the dye introduces new occupied electronic orbitals between the two states where there was a broad band gap initially and in the conduction band of the TiO_2 clusters.

The PDOS spectra of the dye@ $(TiO_2)_5$, dye@ $(TiO_2)_8$ and dye@ $(TiO_2)_{68}$ presented in Figures 72-74 respectively, show the contribution of the atomic orbitals in the occupied states and unoccupied states. The PDOS results for the clusters alone show that both the oxygen and titanium atomic orbitals contribute to the valence states, the oxygen $2p$ atomic orbitals contribute mostly to the highest occupied valence band state, whereas the lowest unoccupied state of the conduction band is mainly dominated by the contributions of titanium $3d$ atomic orbitals. The valence band is dominated by the p atomic orbitals of oxygen with a little contribution from the p atomic orbitals of titanium. The major contribution in the conduction band comes from the titanium orbitals, especially the d and p orbitals. The PDOS spectra of all the dye@$(TiO_2)_5$, dye@$(TiO_2)_8$ and dye@$(TiO_2)_{68}$ show major contributions from the $3d$ orbitals of titanium, $2p$ orbitals of carbon, $2p$ orbitals oxygen, p orbitals of hydrogen to the valence states. Carbon p orbitals contribute majorly to the conduction band.
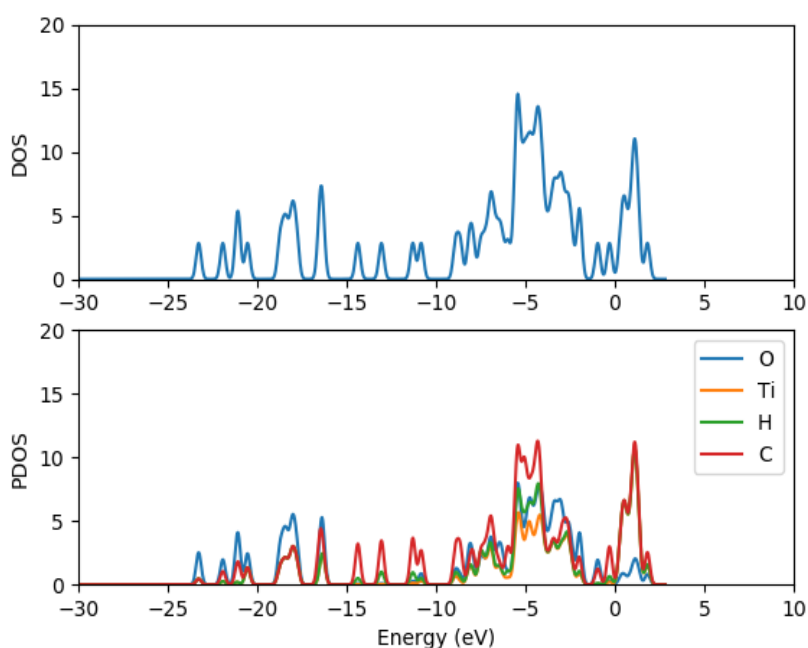
(a) CR1@$(TiO_2)_5$ DOS
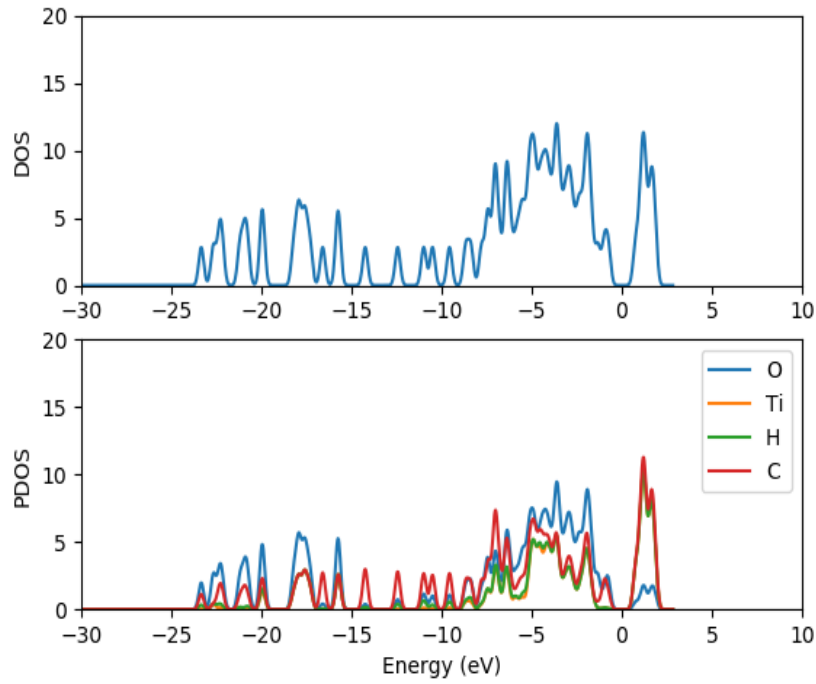
(b) CR2@(TiO$_2$)$_8$ DOS

Figure 72: Total density of states and projected density of state spectra of croconate dye absorbed on (TiO$_2$)$_5$ nanocluster (a) CR1@(TiO$_2$)$_5$ DOS and PDOS (b) CR2@(TiO$_2$)$_5$ DOS and PDOS.
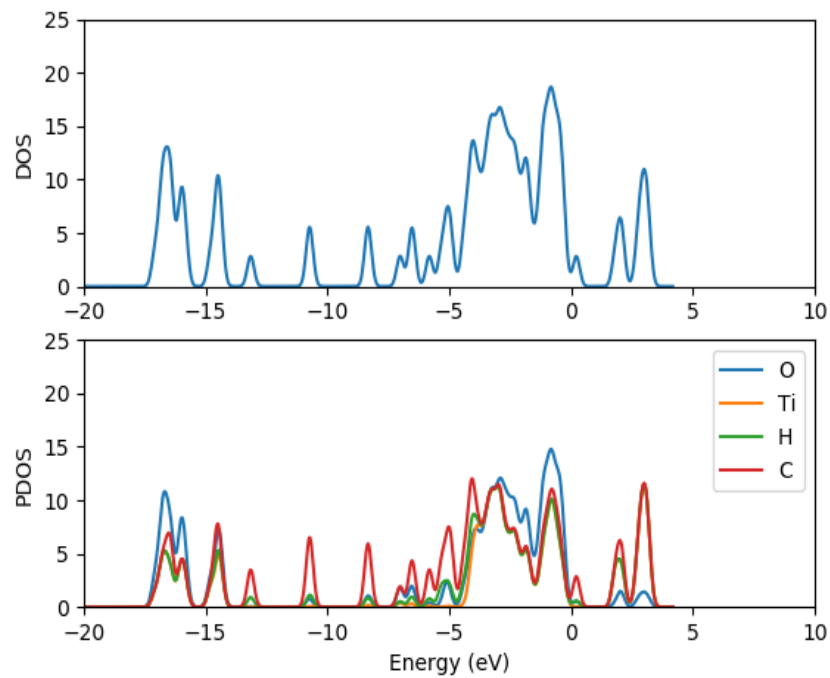
(a) CR1@(TiO$_2$)$_8$ DOS
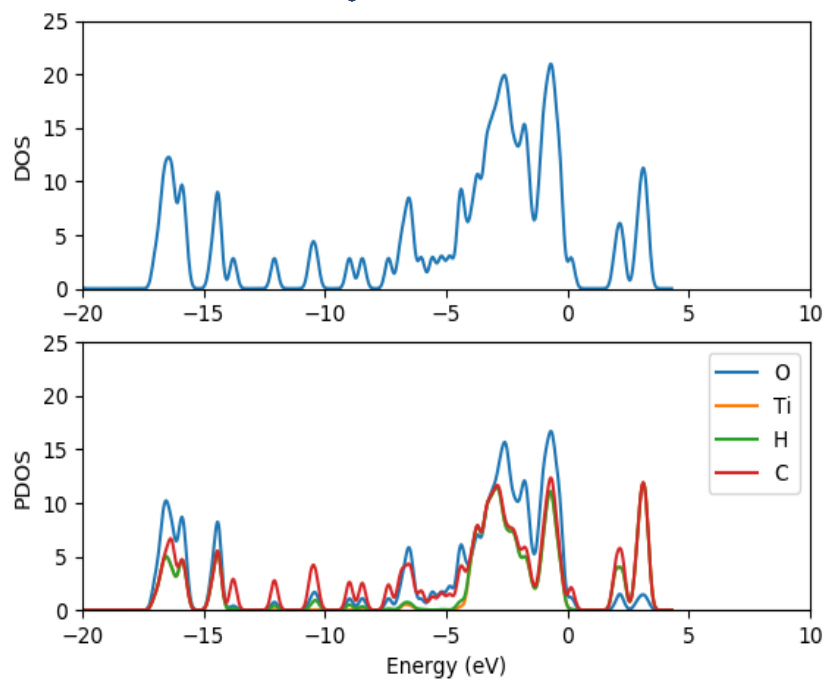
(b) CR2@$(TiO_2)_8$ DOS

Figure 73: Total density of states and projected density of state spectra of croconate dye absorbed on $(TiO_2)_8$ nanocluster (a) CR1@$(TiO_2)_8$ DOS and PDOS (b) CR2@$(TiO_2)_8$ DOS and PDOS.
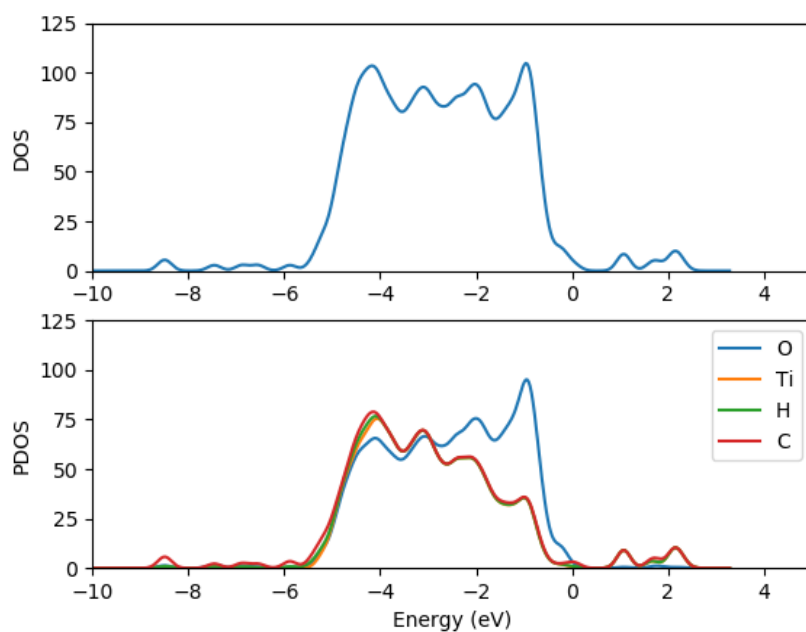
(a) CR1@$(TiO_2)_{68}$ DOS
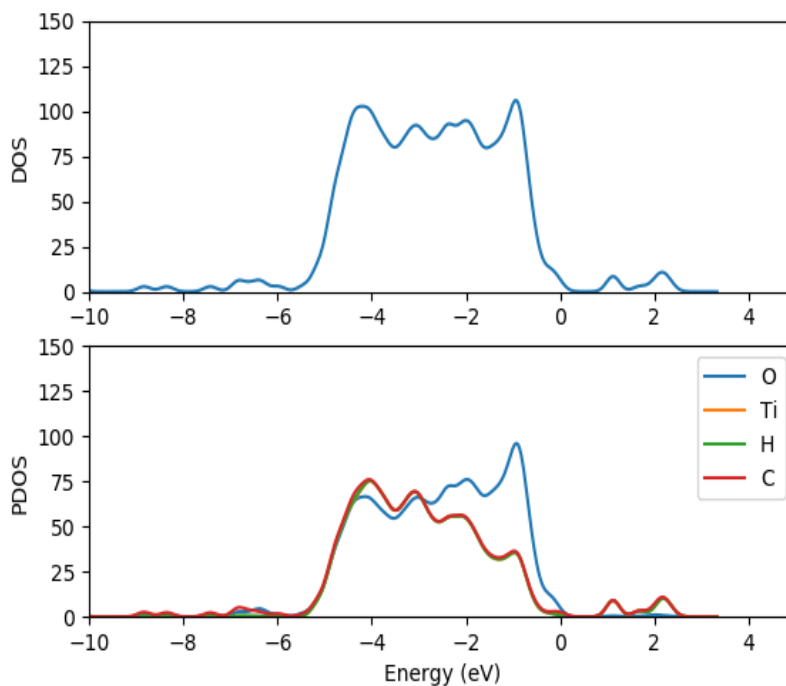
(b) CR1@(TiO$_2$)$_{68}$ DOS

Figure 74: Total density of states and projected density of state) spectra of croconate dye absorbed on (TiO$_2$)$_8$ nanocluster (a) CR1@ (TiO$_2$)$_8$ DOS and PDOS (b) CR2@ (TiO$_2$)$_8$ DOS and PDOS.

6.6 Absorption of Ruthenium N3 complex (TiO$_2$)$_n$, n=5, 8, 68   brookite cluster

6.6.1 Introduction

The ruthenium N3 complex has been widely used as sensitizers in the architecture of DSSCs and power conversion efficiency of 11-12% has been achieved with the use of ruthenium N3 complex as sensitizers for DSSC [51, 70, 84]. Information about the interfaces of ruthenium N3 complex is of great importance in understanding and optimizing light harvesting efficiencies, photo conversion function and photocurrent densities in DSSCs. A systematic density functional theory on adsorption geometry of Ru and YE05 sensitizer on TiO$_2$ substrate for DSSCs application has been reported in literature The study reported that the Ru and YE05 sensitizer binds with the carboxylic group unto the surface of TiO$_2$ [50]. In this study, the optical properties of the interplay of brookite semiconductor with ruthenium N3 dye molecules are investigated in order to optimize photon current densities in DSSCs. The ruthenium N3 dye molecules were absorbed on (TiO$_2$)$_5$, (TiO$_2$)$_8$ and (TiO$_2$)$_{68}$ brookite clusters by bidentate absorption mode as presented in Figures 75 – 77 respectively. The presented results include

relaxation energies, adsorption energies, excitation spectrum, free energy of electron injection, DOS and PDOS and isodensity surfaces of the key molecular orbital involved in excitation.
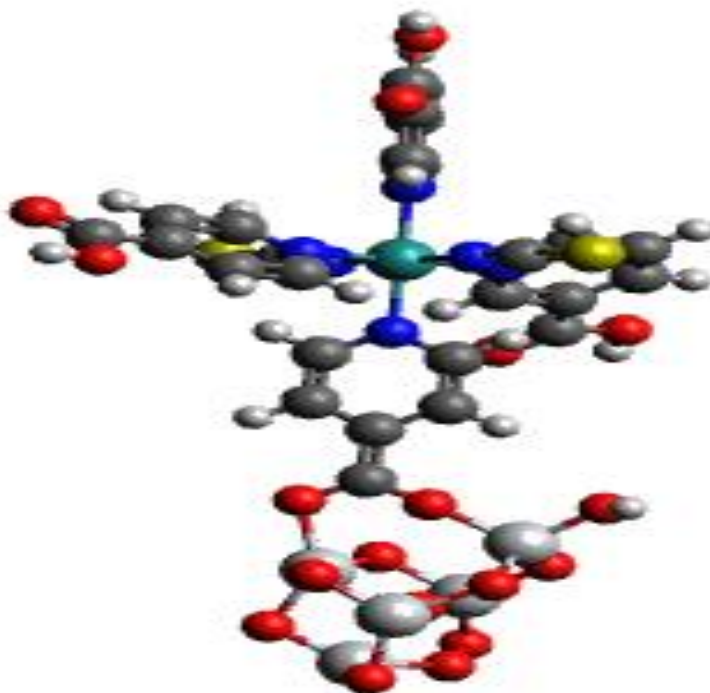
Figure 75: Ruthenium N3 complex absorbed on $(TiO_2)_5$ brookite cluster
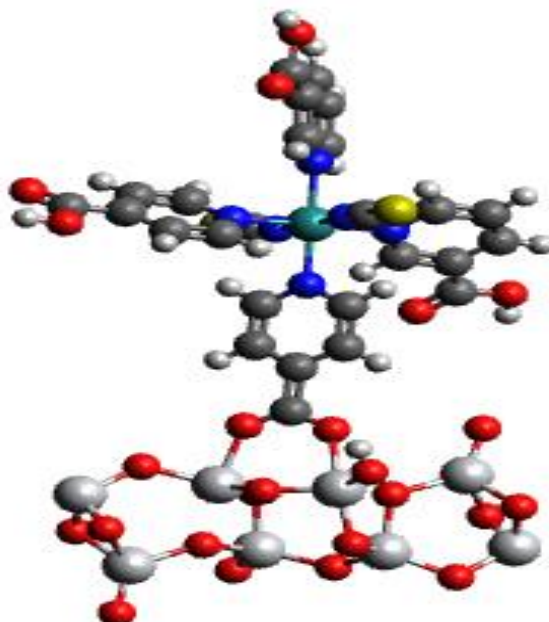
Figure 76: Ruthenium N3 complex absorbed on $(TiO_2)_8$ brookite cluster
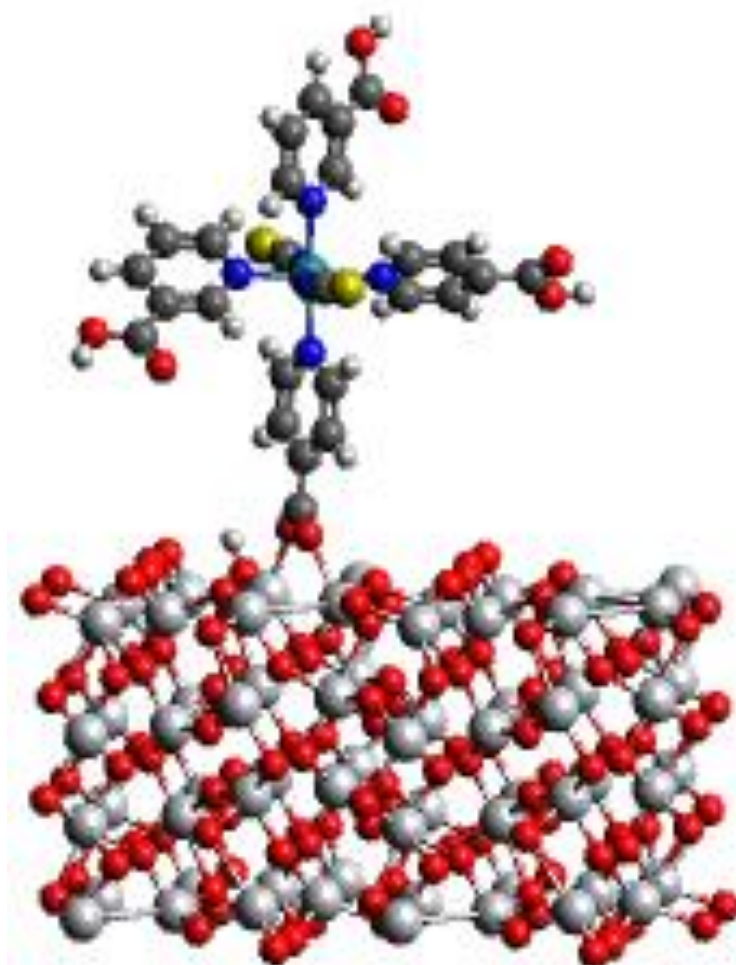
Figure 77: Ruthenium N3 complex absorbed on $(TiO_2)_8$ brookite cluster

6.6.2 Adsorption energies of ruthenium N3 dye molecule absorbed on $(TiO_2)_n$, n=5, 8, 68 brookite complex

The relaxation energy for ruthenium N3 dye is -432.91 eV. The energies of the clusters are -119.98 eV, -198.31 eV, -1635.55 eV for $(TiO_2)_5$, $(TiO_2)_8$ and $(TiO_2)_{68}$ respectively as presented in Table 24.

Table 24: Relaxation energies of ruthenium N3 dye molecule absorbed $(TiO_2)_5$, $(TiO_2)_8$ and $(TiO_2)_{68}$ brookite cluster

System	Relaxed Energy (eV)	Energy$_{slab}$ $(TiO_2)_n$ cluster (eV)	Energy$_{(slab +molecule)}$ Dye@$(TiO_2)_n$ (eV)
Ruthenium N3	-432.919		
$(TiO_2)_5$		-119.985	
$(TiO_2)_8$		-198.308	
$(TiO_2)_{68}$		-1635.558	
Ruthenium@$(TiO_2)_5$			-554.499
Ruthenium@$(TiO_2)_8$			-632.953
Ruthenium@$(TiO_2)_{68}$			-2072.267

The adsorption energies of ruthenium N3 dye on $(TiO_2)_5$ and $(TiO_2)_8$ and $(TiO_2)_{68}$ brookite cluster were computed using Equation (80).

The computed adsorption energies are presented in Table 25.

The adsorption energy of ruthenium N3 dye@ $(TiO_2)_5$ is 1.70 eV, ruthenium N3 dye @ $(TiO_2)_8$ is 1.73 eV, ruthenium N3 dye @ $(TiO_2)_{68}$ is 3.76 eV. These positive adsorption energies denote the binding ability of the dye molecules to the surface of $(TiO_2)_5$, $(TiO_2)_8$ and $(TiO_2)_{68}$ clusters. The adsorption energies of ruthenium N3 dye on $(TiO_2)_{68}$ $(TiO_2)_8$ and $(TiO_2)_5$ brookite cluster are in the order 3.84 eV > 1.73 eV > 1.61 eV, which implies that adsorption energy of ruthenium N3 dye @ $(TiO_2)_{68}$ > ruthenium N3 dye @ $(TiO_2)_8$ > ruthenium N3 dye @ $(TiO_2)_5$. The results showed that the ruthenium N3 dye binds more strongly to the surface of the larger nanocluster $(TiO_2)_{68}$ brookite than the corresponding $(TiO_2)_8$ and $(TiO_2)_5$ brookite clusters that are small in size.

Table 25: Adsorption energies of ruthenium N3 dye molecule absorbed $(TiO_2)_5$, $(TiO_2)_8$ and $(TiO_2)_{68}$ brookite complex.

Adsorption Energy of Dye@$(TiO_2)_{n=5,8,68}$ (eV)		
Dye@$(TiO_2)_5$	Ruthenium@$(TiO_2)_5$	1.695
Dye@$(TiO_2)_8$	Ruthenium@$(TiO_2)_8$	1.726
Dye@$(TiO_2)_{68}$	Ruthenium@$(TiO_2)_{68}$	3.76

6.6.3 Free energy of electron injection (ΔG^{inject}) of ruthenium N3 dye molecule

The free energy of electron injection of ruthenium N3 dye molecules into TiO_2 semiconductor was computed in order to investigate the possibility of electron injection and electron injection kinetics of the dye into the conduction band of TiO_2. (ΔG^{inject}) values of ruthenium N3 complex were computed using equation (81). The results are presented in Table 26.

Table 26: Free Energy of Electron Injection (ΔG^{inject}) of ruthenium N3 complex

Dye	Eox^{dye} (eV)	ΔE (eV)	Eox^{dye*} (eV)	(ΔG^{inject}) (eV)
Ruthenium	5.360	2.650	2.710	-1.290

The $\Delta G^{inject}\ and\ Eox^{dye*}$ of ruthenium N3 complex were computed using Equation (81) and (82). The calculated ΔG^{inject} for ruthenium N3 dye molecule is -1.29 eV. This suggests that the dye excited state lies above the conduction band of TiO_2, which favours electron injection into TiO_2 substrate. The negative value of ΔG^{inject} for ruthenium N3 indicates spontaneous injection of electron from the dye into the conduction band of TiO_2.

6.6.4 Absorption spectrum of ruthenium N3 dye absorbed on $(TiO_2)_5$ and $(TiO_2)_8$ brookite cluster

The optical spectra of the typical ruthenium N3 dye absorbed on $(TiO_2)_5$ and $(TiO_2)_8$ are presented in Figure 78 and Figure 79 respectively. The absorption spectrum in Figure 78 depicts the optical excitation of the ruthenium N3 dye absorbed on $(TiO_2)_5$, the spectrum in Figure 78 is compared with the absorption spectra of the $(TiO_2)_5$ cluster alone reported in Figure 49 previously. It is noted that the absorption spectrum of the cluster alone shows excitation in the UV region around 200 nm and 400 nm while it is clearly seen from the absorption spectrum of ruthenium N3 dye absorbed on $(TiO_2)_5$ in Figure 78 that the absorption maxima have shifted to higher wavelength. The ruthenium@ $(TiO_2)_5$ absorption spectrum shows absorption in the visible region around 400 nm – 600 nm, and in the near infra-red region around 700 nm to 1000 nm. The absorption maxima is situated at 1000 nm.

The absorption spectrum in Figure 79 depicts the optical excitation of the ruthenium N3 dye absorbed on $(TiO_2)_8$, compared with the absorption spectra of the $(TiO_2)_8$ cluster alone reported in Figure 50, the absorption spectra of $(TiO_2)_8$ cluster alone shows excitation in the UV region around 200 nm to 400 nm while the one with ruthenium N3 dye absorbed on $(TiO_2)_8$ in Figure 79 shows that the absorption maxima of the dye have shifted to higher wavelength. Thus, the ruthenium@ $(TiO_2)_8$ absorption spectrum shows absorption in the visible region around 400 nm – 600 nm, and slight absorption in the near infra-red region around 1080 nm. The absorption maxima is situated at 1080 nm.

The results generally suggest that the absorption of the ruthenium N3 dye molecule on $(TiO_2)_5$ and $(TiO_2)_8$ brookite clusters result in bathocromatic shift of the absorption maxima to higher wavelength, and also absorption over a wide range of the solar spectrum in the visible and near infra-red region of the solar spectrum. The red spectra shift observed upon absorption on ruthenium N3 dye on $(TiO_2)_5$ and $(TiO_2)_5$ brookite clusters also suggests good optical properties of the ruthenium N3 dye molecules and corroborates with earlier reports that brookite TiO_2 exhibits good photocatalytic properties [71, 75, 76].
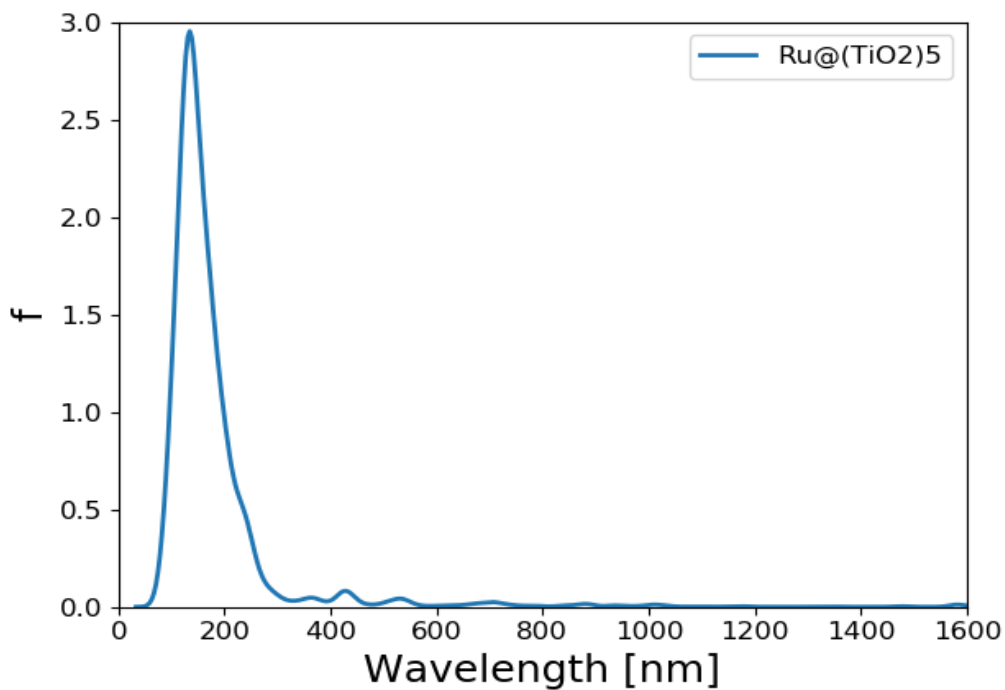
Figure 78: UV/Vis absorption spectrum of ruthenium N3 complex absorbed on (TiO2)5 brookite cluster.
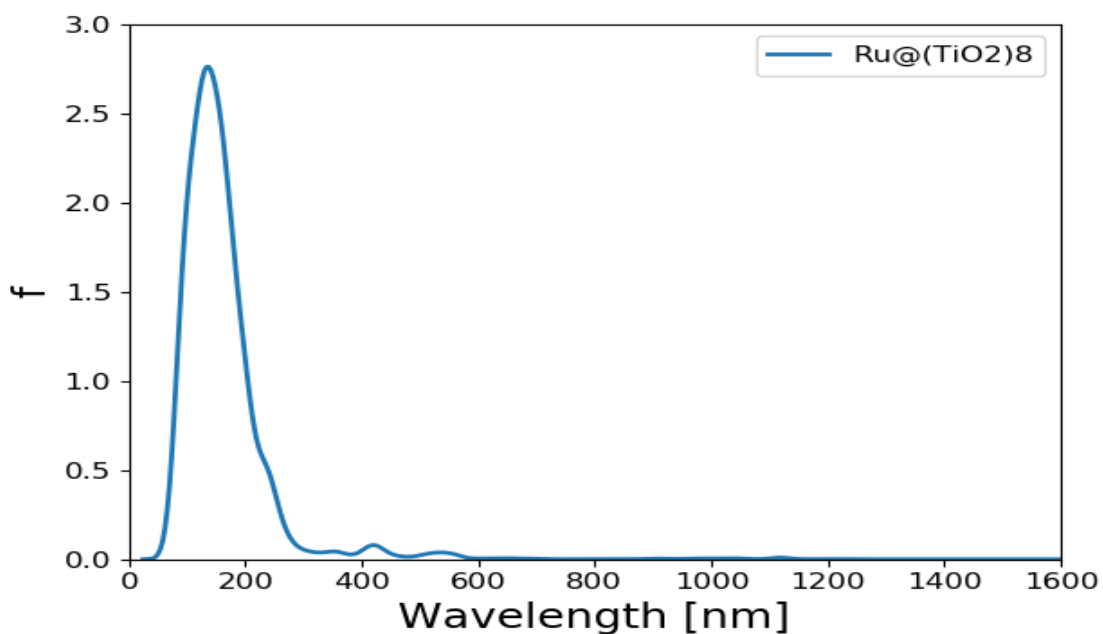
Figure 79: UV/Vis absorption spectrum of ruthenium N3 complex absorbed on (TiO2)8 brookite cluster

6.6.5 Isodensity surfaces of the ruthenium N3 dye absorbed on $(TiO_2)_n$, n=5, 8, 68 brookite cluster

The isodensity surfaces of the key molecular orbital involved in photoexcitation of the ruthenium N3 complex absorbed on $(TiO_2)_5$, $(TiO_2)_8$ and $(TiO_2)_{68}$ clusters are presented in Figures 80 - 82 respectively. The results show that the HOMO is localized on the entire NCS moiety of the dye molecule and it is mainly concentrated on the donor moiety where the occupied electronic orbitals are located, while the LUMO is localized over the TiO_2 clusters where the unoccupied electronic states are located. This suggests good electronic coupling between the occupied excited state of the dye and the unoccupied acceptor levels of the semiconductor conduction band. The localization of the HOMO electronic levels on the dye molecules and the LUMO electronic level on the TiO_2 clusters in Figures 80 - 82 implies efficient separation of charge upon adsorption and electron injection from the dye excited state into the TiO_2 semiconductor conduction band.

(a)   (b)
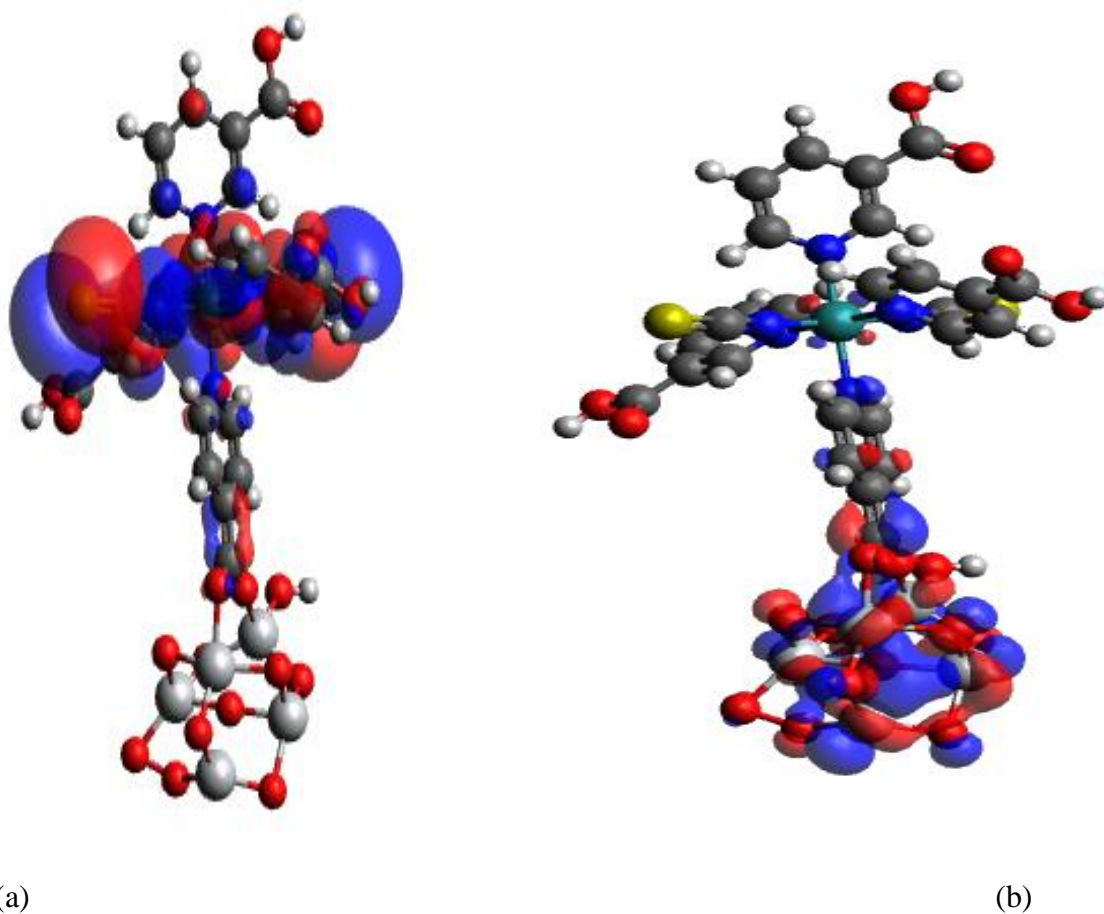
Figure 80: Isodensity surfaces of the molecular orbitals of (a) HOMO of ruthenium N3@ $(TiO_2)_5$ brookite cluster (b) LUMO of ruthenium N3@ $(TiO_2)_5$ brookite cluster
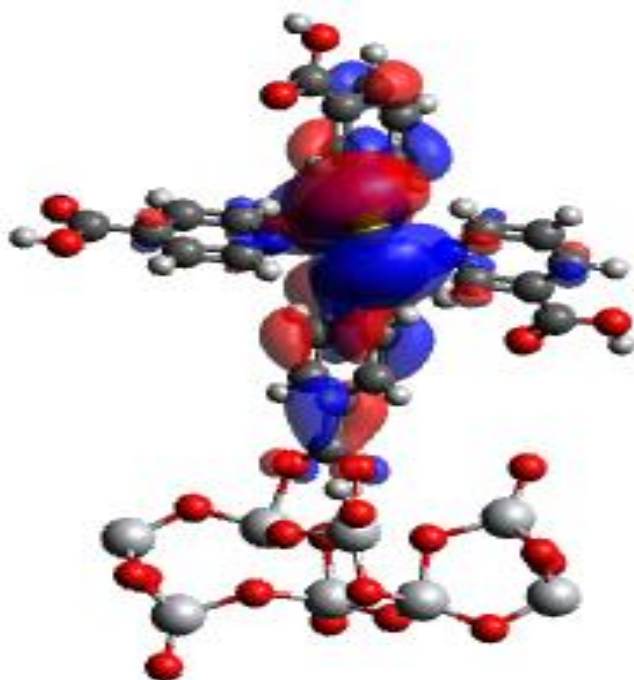
(a)
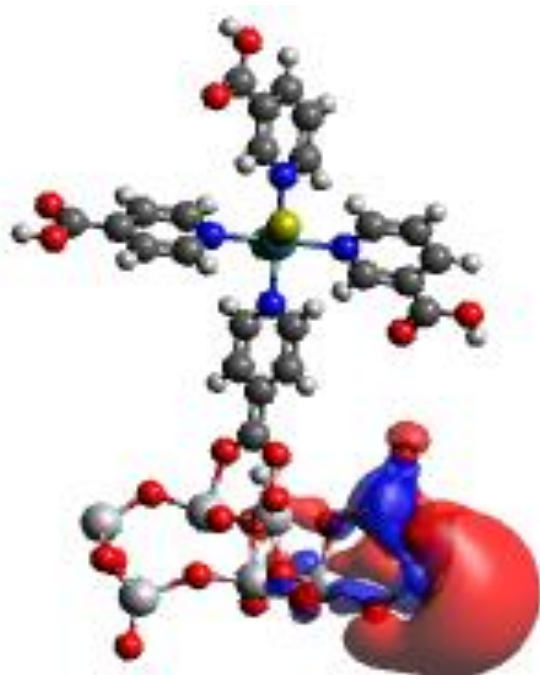
(b)

Figure 81: Isodensity surfaces of the molecular orbitals of (a) HOMO of ruthenium N3@ $(TiO_2)_8$ brookite cluster (b) LUMO of ruthenium N3@ $(TiO_2)_8$ brookite cluster
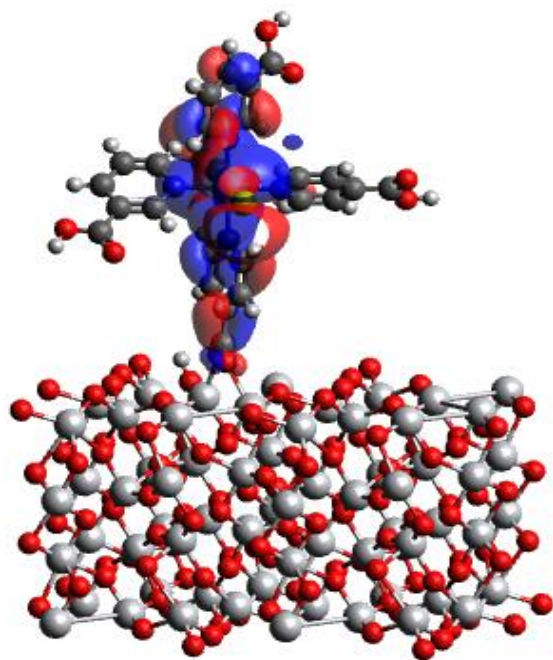
(a)
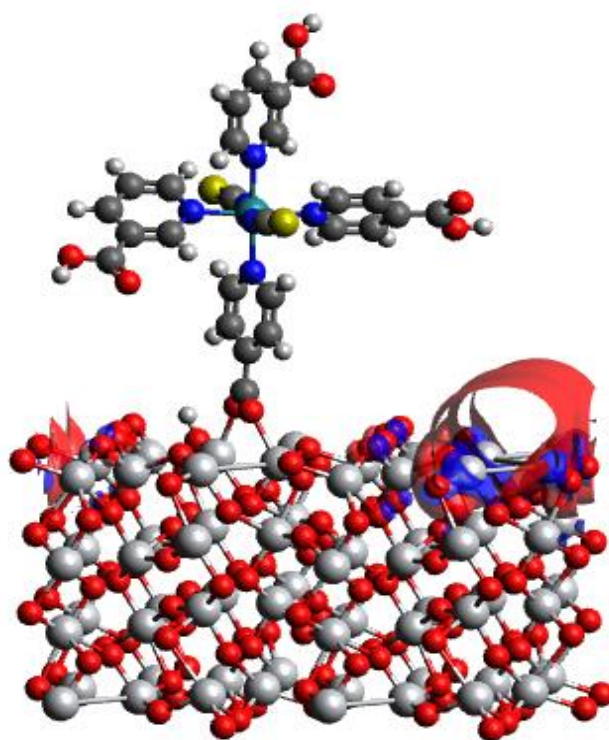
(b)

Figure 82: Isodensity surfaces of the molecular orbitals of (a) HOMO of ruthenium N3@ $(TiO_2)_{68}$ brookite cluster (b) LUMO of ruthenium N3@ $(TiO_2)_{68}$ brookite cluster

6.6.6 Electronic properties of ruthenium N3 dye molecule absorbed on TiO₂ clusters

GPAW and PBE exchange correction functionals were used to compute the density of states and the projected density of states of ruthenium N3 dye molecule absorbed on $(TiO_2)_5$, $(TiO_2)_8$ and $(TiO_2)_{68}$ in order to understand their electronic structure. The results are presented in Figures 83 - 85 respectively. The DOS contains the surface valence and conduction bands separated by a wide band gap. Upon the adsorption of the dye molecules on TiO₂ clusters, the dye introduce sharp occupied molecular energy levels in the band gap as seen in Figures 83-85. The DOS results reveal that the new occupied electronic orbitals are introduced between the two states where there was a broad band gap initially and in the conduction band of the TiO₂ clusters.

It is observed that the occupied and unoccupied states are broadened and shifted upon absorption due to coupling of the electronic states between the orbitals of the TiO₂ and the adsorbed dye molecules. Also, the edge of the occupied orbital shifted to higher energy level, the effect of the shifting of the two states results in narrowed band gap between the two states. This suggests the red spectral shift observed in the optical absorption spectrum of the ruthenium dye@TiO₂ spectrum presented in Figure 78 and Figure 79 observed upon the absorption of the dye unto the TiO₂ cluster.

The PDOS spectrum of the ruthenium N3 dye@ $(TiO_2)_5$, ruthenium N3 dye @ $(TiO_2)_8$ and ruthenium N3 dye @ $(TiO_2)_{68}$ are presented in Figures 83 - 85 respectively. The spectrum clearly shows the contribution of the atomic orbitals to the occupied states and unoccupied states. The PDOS results for the clusters alone show that both the oxygen and titanium atomic orbitals contribute to the valence states, the oxygen $2p$ atomic orbitals contributes mostly to the highest occupied VB state, whereas the lowest unoccupied state of the conduction band is mainly dominated by the contributions of titanium $3d$ atomic orbitals.

The valence band is dominated by the p atomic orbitals of oxygen with a little contribution from the p atomic orbitals of titanium. The key contribution in the conduction band comes from the titanium orbitals, especially the d and p ones. The PDOS spectra of the ruthenium N3 dye@$(TiO_2)_5$, dye@$(TiO_2)_8$ and dye@$(TiO_2)_{68}$ reveal major contributions from the $4d$ orbital of ruthenium, $3d$ orbitals of titanium, $2p$ orbitals of carbon, $2p$ orbitals oxygen, $2p$ orbitals of

nitrogen, $3p$ orbitals of sulphur and p orbitals of hydrogen to the valence states. Ruthenium, sulphur and oxygen p orbitals show minor contribution to the conduction band. The main atomic orbital contributing mainly to the valence state belongs to the dye molecules. This explains the concentration of the electron densities of the highest occupied molecular orbital on the dye molecules as seen in the Figures 80 - 82. In summary, the results show that the absorption of the dye introduces new molecular orbitals to the band gap of TiO_2 semiconductor band.
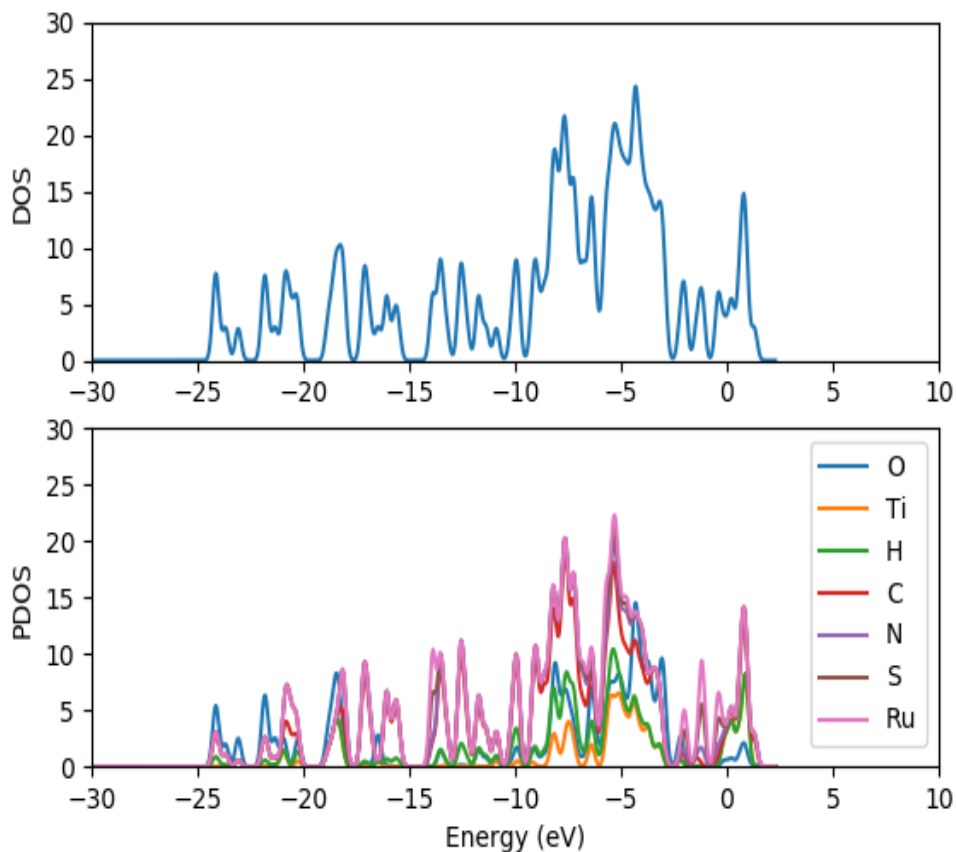
Figure 83: Density of states (DOS) and projected density of state (PDOS) spectrum of ruthenium N3 dye absorbed on $(TiO_2)_5$
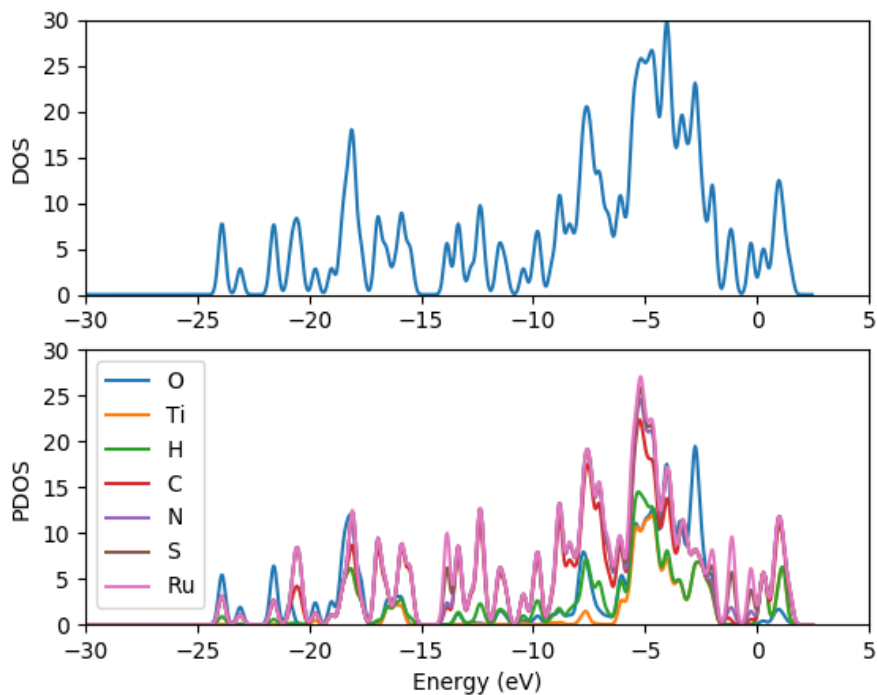
Figure 84: Density of states (DOS) and projected density of state (PDOS) spectrum of ruthenium N3 dye absorbed on $(TiO_2)_8$
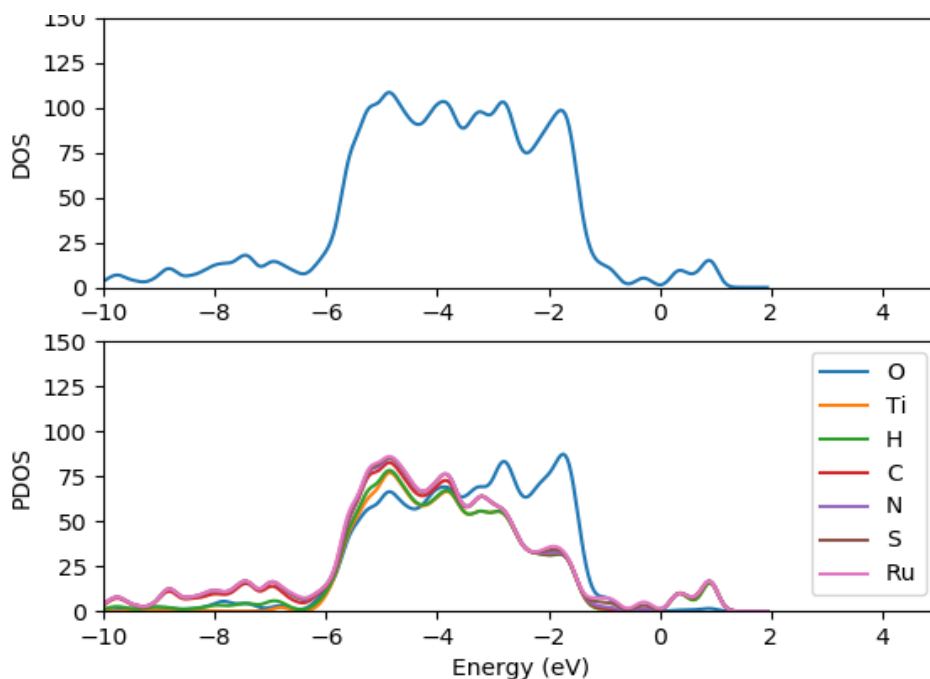
Figure 85: Density of states (DOS) and projected density of state (PDOS) spectrum of ruthenium N3 dye absorbed on $(TiO_2)_{68}$

CHAPTER SEVEN

7.0 CONCLUSION SUMMARY AND RECOMMENDATION

7.1 Conclusion and summary

The photoanode of DSSCs comprises of dye molecules anchored to the surface of semiconductors, typically nanostructured form of TiO_2 is employed. Understanding the interaction of dye molecules with the surfaces of TiO_2 is crucial because light harvesting and electron collection determine the efficiency of DSSCs. Therefore, information about the interfaces is of great importance in understanding and optimizing light harvesting, photo conversion function and photocurrent densities in DSSCs. TiO_2 exists in three major polymorphs which are anatase, brookite and rutile. The optical properties of brookite semiconductor have not been much studied although brookite has been reported to have good photocatalytic properties.

In this work, we used DFT computational approach to explore the properties of TiO_2 brookite and three groups of dye molecules, namely; (i) the typical ruthenium N3 complex, (ii) polyenediphenyl-aniline dye moiety and (iii) two croconate dye molecules for application in DSSCs. Photocatalytic properties of three modelled clusters of brookite, which are $(TiO_2)_5$, $(TiO_2)_8$ and $(TiO_2)_{68}$ obtained from its ground state optimized brookite bulk structure were investigated. The afore-mentioned dye molecules were absorbed on the three brookite TiO_2 nanoclusters in order to understand the interfacial properties between brookite TiO_2 semiconductor and the dye molecules. Various quantum mechanical computational software tools were used in this study to achieve various goals as required to fulfil the objectives of the study. The structural properties, relaxation energies, adsorption energies, UV/Vis optical absorption properties, free energy of electron injection, light harvesting efficiencies, HOMO-LUMO energy gap, isodensity surfaces of key molecular orbital, electronic DOS and PDOS were presented and discussed for various systems. The presented results were based on bulk brookite structure, modelled $(TiO_2)_{n = 5, 8, 68}$, brookite clusters, ruthenium N3 dye molecule, D5, D7, D9 and D11 polyenediphenyl-aniline dye molecules, croconate dye and the dye absorbed on brookite clusters.

The ruthenium N3 complex was investigated successfully using hybrid density functional theory for application in dye sensitized solar cells. The optical absorption, UV-Vis spectrum

and light harvesting efficiency of the dye molecule showed that the HOMO of N3 lies at -3.01 eV and was centralized on the NCS moiety where the donor group is situated while the LUMO lies at -5.03 eV and was centralized on the 4, 4-dicarboxy-2, 2-bipyridine moiety where the acceptor group is situated. The calculated results show that light harvesting efficiency depend on the absorption (oscillator strength) of the dye.

Four polyenediphenyl based photosensitizers D5, D7, D9 and D11 were studied computationally using DFT and TD-DFT methods. Our findings reveals that D5 and D7 dye absorb in the visible region while a red shift absorption was observed for D9 and D11 owing to their reduced HOMO-LUMO energy gap and addition of the methoxy group. It was also observed that the D9 and D11 dye with methoxy groups in their donor moiety depicted a broader peak and improved red spectra response than D5 and D7 dye without methoxy group. The D9 and D11 sensitizers with two diphenylaniline donor moiety showed the highest light harvesting efficiencies. The low HOMO-LUMO energy gap, absorption spectra and high light harvesting efficiency suggest that the addition of the methoxy groups to the donor moiety of D9 and D11 is responsible for their improved optical performance. The results suggested that the dye are promising sensitizers for DSSCs application.

Furthermore, two croconate dye molecules coded as CR1 and CR2 were successfully simulated using hybrid density functional theory for application in dye sensitized solar cells. The findings showed that that the carboxyl group (-COOH) contained in CR2, reduces the energy gap more than methyl group contained in CR1 and shifted the absorption to near infrared region. Similarly, the results suggest that light harvesting efficiency depend on the absorption (oscillator strength) of the dye.

The investigations on absorption of dye molecules on brookite $(TiO_2)_5$, $(TiO_2)_8$ and $(TiO_2)_{68}$ complexes all showed positive values of the absorption energies. Thus, suggesting that the ruthenium N3 complex, croconate dye and polyenediphenyl-aniline dye molecules all bind strongly to the surface of brookite $(TiO_2)_5$, $(TiO_2)_8$ and $(TiO_2)_{68}$ clusters. This correlates to previous findings that the stable grafting of the dye molecules unto TiO_2 semiconductor enhances stability of DSSCs.

The findings on the optical absorption spectrum of ruthenium N3 dye, croconate dye and polyenediphenyl-aniline dye molecule absorbed on $(TiO_2)_5$ and $(TiO_2)_8$ brookite cluster showed bathocromatic shift of the absorption maxima to higher wavelength and improved optical response of TiO_2 brookite cluster. A red spectra shift and absorption over a wide range of the solar spectrum in the visible and near infra-red region of the solar spectrum was achieved upon absorption of the ruthenium N3 complex and polyenediphenyl-aniline dye molecules on $(TiO_2)_5$ and $(TiO_2)_5$ brookite cluster. The results are in agreement with literature results that the ruthenium N3 dye molecule exhibit good optical properties and also suggest that polyenediphenyl-aniline the dye molecules are potential and promising candidate for TiO_2 sensitization for photocatalytic applications.

All the results for simulated dye-TiO_2 complexes showed that the HOMO is localized on the dye molecule and it is mainly situated on the donor moiety where the unoccupied electronic states are situated while the LUMO is delocalized entirely over the TiO_2 clusters where the unoccupied electronic state are located. The localization of the electron densities of the HOMO on the dye molecules and the electron densities of LUMO on the TiO_2 brookite suggests good electronic coupling between the occupied excited state of the dye and the unoccupied acceptor levels of the semiconductor conduction band. The HOMO electronic levels on the dye and the LUMO electronic levels on TiO_2 clusters imply efficient separation of charge upon adsorption and electron injection from the dye excited state into TiO_2 semiconductor conduction band. The positions of the HOMO and LUMO isodensity surfaces of the dye absorbed on TiO_2 imply efficient separation of charge upon adsorption and electron injection from the dye excited state into the TiO_2 semiconductor conduction band.

The negative values of free energy of electron injection ΔG^{inject} obtained for ruthenium N3 dye and polyenediphenyl-aniline dye molecule absorbed on $(TiO_2)_5$, $(TiO_2)_8$ and $(TiO_2)_{68}$ brookite clusters suggest spontaneous injection of electron from the dye excited state into the conduction band of TiO_2 brookite semiconductor.

The density of states results showed that the adsorption of the dye on TiO_2 brookite clusters results in a shift of the conduction band edge of TiO_2 brookite cluster to higher energy levels,

and consequently narrowing of the band gap between the occupied valence states and the unoccupied conduction band. Also, the absorption of the dye molecules on the TiO_2 brookite clusters revealed that the adsorption of the dye introduces new occupied electronic orbitals between the two states where there was a broad band gap initially and in the conduction band of the TiO_2 clusters which consequently narrow the band gap of the TiO_2 semiconductor. This explains the reason for the red shifting of the absorption maxima on the UV-Vis spectra and good electronic coupling observed from isodensity surfaces of the dye absorbed on TiO_2 complex.

The results generally suggest that the absorption of dye molecules on TiO_2 brookite cluster improves its spectral responsivity in the UV region and make it possible to absorb over the whole spectra range, that is, the UV visible and near infra–red region suggesting higher photocurrents density in DSSCs. This study was able to elucidate that brookite exhibit good photocatalytic properties. It also deduced that understanding molecular properties of dye-TiO_2 complexes is key to achieving higher photocurrent densities and relatively improving the overall device efficiencies.

7.2 Recommendation

The results generally show good spectral properties, optical excitation, electron injection kinetics, strong electronic coupling of TiO_2 brookite polymorph and also signal that brookite semiconductor exhibits fascinating properties and hence suggests more research on the synthesis and characterization of this polymorph and subsequently fabrication of brookite semiconductor based DSSCs.

REFERENCES

1. BP, BP Statistical Review of World Energy June (2015). bp.com/statistical review. Available online. Accessed August 2016.

2. Junhao Chu. (2012). Shanghai Institute of Technical Physics, Chinese Academy of Sciences Development of Photovoltaic Solar Cell Technology, **22** No. 4. AAPPS BULLETIN. 10-14.

3. Intergovernmental Panel on Climate Change (2007). *IPCC Fourth Assessment Report (AR4)*, Intergovernmental Panel on Climate Change, Geneva, Switzerland. 104.Retrievedfromhttp://www.ipcc.ch/publications_and_data/publications_ipcc_fo urth_assessment_report_synthesis_report.htm. Available online. Accessed August 2016.

4. Dr. Alan Doolittle, Ga Tech, the nature of sunlight (PVCDROM.PVE EDUCATION.org). Available online. Accessed August 2016.

5. European Photovoltaic Industry Association, (EPIA) Solar Generation (2006).

6. Michael, D. Oisamoje, Esther, E. Oisamoje. (2013.) Exploring the Economic and Environmental Benefits of Solar Energy Generation in Developing Countries: The Nigerian Perspective. *Journal of Energy Technologies and Policy,* **3**, (6), 23 – 31.

7. International Energy Agency's (IEA), World Energy Outlook (WEO) (2015).

8. Walters, S. (1977). Low loss energy storage flywheel. Mech. Eng. J. **99**: 48.

9. Ogunleye, I.O and Awogbemi, O. (2011). Constraints to the use of solar photovoltaic as a sustainable power source in Nigeria. *American Journal of Scientific and Industrial Research.* **2** (1), 11-16.

10. Lewis, N. S. (2007). Toward Cost-Effective Solar Energy Use. *Science*, **315**, 798-801.

11. Mohammad Tawheed Kibria, Akil Ahammed, Saad Mahmud Sony, Faisal Hossain, Shams-Ul-Islam. (2014). Comparative studies on different generation solar cells technology, Institute of Energy, University of Dhaka, Dhaka-1000, Bangladesh *Proceedings of 5th International Conference on Environmental Aspects of Bangladesh [ICEAB]* E33, 51-53.

12. Williams, R.H; and Carl, J.W. (1990). Energy from the Sun. Amer. Sci. J. **43**: 41.

13. http://www.pv.cdrom.edu.com. Available online. Accessed August 2016.

14. Dr. Alan Doolittle, Ga Tech, the nature of sunlight. Available online. Accessed August 2016.

15. Hoff, E.; and Cheney, M. (2000). The Idea of Low Cost Photovoltaic. *Energy Journal*. **93,** 17.

16. Satyen, K. D. (2000). Recent development in high efficiency solar cells. National Renewable Energy Laboratory, 1617, Cole Boulevard. Golden, Colorado 80401-3393.

17. International Renewable Energy Agency (Irena) (2012). Renewable Energy Technologies: Cost Analysis Series *Vol 1: Power Sector* Issue 4/5.

18. National Energy Education Development Program (NEED) (2015). Exploring Photovoltaics, Student Guide. 8408 Kao Circle, Manassas, VA 20110. 1-39.

19. Sokolský, Michal. Cirák, Július. (2010). Dye-Sensitized Solar Cells: Materials and Processes, *Acta Electrotechnica et Informatica,* **10**, 3, 78-81.

20. NEDO white paper on renewable energy. Available online, Accessed August 2011.

21. Penick, T. Louk, B. (2011). European Photovoltaic Industry Association (EPIA), solar generation 6. Solar photovoltaic electricity empowering the world 1-98.

22. Mints, P. (2011). Photovoltaic Manufacturer Shipments, Capacity & Competitive Analysis 2010/2011. Palo Alto, CA: Navigant Consulting Photovoltaic Service Program. Report NPS-Supply6 (April 2011).

23. Hegedus, S. S.; Luque, A. (2003). Status, trends, challenges and the bright future of solar electricity from photovoltaics. In Handbook of Photovoltaic Science and Engineering, Edited by: Hegedus, S.S. and Luque, A. John Wiley & Sons, West Sussex.

24. Boreland, Matt. Bagnall, Darren (2006). Current and future photovoltaics. Report for Office of Scence and Innovation Foresight and Horizon Scanning Centre – Energy Project. 1-21.

25. Goetzberger, A., C. Hebling, and H.W. Schock (2003). Photovoltaic materials, history, status and outlook. *Materials Science & Engineering R-Reports*, **40** (1) 1-46.

26. Mehta, S. (2010). PV Technology, Production and Cost Outlook *2010-2015*, Greentech Media Research, October 2010, Boston, MA.

27. Green, M. A. (2001). Clean Energy from Photovoltaics, World Scientific Publishing Co., Hackensack, NJ.

28. Aramoto T., Kumazawa S., Higuchi H., Arita T., Shibutani S., Nishio T., Nakajima J., Tsuji M., Hanafusa A., Hibino T., Omura K., Ohyama H. and Murozono M. (1997). 16% efficient thin-film CdS/CdTe solar cells. *Proc. 26th IEEE PVSC,* Anaheim, 343-346.

29. Green, M.A., Keith E., Yoshihiro H. and Wilhelm W. (2011). Solar Cell Effciency Tables (Version 37), *Progress in Photovoltaics: Research and Applications,* **19**, 84-92, John Wiley & Sons Ltd., N.J.

30. Romeo, A., Terheggen M., Abou-Ras D., Ba¨tzner D. L., Haug F.-J., Ka¨lin M., Rudmann D. and Tiwari A. N. (2004). Development of thin-film Cu (In, Ga) Se2 and CdTe solar cells. *Progress in Photovoltaic Research and Applications.* **12**, 93-111.

31. Green, Martin A. (2006). Third generation photovoltaics: advanced solar energy conversion. Publisher, Berlin: Springer

32. Global Energy Network Institute (GENI) Chu, Y. (2011). Review and Comparison of Different Solar Energy Technologies.1-52

33. Chu J. (2012). Development of Photovoltaic Solar Cell Technology, 22, **4**, 10-14

34. International Energy Agency (IEA) (2010). Technology Roadmap: Solar Photovoltaic Energy, IEA/OECD, Paris.

35. Nature Photonics (2010), Future Perspectives of Photovoltaics, Proceedings of the Conference, Nature Publishing Group, Nature Asia-Pacific, Tokyo.

36. Gerstmaier T., Röttger M., Zech T., Moretta R. Braun C. and Gombert A (2014). Five Years of CPV Field Data: Results of a Long-term Outdoor Performance Study, in: Proceedings of the 10th International Conference on Concentrating Photovoltaic Systems. (Albuquerque, NM, USA).

37. Yinghao Chu. Global Energy Network Institute (GENI). 2011. Available online. Accessed August 2016.

38. OrgaPVnet (2009). Technology Roadmap towards Stable & Low-cost Organic Based Solar Cells, OrgaPVnet, Brussels.

39. Elias Stathatos (2011). Dye Sensitized Solar Cells as an Alternative Approach to the Conventional Photovoltaic Technology Based on Silicon - Recent Developments in the Field and Large Scale Applications, Solar Cells - Dye-Sensitized Devices, Prof. Leonid A. Kosyachenko (Ed.), ISBN: 978-953-307-735-2.

40. Abodunrin, T.J., Obafemi, O., Boyo, A.O., Adebayo, T. and Jimoh, R. (2015). The Effect of Electrolyte on Dye Sensitized Solar Cells Using Natural Dye from Mango (*M. indica* L.) Leaf as Sensitizer. *Advances in Materials Physics and Chemistry*, **5**, 205-213.

41. Barbara Volker, Folarin Wolzl, Thomas Burgi, and Dominic Lingenfelser (2012). Dye Bonding to TiO_2: In Situ Attenuated Total Reflection Infrared Spectroscopy Study, Simulations and Correlation with Dye sensitized Solar cell characteristics. *ACS Publications, American Chemical Society*, **28**, 11354 – 11363.

42. Xuan Pan, Changhong Chen, Kai Zhu and Zhaoyang Fan (2011). TiO_2 nanotubes infiltrated with nanoparticles for dye sensitized solar cells. *Nanotechnology*, **22**, 235402, 1-7.

43. Shahzad, N., pugliese, D., lamberti, A., Sacco, A., Virga, A., Gazia, A., Bianco, S., Shahzad, M.I., Tresso and pirri, C.F. (2013). Monitoring the dye impregnation time of nanostructured photoanodes for dye sensitized solar cells. *Journal of Physics*, **439**. 1-12.

44. Janne Halme (2002). Dye-sensitized nanostructured and organic photovoltaic cells: technical review and preliminary tests. Helsinki University of Technology.

45. Shun Fukutomi, Kazuaki Tamiya, Takaharu Watanabe, Kozo Taguchi. (2015). Electrophoretic Deposition of Carbon Nanotubes Electrode for Dye-Sensitized Solar

University of Venda

Cells. *International Conference of Electrical, Automation and Mechanical Engineering* (EAME 2015) 55-58.

46. Suriati Suhaimi1, Mukhzeer Mohamad Shahimin, Z.A. Alahmed, J. Chyský, A. H. Reshak (2015). Materials for Enhanced Dye-sensitized Solar Cell Performance: Electrochemical Application. *International. Journal of Electrochemical Sci*ence, **10**, 2859 – 2871.

47. Khalil Ebrahim Jasim (2007). Dye Sensitized Solar Cells - Working Principles, Challenges and Opportunities. Solar Cells - Dye-Sensitized Devices, Prof. Leonid A. Kosyachenko (Ed.), ISBN: 978-953-307-735-2, InTech.

48. Brian E. Hardin, Henry J. Snaith2 and Michael D. McGehee (2012). The renaissance of dye-sensitized solar cells. *Nature Photonics*. **6** .162-169.

49. Lu-Lin Li and Eric Wei-Guang Diau (2013). Porphyrin-Sensitized solar cells. Chem.Soc.Rev. **42,** 291-304.

50. Fillippo De Angelis, Simona Fantacci, Annabella Selloni, Mohammad K. Nazeeruddin and Michael Gratzel (2010). First-principles Modelling of the Adsorption Geometry and Electronic Structure of Ru(II) Dye on Extended TiO_2 substrates for Dye-Sensitized Solar Cell Application. *Journal of Physical Chemistry,* **114**, 6054-6061.

51. Nazeeruddin, M.K.; de Angelis, F.; Fantacci, S.; Selloni, A.; Viscardi, G.; Liska, P.; Ito, S.; Bessho, M.; Gratzel, T. (2005). Combined experimental and DFT-TDDFT computational study of photoelectrochemical cell ruthenium sensitizers. *Journal of American Chemical Society,* **127,** 16835–16846.

52. Claudia Longo, Marco- A. De paoli (2003) Dye-Sensitized solar cells. *Journal of Brazilian. Chemical Society*. **14**, 1-14.

53. Hao Yang, Jia Li, Gang Zhou, Sum Wai Chiang, Hongda Du, Lin Gan, Chengjun, Feiyu Kang and Wenhui Duan. (2015). First principles study of ruthenium (II) sensitizer adsorption on anatase TiO_2 (001) surface. *Royal Society of Chemistry Advances*, **5**, 60230-60236.

54. Emildo Marcano (2017) DFT study of anthocyanidin and anthocyanin pigments for Dye-Sensitized solar cells: Electron injecting from the excited states and adsorption onto TiO_2 (anatase) surface. *De Gruyter*. **2** 1-10.

55. Hara, K. & Arakawa, H. (2003). Dye-sensitized Solar Cells, In: Handbook of Photovoltaic Science and Engineering, A. Luque and S. Hegedus, (Ed.), Chapter 15, 663-700. John Wiley &Sons, Ltd, ISBN: 0-471-49196-9.

56. Hagfeldt, A., Boschloo, G., Sun, L., Kloo, L., Pettersson, H. (2010). Dye-sensitized solar cells. *Chemical Reviews*, 110, 6595 – 6663.

57. Daniel P. Hagberg, Tomas Edvinsson, Tannia Marinado, Gerrit Boschloo, Anders Hagfeldt and Licheng Sun (2006). A novel organic chromophore for dye-sensitized nanostructured solar cells. *Chemical Communications*, **42**, 2245–2247.

58. Maria Hahlin, Erik M. J. Johansson, Stefan Plogmaker, Michael Odelius, Daniel P. Hagberg, Licheng Sun, Hans Siegbahna and Ha°kan Rensmo (2010). Electronic and molecular structures of organic dye/TiO_2 interfaces for solar cell applications: a core level photoelectron spectroscopy study. *Physical Chemistry Chemical Phys*ics, **12**, 1507–1517.

59. Asif Mahmood, Salah Ud-Din Khan, Usman Ali Rana, Mudassir Hussain Tahir (2014). Red shifting of absorption maxima of phenothiazine-based dye by incorporating electron-deficient thiadiazole derivatives as π-spacer, *Arabian Journal of Chemistry*, 1-7. http:/dx.doi.org/10.1016/j.arabjc.2014.11.007.

University of Venda

60. Li, J. G., Ishigaki, T., Sun, X. (2007). Anatase, Brookite, and Rutile Nanocrystals via Redox Reactions under Mild Hydrothermal Conditions: Phase-Selective Synthesis and Physicochemical Properties. *Journal of Physical Chemistry C*, **111**: 4969-4976.

61. Mengmei P., Niu H., Xingzhang Zhao J., and Xiaoli Z., (2013). Enhanced efficiency of Dye sensitized solar cell by high surface area anatase TiO_2 modified P25 paste. *Journal of Nanometals*, **2013**.

62. Elias Stathatos (2011). Dye Sensitized Solar Cells as an Alternative Approach to the Conventional Photovoltaic Technology Based on Silicon - Recent Developments in the Field and Large-Scale Applications, Solar Cells - Dye-Sensitized Devices, Prof. Leonid A. Kosyachenko (Ed.), ISBN: 978-953-307-735-2.

63. Diebold, U. 3003, Structure and properties of TiO_2 surfaces: a brief review. *Application Physics,* **76**, 681-687.

64. Yaqin Wang, Ruirui. Zhang, Jianbao Li. Liangliang Li and Shiwei Lin (2014). First principle study on Transition metal doped anatase TiO_2. *Nanoscale Research Letters Springer*, **9**, 1 - 8.

65. Rengifo-Herrera J. A., Pierzchaa, K., Sienkiewicz, A., Forr, L., Kiwi, J., Moser, J. E., Pulgarin, C. (2010). Synthesis, Characterization, and Photocatalytic Activities of Nanoparticulate N, S codoped TiO2 having Different Surface-to-volume Ratios. *Journal Physical Chemistry C*, **114**, 2717–2723.

66. Xiang Wu, Eva Holbig and Gerd Steinle-Neumann (2010) Structural stability of TiO_2 at high pressure in density-functional theory-based calculations. *Journal of Physics Condensed Matter,* **22**, 295501, 1-7.

67. Ferreira, V. C. Nunes, M. R. Silvestre, A.J. and Monteiro, O.C. (2013) Synthesis and properties of Co- doped titanate nanotubes and their optical sensitization with methylene blue. *Material Chemistry Phys*ics, **142**, no. 1, pp. 355-362.

68. Landmann, M., Rauls, E. and Schmidt, W. G. (2012). The electronic structure and optical response of rutile, anatase and brookite TiO2. *Journal of Physics: Condensed Matter*, **24**, 195503 (6pp).

69. Sheka, E.F., Nikitina, E.A., Zayets, V.A., Ginzburg, I.Ya. and Schoonma, J. (2007). Carboxylic species adsorption on TiO_2 nanoparticles. *Physics Solid State*, **49**: 154-163.

70. Y. Qin, Q. Peng. (2012). Ruthenium sensitizers and their applications in dye-sensitized solar cells. *International Journal of Photoenergy*, **2012**, 1-21.

71. Agatino Di Paola, Marianna Bellardita and Leonardo Palmisano. (2013). Brookite, the Least Known TiO2 Photocatalyst. *Catalysts,* **3**, 36-73.

72. Gong, X., Selloni, A. (2007). First-principles study of the structures and energetics of stoichiometric brookite TiO2 surfaces. *Physical Reviews* B, **76**, (23), 235307.

73. Schaub R, Wahlstrom E, Ronnau A, Laegsgaard E, Stensgaard I, Besenbacher F (2003). Oxygen-mediated diffusion of oxygen vacancies on the TiO_2 (110) surface. *Science*, **299**, 377–379.

74. Ken Onda, Bin Li, Jin Zhao, Kenneth D. Jordan, Jinlong Yang, Hrvoje Petek (2005). Wet Electrons at the H_2O/TiO_2 (110) surface. *Science,* **308**, 1154-1158.

75. Zallen R, Moret M.P (2006). The optical absorption edge of brookite TiO_2. *Solid State Communications,* **137**, 154-157

76. Monique M. Rodriguez, Xihong Peng, Lianjun Liu, Ying Li, and Jean M. Andino (2012). A density functional theory and experimental study of CO_2 interaction with brookite TiO_2. *Journal of Physical Chemistry,* **116**, 19755-19764.

77.   Material Studio Accerlrys Inc 2016 from Dassault Systèmes BIOVIA

78.   Frisch M J, Trucks G W, Schlegel H B, Scuseria G E, Robb M A, Cheeseman J R,
       Montgomery J A, Jr Vreven T, Kudin K N, Burant J C, Millam J M, Iyengar S S,
       Tomasi J, Barone V, Mennucci B, Cossi M, Scalmani G, Rega N, Petersson G A,
       Nakatsuji H, Hada M, Ehara M, Toyota K, Fukuda R, Hasegawa J, Ishida M,
       Nakajima T, Honda Y, Kitao O, Nakai H, Klene M, Li X, Knox J E, Hratchian H P,
       Cross J B, Adamo C, Jaramillo J, Gomperts R, Stratmann R E, Yazyev O, Austin A
       J, Cammi R, Pomelli C, Ochterski J W, Ayala P Y, Morokuma K, Voth G A, Salvador
       P, Dannenberg J J, Zakrzewski V G, Dapprich S, Daniels A D, Strain M C, Farkas O,
       Malick D K, Rabuck A D, Raghavachari K, Foresman J B, Ortiz J V, Cui Q, Baboul
       A G, Clifford S, Cioslowski J, Stefanov B B, Liu G, Liashenko A, Piskorz P,
       Komaromi I, Martin R L, Fox D J, Keith T, Al-Laham M A, Peng C Y, Nanayakkara
       A, Challacombe M, Gill P M W, Johnson B, Chen W, Wong M W, Gonzalez C, Pople
       J A (2004). *Gaussian 03, revision D.01* (Wallingford, CT: Gaussian, Inc.).

79.   Chitumalla R. K., Manho L., Xingfa G., Joonkyung J. Substituent effects on the
       croconate dye in dye sensitized solar cell applications: a density functional theory
       study. *Journal of Molecular Model 21*, **297**, 1-8 (2015).

80.   Puyad, A. L., Kumar, C. R., and Bhanuprakash, K. Adsorption of croconate dye on
       TiO_2 anatase (101) surface: A periodic DFT study to understand the binding of
       diketo groups, *Journal of Chemical Sciences*, **124**, 301-310(2012).

81.   Boschloo G, Marinado T, Nonomura K, Edvinsson T, Agrios A.G, Hagberg L. Sun,
       Quintana M, Karthikeyan C.S, Thelakkat M. Hagfeldt A. (2008). A comparative
       study of polyene-diphenylaniline dye and Ru $(dcdpy)_2(NCS)_2$ in electrolyte based and
       solid state-based dye- sensitized solar cells. *Thin Solid Films,* **516**, 7214-7217.

82.   Diabin kuang, Pascal Comte, Shaik M. Zakeeruddin, Daniel P. Hagberg Karl Martin
       Karlsoon, Licheng Sun, Md. K. Nazeeruddin, Micheal Gratzel (2011). Stable dye-

Sensitized solar cells based on organic chromophores and ionic liquid electrolyte. *Solar Energy,* **85**, 1189-1194.

83. O'Regan, B. and Grätzel, M. (1991). A low-cost, high-efficiency solar cell based on dye sensitized colloidal TiO2 films. *Nature,* **353**, 737–740.

84. Nazeeruddin, M. K., Kay, A., Rodicio, I., Humphry-Baker, R., Muller, E., Liska, P., Vlachopoulos, N. & Gratzel, M. (1993). Conversion of Light to Electricity by cis-X2Bis (2, 2'-bipyridil-4, 4'-dicarboxylate) ruthenium (II) Charge Transfer Sensitizer (X=Cl-, Br-, I-, CN- and SCN-). *Journal of American Chemical Society.* **115***,* 6382-6390.

85. Kelly, C. A.; Thompson, D. W.; Farzad, F. & Meyer, G. J. (1999). Excited State Deactivation of Ruthenium (II) Polypyridyl Chromophores Bound to Nanocrystalline TiO$_2$ Mesoporous Films, *Langmuir*, **15**, 731-734.

86. Farzad, F., Thompson, D. W., Kelly, C. A., and Meyer, G. J. (1999). Competitive Intermolecular Energy Transfer and Electron Injection at Sensitized Semiconductor Interfaces. *Journal of American Chemical Society,* **121**, 5577-5578.

87. Qu, P., Thompson, D. W., & Meyer, G. J. (2000). Temperature Dependent, Interfacial Electron Transfer from Ru(II) Polypyridyl Compounds with Low Lying Ligand Field States to Nanocrystalline Titanium Dioxide. *Langmuir*, **16**, 4662-4671.

88. Shoute, L. C. T., & Loppnow, G. R. (2003). Excited-state Metal-to-Ligand Charge Transfer Dynamics of a Ruthenium (II) Dye in Solution and Adsorbed on TiO$_2$.

89. Kleverlaan, C. J.; Indelli, M. T.; Bignozzi, C. A.; Pavanin, L.; Scandola, F. & Hasselmann, Meyer, G. J. (2000*).* Stepwise Photoinduced Charge Separation in Heterotriads: Binuclear Rh (III) Complexes on Nanocrystalline Titanium Dioxide. *Journal of American Chemical Society*, **122**, 2840-2849.

90. Yella, A.; Lee, H.W.; Tsao, H.N.; Yi, C.; Chandiran, A.K.; Nazeeruddin, M.K.; Diau, E.W.G.; Yeh, C.Y.; Zakeeruddin, S.M.; Gratzel, M. (2011). Porphyrin-sensitized solar cells with cobalt (II/III)-based redox electrolyte exceed 12 percent efficiency. *Science* **334**, 629–634.

91. Cai-Rong Zhang, Zi-Jiang Liu, Yu-Hong Chen, Hong-Shan Chen, You-Zhi Wua, WangJun Feng, Dao-Bin Wang (2010). DFT and TD-DFT study on structure and properties of organic dye sensitizer TA-St-CA, *Current Applied Physics,* **10,** 77-83

92. Jungsuttiwong S. Tarsang R. Pansay S. Yakhantip T. Promarak V. Sudyoadsuk T. Kaewin T. Saengsuwan S. Namuangrak S. (2011) Theoretical investigation of Carbzole-based D-D-π-A organic dye for efficient dye-sensitized solar cell. International Journal of Chemical, Molecular, Nuclear, Materials and Metallurgical Engineering. World Academy of Science, Technology and Engineering. 77, 561-567

93. Mishra, A., Fischer, M. K. R. & Bauerle, P. (2009) Metal-free organic dye for dye sensitized solar cells: From structure–property relationships to design rules. *Angew Chemistry International. Edition,* **48,** 2474–2499.

94. Irfan. A., Jin. R., Al-Sehemi, A.G., Asiri, A.M., (2013). Quantum Chemical study of donor-pi-acceptor triphenylamine based sensitizers, *Spectrochimica. Acta A,* **110,** 60-66.

95. Umer Mehmood, Ibnelwaleed A.Hussein, Khalil Harrabi and Shakeel Ahmed (2015). Density Functional Theory Study on the Electronic Structures of Oxadiazole Based Dye as Photosensitizer for Dye Sensitized Solar Cells. *Journal of Advances in Material Science and Engineering*, **2015**. 1-8. http:/dx.doi.org/10.1155/2015/286730.

96. Schmidt-Mende, L., Bach U., Humphry-Baker, R., Horiuchi T., Miura H., Ito S., Gratzel M. (2005). Organic dye for highly efficient Solid-State Dye Sensitized Solar cells. *Ersch in Advanced Materials,* **17**, 813-815.

97. Hwang, S., Lee, J.H., Park, C., Lee, H., Kim, C., Park, C., Lee, M.H., Lee, W., Park, J., Kim, K., Park, C., Kim, N.G. (2007). A highly efficient organic sensitizer for dye-sensitized solar cells. *Chemical Communications*, **46**, 4887–4889.

98. Kensuke Takechi and Prashant V. Kamat, Rekha R. Avirah, Kuthanapillil Jyothish, Danaboyina Ramaiah. 2008. Harvesting infrared photons with croconate dye. *Chemistry of Materials*, **20**, 265-272.

99. Jiwon Moon, Minbi Kim, Jeong Sik Lim Joonghan Kim. (2018) Effect of phosphorous on the electronic and optical properties of naphthoxaphospholes: theoretical investigation *Molecular Physics*. 116, 1581-1588.

100. Reda M. El-shishtawy, Shaaban A. Elroby, Abdullah M. Asiri and Klaus Mullen (2016) optical absorption spectra and electronic properties of symmetric and asymmetric squarine dye for use in DSSC solar cells: DFT and TD-DFT studies. *International journal of molecular sciences* 17. 1-12.

101. Malki Z. El, Bouachrine M, Hamidi M., Bejjit L, Haddad M., Serein-Spirau F., Lere Porte J.P, Marc Sotiropoulos J. (2013). New organic materials based on Thiadiazolothienopyrazine-Dithiophene for photovoltaic applications. International research, *Journal of Chemistry*. 4, 1-21.

102. Zhang Cai-Rong, Liu Zi-Jiang, Chen Yu-Hong, Chen Hong-Shan, Wua You-Zhi, Yuan Li-Hua (2009). DFT and TD-DFT study on organic dye sensitizers D5, DST and DSS for solar cells, *Journal of Molecular Structure,* **899,** 86-93.

103. Gupta Shipra Mital and Tripathi Mano A review on TiO_2 nanoparticles *Chinese Science bulletin physical chemistry.* **56** 2011 1639-1657

University of Venda

104. Beltran A., Gracia L. and Andres J. (2006). Density functional study of the brookite surfaces and phase Transitions between natural polymorphs. *Journal of Physical Chemistry B,* **110**. 23417-23423.

105. Tong Zhu and Shang-Peng Gao (2014). The stability, electronic structure, and optical property of TiO_2 polymorhs. *American Chemical Society*, **118**, 11385-11396.

106. Dorian A. H. Hanaor Charles C. Sorrell. (2011). Review of the anatase to rutile phase transformation. *Journal of Material Sciences*, **46**, 855–874.

107. Quiñones C., Vallejo W., Gordillo G. (2010). Structural, optical and electrochemical properties of TiO_2 thin films grown by APCVD method. *Applied Surface Science.* **256**, 4065–4071.

108. Behzad Rezaei, Hamid Mosaddeghi (2006) Applications of Titanium Dioxdie Nanocoating, Nano-*Technology in Environments Conference.* 1-3.

109. Ollis, D.F., Alekabi, Matthews R.W. (1993). Photocatalytic Purification and Treatment of Water and Air. *Elsevier.*

110. John C. I. Petra K, Eugene W. R. and Robert M. C. (1993) Inactivation of Escheria coli by Titanium Dioxide Photocatalytic Oxidation. Applied and Environmental Microbiology. *Applied and Environmental Microbiology,* 59, 1668-1670.

111. Bandaranayake, K.M.P, M.K. I. Senevirathna, P. Weligamuwa, K. Tennakone (2004). Dye sensitized solar cells made from nanocrystalline TiO_2 films coated with outer layers of different oxide materials. *Coordination Chemistry Reviews*, **248**, 1277–1281

112. DuPont (2013) Titanium Oxide (Titania, TiO_2) Nanoparticles Properties, Applications. *AZoNano*. 1-3.

185

113. William A. Vallejo L., Cesar A. Quiñones S. and Johann A. Hernandez S. (2011). The Chemistry and Physics of Dye-Sensitized Solar Cells, Solar Cells - Dye-Sensitized Devices, Prof. Leonid A. Kosyachenko (Ed.), ISBN: 978-953-307-735-2, 400 – 418. InTech. http://www.intechopen.com/books/solar-cells-dye-sensitizeddevices/The-chemistry-and-physics-of-dye-sensitized-solar-cells.

114. Dilli, Z. (2009). Intrinsic and Extrinsic Semiconductors, Fermi-Dirac Distribution Function, the Fermi level and carrier concentrations Review: Charge Carriers in Semiconductors, 1–8.

115. Pankove, J. I. Moustakas T.D. (eds.) (1998). Gallium Nitride I, Semiconductors and Semimetals, 50 (Academic Press, San Diego).

116. Klaus Jäger, Olindo Isabella, Arno H.M. Smets, René A.C.M.M. Copyright Delft University of Technology. Van Swaaij, Miro Zeman. (2014). Solar Energy Fundamentals, Technology, and Systems.

117. Becquerel, A. E. Mémoire sur les effets électriques produits sous l'influence des rayons solaires. Comptes Rendus (1839). **9**, 561-567.

118. Wiedenbeck, W. (2011). How a Photovoltaic Cell Works. *The NEED Project*, 20108.

119. Sze S. M. and Kwok K. Ng (2007). Physics of Semiconductor Devices. Third Edition. John Wiley & Sons, Inc. 1-815.

120. Greg Sun (2010). The Intersubband Approach to Si-based Lasers, Advances in Lasers and Electro Optics, Nelson Costa and Adolfo Cartaxo (Ed.), InTech, DOI: 10.5772/8672. Available from: http://www.intechopen.com/books/advances-in-lasers-and-electro-optics/the-intersubband-approach-to-si-based-lasers56. Chenming Hu 2009. Electrons and Holes in Semiconductors, 1-34.

121. Mi, M. (n.d.). Solar Photovoltaic (PV) Cells Science of Silicon PV Cells.

122. Chenming Hu (2009). Electrons and Holes in Semiconductors, 1-34.

123. Han H, Ba R (2009). Buoyant photocatalyst with greatly enhanced visible-light activity prepared through a low temperature hydrothermal method. *Industrial and Engineering Chemistry Research*, **48** 2891–2898

124. Mills A, Hunte A J. An overview of semiconductor photocatalysis (1997). *Journal of Photochemistry and Photobiology*, **108.** 1–35.

125. Corneliu I. Oprea, Petre Panait, Fanica Cimpoesu, Marilena Ferbinteanu and Mihai A. Gîrţu (2013). Density functional theory (DFT) study of coumarin-based dye adsorbed on TiO$_2$ nanoclusters—Applications to dye-sensitized solar cells. *Materials*, **6** 2372-2392.

126. Kalyanasundaram K., Grätzel, M. (1998). Applications of functionalized transition metal complexes in photonic and optoelectronic devices, *Coordination Chemistry Reviews,* **177**, 347- 414.

127. Elena Galoppini (2004). Linkers for anchoring sensitizers to semiconductor nanoparticles, *Coordination Chemistry Reviews,* **248,** 1283–1297.

128. Maryam Adineh, Pooya Tahay, Mohsen Ameri, Nasser Safari and Ezeddin Mohajerani (2016). Fabrication and analysis of dye-sensitized solar cells (DSSCs) using porphyrin dye with catechol anchoring groups *RSC Adv.* **6**, 14512-14521.

129. Sanchez-de-Armas, R., San Miguel.M.A.,Oviedo, J., Sanz,J.F., (2012). Coumarin derivatives for dye sensitized solar cells: a TD-DFT study. *Physical. Chemistry Chemical Physics,* **14**, 225-233.

130. Pastore M., de Angelis, F. (2012). Computational modelling of TiO_2 surfaces sensitized by organic dye with different anchoring groups: Adsorption modes, structure and implication for electron injection/recombination. *Physical. Chemistry. Chemical Phys*ics, **14**, 920-928.

131. Pérez León C., Kador L., Peng B. and Thelakkat M. (2006). Characterization of the adsorption of Ru-bpy dye on mesoporous TiO_2 films with UV-Vis, Ra man, and FTIR spectroscopies. *Journal of Physical Chemistry B.* **110**, 8723-8730.

132. Prajongtat P., Suramitr S., Nokbin S., Nakajima K., Misuke K. and Hannongbua S. Density functional theory study of adsorption geometries and electronic structures of azo-based molecules on anatase TiO_2 surface for dye-sensitized solar cell applications. *Journal of Molecular Graphics and Modelling.* **76**, 551-561(2017).

133. Chiara A., Edoardo M., Mariachiara P., Enrico R. and Fillipo De Angelis. (2012) Adsorption of organic dye on TiO_2 surfaces in dye-sensitized solar cells: interplay of theory and experiment. *Physical Chemistry Chemical Physics* **14,** 15963-15974.

134. Hou Xing Gang, Huang MeiDong, Wu XiaoLing and Liu AnDong (2009) First-principles calculations on implanted TiO_2 by 3d transition metal ions. *Science China Ser G-Physics Mechanical Astronomy,* **52**, 838-842.

135. Jun Zhang, Lisha Qian, Wei Fu, Junhua Xi and Zhenguo Ji (2014). Alkaline- Earth metal Ca and N codoped with TiO_2 with exposed (001) facets for enhancing visible light photocatalytic activity. *American Ceramic Society***, 97**, 2615-2622.

136. Xu Wenhui, Ma Xingo, Tong Wu, He Zhigi, Wang Huihu and Huang Chuyun (2014). First-principles study on the synergistic effects of codoped TiO_2 photocatalysts codoped with N/V or C/Cr. *Journal of Semiconductors*, **35**. 1-7.

137. Leonardo Triggiani, Ana Belen Munoz-Garcia, Angela Agostiano and Michele Pavone (2015). First principles study of Trimethylamine adsorption on anatase TiO_2 nanorod surfaces. *Theoretical Chemistry Accounts,* 1**34**, 119 1-11.

138. Veronica M. Sanchez, Ezequiel de la Llave and Damian A. Scherlis (2011). Adsorption of R-OH Molecules on TiO_2 Surfaces at the solid-liquid interface. *American Chemical Society*, **27,** 2411-2419.

139. Carsten A. Ullrich (2014). Time-Dependent Density-Functional Theory: Features and Challenges, with a Special View on Matter under Extreme Conditions. *Springer International Publishing Switzerland.* Lecture Notes in Computational Science and Engineering **96**, 1-21.

140. Galadanci G.S.M., Garba Babaji (2013). Computations of the Ground State Cohesive Properties of Alas Crystalline Structure Using Fhi-Aims Code. *Journal of Applied Physics (IOSR-JAP),* **4**, 85-95.

141. Thomas, L. H. (1926). Proc. Cambridge Philos. Soc. 23,542.

142. Fermi E. (1928) *Z. Physics Reviews,* **48**, 73.

143. Hohenberg P., Kohn W. (1964). Inhomogeneous Electron Gas. *Physical Reviews B,* **136**, 864.

144. Jeng-Da Chai and John D. (2004). Weeks Modified Statistical Treatment of Kinetic Energy in the Thomas-Fermi Model. *Journal of Physical Chemistry B,* **108**, 6870-6876.

145. Kohn W., Sham, L. J. (1965). Self-Consistent Equations Including Exchange and Correlation Effects. *Physics Reviews A,* **140**, 1133.

146. St-Amant A., Cornell W. D., Kollman P. A., and Halgren T. A. (1995). Calculation of molecular geometries, relative conformational energies, dipole moments, and molecular electrostatic potential fitted charges of small organic molecules of biochemical interest by density functional theory. *Journal of Computational Chemistry,* **16**, 1483-1506.

University of Venda

147. Perdew J. P., Burke K., Ernzerhof M. (1996). Generalized Gradient Approximation Made Simple. *Physics Review Letter*, **77**, 3865.

148. Becke A. D. (1992). Density-functional thermochemistry. III. The role of exact exchange. *Journal of Chemical Physics*, **98**, 5648.

149. Becke A. D (1988). Density-functional exchange-energy approximation with correct asymptotic behaviour**.** *Physical Reviews. A*, **38**, 3098.

150. Lee C., Yang W., Parr R. G. (1988). Development of the Colle-Salvetti correlation-energy formula into a functional of the electron density. *Physics Reviews B, Condensed Matter,* **37**, 785.

151. Becke A. D., (1989) The Challenge of d and f Electrons: Theory and computation. *American Chemical Society*, **394,** 165-167.

152. Vosko S. H., Wilk L., and Nusair M. (1980). Accurate spin-dependent electron liquid correlation energies for local spin density calculations: a critical analysis. *Canadian Journal of Physics*, **58**, 1200-1211.

153. Eugene S. K. (2013) Density Functional Theory and Molecular Interactions: Dispersion Interactions. *Structural Bond,* **150**, 65–96.

154. Bultinck P., Van Damme S. Acke G. (2015). Hands-on Session: Advanced topics in Gaussian. 1-16.

155. Roothaan C.C.J. (1951). New Developments in Molecular Orbital Theory. *Reviews of Modern Physics,* **23**, 69.

156. Hall G.G. (1951). Proceeding of Royal Society London Sr. A 205, 541.

157. Hall G.G. (1951). Proceeding of Royal Society London Sr. A 208, 328.

University of Venda

158. Blochl P.E (1994) Projector augumented wave method, *Physical Review B*, **50**, 17953.

159. Mortensen J.J, Hansen L.B and Jacobsen K.W (2005). Real space grid implementation of the projector augumented wave method (GPAW). *Physical Review B*, **71**. 035109 1-11

160. Boys S.F. (1950). Electronic wave functions, A general method of calculation of stationary states of any molecular system. *Proceedings of the Royal Society* (London) A 200, 542-544.

161. McWeeny R (1950). Gaussian approximations to wavefunctions. *Nature* **166**, 21-22.

162. Arpan Deb. (2012). Lacunes charg_ees, _etude dans des nano-agr_egats de silicium. Autre [cond-mat.other]. Universit_e de Grenoble, Fran_cais. Study of charged defects of silicon.

163. Ernest R. Davidson, David Feller (1986). Basis set selection for molecular calculations *Chemical Reviews. 86* (4), 681–696.

164. Kobayashi K (1999) Norm-conserving pseudopotential database (NCPS97) *Computational Materials Science,* **14**, 72-76.

165. Vanderbilt David (1990) Soft self-consistent pseudopotentials in a generalized eigenvalue formalism. *Physical Review B, American Physical Society*, **41**, 7892–7895.

166. Clark S.J., Segall M.D., Pickard C.J., Hasnip P.J., Probert M.J., Refson K., Yates J.R., Payne M.C. (2005). Fiirst principle methods using CASTEP. *Zeithchrift fuer Kristallographie* **220** (5-6), 576-570.

167. N.M. O'Boyle, A.L. Tenderholt and K.M. Langner (2008) ADF analyser and GAMESS analyser Analyze ADF GAMESS ADF Analyse Gaussian. *Journal of Computational Chemistry,* **29,** 839-845.

168. Hanwell, Marcus D; Curtis, Donald E; Lonie, David C; Vandermeersch, Tim; Zurek, Eva; Hutchison, Geoffrey R (2012). Avogadro: An advanced semantic chemical editor, visualization, and analysis platform. *Journal of Chemistry inform*ation **4***,* 17. *doi*:*10.1186/1758-2946-4-17. PMC 3542060. PMID 22889332.*

169. Monkhorst H.J Pack J.D. (1976). Special points for Brillouin Zone integrations. *Physical. Reviews. B*, **13**, 5188-5192.

170. Anthonysamy A. Lee Y. Karunagaran et al., (2015) Molecular design and synthesis of ruthenium (II) sensitizers for highly efficient dye-sensitized solar cells. *Journal of Materials Chemistry*, 21**,** 12389-12397.

171. Goncalves L. M., Bermudez V. D Z., Ribeiro H. A., and Mendes A. M. (2008). Dye-sensitized solar cells: A safe bet for the future. *Energy and Environmental Sciences,* **1** 655–667.

172. Mary Rosana N. T., Joshua Amarnath. D., Vincent Joseph K. L., Suresh A., Anandan S., Saritha G. (2014). Natural Sensitizers for Dye Sensitized Solar Cell Applications *International Journal of Scientific & Engineering Research*, **5**, 340-344.

173. Narges M., and Feng W. (2014). First principle study of Carbz-PAHTDDT dye sensitizer and two CArbz-derived dye for dye sensitized solar cells, *Journal of Molecular Model,* **20,** 1-9.

174. Jinxia L., Chun Z., Zexing C. (2013). Electronic and optical properties of the triphenylamine based organic dye sensitized TiO_2 semiconductor: insight from first principles calculations. *Physical Chemistry Chemical Physics*, **15**, 13844-13851.

175. Ito S., Chen P., Comte P., Nazeeruddin M. K., Liska P., Pechy P. and Gratzel M. (2007). Fabrication of Screen-Printing Pastes from TiO$_2$ Powders for Dye-Sensitised Solar Cells. *Progress in Photovoltaics*, **15**, 603-612.

176. Shankar K., Mor G.K., Prakasam H.E., Yoriya S., Paulose M., Varghese O.K. and Grimes C. A. (2007). Highly-ordered TiO$_2$ nanotube arrays up to 220 µm in length: use in water photoelectrolysis and dye-sensitized solar cells. *Nanotechnology*, **18**, 065707.

177. Gratzel M. (2001). Photoelectrochemical cells. *Nature* **414** 338-344.

178. Y Ogomi, T kato, S Hayase. (2006) Dye sensitized solar cells consisting of ionic liquid and solidification. *Journal of photopolymer Science and Technology*, **19** 403-408.

179. Park, J., Viscardi, G., Barolo, C., & Barbero, N. (2013) Near-infrared sensitization in dye-sensitized solar cells. *CHIMIA International Journal of Chemistry*, **67,** 129-135.

180. Ma, W., Zhang, F., & Meng, S. (2014) Atomic Scale Investigation of dye sensitized solar cells interface structure and dynamics. *ArXiv preprint arXiv: 1406.3111.*